

Synthesis and Catalytic Application of Functional Transition Metal Oxides

Dissertation zur Erlangung des Doktorgrades
der Naturwissenschaften

Fakultät für Chemie
Universität Bielefeld

Vorgelegt von
Patrick Mountapmbeme Kouotou
Bielefeld 2014

„Gedruckt mit Unterstützung des Deutschen Akademischen Austauschdienstes“

*This work is dedicated to my family for their unending
love and encouragement throughout my PhD journey.*

ACKNOWLEDGEMENT

It is with pleasure that I show appreciation to all those who have contributed in one way or the other to see me through this uphill task.

First and foremost, I would like to thank God Almighty for giving me the strength and courage to carry out my PhD study successfully over the past three years.

I would like to address heartfelt thanks to the German academic exchange service (DAAD) for the financial support that has made this study possible and easy in Germany.

I am especially and sincerely grateful to my supervisor Prof. Dr. Katharina Kohse-Höinghaus to have accepted me as PhD student in her research group, thus giving me the opportunity to meet all the nice people I worked with. I am very grateful for her continuous support and understanding during these three years. She was always there for open discussion, related or not to my research topic.

I would like kindly to thank PD Dr. Tilman Kottke for his academic support, his willingness to be the second examiner of this work and for giving his precious time to review this work.

At the same time I would like also to thank our secretary Frau Regine Schröder for her great help in administrative staff and above all for her kindness which made me feel welcome since I joined the PC 1 group. Mr. Harald Warterbör is acknowledged for his precious assistance.

I give my thanks to the former CVD group members for all the help that they offer: to Prof. Dr. Zhenyu Tian for his useful contribution in shaping this thesis, to Dr. Vincent Vannier, Dr. Patrick Hervé Tchoua Ngamou, for their experiences shared with me, and last but not at least, to Mr. Udo Mundloch and Mr. Ashraf El-Kasmi.

I am grateful to the whole PC1-group whom I cannot name individually; specific thanks go to apl. Prof. Andreas Brockhinke for the laboratory security instruction, to the inseparable Ms. Julia Krüger and Ms. Lena Böhling for having facilitated wherever possible my integration in Germany. Mr. Daniel Felsmann, Ms. Marina Schenk, Ms. Friederike Herrmann who showed me how challenges should be overcome in a “proper German way”.

I extend my thanks to Dr. Naoufal Bahlawane for his precious and helpful suggestions in the beginning of my thesis.

To my entire African friends in Germany, for their encouragement during the difficult moments.

Last but not least, I would like to thank my wife Eveline Mountapmbeme Ndoyoum, my children Gloria and Jessy who have supported with patience my absence during the last two years of my PhD study. My sister Charlotte K. Pelumo is kindly acknowledged for her unending support.

LIST OF ABBREVIATIONS

acac	Acetylacetonate ($\text{CH}_3\text{COCHCOCH}_3$)
CVD	Chemical Vapor Deposition
DME	Dimethyl ethers
Ea	Activation Energy
EDS	Energy Dispersive Spectrometer
FTIR	Fourier Transform InfraRed
HIM	Helium Ion Microscopy
MBMS	Molecular Beam Mass Spectrometer
MOCVD	Metal Organic Chemical Vapor Deposition
PSE-CVD	Pulsed Spray Evaporation Chemical Vapor Deposition
PVD	Physical Vapor Deposition
SEM	Scanning Electron Microscopy
TMO	Transition Metal Oxide
THF	Tetrahydrofuran
UV-Vis	Ultra-Violet Visible
WHSV	Weight Hourly Space Velocity
XRD	X-Ray Diffraction
XPS	X-ray Photoelectron Spectroscopy

ABSTRACT

Carbon monoxide and volatile organic compounds (VOCs) are serious air pollutants that may give rise to deleterious health and environmental effects. Such compounds are commonly found in the atmosphere at ground level in all urban and industrial centers. Total catalytic combustion has been considered as an effective and viable approach in controlling environmental emission; however some problems such as the non-availability of catalysts with low cost, high activity and stability in prevailing conditions remain. Hence, this thesis aims at developing economic combustion catalysts such as transition metals oxides (TMOs), using an elaborated Pulsed Spray Evaporation Chemical Vapor Deposition (PSE-CVD) approach and improved understanding of their behavior.

Catalysts based on TMOs were successfully synthesized by PSE-CVD. Comprehensive characterization techniques, e.g. X-ray diffraction (XRD), Raman spectroscopy, Fourier transformed infrared spectroscopy (FTIR), Scanning electron microscopy (SEM), Helium ion microscopy (HIM), Energy dispersive spectroscopy (EDS), X-Ray photoelectron spectroscopy (XPS) and Ultra-Violet Visible spectroscopy (UV-Vis) as well as temperature-programmed reduction/re-oxidation (TPR/TPO) techniques were used to characterize the obtained films. To assess their functionality, the catalytic performance of the prepared catalysts was investigated for the conversion of some representative volatile organic compounds which may be contained in exhaust stream of industrial processes.

One important conclusion that can be drawn based on the results presented is that TMOs are active catalysts with real potential mainly in processes relevant to air pollution control. Aiming for eventual commercial applications of some very active TMOs catalysts, fundamental studies concerning various aspects of TMOs catalysis have been carried out throughout this thesis. The investigations have been performed using TMO-based catalysts deposited on supports, with grid mesh of stainless steel as the common used substrates. Five main types of TMO-based catalysts were prepared, including single oxides such as Co_3O_4 , Mn_3O_4 , $\alpha\text{-Fe}_2\text{O}_3$, CuO and mixed oxides (Co-Fe oxides). Several reactions with direct relevance to air-pollution control were studied, i.e. oxidation of carbon monoxide (CO), propene (C_3H_6), *n*-butene (*n*- C_4H_8), dimethyl ether ($\text{C}_2\text{H}_6\text{O}$) and *n*-butanol (*n*- $\text{C}_4\text{H}_8\text{O}$) in the presence of argon and oxygen. The catalytic performance of the chosen oxides was compared to reference results from the literature.

Different aspects of these reactions were studied: (i) the effect of solvent and deposition temperature on the catalyst morphology, (ii) the effect of the deposition condition (substrate temperature), the thermal properties, the morphology and the doping on the catalyst performance. In our preliminary results, we briefly describe the controlled synthesis of Co_3O_4 spinel using $\text{Co}(\text{acac})_3$ as precursor; in this investigation, special attention was focused on the role played by solvents, deposition temperature and pressure on the thin film growth and morphology. As application, the performance of the deposited Co_3O_4 samples was tested towards CO and C_3H_6 conversion (**Publication 1**). As interesting materials, $\alpha\text{-Fe}_2\text{O}_3$, CuO and Mn_3O_4 were also prepared. Thin films of $\alpha\text{-Fe}_2\text{O}_3$ were selectively synthesized, and the effect of the deposition temperature and lattice oxygen on the catalytic combustion of C_3H_6 and CO was studied (**Publications 2 and 3**).

In the same logic, copper oxide was prepared and found to be catalytically active towards CO and C_3H_6 oxidation (**Publication 4**). Besides the activity, the thermal properties of the catalyst were investigated, and a detailed study of the synthesis of the catalytically active Mn_3O_4 spinel and its thermal stability were performed. The obtained Mn_3O_4 exhibited high thermal stability and good catalytic performance in the combustion of CO and C_3H_6 (**Publication 5**).

Based on the results obtained with Co_3O_4 and $\alpha\text{-Fe}_2\text{O}_3$, we have prepared a mixed oxide of cobalt and iron (Co-Fe-O). Cobalt ferrite with spinel structure has presented technologically interesting solid-solution phases. In fact the combination of Fe and Co at different ratios has improved the physico-chemical properties and the catalytic performance of the materials. It was noticed that the composition played a significant role concerning the film morphology, band gap energy and the redox properties with consequence for the catalytic behavior of the material. For example, just small amounts of cobalt in cobalt ferrite mixed oxides were sufficient to enhance the performance in the CO oxidation (**Manuscript 1**) and the deep oxidation of olefins (such as for *n*-butene and propene) and DME (**Manuscript 2**).

In the framework of a cooperation project with Moroccan partners with the topic “Catalytic application of natural clay”, we have compared the catalytic performance of Moroccan natural clays with Co_3O_4 and $\alpha\text{-Fe}_2\text{O}_3$ towards the conversion of *n*-butanol (**Publication 6**).

SCIENTIFIC CONTRIBUTIONS

Peer-reviewed publications

- 1) **P. Mountapmbeme Kouotou**, Z.-Y. Tian, U. Mundloch, N. Bahlawane and K. Kohse-Höinghaus, Controlled synthesis of Co_3O_4 spinel with $\text{Co}(\text{acac})_3$ as precursor. *RSC Advances* **2**, 10809-10812, 2012.
- 2) **P. Mountapmbeme Kouotou**, Z.-Y. Tian, H. Vieker, A. Beyer, A. Götzhäuser and K. Kohse-Höinghaus, Selective synthesis of $\alpha\text{-Fe}_2\text{O}_3$ thin films and effect of the deposition temperature and lattice oxygen on the catalytic combustion of propene. *Journal of Materials Chemistry A* **1**, 10495-10504, 2013.
- 3) **P. Mountapmbeme Kouotou**, Z.-Y. Tian, H. Vieker and K. Kohse-Höinghaus, Pulsed-spray evaporation CVD synthesis of hematite thin films for catalytic conversion of CO. *Surface and Coatings Technology* **230**, 59-65, 2013.
- 4) Z.-Y. Tian, H. J. Herrenbrück, **P. Mountapmbeme Kouotou**, H. Vieker, A. Beyer, A. Götzhäuser and K. Kohse-Höinghaus, Facile synthesis of copper oxide from alcohol-assisted CVD. *Surface and Coatings Technology* **230**, 33-38, 2013.
- 5) Z.-Y. Tian, **P. Mountapmbeme Kouotou**, N. Bahlawane, and P. H. Tchoua Ngamou, Synthesis of catalytically active Mn_3O_4 spinel and its thermal properties. *Journal of Physical Chemistry C* **117**, 6218-6224, 2013.
- 6) Z.-Y. Tian, T. Chafik, M. Assebban, S. Harti, N. Bahlawane, **P. Mountapmbeme Kouotou** and K. Kohse-Höinghaus, Towards biofuel combustion with an easily extruded clay as a natural catalyst. *Applied Energy* **107**, 149-156, 2013.
Corrigendum to: Z.-Y. Tian, T. Chafik, M. Assebban, S. Harti, H. J. M. Gatica, G. A. Cifredo, N. Bahlawane, **P. Mountapmbeme Kouotou**, K. Kohse-Höinghaus, Towards biofuel combustion with an easily extruded clay as a natural catalyst [*Applied Energy* 107 (2013) 149-156] *Applied Energy* **108**, 528-529, 2013.

Manuscripts revised

- M1) **P. Mountapmbeme Kouotou**, H. Vieker, Z.-Y. Tian, P. H. Tchoua Ngamou, A. El Kasmi, A. Beyer, A. Götzhäuser and K. Kohse-Höinghaus, Structure-activity relation of Fe-Co spinel-type oxide in CO oxidation. *Catalysis Science Technology* (**Revised**).
- M2) Z.-Y. Tian, **P. Mountapmbeme Kouotou**, A. El Kasmi, P. H. Tchoua Ngamou, K. Kohse-Höinghaus, H. Vieker, A. Beyer and A. Götzhäuser, Low-temperature deep oxidation of olefins and DME over cobalt ferrite. *Proceedings of the Combustion Institute* (**Revised**).

Conference papers

- 1) **P. Mountapbeme Kouotou***, Z.-Y. Tian, U. Mundloch, M. Assebban and P. H. Tchoua Ngamou, Functional materials for catalytic combustion. *Proceedings of the 6th European Combustion Meeting 2013*, Lund, Sweden.
- 2) Z.-Y. Tian and **P. Mountapbeme Kouotou**, Facile synthesis and catalytic application of oxide thin films on flexible substrates. *Proceedings of the 6th European Combustion Meeting, 2013*, Lund, Sweden.

Presentations

- 1) **P. Mountapbeme Kouotou**, Z.-Y. Tian and K. Kohse-Höinghaus, Synthesis of Co₃O₄ spinel by PSE-CVD and its application in catalytic combustion of *n*-butanol. *111. Hauptversammlung der Deutschen Bunsen-Gesellschaft für Physikalische Chemie* 17.-19.5.2012, Leipzig, Germany. **(poster)**
- 2) **P. Mountapbeme Kouotou**, Z.-Y. Tian*, U. Mundloch and K. Kohse-Höinghaus, Catalytic combustion of CO and propene over Co₃O₄ spinel prepared by chemical vapor deposition. *The 34th International Symposium on Combustion*, 29.7.-3.8.2012, Warsaw, Poland. **(poster)**
- 3) Z.-Y. Tian*, T. Chafik, M. Assebban, S. Harti, N. Bahlawane, **P. Mountapbeme Kouotou** and K. Kohse-Höinghaus, Catalytic activity of natural clay toward the combustion of biofuel. *The 34th International Symposium on Combustion*, 29.7.-3.8.2012, Warsaw, Poland. **(poster)**
- 4) **P. Mountapbeme Kouotou***, U. Mundloch and Z.-Y. Tian, Synthesis of functional transition metal oxides by PSE-CVD and investigation of their activity towards the catalytic combustion of biofuel, VOC and exhaust stream. *The 2nd German-Japanese workshop: Nanomaterials for Energy application*, 9.7.2012 Duisburg-Essen, Germany. **(poster)**
- 5) Z.-Y. Tian* and **P. Mountapbeme Kouotou**, Facile synthesis and catalytic application of oxide thin films on flexible substrates. *The 6th European Combustion Meeting*, 25.-28.6.2013, Lund, Sweden. **(poster)**
- 6) **P. Mountapbeme Kouotou***, Z.-Y. Tian, U. Mundloch, M. Assebban and P. H. Tchoua Nganou, Functional materials for catalytic combustion. *The 6th European Combustion Meeting*, 25.-28.6.2013, Lund, Sweden. **(poster)**
- 7) **P. Mountapbeme Kouotou** and Z.-Y. Tian*, Easy synthesis of hematite thin film by pulsed spray evaporation CVD. *EuroCVD 19*, 1.-6.8.2013, Varna, Bulgaria. **(poster)**
- 8) Z.-Y. Tian* and **P. Mountapbeme Kouotou**, Facile synthesis of copper oxide from alcohol-assisted CVD, *EuroCVD 19*, 1.-6.8.2013, Varna, Bulgaria. **(talk)**

- 9) H. Vieker*, A. Beyer, Z.-Y. Tian, **P. Mountapbeme Kouotou**, A. El Kasmi, K. Kohse-Höinghaus and A. Gölzhäuser, HIM of CVD-grown films: transition metals and catalytically active transition metal oxides. *AVS 60th International Symposium & Exhibition*, 27.10.-1.11.2013, Long Beach, CA, USA. **(talk)**
- 10) Z.-Y. Tian*, **P. Mountapbeme Kouotou** and K. Kohse-Höinghaus, Catalytic combustion of propene over transition metal oxides The International Workshop on Frontiers of Combustion Chemistry, 26.-29.09.2013, Huangshan, China. **(talk)**
- 11) Z.-Y. Tian*, **P. Mountapbeme Kouotou**, A. El Kasmi, P. H. Tchoua Ngamou, K. Kohse-Höinghaus, H. Vieker, A. Beyer and A. Gölzhäuser. Low-temperature deep oxidation of olefins and DME over cobalt ferrite. *The 35th International Symposium on Combustion*, 3-8. 8. 2014, San Francisco, California, USA. **(talk)**

* *The presenter is identified with an asterisk.*

TABLE OF CONTENTS

ACKNOWLEDGEMENT	i
LIST OF ABBREVIATIONS	iii
ABSTRACT	v
SCIENTIFIC CONTRIBUTIONS	vii
TABLE OF CONTENTS	xi
1 INTRODUCTION	1
1.1 Research motivation and theoretical background.....	3
1.1.1 Atmospheric pollution and consequences	3
1.1.2 Catalysis and catalytic combustion	4
1.1.3 Catalysts for catalytic combustion.....	6
2 EXPERIMENTAL.....	9
2.1 Chemical vapor deposition process	9
2.1.1 Pulsed spray evaporation CVD reactor and systems	10
2.1.2 Thin film preparation.....	12
2.2 Thin film characterization techniques	14
2.2.1 Structure characterization	14
2.2.2 Morphology and chemical composition	19
2.2.3 Optical properties: UV-Vis spectroscopy.....	24
2.2.4 Thermal properties.....	25
2.2.5 Molecular beam mass spectrophotometer (MBMS).....	26
2.2.6 Catalytic performance investigation.....	27
3 RESULTS.....	31
3.1 PSE-CVD of Co_3O_4 starting from β -diketonate precursor in different solvent system.....	31
3.1.1 Effect of aging on the stability and UV-Vis spectrum of the liquid feedstock.....	32
3.1.2 Co_3O_4 thin film growth and structural characterization.....	33
3.1.3 Catalytic performance of Co_3O_4 towards CO and propene combustion.....	35
3.2 PSE-CVD of catalytically active α - Fe_2O_3 thin films for the deep oxidation of C_3H_6	38
3.2.1 Growth and characterization.....	38
3.2.2 Thermal properties.....	42
3.2.3 Catalytic performance	43
3.3 PSE-CVD of catalytically active CuO thin film catalyst for CO and C_3H_6 oxidation	47
3.3.1 Growth and phase dependence on deposition condition.....	47
3.3.2 Catalytic performance	49

Table of contents

3.4	PSE-CVD of Mn_3O_4 and investigation of its catalytic properties and thermal stability	52
3.4.1	Growth and characterization.....	52
3.4.2	Catalytic performance	54
3.5	Active cobalt ferrite for low temperature catalytic combustion	57
3.5.1	Growth and characterization.....	57
3.5.2	Catalytic performance in the total oxidation of CO, C_3H_6 , $n-C_4H_8$ and C_2H_6O	61
4	SUMMARY AND OUTLOOK.....	65
A)	Publication 1.....	69
B)	Publication 2.....	81
C)	Publication 3.....	101
D)	Publication 4.....	111
E)	Publication 5.....	119
F)	Manuscript 1	133
G)	Manuscript 2.....	149
H)	Publication 6.....	177
	Bibliographic References	189

Major parts of this work have been published in the literature [1-6]. Therefore, the present work is limited to a brief presentation of the experimental procedures and a summary of the obtained results and main findings of the attached publications.

1 INTRODUCTION

In the last two decades, the rapid growth in population, industrialization and transportation have caused an ever-increasing demand for energy [7]. The need to satisfy the population's demand has created other problems such as pollution. Over the years, we have met our energy needs by exploiting two main sources: natural gas and crude oil. However, this is not a recipe for the successful and continuous increase of energy needs. As the most used source of energy, fossil fuels are responsible for high emissions of VOCs, exhaust streams and polynuclear aromatics associated with the combustion systems used to produce energy [8].

VOCs are considered as an important class of air pollutants [8]. It is a widely ranging class of chemicals commonly occurring in many commercial waste streams, and has been linked to the increase in photo-chemical smog, the depletion in atmospheric ozone, the production of ground-level ozone, as well as the noxious effects on human health [8].

The significance of abatement technologies for the reduction of emissions has increased in importance with the introduction of legislation to control their release to the environment. Various techniques have been proposed, one of these being heterogeneous catalytic oxidation. It has the advantage over the more common thermal oxidation process, since it requires little or no supplementary fuel and is therefore a less expensive process. Catalytic oxidation is less expensive only for relatively dilute streams of VOCs-containing gases and exhaust stream. For more concentrated gas streams, thermal oxidizers, which are less capital-intensive, may be less costly to operate if the VOC content is highly enough to be thermally self-sustaining. However, relatively dilute VOC-containing effluent streams are by far the most prevalent and, consequently, catalytic oxidation is an important process.

However, the characteristics of the catalyst selected for this process are of vital importance for successful process operation, and associated problems such as deactivation must be overcome if heterogeneous catalytic oxidation is to be useful commercially. Catalysts currently in use include noble metals, notably gold, platinum and palladium, and those based on metal oxides. Irrespective of the type of catalyst, the prime characteristics required are activity and selectivity as well as stability for combustion. On one hand, noble metals offer high catalytic performance at low temperature, but they are generally costly, thermally unstable and are

easily deactivated due to the trend of particle agglomeration and thus decrease of the surface area [9]. On the other hand transition metal oxides (TMOs) are very cheap and show also comparable activity with precious metals; moreover they possess good thermal properties. Therefore special attention has been focused on different kinds of transition metal oxides and their mixed oxides [10].

As an intended contribution to the heterogeneous catalysis and catalyst synthesis, the present PhD study was proposed and developed. The aim is to achieve clean materials for green sustainable chemistry, which strives to reduce environmental emissions and associated risks, hazards and costs. A series of active and low-cost transition metal oxides were prepared, by means of pulsed spray evaporation chemical vapor deposition (PSE-CVD). The synthesized samples were comprehensively characterized in terms of growth, structure, morphology, optical, thermal and redox properties. Their catalytic performance was tested against the deep oxidation of real fuels and exhausts gases such as propene (C_3H_6), *n*-butene (*n*- C_4H_8), dimethyl ether (C_2H_6O), carbon monoxide (CO) and *n*-butanol (*n*- C_4H_8O).

In this work, the synthesis of a number of catalysts for the total oxidation of compounds that may be classified as VOCs, biofuel and Carbon monoxide are reported, and the important features of the catalyst highlighted using oxygen as oxidant. The following discussion is not intended to be an exhaustive account of all possible catalysts, but should provide an overview of the current state of research in this area, with the aim of identifying the types of catalysts that are likely to be of use in the future, and the obstacles that must be overcome to produce a commercially viable catalyst. The development of a catalyst that may be used for the combustion of all classes of compounds under the general term VOC presents a major challenge for future research.

The structure of the thesis is as follows: **Part 1** is a theoretical background and research motivation. **Part 2** reports briefly the comprehensive presentation of preparation methods as well as all sample characterization techniques used in this thesis (XRD, Raman, FTIR, SEM/HIM, UV/Vis, TPO/TPR, XPS and EDS). **Part 3** gives a summary of the obtained results while the last **Part 4** gives general conclusions of the most relevant results presented in the form of journal articles.

1.1 Research motivation and theoretical background

1.1.1 Atmospheric pollution and consequences

Air is essential for the survival of human beings as well as the whole environment. No life is possible without air. Therefore, the lack of clean air can lead to severe health problems and even to death. Today, some disturbances are observed on the ozone layer, on human, plant, and animal health which are caused by the release of substances into the air by human activities. Smog, soot, acid rain, the greenhouse effect, and "holes" in the ozone layer are generally discussed as the main types of pollution [8]. Each of these problems has serious implications for our health and well-being as well as for the whole environment. Research during the past 20-30 years confirms that air pollution contributes to morbidity and mortality [11,12]. Whereas some effects may be related to short-term exposure [13], others have to be considered contributions of long-term exposure [14,15]. Despite decades of efforts to fight against air pollution, humankind seems to lose the battle of clean air. Today, more than a billion people live in communities that do not meet air quality standards given by the World Health Organization [8]. Consequently, once considered as an urban phenomenon in industrial countries, air pollution has spread worldwide, also as a result of further industrialization. Among the different types of air pollution, great attention should be paid to the release of particles into the air from burning fuel for energy. A good example of these particularly small parts of matter release into the atmosphere is diesel smoke, contributing to "black carbon" pollution. However, the major sources of air pollution are the exhaust gases from fuels burning in automobiles and industries [16]. The release of noxious gases like carbon monoxide, nitrogen oxides (NO_x), sulfur oxides (SO_x), VOCs and chemical vapors contributes to further chemical reactions once they are in the atmosphere and may be responsible of serious damage in the human health and environment [17].

Thousands of people in the world die each year due to heart and lung diseases that result from air pollution [18]. In fact, associations with acute exposure to particulate air pollution are responsible of various morbidity health endpoints, including increased health care visits for respiratory illness, exacerbations of asthma, increased incidence and duration of respiratory symptoms, and declines in measures of lung function [19]. Therefore it is very urgent to reduce emission and many investigations are currently made by scientists for that purpose. As an example, catalytic combustion is developed as viable approach and numerous investigations on the development of clean materials such as catalyst are one of the main research topics today.

1.1.2 Catalysis and catalytic combustion

The words catalysis, catalysts and catalytic combustion are commonly used in the field of chemistry, chemical engineering, materials science and biology. Catalysis is a key technology in chemical industry and plays a vital role in our modern society [20]. Most of the products and chemicals used in our daily life are produced by the use of catalysis at one stage or another [20]. Catalysts are widely used in the pharmaceutical industry, in the production of fuels and plastics, and in solving air and water pollution problems [20]. Because most aspects of modern living is dependent on catalysis, it has become a topic that is well worth studying and understanding [21,22] and a significant investigation is devoted to its improvement. In fact, what is catalysis?

It was in 1836 that the field of catalysis was introduced for the first time, when J. J. Berzelius defined the phenomenon of catalysis in order to explain different transformation reactions [23]. Few years later, W. Ostwald proposed in 1895 a definition for a catalytic material (Nobel Prize 1909) that is still valid today. According to Ostwald, "A catalyst is a substance, which affects the rate of a chemical reaction without being part of its end products." [24]. From the Ostwald definition of catalyst, catalysis can be defined as an increase in the rate of a chemical reaction due to the participation of a chemical substance. This chemical substance called catalyst is usually used in small amounts relative to the reactants; it modifies and increases the rate of the reaction without being consumed in the process. A chemical process which uses a catalyst to speed desired oxidation reactions of a fuel and reduces the formation of undesired products is called catalytic combustion. This chemical reaction involves breaking of bonds between atoms and the formation of new ones [25]. The process is associated with transformation of energy and the energy diagram, illustrating the progress of a reaction $A+B \rightarrow C$ is presented schematically in Figure 1.1. The activation energy E_a to be surmounted can be determined from the Arrhenius equation (1.1):

$$k = A e^{-\frac{E_a}{RT}} \quad (1.1)$$

where k is the rate constant of chemical reactions, T is the temperature, A is the pre-exponential factor and R is the universal gas constant. Accordingly not all molecular encounters will be successful, but only a fraction $e^{-E_a/RT}$. An increase of the reaction rate can be achieved by either increasing the temperature or by lowering the activation energy E_a [25]. The latter is provided by the catalyst which, through the formation of intermediate compounds with the molecules involved in the reaction, enables an alternate reaction path as presented in

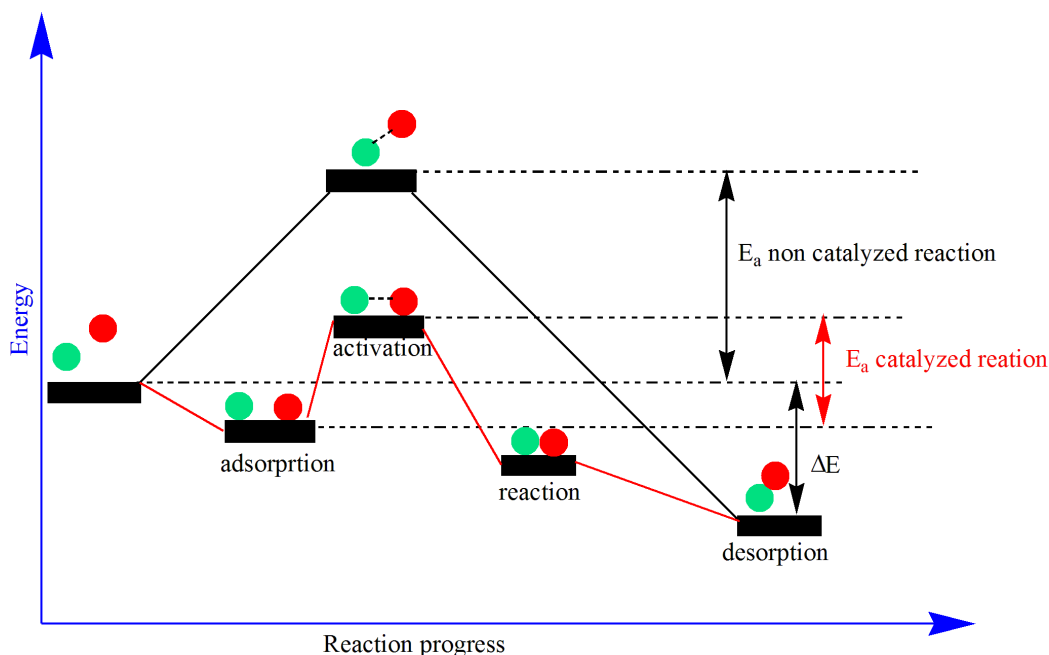


Figure 1.1: Comparison of the E_a barriers of a reaction with and without a catalyst. A substantial energy barrier has to be overcome in the non-catalyzed reaction and, therefore, has a slower rate. The catalyst lowers the energy barrier but does not affect the actual energies of the reactants or products. Adapted from [25].

Figure 1.1, which is associated with smaller activation barriers and hence a higher overall reaction rate. In the last step the product molecules are released from the catalyst which now is available for the next reaction cycle.

Catalysis can be divided into two categories: homogeneous and heterogeneous catalysis. Homogeneous catalysis is a sequence of reactions that involve a catalyst in the same phase as the reactants, while heterogeneous catalysis reaction involves a catalyst and reactants in different phases. Phase here refers to solid, liquid, or gas. This thesis deals with heterogeneous catalysis operated in a flow reactor (at atmospheric pressure), where the reactants (gas) and the catalyst (solid) are in different phases. Usually the catalyst is a solid and the reactants are either gases or liquids [26]. Heterogeneous catalysts are often composed of metals and metal oxides. The initial step in heterogeneous catalysis is usually the adsorption of reactants. In technical reactions mostly the interaction of molecules with the surface of a solid is decisive [25]. The principle of the heterogeneous catalysis is depicted schematically in Figure 1.2. The atoms in the surface layer of a solid have fewer neighbors than those in the bulk and are hence chemically unsaturated and may form new bonds (= chemisorption) with suitable molecules impinging from the adjacent gas or liquid phase [25]. By this step, existing bonds will be modified or may even be broken (= dissociative chemisorption). The surface species formed may jump from one site to neighboring ones, then

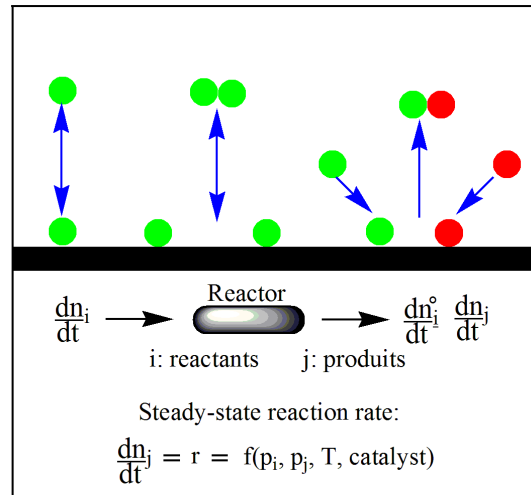


Figure 1.2: Principle of heterogeneous catalysis adapted from G. Ertl [25].

may react with others and the formed produced molecules eventually leave the surface (= desorption). If operated in a flow reactor as in the present work, the catalyst can in this way continuously operate without being consumed. A good example of the heterogeneous catalysis application is removal of toxic substances from automotive exhaust. Most modern cars are equipped with a catalytic converter removing most of the toxic exhaust gases from the processes in a combustion engine. The catalytic converter used in most combustion gasoline engines consists of precious metal particles called Three Way Catalyst (TWC) [27,28]; however in general, most industrially important reactions are catalyzed by the surfaces of solids mainly metals and metal oxides.

1.1.3 Catalysts for catalytic combustion

Among the catalysts used in heterogeneous catalysis, most are noble metal particles and metal oxides, mainly transition metal oxides generally coated on a support. Different kinds of support or carrier including γ - Al_2O_3 , SiO_2 , stainless steel, carbon or zeolites are used and the catalytically active components, typically in a low concentration, are deposited, preferably in a highly dispersed state. This support often presents no catalytic activity on the reaction sequence. However, to improve the efficiency of some catalysts by chemical means, other components, including those with catalytic activity, are added as chemical promoters or additives [29-32]. Nano subunits and surfactants have been also used to improve the catalyst's effectiveness by modifying the shape or morphology [33-34].

In general, precious metals are well-known catalysts with high performance widely used for control exhaust gas emissions such as VOCs, hydrocarbons (HCs) and CO [35-37]. Of the

precious metals, Au, Pt, Rh and Pd are the most used due to their higher specific activities in the catalytic combustion of exhaust stream and hydrocarbons at low temperature [37]. However these metals show a high tendency to poisoning [38], selectivity to some oxidation reactions [39], high cost, relative low thermal stability as well as their limited availability, encouraging the scientific community to develop new catalysts such as transition metal oxides (TMOs).

Metal oxides in general and specially transition metal oxides are presented as an alternatives to noble metals catalysts for complete oxidation due to their low cost and better stability [40,41]. They present sufficient activity, although they are typically less active than precious metals at low temperatures. However, at high temperatures the activities are similar [42]. In addition, some combinations of oxides may have high catalytic performance and high thermal stability compared to single components [43,44]. The need for catalytic materials that remain stable and active over long periods at high operation temperatures presents a challenge. A huge spectrum of transition metal oxides with spinel and perovskites structure exists and is very attractive due to their capacity to release oxygen with high mobility, required in the catalytic combustion reaction with oxides catalyst [43]. Today the large majority of catalysts used in modern chemical industry are oxides of transition metals, owed to their ability to take part in the exchange of electrons, as well as in the oxygen exchange. Moreover these materials offer doping strategies to improve their stability and properties [45-47]. Because of the interesting and attractive characteristics listed above, TMOs have been the main focus in this thesis.

The most active metal oxide catalysts for complete oxidation of a variety of oxidation reactions are the oxides of Co, Fe, Cu Mn, Cr, V, Ni and Ag [48-52]. Among these oxides mentioned in the literature, a few seem particularly promising. As example, cobalt oxide is known to be an effective catalyst for total oxidation reactions [53,54]. CuO is a well-known component of oxidation catalysts [55] and high interest is also devoted to Fe₂O₃ for catalytic and gas-sensing applications, regarding their high thermal stability and environmentally-friendly nature [56]. CuO-based catalysts show comparable activity to noble metal catalysts for CO oxidation [57] and exhibit, together with Co₃O₄, and Mn₃O₄, a good ability to maintain oxidative capacity of organic air pollutants [58]. In general Cu-, Co-, Mn- and Fe-based oxides have been found to be active for both CO and VOCs [57].

Surprisingly, in spite of significant work devoted to the preparation and application of the metal oxides catalysts listed above, these materials were scarcely used for the complete and

low-temperature oxidation of real fuel including: olefins, dimethyl ether (DME) and biofuels. More importantly, the relationship between the synthesis approach and the performance of the prepared materials in the catalytic combustion processes is not well understood on a fundamental level. In fact, controlled synthesis of precise structures of active metal oxides with ordered morphologies on solid surfaces is one of the most important issues in designing high-performance heterogeneous catalysts [48]. Materials with the above-mentioned characteristics have been recently reported to possess better mechanical strength and enable a lower pressure drop which permits higher reactant gas velocities than fine powder catalysts [56]. In addition, it is known that the surface morphology and bulk composition of the films depend upon the preparation methods and conditions which may affect the films' properties [45]. Therefore, the choice of the synthesis approach, capable to produce pure and catalytically active thin films with good reproducibility by an easy control of the structure, phase, morphology and composition remains an uphill task. In this thesis, thin films of TMOs were synthesized, systematically characterized and used as catalysts for the complete combustion of representative fuels in a home-made flow reactor operating at atmospheric pressure. Details about the flow reactor characteristic will be given in the experimental part.

Firstly PSE-CVD was used for the tailored synthesis of TMOs such as: Co_3O_4 , $\alpha\text{-Fe}_2\text{O}_3$, CuO , Mn_3O_4 and Co-Fe mixed oxides. Many aspects of the synthesis approach were optimized to produce thin films with specific phase, structure, morphology and composition. Secondly, the performance of the deposited materials was tested for the complete oxidation of real fuel such as CO , C_3H_6 , $n\text{-C}_4\text{H}_8$, $\text{C}_2\text{H}_6\text{O}$ and $n\text{-C}_4\text{H}_{10}\text{O}$, in a home-made fixed-bed quartz flow reactor under plug-flow conditions. An attempt was made to understand the fascinating and indispensable phenomenon of catalysis as well as to answer some questions related to the type of reaction process involved in the catalytic oxidation in relation with the properties of the prepared catalysts materials. Particularly the influence of the redox properties, the film morphology and the environment of the surface of the deposited thin films were correlated with the catalytic behavior, and the mechanisms of the catalytic oxidation of the fuels over the prepared oxides were proposed.

2 EXPERIMENTAL

Developments of highly active thin film catalysts impose the improvement of the quality of existing techniques and the development of new ones. Achieving these goals required the development of a controlled preparation approach capable to achieve the growth of materials with excellent quality at low costs. In order to overcome these requirements, Pulsed Spray Evaporation-chemical vapor Deposition (CVD) was employed in this thesis for the synthesis of functional transition metals oxides catalysts with variable structures. To understand the relationship between the growth, the structure and the catalytic properties, systematic characterization techniques such as X-ray diffraction (XRD), Raman spectroscopy, Fourier Transformed Infrared (FTIR) spectroscopy, Scanning Electron Microscopy (SEM), Helium Ion Microscopy (HIM), Energy Dispersive Spectroscopy (EDS), X-Ray Photoelectron Spectroscopy (XPS) and Ultra-Violet Visible spectroscopy (UV-Vis) as well as Temperature-Programmed Reduction/re-Oxidation (TPR /TPO) were systematically applied. In-situ emission and absorption FTIR were performed as useful techniques to explore catalytic performance of functional materials. In the following chapter the experimental procedures as well as the analytical techniques are introduced and briefly explained.

2.1 Chemical vapor deposition process

Chemical vapor deposition may be defined as the deposition of a solid on a heated surface from a chemical reaction in the vapor phase. It belongs to the vapor-transfer processes: that is the deposition species are atoms or molecules or a combination of these. Besides CVD, various physical-vapor-deposition processes (PVD) such as evaporation, sputtering, molecular-beam epitaxy, and ion plating are known. In many respects, CVD competes directly with the PVD processes, but it is also used in conjunction with them, and many of the new processes are actually combinations of two systems such as plasma-enhanced CVD or activated sputtering.

CVD is well known for the production of coatings of uniform thickness, great purity, and high density, with the possibility to reach high deposition rates [59,60]. The CVD approach can also be used for the production of powders, and even single crystals [64]. It allows numerous advantages over the PVD technique. CVD offers relatively low processing costs, since in most cases, the processes do not require high vacuum or strong electric power. CVD enables the uniform coverage of complex-shaped components. Overall, materials deposited by this technique find application in several domains such as microelectronics, optoelectronics,

protective and optical coatings as well as catalysis. The CVD approach is complex and can differ in its specific characteristics. In general, CVD always involves a series of gas-phase and surface reactions that usually follow a common reaction scheme. The principal steps of a typical CVD process can be summarized as follows:

- ❖ evaporation of the reactant species (precursors),
- ❖ transport of the gaseous species into the reaction chamber,
- ❖ gas-phase reactions leading to reactive intermediates and gaseous by-products,
- ❖ transport of the reactants through the boundary layer to the surface of the substrate,
- ❖ adsorption of the gaseous reactants onto the substrate and heterogeneous reaction at the interface, producing the deposit and by-product species,
- ❖ diffusion of the deposit to nucleation sites on the surface,
- ❖ desorption and transport of by-products away from the reaction zone.

In this process, the large part of the deposition involves chemical reactions. They can occur in the gas phase to form intermediate species, which then react further, either in the gas phase or at the interface with the substrate. It is worth mentioning that the deposition parameters such as temperature and pressure will play key roles in the deposition process. After the brief description of the general principles of CVD, the characteristics of the CVD technique used for the deposition of thin films will be exposed.

2.1.1 Pulsed spray evaporation CVD reactor and systems

Pulsed spray evaporation CVD (PSE-CVD) is a variant of the conventional CVD method. In this approach, the precursors are dissolved in an organic solvent and directly injected into the reactor through a spray nozzle. It is, to a few minor differences, similar to the pulsed injection MOCVD (PICVD) deposition process, generally used for the deposition of metal oxides [61]. This deposition method is based on a concept elaborated by Sénateur et al. [62], who patented the process in 1993. The innovation of this technique is the method of precursor delivery, which relies on the sequential injection of micro amounts of a volatile metal-organic precursor solution into an evaporator. The solution is injected through a high-speed micro-electrovalve with the aid of a pressurized inert gas. Evaporation takes place instantly due to the small amounts injected (a few μL) and to the vacuum and temperature conditions residing in the evaporator. The vapors of the precursor are then transported by a gas flow to the substrate, which is maintained at the desired temperature. This method offers distinct advantages over conventional CVD precursor delivery sources, like using a bubbler or sublimator [61,63]:

- ❖ the instantaneous evaporation allows the use of less stable precursors since they are only heated for a short time, insufficient for a chemical degradation to occur,
- ❖ the precision of the micro-dosing and the possibility to easily change the injection parameters enables the precise control of the vapor pressure, growth rate, and improve the reproducibility of the film properties,
- ❖ the thickness can be easily controlled by the number of drops injected,
- ❖ the use of several injectors allows the production of multilayered structures of different compositions.

This variant of the CVD process was largely applied for the deposition of common metal oxides, like spinel cobalt oxide [64,65] or yttrium-stabilized zirconia [66], to more complex high-temperature superconductor structures [61] and multilayered compounds [67]. It was noticed that the presence of the organic solvent in the reaction zone may be a disturbance for the deposition reaction but its effect can be countered with a higher flow of oxygen [63,65]. The following parameters can be adjusted, once the precursor and solvent for the reaction have been determined:

- ❖ precursor concentration,
- ❖ injection pulse frequency,
- ❖ injection pulse opening time,
- ❖ evaporation temperature,
- ❖ vector gas flow velocity,
- ❖ total pressure,
- ❖ substrate temperature.

The main difference is the pulsed method of injection of the precursor solution, which leads to a high vapor pressure. This can induce a high supersaturating ratio, resulting in an easier nucleation of the film. In this study, the depositions were performed in a home-made vertical cold-wall type reactor as schematically shown in Figure 2.1. The reactor was equipped with a pulsed-spray evaporator (PSE) system for the delivery of the liquid feedstocks. Metal acetylacetonate precursors were dissolved in the selected solvent with a desired ratio and kept at room temperature under atmospheric pressure during the deposition process. The β -acetylacetonate precursors were selected considering their stability and solubility in the solvent used in this investigation (ethanol, tetrahydrofuran (THF), and toluene). The optimal use of the PSE delivery was achieved with a valve opening time varying from 2-2.5 ms and a frequency fixed at 4 Hz. The evaporation of the injected feedstock takes place under vacuum at the evaporation temperature of the precursor in the 30 cm-long evaporation chamber zone

B) Selection of the precursors

Two factors were determinant for the choice of the precursor: the precursor stability and solubility.

❖ **Precursor stability:** In order to avoid oxidation states variation in the liquid feedstock, the precursors were used in their high oxidation state. In this study for example, the Co(III) precursor was preferred to Co(II) for the Co_3O_4 spinel synthesis [1], and Fe(III) was preferred to Fe(II) for the hematite thin film synthesis [2].

❖ **Precursor solubility:** The solubility of the precursor salts was examined by a series of pretests. For this, amounts of salt were weighed in the solvent and were stirred at room temperature up to 5 hours. If this did not result in a homogeneous solution free of residuals the temperature was raised to 50 °C and stirring was continued for another 2 hours. Afterwards the precursors were assessed to either have a too low solubility or to be sufficiently soluble and thus to be suitable for the CVD process.

C) Substrates used

For all experiments in this study, five different types of substrates were used: 18 x 18 mm thin glasses (cover glass), 76x26x1 mm microscope slides (thick glass), 4x7 mm chips of silicon wafer, planar stainless steel and grid mesh of stainless steel. Just before coating, these substrates were cleaned in a laboratory ultrasonic bath with ethanol. Grid mesh of stainless steel was used here as support due to its flexibility to be loaded in any form of reactor, and the narrow pores (micron-retention 36-45 μm) capable to retain even very small size catalysts. More importantly, grid mesh of stainless steel exhibits no catalytic activity, thus enabling the real evaluation of the catalytic performance of the deposited thin films. Substrates before and after coating and SEM micrograph of Co_3O_4 thin film are presented in Figure 2.2.

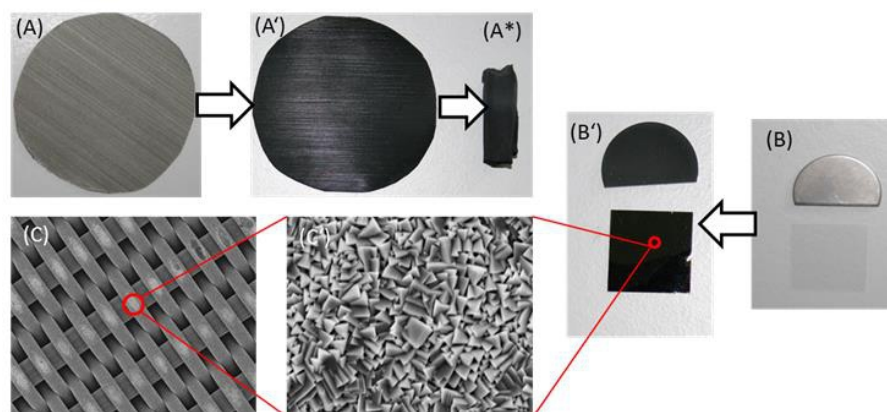


Figure 2.2: Non-coated (A), Co_3O_4 -coated (A') grids mesh of stainless steel and Co_3O_4 -coated (A*). Non-coated planar stainless steel, thin glass (B) and Co_3O_4 -coated ((B')). SEM micrograph of Co_3O_4 -coated grid mesh (C) and Co_3O_4 film morphology.

The deposition conditions are given in Table 2.1.

Table 2.1 Experimental Deposition conditions

Deposition Parameters	
Precursors	Co(acac) ₃ , Cu(acac) ₂ , Fe(acac) ₃ , Mn(acac) ₃
Solvent	EtOH, THF, toluene
Concentration of precursor	5 mM
Frequency	4 Hz
Opening time	2-2.5 ms
Evaporation temperature	180-220 °C
Transportation temperature	200-240 °C
Substrate temperature	250-500 °C
System pressure	10-40 mbar
N ₂ (SLM) / O ₂ (SLM)	0.16-0.2 slm / 0.5-1.0 slm
Substrates	Glass, silicon, planar, or grid mesh steel

2.2 Thin film characterization techniques

To better understand the behavior of functional materials, comprehensive and systematic characterization techniques need to be performed. Many of these methods, with the exception of the more recently developed Helium Ion Microscopy (HIM) used here, are standard tools in material characterization. It is important to mention that HIM imaging and XPS analysis were performed in cooperation with the Physical department at the University Bielefeld. A comprehensive and systematic characterization is thus expected to be performed, prior to and in connection with testing the materials for their catalytic performance. The following analysis techniques which were used for the thin film characterization are shortly described in this part in order to explain their contribution in the understanding of the properties of the functional materials synthesized in this thesis.

2.2.1 Structure characterization

In order to characterize the structure of the TMOs thin films prepared in this study, the following approaches were employed.

❖ **Gravimetric analysis**

The thicknesses of the samples were determined by the gravimetric method. For this purpose, the samples were weighed, before and after the deposition, using a microbalance (METTLER ME 30) with a precision of 0.005 mg. It is necessary for this calculation to know the exact composition and the nature of the crystalline phase of the deposited material. With the assumption that the films are dense and homogeneous, the thickness d can be calculated with the following equation (2.1):

$$d = \frac{\Delta m}{A\rho} \tag{2.1}$$

Δm : mass difference before and after the deposition

A : surface of the sample

ρ : density of the phase.

❖ **X-ray diffraction**

X-ray diffraction (XRD) is a fundamental analysis technique for material science. This non-destructive technique yields information about the nature of the crystalline phases of the films which were deposited. The principle of XRD analysis is the diffraction of monochromatic X-rays by the crystalline lattice, as illustrated in Figure 2.2. When the radiation beam interacts with a set of planes in a crystal, it will be diffracted only if the geometry of the crystal fulfills specific conditions, defined by Bragg's law. The interplanar distances depend on the crystalline lattice of the material, and can be calculated by the following relation (2.2):

$$\frac{1}{d_{hkl}} = \frac{h^2}{a^2} + \frac{k^2}{b^2} + \frac{l^2}{c^2} \tag{2.2}$$

where h, k, l are the Miller indices defining the plane, and a, b, c the dimensions of the primitive unit cell used for representing the crystalline lattice (see Figure 2.3).

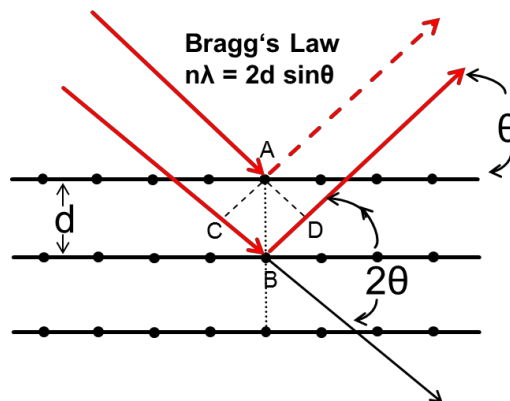


Figure 2.3 Graphic illustration of Bragg's Law [68].

The XRD analysis results in a list of the refraction angles with their respective signal intensity. By comparing the obtained signals to the XRD database, it is possible to identify the crystalline phases present in the composition of the film. Complementary information like size of the particles and lattice strain can be derived from the width of the peaks. For this purpose, the Scherrer equation [69] gives an approximation of the particle size, based on the full-width at half-maximum of the signal:

$$d = \frac{k\lambda}{\beta \cdot \cos\theta} \quad (2.3)$$

d : particle size,

k : constant value equal to $2\frac{\sqrt{\ln 2}}{\pi}$ in the original article, where particles are assumed to be cubic, and refined in further work for other shapes. In the absence of precise information about the particles' shape, $k = 0.9$ is considered as a good approximation [70],

λ : wavelength of the radiation,

β : full-width at half-maximum of the considered refraction signal,

θ : diffraction angle.

All diffraction spectra were recorded at room temperature, using a Phillips X'Pert Pro MRD (PW3830) instrument equipped with a Cu $K\alpha$ ($\lambda = 0.154056$ nm) radiation source and operated at 40 kV and 30 mA. Data were recorded in the 2θ range from 20° to 80° , with a step size of 0.05° .

❖ Raman spectroscopy

Raman spectroscopy is a widely employed and powerful characterization technique used to gain insights into the crystal structure. A Raman spectrum is obtained by exposure of a sample to a monochromatic source of exciting photons and measurement of the frequencies of the scattered light. In contrast to IR spectra, Raman spectra can be measured in the UV-Visible region where the excitation as well as Raman lines appear. According to classical theory, Raman scattering can be explained as follows: The electric field strength (E) of the electromagnetic wave (laser beam) fluctuates with time (t) as shown by the following equation (2.4):

$$E = E_0 \cos 2\pi\nu_0 t \quad (2.4)$$

where E_0 is the vibrational amplitude and ν_0 is the frequency of the laser. Although Raman spectra are normally observed for vibrational and rotational transitions, it is possible to observe Raman spectra of electronic transitions between ground states and low energy excited

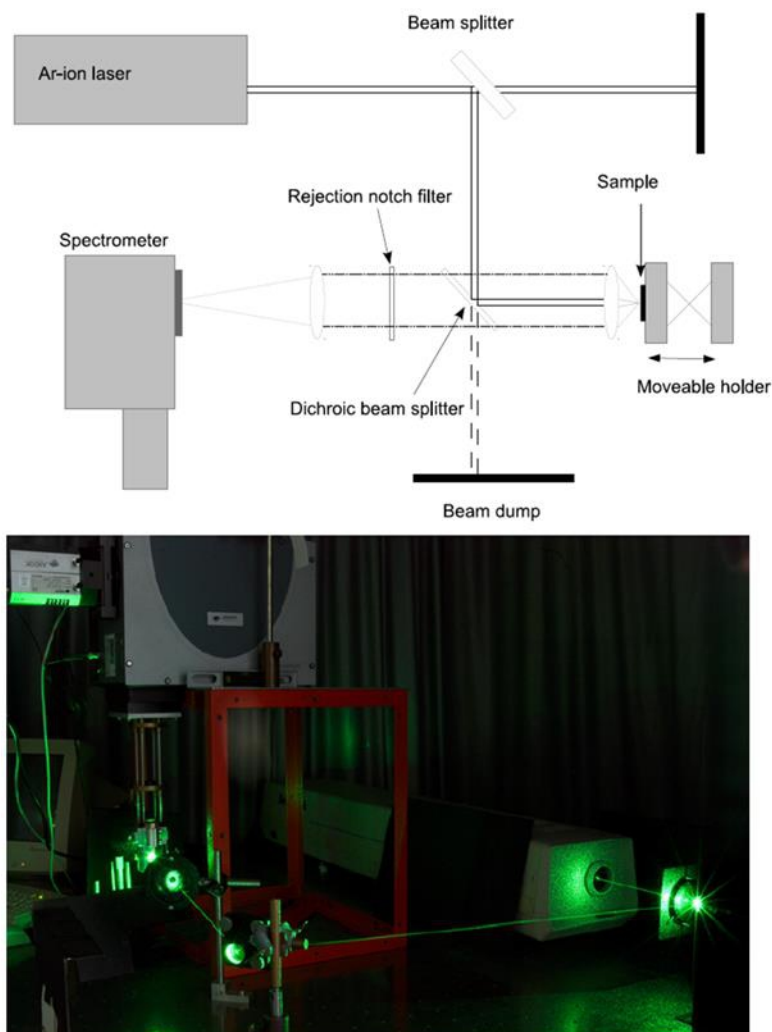


Figure 2.4 On the top the schematics of the home-made Raman spectrometer and at the bottom picture of the setup of the visible laser pathway from [71].

states. The observed active Raman modes provide information about the purity of the deposited films. A home-built Raman spectrometer with spectral resolution of 4 cm^{-1} has been used in this study to identify the metal-oxygen vibration modes in the prepared samples following the procedure outlined by Vannier [71]. It enables in this investigation the confirmation of the hematite phase of the obtained oxide from [2]. An argon-ion laser (SPECTRA-PHYSICS, BEAMLOK 2080) was chosen as excitation source and configured for using only the monochromatic 514.5 nm line. A spectrometer consisting of a SHAMROCK SR-303i spectrograph and an iDUS CCD camera served as detection unit. A beam-splitter (SEMROCK LPD01-514RU-25) was used for selectively reflecting the excitation line down on the sample, and filtering out the Rayleigh signal from the radiations emitted by the measured sample. The Rayleigh signal is further filtered through a holographic notch rejection filter positioned in the vertical optical path collecting the signal to the spectrometer. Figure 2.4 above presents a schematic view and picture of the setup.

❖ Fourier transformed infrared (FTIR) spectroscopy

FTIR is a technique used to evaluate qualitative and quantitative features of IR-active molecules in organic or inorganic solid, liquid or gas samples. It is a rapid and relatively inexpensive method for the analysis of solids that are crystalline, microcrystalline, amorphous, or films. FTIR technique can also provide information about the “light elements” (e.g., H and C) in inorganic or organic substances. FTIR is based on the interaction of IR radiation with the material, resulting in an excitation of selected vibrational modes depending on the material and the wavelength used to excite the sample. In FTIR, IR radiation is passed through a sample. Some of the infrared radiation is absorbed by the sample and some of it is passed through (transmitted). The resulting spectrum represents the molecular absorption and transmission, creating a molecular fingerprint of the sample. Like a fingerprint no two unique molecular structures produce the same infrared spectrum. This makes infrared spectroscopy useful for several types of analysis. The principle of this technique is based on the Michelson interferometer illustrated in Figure 2.5. The beam from the source passes through a beam splitter which conducts half the beam to a moving mirror and reflects the remaining half to a stationary mirror. The two beams are reflected from their respective mirrors and recombined either constructively or destructively at the beam splitter depending on the moving mirror position. A moving mirror inside the apparatus alters the distribution of infrared light that passes through the interferometer. The signal directly recorded, called an "interferogram", represents light output as a function of mirror position [72]. The interferogram is transformed into IR absorption spectrum that is recognizable with absorption intensity or % transmittance plotted against the wavelength or wavenumber as following (2.4):

$$A = \log_{10} \frac{1}{T} = -\log_{10} T = -\log_{10} \frac{I}{I_0} \quad (2.4)$$

The ratio of radiant power transmitted by the sample (I) relative to the radiant power of incident light on the sample (I_0) results in quantity of Transmittance, (T). Absorbance (A) is the logarithm to the base 10 of the reciprocal of the transmittance (T). The infrared (IR) absorption frequencies of oxides and organic compounds were interpreted by comparison with IR absorption spectra in databases.

In this thesis a FTIR with spectral resolution of 4 cm^{-1} was used for two purposes: the analysis of the prepared TMOs chemical structure and for the monitoring of the exhaust gas composition during the catalytic combustion tests. The study of the chemical structure of the oxides was systematically evaluated in ambient air with emission-FTIR spectroscopy using a

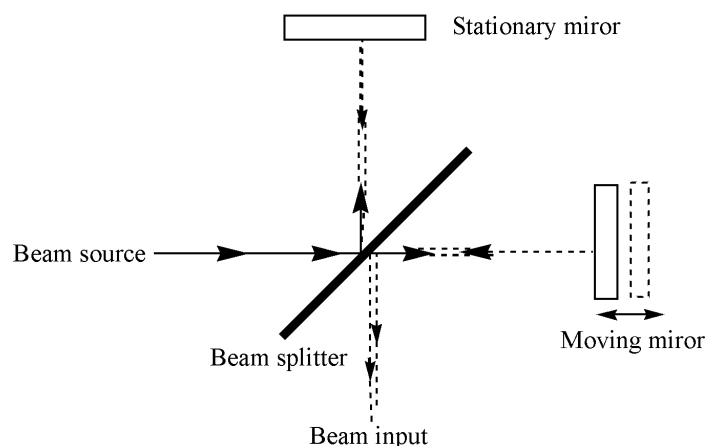


Figure 2.5 Diagram of the Michelson interferometer adapted from [72]

home-made emission cell, whereas the exhaust gas during the catalytic test was detected using a home-made transmission-FTIR cell. Both emission and transmission FTIR cells were attached to a FTIR spectrometer (THERMO NICOLET-5700) with absorption range between 4000 cm^{-1} and 500 cm^{-1} .

2.2.2 Morphology and chemical composition

The morphology and chemical composition at the surface of the functional materials play an important role in the catalytic properties of the materials. In fact, heterogeneous catalysis refers to a chemical reaction occurring on the surface of a solid catalyst. Therefore, size and shape of the catalysts control the reaction efficiency. In this investigation, two different methods of morphology inspection were performed to probe the film morphology in deep: Scanning Electron Microscopy (SEM) and Helium Ion Microscopy (HIM). With the involvement of a focused beam of helium ions, HIM exhibits superior resolution and outstanding performance on insulating samples [73,74]. For the composition analysis, both Energy Dispersive Spectrometry (EDS) and X-ray Photoelectron Spectroscopy (XPS) were performed. EDS provides composition information in the bulk of the films, while XPS gives the chemical composition and ionic states at the surface of the materials (M2p, O1s and C1s core shell (M = Metal, O = lattice and adsorbed Oxygen and C = Carbon)). These results would help further understanding the surface and bulk details of the obtained films.

A) Morphology

❖ Scanning electron microscopy (SEM)

The SEM uses a focused beam of high-energy electrons to generate a variety of signals at the surface of solid specimens which are measured as signals. The signals that derive from electron-sample interactions reveal information about the sample including external

morphology (texture), chemical composition, crystalline structure and orientation of materials making up the sample. Areas ranging from approximately 1 to 5 cm microns in width can be imaged in a scanning mode using conventional SEM. As an advantage, the SEM is equipped with an EDX analyzer for quantitative and qualitative chemical analysis. The model used here was with an EDAX photonic system (Figure 2.6). Here an electron beam with significant amounts of the kinetic energy is generated by a field emission gun and its energy is dissipated as a variety of signals produced by electron-sample interactions when the incident electrons are decelerated in the solid sample. These signals include secondary electrons that produce SEM images. The path of the beam describes a raster which is correlated to a raster of gray level pixels on a screen. As a consequence the magnification is simply computed by the ratio of the image width of the output medium divided by the field width of the scanned area.

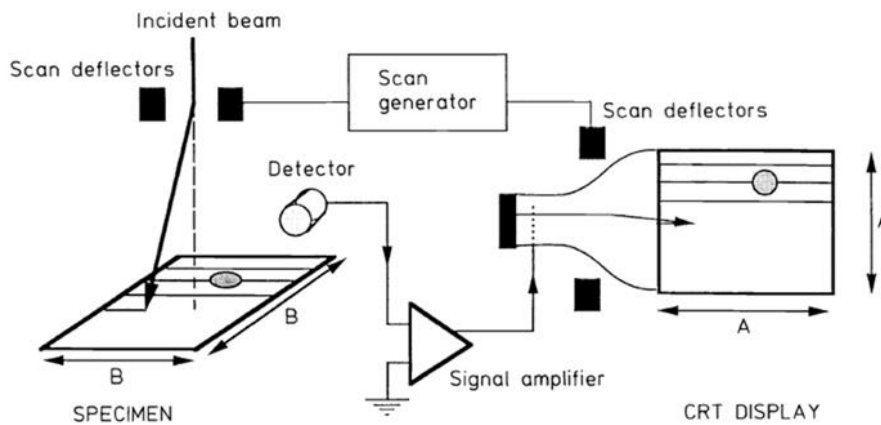


Figure 2.6 On the top the schematic representation [75] and at the bottom picture of the SEM setup imaging of samples with a relative humidity of up to 100% under low-vacuum conditions.

❖ **Helium Ion microscopy (HIM)**

In order to get high resolution images from any scanning beam microscope one must be able to produce a sufficiently small probe, have a small interaction volume in the substrate and have an abundance of information-rich particles to collect and create the image [76]. The Orion helium ion source enables this new generation microscope to achieve these requirements. This technique was employed here because it offers higher resolution and better contrast than SEM [73]. In fact, the helium ion microscope operates somewhat like a typical focused ion beam system. There is a source, which produces a stream of helium ions, a column which accelerates, collimates, focuses and scans the beam, and a vacuum chamber that contains the sample to be imaged. A variety of detectors provide the flexibility of generating images. The Orion helium ion microscope uses a beam of helium ions as the imaging particles. Since ions can be focused into a smaller probe size and have less sample interaction than electrons, the HIM can generate higher resolution images with more material contrast so that more details can be seen. The helium ion beam was operated at 35 kV acceleration voltages at a current of 0.8 pA. A 5 μm aperture at Spot Control 4 was used. The working distance was 9 mm at a sample tilt of 0°. The secondary electrons were collected by an EVERHART-THORNLEY detector at 500 V grid voltages. The samples were plasma-cleaned in the HIM load-lock for 8 minutes before measurement.

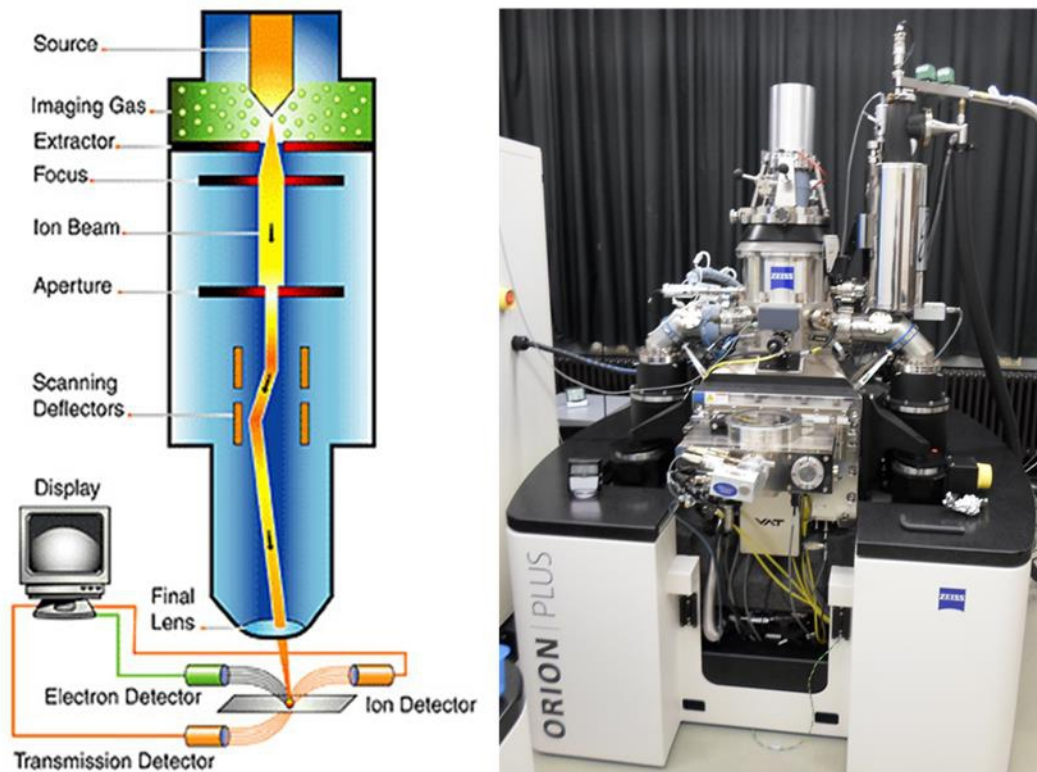


Figure 2.7 Left schematic representations [76] of the HIM and right picture of HIM set-up

B) Chemical composition

❖ Energy dispersive X-ray spectroscopy

To evaluate the chemical composition of the TMOs samples prepared in this work, Energy Dispersive Spectroscopy (EDS) analysis was performed. EDS is a complementary experiment to SEM; it uses the X-ray produced by inelastic collisions of the incident electrons with electrons in discrete orbitals (shells) of atoms in the sample as schematically represented in Figure 2.8. As the excited electrons return to lower energy states, they yield X-rays that are of a fixed wavelength (that is related to the difference in energy levels of electrons in different shells for a given element). Thus, characteristic X-rays are produced for each element in a mineral that is "excited" by the electron beam. All elements from atomic number 4 (Be) to 92 (U) can be detected in principle, though not all instruments are equipped for 'light' elements ($Z < 10$) [75]. EDS analysis is considered to be "non-destructive"; that is, X-rays generated by electron interactions do not lead to volume loss of the sample, so it is possible to analyze the same materials repeatedly. Qualitative analysis involves the identification of the lines in the spectrum and is fairly straightforward owing to the simplicity of X-ray spectra. Quantitative analysis (determination of the concentrations of the elements present) entails measuring line intensities for each element in the sample and for the same elements in calibration standards of known composition. By scanning the beam in a television-like raster and displaying the intensity of a selected X-ray line, element distribution images or 'maps' can be produced.

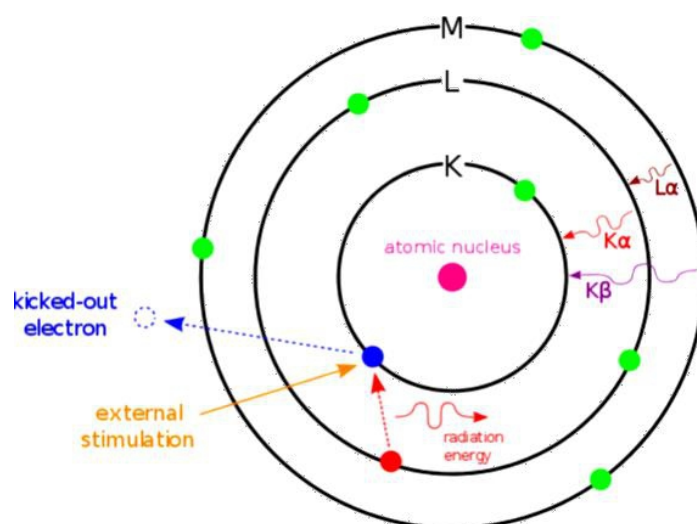


Figure 2.8 Sketch of atomic energy levels and X-ray photon generation [75].

❖ X-Ray photoelectron spectroscopy (XPS)

XPS is the most widely used surface analysis technique because of its relative simplicity in use and data interpretation [77]. The information XPS provides about surface layers or thin

film structures is of value in many industrial applications. Here, the XPS technique was used to determine the elemental chemical composition and the electronic states in the TMO surface by irradiating a specimen with monochromatic X-ray radiation and analyzing the emitted photoelectrons. The fundamental experiment in XPS involves exposing the specimen to be studied to a flux of nearly mono-energetic radiation with mean energy $h\nu$, and then observing the resultant emission of photoelectrons, whose kinetic energies (KE) will be described most simply by the photoelectric equation [77]:

$$KE = h\nu - (BE + \phi), \tag{2.5}$$

in which, KE is the photoelectron kinetic energy, BE is the binding energy and ϕ is the work function of the spectrometer. In this figure CL represent the core level, VB the valence band, FL the Fermi level, and VL the valence level

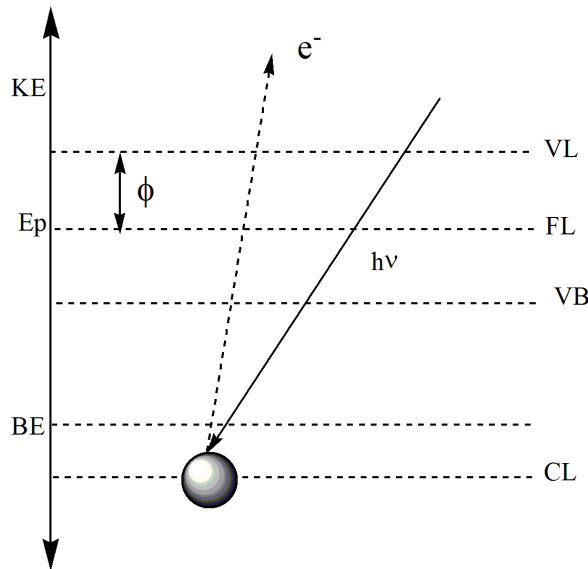


Figure 2.9: XPS fundamental principles reproduced from [77].

Its characterization capabilities are due in large parts to the fundamental principle that each element has an unique atomic structure allowing X-rays that are characteristic of an element's atomic structure to be identified uniquely from one another [77]. The principle is schematically represented in the Figure 2.9. To stimulate the emission of characteristic X-rays from a specimen, a high energy beam of charged particles such as electrons or protons or a X-ray beam, is focused into the sample being studied. The incident beam may excite an electron in an inner shell, ejecting it from the shell while creating an electron hole where the electron was. An electron from an outer higher energy shell then fills the hole, and the difference in energy between the higher and lower energy shell may be released in the form of an X-ray.

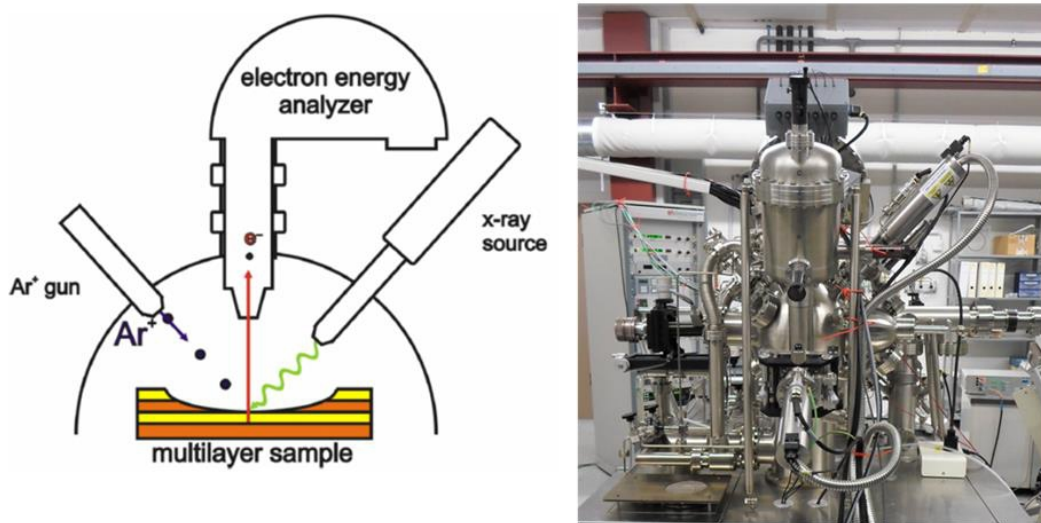


Figure 2.10 Left: Schematic diagram of the XPS apparatus [77], illustrating the depth profiling of a multilayer sample and right the picture of the model available in the Physical Department at the Bielefeld University.

The number and energy of the X-rays emitted from a specimen can be measured by an energy-dispersive spectrometer.

In this thesis, except for Manganese-Oxides samples the chemical composition both in the bulk and on the surface of the entire samples were determined by the means of XPS MULTIPROBE, OMICRON nano-technology presented in Figure 2.10. XPS was performed in a multi-technique UHV instrument using a monochromated Al $K\alpha$ X-ray source (1486.7 eV, 250 W). The sample was under an angle of 13° from the surface normal to the electron detector. The chamber pressure was $5 \cdot 10^{-10}$ mbar. CasaXPS was used for the analysis of the XP spectra, and a Shirley background subtraction procedure was employed.

2.2.3 Optical properties: UV-Vis spectroscopy

The optical properties of functional materials are one of the important characteristics for the evaluation of its optical and photo-catalytic activity [78]. This technique was used here for the evaluation of the band gap energy of the prepared oxides. UV-Vis absorption is a method in which the outer electrons of atoms or molecules absorb radiation and undergo transitions to higher energy levels. The operating principle is based on the Lambert-Beer's law. The absorbance A , is related to the incident light intensity I_0 , and transmitted light intensity I , concentration of a solution sample c , path length of the sample l , absorption coefficient α , and molar absorptivity, ε , by the following equation (2.6):

$$A = \log I/I_0 = \epsilon lc = \alpha c \quad (2.6)$$

The absorption coefficient is wavelength-dependent, and a plot of α as a function of wavelength λ is the spectrum of interest. The spectrum is often characteristic of a given sample and reflects the fundamental electronic properties of the samples [79]. For solid samples as it is the case in this work, concentration, c , has no meaning and similar expression can be derived in terms of the thickness of the sample. The solid sample needs to be thin enough to avoid saturation of the absorption. In this procedure, the spectrum obtained can be analyzed to acquire the energy band gap of the semiconductor nano-materials by the mean of Tauc's equation (2.7):

$$\alpha hv = A(hv - E_g)^n \quad (2.7)$$

where α represent the absorption coefficient, hv is the photon energy, A is the refractive index constant, E_g is the direct band gap energy and n is a constant relaying on the nature of the transition (1/2 for direct allowed transitions). E_g is estimated from the interception point of the extrapolated linear fit to the experimental data of $(\alpha hv)^2$ vs hv .

The spectrometer used in this work was a SHIMADZU UV-2501 PC. The measured samples were deposited on thin glass, and a non-coated thin glass sample was used as reference. Measurements were done in the range from 200 to 900 nm.

2.2.4 Thermal properties

The thermal stability and the reducibility of the entire samples prepared in this study were investigated using a home-made emission cell attached to a FTIR spectrometer (Thermo Nicolet 5700) as schematically represented in Figure 2.11. The thermal stability was analyzed in atmospheric air.

❖ Thermal stability

In order to determine the stability limit of the prepared samples, the thermal stability was investigated. The thermal stability of active catalysts is an important issue since it might be the factor limiting the performance. The FTIR emission can be used to reveal the catalyst deactivation due to crystalline phase transition during operation and to investigate its kinetics. In this test, the temperature of the catalyst was increased from 100 °C to 900 °C with a ramp of 5 °C min⁻¹. The typical features of the characteristics bands of the TMOs disappear progressively with increasing temperature, indicating the gradual loss of its crystallinity. The sample gradually releases its lattice oxygen, permitting an accurate determination of the limit

of the lattice stability. The catalytic tests were performed within the obtained thermal stability temperature.

❖ Redox properties

The redox properties of the deposited samples were investigated by Temperature-Programmed Oxidation and Reduction (TPO/TPR) using emission FTIR as an in situ monitoring technique. TPO and TPR are widely used thermo-analytical techniques for the characterization of chemical interaction between gaseous reactants and solid substances. These methods allow the characterization of the redox properties of materials by delivering spectra containing information about the mechanism and the kinetics. The TPO/TPR test was performed using also a temperature range of 5°C/min in an atmosphere of argon containing 5vol% of hydrogen (TPR) and 5vol% of oxygen (TPO). This method has been successfully used before to characterize the thermal properties of the deposited oxide thin films [5,80-83] for example, the reduction of Co_3O_4 to CoO has been clearly demonstrated [83]. TPR was carried out with ~350 nm thick films. The TPR/TPO profiles of the samples are obtained by integrating the specific emission bands characteristic of the M-O-M (M = transition metals) stretching vibration mode. The decrease of the relative intensity indicates the consecutive loss of the TMOs structure upon reduction/oxidation.

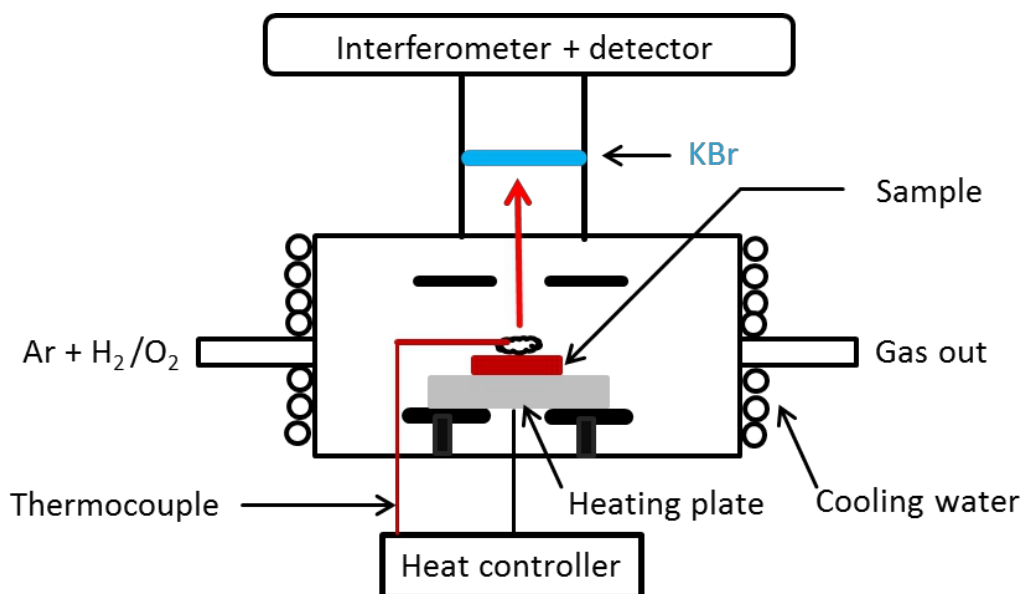


Figure 2.11 Schematic diagrams of the emission FTIR for in situ characterization of the catalysts.

2.2.5 Molecular beam mass spectrophotometer (MBMS)

Mass spectrometry (MS) describes a powerful analytical technique employed in analytical chemistry. This technique enables the determination of the structure of molecules and the

 composition of complex mixtures. It is generally used for flame diagnostics [85] as a constantly evolving technology [86,87]. Experimental developments related primarily to the analysis and evaluation in a reaction mixture of C, H, N, O-containing species. In this work, a Molecular Beam Mass Spectrometer (MBMS) was used for the monitoring of the gas phase in the CVD process. The principle of the MS is based on the ionization, mass separation and detection:



The system used in this work contains a two-stage ion subtraction by Wiley and McLaren [84] and a repeller. The ionization process of the molecules is followed by mass analysis, i.e. the separation of the molecular fragments in terms of the mass-charge ratio along a time (Time of Flight, TOF). Figure 2.12 shows the schematic structure and picture of the system used in Bielefeld. A detailed description can be found elsewhere [88].

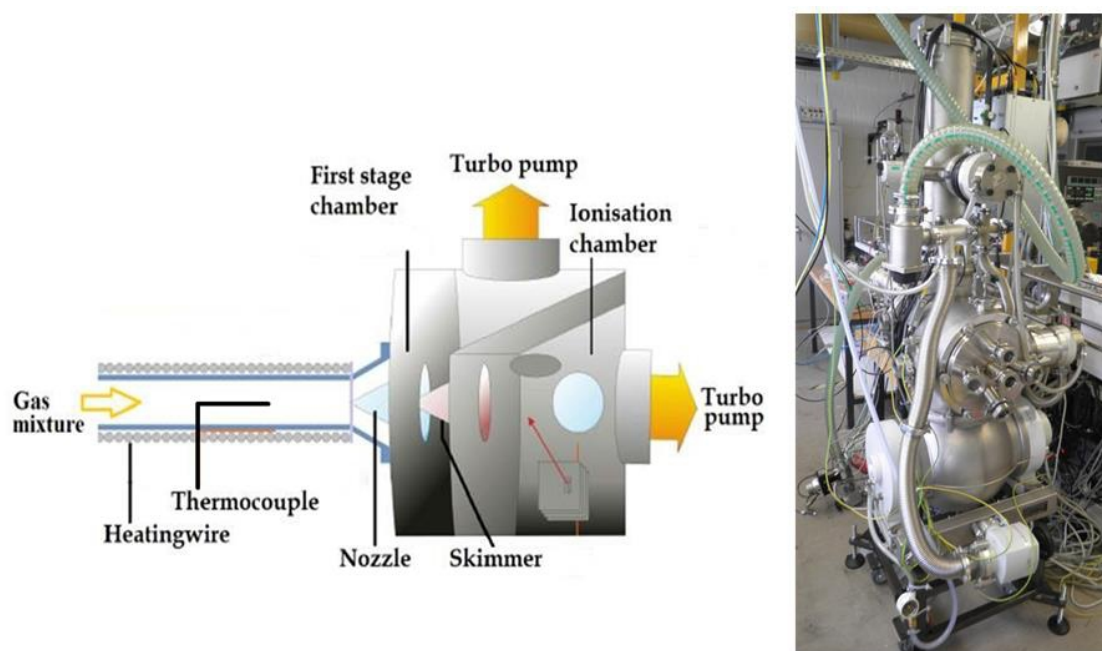


Figure 2.12 Left: Schematic representation [88] and right picture of the structure of the MBMS system present at the University of Bielefeld.

2.2.6 Catalytic performance investigation

The performance of the entire samples synthesized in this study was tested against the catalytic oxidation of CO, C₃H₆, n-C₄H₈, DME and n-C₄H₁₀O at atmospheric pressure in a fixed-bed quartz reactor (30 cm long and 9.0 mm inner diameter). The experiments were performed in a home-made flow reactor, as shown in Figure 2.13. The exhaust gas was analyzed using a home-made KBr transmission cell that was attached to an FTIR spectrometer

 (NICOLET 5700, Germany). In this work, the FTIR spectrometer was used in the spectral range of 400-4000 cm^{-1} with a spectral resolution of 0.04 cm^{-1} . The catalyst supported on stainless steel grid mesh, SPW 40, 80 x 400, micron-retention 36-45 μm was loaded inside the catalytic reactor. Flow rates of Ar, O₂ and fuel gases were controlled by MKS mass-flow controllers, whereas the temperature inside the reactor was increased with a ramp of 5°C/min using a HT60 controller (HORST, Germany). The temperature of the mesh inside the reactor was recorded using K-thermocouples and a digital thermometer GREISINGER GMH3250. The experimental conditions for the catalytic tests, listed in Table 2.2, correspond to a total flow rate (Fuel + O₂ + Ar) of 15 sccm and a total pressure of 1 atm.

To evaluate the consumption of the fuel and the products of the reactions, the exhaust gas was quantitatively analyzed during the temperature-programmed reaction. The catalytic performance was evaluated referring to T₁₀, T₅₀ and T₉₀ which are defined as the temperature at which 10%, 50% and 90% respectively of the fuel is oxidized during the temperature-programmed reaction.

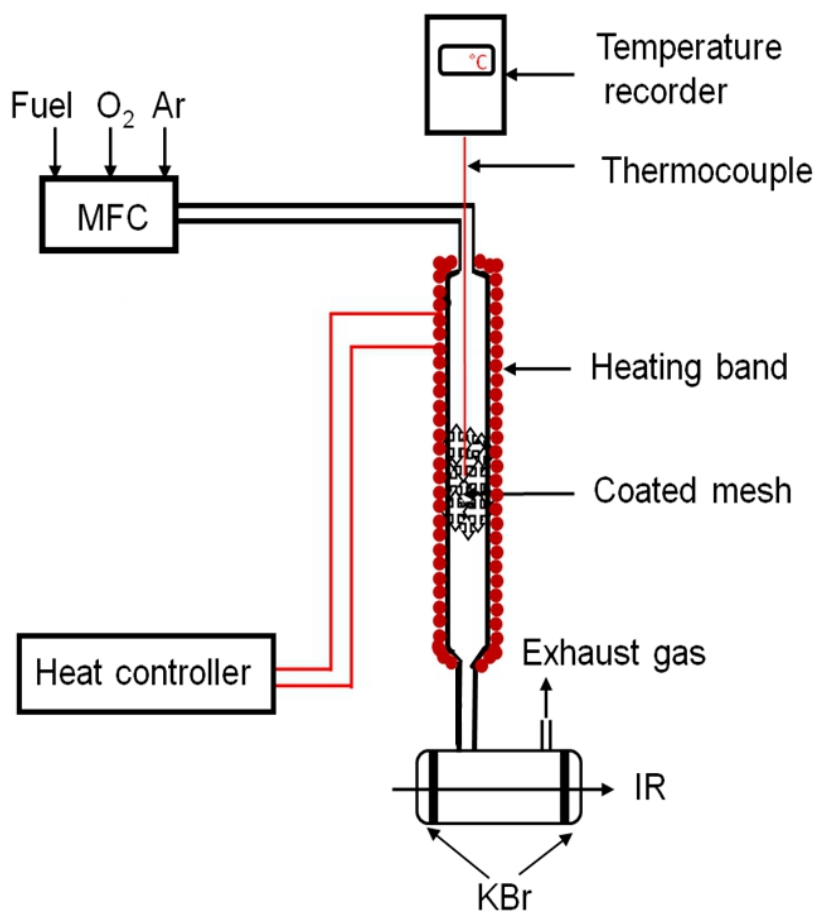


Figure 2.13 Schematic representation Home-made flow reactor used for catalytic test [2].

Table 2.2: Experimental conditions for the catalytic tests.

System (%)	Flow rate (15 ml/min)		
	Fuel inlet	O ₂	Ar
CO/O ₂ /Ar	1	10	89
C ₃ H ₆ /O ₂ /Ar	1	10	89
<i>n</i> -C ₄ H ₈ / O ₂ /Ar	1	10	89
C ₂ H ₆ O/ O ₂ /Ar	1	10	89
<i>n</i> -C ₄ H ₁₀ O /O ₂ /Ar	1	10	89

3 RESULTS

In this chapter, results discussed have been described in details in the publications; just some examples to illustrate the work are given here with discussion following those in the papers, and some of the most relevant results are also reproduced from the publications.

3.1 PSE-CVD of Co_3O_4 starting from β -diketonate precursor in different solvent system

Co_3O_4 is known as promising material due to its extensive application in lithium-ion batteries, gas sensing, data storage, electrochromic devices and catalysis [89-91]. Co_3O_4 is very attractive in the application of oxidation reactions because of the presence of mobile oxygen, i.e. unsupported Co_3O_4 is an active catalyst in air pollution control for the abatement of CO [92], NO_x [93] and VOCs from effluent streams [94]. Most efforts to synthesize Co_3O_4 spinel by different variants of CVD techniques involved several precursors, solvents and suitable deposition temperatures. Among the precursors used, metal-organic precursors are the most preferred since they are either commercially available or can be easily prepared in the laboratory. For all metal organic compounds (MOC), cobalt β -diketonates serve as non-toxic, volatile and inexpensive precursors. In the family of β -diketonates, cobalt acetylacetonates are the easiest to be prepared, requiring no special atmosphere or environment [95]. However, the combination of this precursor with appropriate solvent required special attention. In fact, the solvent used to dissolve the precursor molecule has been shown to influence the chemistry of the CVD process [67]. It was already noticed by Sénateur et al [67] that its presence in the reaction zone may need a higher flow of oxygen for the deposition of metal oxides. Also Borgharkar et al. [96] demonstrated an improvement in the deposition rate for the CVD of copper, using the reduction of copper β -diketonates with hydrogen and alcoholic solvents. The enhancement of the growth rate was then shown to depend on the gas phase pKa value of the alcohol used. Recent investigations reported the use of cobalt(II)acetylacetonate ($\text{Co}(\text{acac})_2$) for the synthesis of Co_3O_4 [97]. However, this precursor shows instability in several solvents, and the selection of alcohol as solvent presents a particularly complicated effect on the formed cobalt phase [97]. In contrast to other solvents, alcohols exhibit certain reactivity with cobalt acetylacetonate under deposition conditions. This reactivity could lead to the formation of carbide phases at low temperature in the absence of oxygen [98]. It becomes clear that the type and nature of precursor and solvents may influence the CVD of metal oxides. Therefore, the synthesis of Co_3O_4 starting from the most stable cobalt acetylacetonate precursor in different solvent system is of great interest.

In this investigation, two precursors ($\text{Co}(\text{acac})_2$ and $\text{Co}(\text{acac})_3$), and three different kind of solvents were used for the synthesis of Co_3O_4 in a temperature range between 350-500 °C and a pressure of 10-40 mbar. The starting point of this study was the selection of the most stable precursor. The appropriate selected precursor was then dissolved in solvents to form liquid feedstock. During the preparation, special attention was paid to the effect of solvent and substrate temperature on the as-prepared thin films.

3.1.1 Effect of aging on the stability and UV-Vis spectrum of the liquid feedstock

$\text{Co}(\text{acac})_2$ and $\text{Co}(\text{acac})_3$ were respectively dissolved in ethanol to obtain a concentration of 5 mM (green and pink) solution. 10 mL of each solution was stored in a closed atmosphere for three days. The evolution of the color of the solutions was filmed and is presented in Figure 3.1. For the $\text{Co}(\text{acac})_2/\text{EtOH}$ solution (A, C and E), the pink color transforms gradually into dark green, while no color changed was observed for $\text{Co}(\text{acac})_3/\text{EtOH}$ solution (B, D and F). The investigation of the UV-Vis spectra revealed a progressive broadening of the optical absorption band peaking at 590 nm after three days for the liquid feedstock composed of $\text{Co}(\text{acac})_2/\text{EtOH}$. However no change was noticed in the UV-Vis spectra for $\text{Co}(\text{acac})_3/\text{EtOH}$ solution, as shown in Figure 3.2. The absorption peak is characteristic of an octahedral Co(III) species [99], which indicates that $\text{Co}(\text{acac})_3$ is more stable than $\text{Co}(\text{acac})_2$ and thus more suitable for the CVD processes with liquid-feedstock's. It is worth noting that $\text{Co}(\text{acac})_3$ has been reported by Atakan et al. [100] to be thermally more stable than $\text{Co}(\text{acac})_2$. Therefore only $\text{Co}(\text{acac})_3$ was used as precursor for the rest of the investigation.

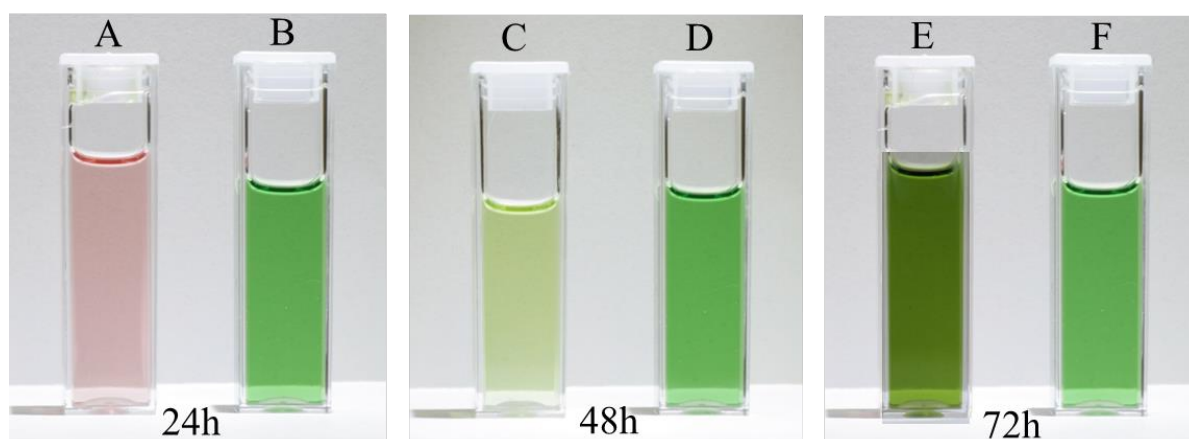


Figure 3.1 Evolution of the coloration of EtOH solution of $\text{Co}(\text{acac})_2$ (A, C, and E) and $\text{Co}(\text{acac})_3$ (B, D and F) adapted from [1].

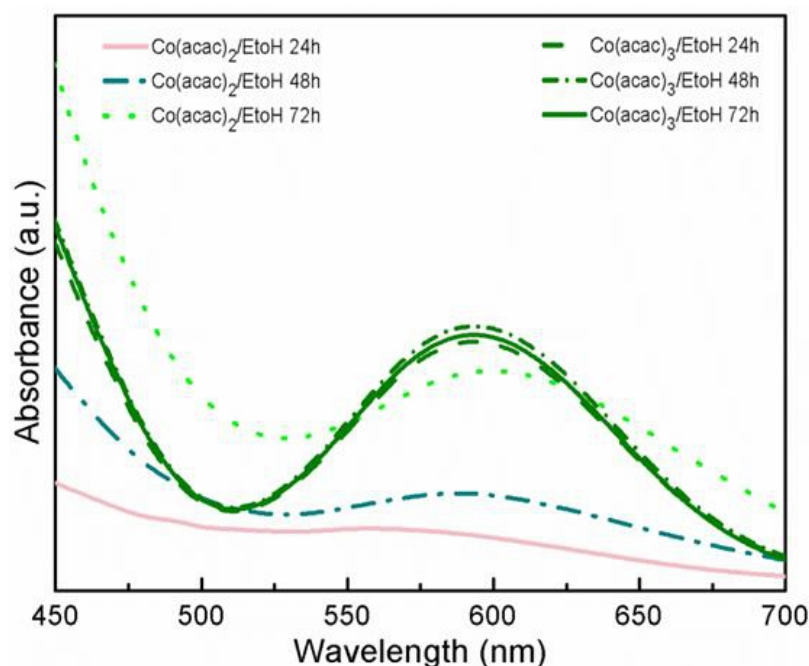


Figure 3.2 UV-Vis spectra of the EtOH solution of Co(acac)₂ and Co(acac)₃ respectively in EtOH adapted from [1].

3.1.2 Co₃O₄ thin film growth and structural characterization

❖ Effect of the deposition temperature on the obtained phase

The growth of cobalt oxide thin films was made in a cold-wall CVD reactor. The description of the experiment was given in the experimental part (see Figure 2.1). The metal organic precursors Co(acac)₃ complex was dissolved in ethanol (EtOH) as well as in toluene (C₇H₈) and tetrahydrofuran (THF) to a concentration of 5 mM and used as liquid feedstock. The films were obtained at deposition temperatures of 350 °C and 450 °C and presented different XRD patterns for the two deposition temperatures. The EtOH, toluene and THF precursor solution leads to the growth of films starting at a temperature of 350 °C, with Co₃O₄ as the dominant crystalline phase in the entire investigated temperature range of 350-500 °C. The highest growth rate was obtained with THF at 350 °C, whereas weak and complete diffraction peak corresponding to Co₃O₄ can be observed at 450 °C (see Publication 1). A clear identification of the spinel cobalt oxide thin layer by XRD was obtained for the grown film at 450 °C with a thickness of about 300 nm over silicon and glass substrates independently of the solvent. The positions of the diffraction peaks fit well to the cubic spinel-type structure of polycrystalline Co₃O₄ (JCPDS No. 74-1656). No peaks associated to other crystalline forms related with the starting precursor Co(acac)₃ could be detected in the pattern, indicating that the product is of high purity and crystallinity.

❖ Effect of the solvents on the growth and film morphology

This investigation was performed to explore the behavior of different solvents with different physical properties on the growth and morphology of the Co_3O_4 thin films. A rapid solubility of $\text{Co}(\text{acac})_3$ in THF and toluene in contrast of relative slow solubility in EtOH was observed. The precursor thus crystallizes upon prolonged use, which leads to the blockage of the spray nozzle and limits its usefulness as pulsed spray of the liquid feedstock. Hence, THF and toluene in which $\text{Co}(\text{acac})_3$ dissolves freely, were found to be suitable solvent in this investigation. The results indicate that the growth rate varies slightly depending on the solvents and a maximum value of $\sim 3 \text{ nm min}^{-1}$ was obtained with THF.

Besides the general effect of the temperature and solvent on the growth rate and composition, it was demonstrated that the morphology of the deposited Co_3O_4 was also be influenced by the choice of the solvents. As displayed in Figure 3.3, the morphology of the deposited films indicates compact and geometrical particles, which differ with the substrates temperature (T_s) and solvents. The coverage of the surface was homogeneous with THF and toluene, and was consisted of well-connected micrometer sized agglomerates, whereas films were less defined

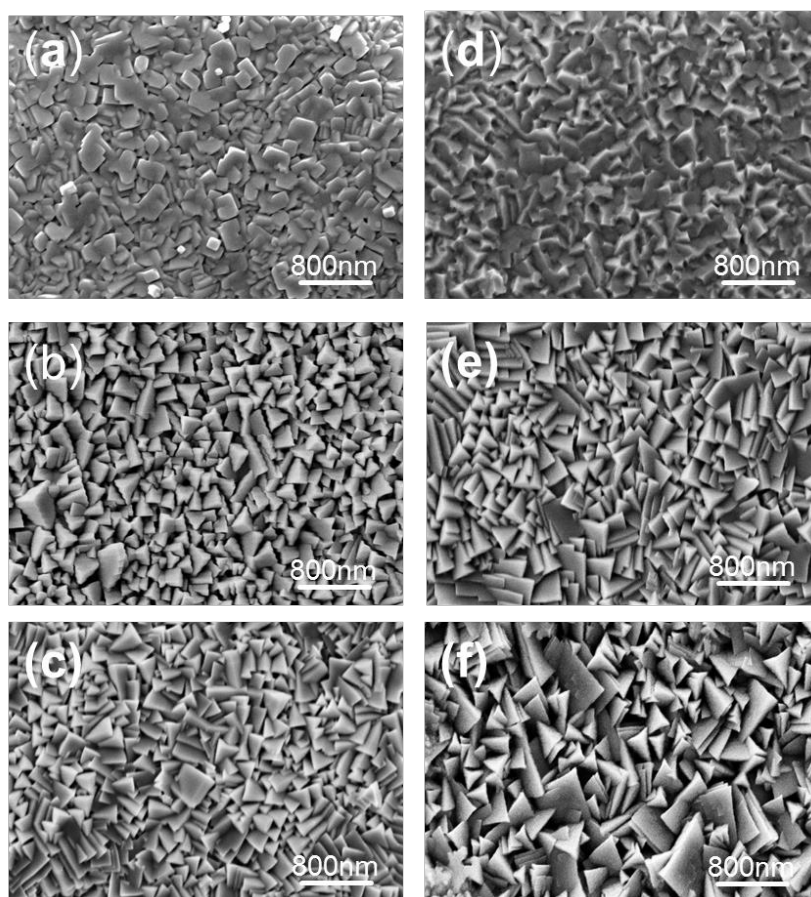


Figure 3.3 SEM micrographs of Co_3O_4 obtain respectively at 350 and 450 °C (a, d) with EtOH; (b, e) with toluene; (c, f) with THF [1].

with EtOH. Films deposited at 350 and 450 °C using EtOH as solvent were randomly oriented with poorly crystallized grains. When THF and toluene were employed, the obtained films were well crystallized and present better defined facets. The Co₃O₄ crystallites showed trigonal pyramidal shape for films deposited at 350/450 °C with THF and toluene. In the explored temperature range, the increase of the growth rate as a function of the deposition temperature and the nature of the solvent has been explained in terms of variation of the surface diffusion with temperature and the co-adsorbed solvent. With EtOH at Ts = 350/450 °C, due to its reducing tendency, the nucleation density becomes higher, giving rise to a fine-grained thin layer with low crystallinity. However, the surface diffusion was increased at the same Ts with THF/toluene, the chemical nature of which does not exhibit the reducing tendency. Consequently, the nucleation density was decreased, which could result in larger and well-crystallized particles. The temperature and the nature of the solvent were proven to dominate the film growth and affect its morphology.

To understand the phenomena responsible for the film morphology variation, an investigation of the CVD process with mass spectrometry was performed (see supplement information publication 1). Electron impact with energy of 25 eV was used as the ionization source to perform the experimental investigation. In addition to the fragments generated by the high electron energy, some products, such as C₂H₂ and CH₃O become detectable. At high temperatures, pyrolysis as well as oxidation of the solvent were observed by giving more water (m/e = 18), carbon dioxide (m/e = 44), furan (m/e = 68) and other products, which reveals the occurrence of the gas phase reaction. These may affect the kinetics of the film growth during the grow process.

3.1.3 Catalytic performance of Co₃O₄ towards CO and propene combustion

In the present work, Co₃O₄ spinel type catalyst is tested against the oxidation of C₃H₆ and CO. With the deposition process optimized and properties analyzed using Co(acac)₃ as precursor, it was interesting to evaluate the catalytic performance of the prepared Co₃O₄ thin film. In this work, no particular enhancement of the specific surface area and porosity can be noticed in the sample obtained with THF and toluene as solvent. Thus the analysis of the catalytic activity was simplified by choosing the sample prepared at 350 °C with THF as solvent. The as-synthesized catalyst was shown to be active for the conversion of propene and carbon monoxide to carbon dioxides. As illustrated in Figure 3.4, starting at around 230 °C, the total conversion of the investigated compounds to CO₂ was obtained at around 380 °C for C₃H₆ and 350 °C for CO, which gives an obvious temperature shift relative to the non-coated mesh.

This result shows that Co_3O_4 is active for total oxidation of CO and C_3H_6 . The excellent catalytic performance towards the oxidation of CO and C_3H_6 was attributed to the surface oxygen (lattice and adsorbed) and to the abundance of active Co^{3+} cations and oxygen vacancies generally present at the film surface of the transition metal oxides. For example, Co^{3+} cations and oxygen vacancy acted as the active site for CO oxidation and were key parameters governing the conversion rate of CO in the catalytic process [101,102]. In fact, in the presence of CO, C_3H_6 and O_2 , CO and C_3H_6 can be adsorbed on the Co^{3+} sites of Co_3O_4 and react with the weakly bound surface oxygen species such as bridged $\text{Co}^{3+}\text{-O}_2\text{-Co}^{2+}$, leading to the production of CO_2 , and the resulting oxygen vacancy is subsequently filled by reaction with O_2 [103] through Mark van-Krevelen mechanism.

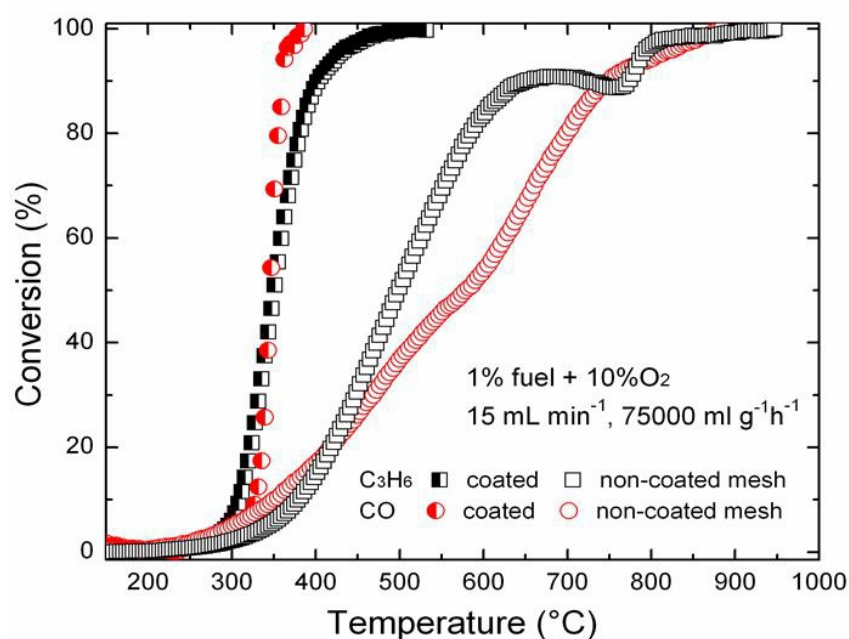


Figure 3.4 Light-off curve of C_3H_6 and CO conversion over Co_3O_4 [1].

Summary

In summary, the nature of the solvent was proven to influence the growth rate and even the morphology of the films. The fastest deposition rates were obtained with the precursor dissolved in toluene or THF. The importance of the selection of the solvent, precursor and the deposition temperature was clearly demonstrated with $\text{Co}(\text{acac})_3$ which exhibited a better stability in the selected solvent than $\text{Co}(\text{acac})_2$. This allows the growth of Co_3O_4 in a controllable way under different conditions, making the one-pot synthesis of TMO materials by PSE-CVD possible. The PSE-CVD process comes with multiple advantages, making it an

attractive alternative to conventional techniques. Systematic investigation of the PSE-CVD of Co_3O_4 starting from different precursors and solvents system allowed evidencing that:

- ❖ $\text{Co}(\text{acac})_3$ is more stable than $\text{Co}(\text{acac})_2$ in EtOH as solvent, indicating how important is the choice of the precursor in the PSE-CVD of TMOs. Therefore, only transition metals with stable oxidation state in the solvent system will be utilized in the rest of this study.
- ❖ Nonalcoholic solvents such as THF and toluene are preferable than EtOH for the fast growth of TMOs with complex and fine crystal shape.
- ❖ Some products and intermediates such as H_2CO , C_2H_2 and $^*\text{CH}_3\text{O}$ are observed during the decomposition of the liquid feedstock in the gas phase. Therefore, it is suggested that the adsorption of these species at the surface of the substrate play a crucial role during the film morphology formation.
- ❖ Deposition conditions such as the substrate temperatures plays significant role and should be carefully optimized in the metals oxides prepared with the PSE-CVD process.

3.2 PSE-CVD of catalytically active α -Fe₂O₃ thin films for the deep oxidation of C₃H₆

The design and fabrication of solid nano-materials is one of the core issues in heterogeneous catalysis to achieve desired performance. Traditionally, a major approach is to reduce the size of the catalyst particles for maximizing the number of active sites. In recent years, the rapid advancement in materials science has enabled the fabrication of catalyst particles with tunable morphologies. Consequently, both size modulation and morphology control of catalyst particles at the nanometer level can be achieved independently or synergistically to optimize their catalytic performance. Both the size and the shape of the catalyst particles at nanometer level can alter their reaction performance tremendously, not only accelerating the reaction rate but also mediating the product selectivity [104,105]. Heterogeneous catalysis refers to a chemical reaction occurring on the surface of a solid catalyst particle. Therefore, the surface atomic configurations that are determined by the size and morphology of the catalyst particle control the reaction efficiency [106]. Based on this principle, fabrication of catalytic materials with tunable size and shape at the nanometer level has now advanced to the top priorities in heterogeneous catalysis. In particular, morphological control of catalyst nanoparticles can selectively expose reactive crystal planes, and hence drastically promote their reaction efficiency. However, to tune their morphology, most catalysts including Fe₂O₃ nanomaterial, have been prepared only in the presence of complex structure-directing substances such as capping agents or surfactants [56]. The shape was then readily controlled by mediating the relative growth rates of different crystal planes, realizing an anisotropic growth pattern. However, surfactants which were used to maintain the specific shapes may in part remain and their effect on the catalytic properties may be questionable in interpreting the catalytic properties. Therefore, more facile and efficient routes to prepare Fe₂O₃ nanomaterial with tunable shape and without the presence of surfactants are highly expected.

In this study, we report a facile synthesis (PSE-CVD) route which was used with good reproducibility to prepare catalytically active α -Fe₂O₃ thin films with complex geometrical shapes *without any surfactants or capping agents*. Our strategy is based on the preparation method, the choice of the solvent, the precursor and the deposition conditions.

3.2.1 Growth and characterization

Thin films of α -Fe₂O₃ were prepared and the characterization of the crystalline structure and the purity of the deposited thin films were performed using XRD. The XRD patterns of all the samples present peaks were matching well with the cubic spinel-type structure of Fe₂O₃

 (JCPDS No. 39-0238), giving evidence to the existence of the Fe₂O₃ phase. By increasing the deposition temperature from 350 °C to 450 °C, the crystallinity of the deposited films improves (see Publication 2). In the investigated deposition temperature range, the absence of peaks corresponding to other iron oxide structures such as FeO or Fe₃O₄ indicates the high purity of the deposited films.

Since XRD cannot differentiate the α -, β - and γ -Fe₂O₃ phases, Raman spectroscopy was used to identify the phase of the prepared Fe₂O₃ oxide. According to the Raman results, the presence of peaks associated with the γ - and β -phase or magnetite (Fe₃O₄) can be definitively ruled out. All samples exhibit similar spectral signatures characteristic of α -Fe₂O₃ (see Publication 2), supporting the conclusion that the hematite (α -phase) was observed as the unique phase. The Raman spectrum definitively identified the prepared phase as α -Fe₂O₃ and further attests the purity of the films.

❖ Composition and ionic states

Energy-dispersive X-ray Spectroscopy (EDS) and X-ray Photoelectron Spectroscopy (XPS) were used to determine the chemical composition and the ionic state of the synthesized α -Fe₂O₃ thin films (see Publication 2). The EDS results have indicated that the films were mainly composed by Fe and O. The atom ratios of O/Fe were about 60/40 for all samples in the investigated temperature range. No variation of the bulk composition was observed with the increase of the deposition temperature. The ratios correspond well with the values calculated from the formula of hematite and are in good agreement with the literature [107].

The XPS results shows binding energies of Fe 2p_{3/2} and Fe 2p_{1/2} observed at 710.94 and 724.02 eV, respectively, which are characteristic of the Fe³⁺ state in the α -Fe₂O₃ thin film [107,108]. The spectra of the O1s core-shell have been deconvoluted by means of four contributions with binding energies ranging from 529.0 to 536.0 eV. The lowest binding energy located at 530 eV corresponds to the main lattice oxygen (O_{Lattice}) contribution and is attributed to the oxygen present in the form of oxide (O²⁻). The other three bands expanded until 535.87 eV can be assigned to adsorbed oxygen (O_{adsorbed}), including OH⁻, C–O, O–C=O) and some moisture from air (H₂O). The obtained positions of all components are in reasonable accordance with the reported values in the literature [109,110]. Also C1s signal showing large amount of carbon resolved into three components corresponding to adventitious carbon, C–O, and O–C=O moieties respectively was observed. The XPS results experiment was carried out to obtain information of the species involved in the catalytic reaction, therefore will enable the

 understanding of the catalytic reaction that occur at the surface of the prepared α -Fe₂O₃.

❖ **Thin films morphology inspection by SEM and HIM**

Quantitative description of the morphology of rough surfaces and interfaces of thin films has been a challenge for many years [111], largely because of the complexity and variation of the surface topography and the lack of universal technology to address this issue. Many approaches have been proposed to describe the surface topography at micro- and nano-scales. The surface morphology of thin film is usually treated as gray scale images in which the brightness of the image pixels is correlated to the surface relief. Two-dimensional signals (i.e. images with two dimensions of space, x and y, and gray levels) representing the relief of the surfaces can easily be constructed. Construction and analysis of these gray scale images of thin films are, however, not yet fully recognized. Numerous approaches and techniques have been proposed to characterize thin film surface textures [112]. In this thesis the well-known SEM and HIM were used to probe the thin film morphology of the hematite thin films samples. Figure 3.5 shows the surface morphology of the α -Fe₂O₃ thin films revealed by the scanning electron microscopy (SEM). The film morphology obtained at 350 °C is composed of small grains embedded in the matrix, with an average crystalline size of ~50 nm. At 400 °C, the film presents a uniform densely packed microstructure with grains in octahedral shape. It is well structured and composed of stacked shaped crystals superimposed on each other with precise orientation. At 450 °C, the film exhibits needle-like structures, each of which could result from the incorporation and agglomeration of small individual particles.

The possibility to focus the helium ion beam into a smaller probe size, providing a much smaller interaction volume at the sample surface than for typical electron microscopy motivates its usage in this study, since it was possible to obtain superior resolution and depth of field. HIM images of the synthesized α -Fe₂O₃ thin films present a morphology that varies with the deposition temperature. As shown in Figure 3.6, the films are composed of ordered pallets with arrangement and orientation depending on the substrate temperatures from 350 to 400 °C. However, the film obtained at 450 °C is composed of continuous grains with poor structural shape in contrast to those observed at lower temperatures. This method enables us to probe the microstructure of the samples more in depth than the commonly used SEM. In general, the increase of the substrate temperatures from 350 to 450 °C gives rise to significant changes of α -Fe₂O₃ morphology. The films produced at 350 and 400 °C show fine geometric crystal structures. The grain size of the sample obtained at 350 °C was estimated to be 34 nm, which was much smaller than those prepared at 400 °C (56 nm) and 450 °C (60 nm). As the

small grain size typically exhibits high specific surface area, the observation of temperature-dependent grain size might influences the physicochemical properties, and finally the catalytic performance.

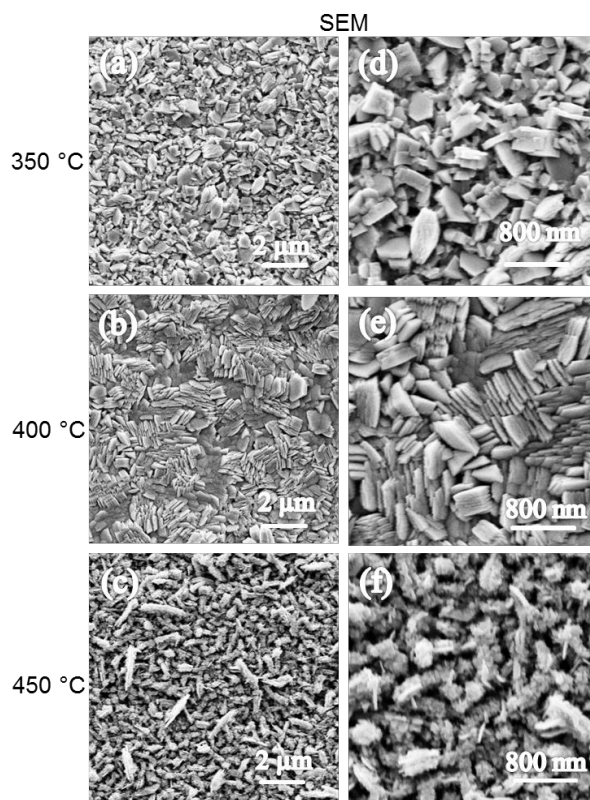


Figure 3.5 SEM images of α -Fe₂O₃ thin films coated on stainless steel, adapted from [2].

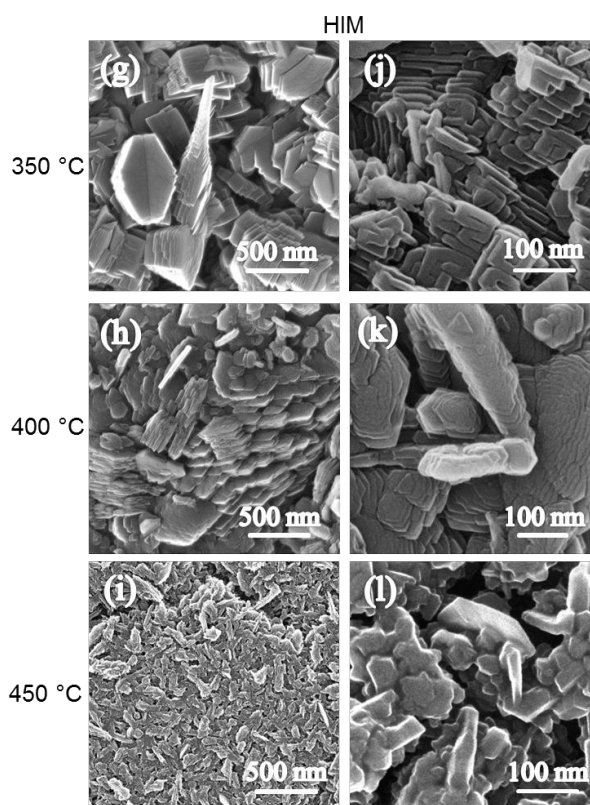


Figure 3.6 HIM images of α -Fe₂O₃ thin films coated on stainless steel adapted from [2].

3.2.2 Thermal properties

❖ Thermal stability

Thermal stability is one of the most important catalyst properties, because the catalytic tests have to be performed within the catalyst stability limit. The limit of the α -Fe₂O₃ lattice stability was found to be ~550 °C. One important conclusion is that, the lattice stability of the entire films was independent of the preparation condition such as the deposition temperature. The obtained thermal stability temperature was in line with early reported values [113].

❖ Temperature-programmed reduction (TPR)

TPR is a widely used tool for the characterization of metal oxides, mixed metal oxides, and metal oxides dispersed on a support. The TPR method yields quantitative information of the reducibility of the oxide's surface, as well as the heterogeneity of the reducible surface. It is important to perform such experiment since it can provide information about the materials properties. The reducibility of α -Fe₂O₃ was investigated with emission FTIR as an in-situ monitoring technique. Figure 3.7 shows the TPR profiles of the samples obtained by integrating the two specific emission bands characteristic of the Fe-O-Fe stretching vibration mode of Fe₂O₃. As shown in Figure 3.7, complete reduction was observed at 306 °C, 345 °C and 375 °C for samples prepared at 350 °C, 400 °C and 450 °C, respectively. Sample α -Fe₂O₃-350 °C exhibits the lowest temperature, and progressive shifts of the reduction towards higher temperatures are observed for α -Fe₂O₃ 400°C and α -Fe₂O₃ 450°C. The presence of anionic vacancies at higher temperatures was reported to be responsible for the lower reducibility in some metal oxides [114]. This effect could also occur in the current case for the films prepared at the higher temperatures.

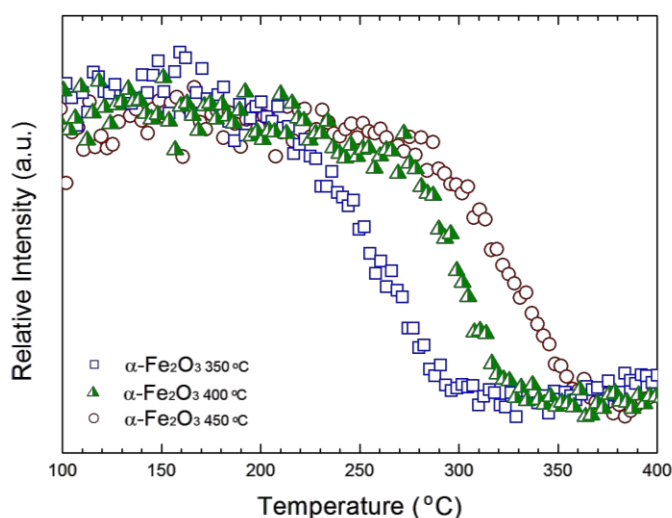


Figure 3.7 TPR profiles obtained for α -Fe₂O₃ thin films, showing variation of the reduction properties in function of deposition temperature [2].

3.2.3 Catalytic performance

Since the samples show different morphology, oxygen states distribution (O_{adsorbed} and O_{Lattice}) and reducibility, the catalytic test was performed for all samples to investigate these effects on the catalytic performance. To analyze the catalytic behavior after re-oxidation as a prerequisite for application in consecutive cycles, the catalytic conversion of C_3H_6 was carried out before and after pre-treatment of the catalyst under oxygen flow. This was done because the observed large amount of adventitious carbon, C–O, and O–C=O for the samples prepared at 400 and 450 °C would be expected to limit their performance. The presence of these carbonaceous species on the surface might lead to the formation of a barrier layer between the gas phase and the active solid phase on the catalyst surface, and thus reduce the interaction of gaseous oxygen with the surface. The catalytic tests on fresh samples were performed over catalysts prepared at 350 °C and 450 °C which present the lowest and the highest concentration of carbonaceous species, respectively. In addition, all pre-treated samples were used twice in the catalytic test to assess the reproducibility. Figure 3.8 displays the light-off pre-treated samples (Figure 3.8b).

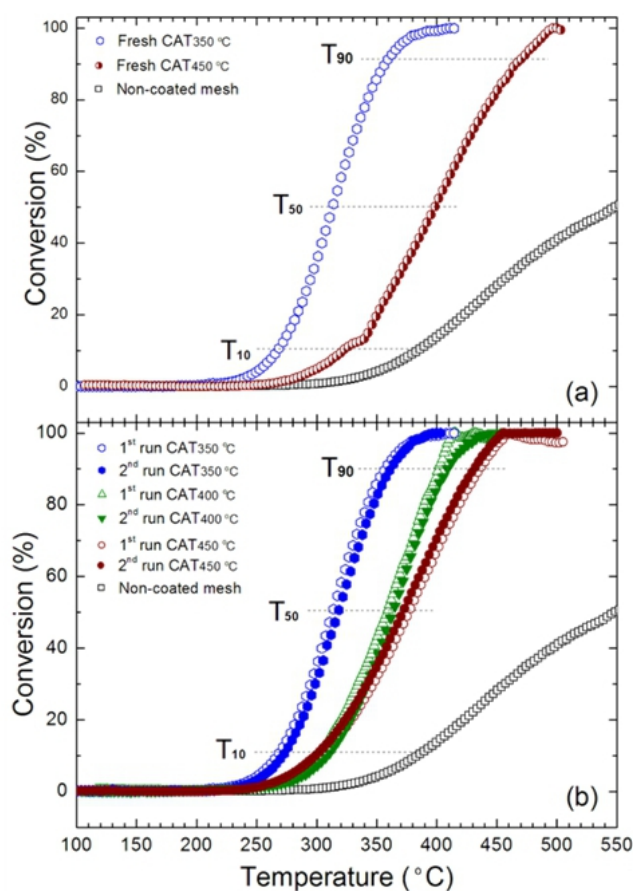


Figure 3.8 C_3H_6 conversion over $\alpha\text{-Fe}_2\text{O}_3$ coated and non-coated mesh. C_3H_6 oxidation result obtained with fresh samples (a) and pre-treated samples (b), reproduced from [2].

With fresh samples, the sample $\alpha\text{-Fe}_2\text{O}_3$ $_{350^\circ\text{C}}$ with lower adsorbed species presents the best catalytic performance towards C_3H_6 combustion than $\alpha\text{-Fe}_2\text{O}_3$ $_{450^\circ\text{C}}$. Starting at 100°C , pre-treated samples exhibit no effect on the catalytic conversion of C_3H_6 up to 225°C . For each sample, the conversion begins at around 250°C . Temperatures for 10%, 50% and 90% C_3H_6 conversion are presented in Table 3.1 for fresh and pre-treated samples. The film prepared at 350°C is the most active one regarding the conversion profile as a function of temperature; followed by the films obtained at 400°C and 450°C , respectively. The experiments were repeated several times and the results were reproducible (Figure 3.8b). Especially, the surface morphology and composition were found to remain the same by measuring the samples before and after the catalytic tests with XPS as shown in the supplement part of Publication 2. Together with the reproducibility results in Figure 3.8b, it can be predicted that the catalytic properties are not largely affected, which is also supported by the morphology and composition results. This observation further confirms that the adsorbed oxygen at the surface of the catalysts does not play a major role in the conversion of C_3H_6 . In total, $\alpha\text{-Fe}_2\text{O}_3$ is active, reusable, and reproducible and no deactivation was observed after several times of use. It is worth to mention that, no trace of carbon monoxide was observed with the entire $\alpha\text{-Fe}_2\text{O}_3$ samples, indicating that hematite can be efficiently use for CO conversion to CO_2 . Moreover, $\alpha\text{-Fe}_2\text{O}_3$ presents competitive activity to that reported for supported noble metals as evident from Table 3.1. Table 3.1 presents an overview of the catalytic performance of the as-prepared $\alpha\text{-Fe}_2\text{O}_3$ and selected catalysts in the literature. Special attention is devoted to the comparison of the catalytic performance with noble metals and transition metals oxides. As crucial factors, the weights of the catalyst and the weight hourly space velocity (WHSV) have been taken in account. Even though the experimental conditions are somewhat different, it can be seen from the table that $\alpha\text{-Fe}_2\text{O}_3$ exhibit excellent catalytic performance compared to some of the selected catalysts in the literature. As an example, with only 20 mg of $\alpha\text{-Fe}_2\text{O}_3$ deposited at 350°C , the oxidation of 50 % of propene was reached at a low temperature of 331°C , whereas that of 200 mg $\text{Au}/\text{Al}_2\text{O}_3$, and $\text{La}_{1.7}\text{Sr}_{0.3}\text{CuO}_4\text{S}_{0.2}$ was obtained at 365°C and 419°C respectively.

To clearly identify the phenomenon governing the difference in activity between the three catalysts, a correlation between the catalytic behavior and the $\alpha\text{-Fe}_2\text{O}_3$ characterization results was made. The XPS results revealed the presence of both adsorbed and lattice oxygen. The $\text{O}_{\text{adsorbed}}/\text{O}_{\text{Lattice}}$ ratio of $\alpha\text{-Fe}_2\text{O}_3$ - 350°C was the lowest for the three samples. The catalytic tests over fresh and pre-treated samples reveal the negligible role of the adsorbed oxygen,

 suggesting that the lattice oxygen plays a key role in the reaction sequence. This was corroborated by the TPR experiments. Based on these and the XPS results, the possible oxidation mechanism of C₃H₆ over the as-prepared catalysts has been discussed.

Table 3.1 Overview of the catalytic performance of the as-prepared α -Fe₂O₃ and some catalysts in the literature; adapted from ESI [2].

Material	Weight (mg)	Gas composition	WHSV ^a (ml g ⁻¹ h ⁻¹)	T ₁₀ ^b (°C)	T ₅₀ ^b (°C)	T ₉₀ ^b (°C)	Ref.
α -Fe ₂ O ₃ 350 °C	20	1% C ₃ H ₆ /10% O ₂ in Ar	45000	260	313	350	This work
α -Fe ₂ O ₃ 400 °C				295	355	400	
α -Fe ₂ O ₃ 450 °C				302	380	435	
Co ₃ O ₄	41.5	2% C ₃ H ₆ /20% O ₂ in Ar	73000	293	327	356	[115]
Co ₃ O ₄	12	2% C ₃ H ₆ /20% O ₂ in Ar	75000	325	354	385	[80]
Cu _{0.72} Co _{2.28} O ₄	40	13% C ₃ H ₆ /52% O ₂ in N ₂	15000	230	275	>400	[116]
Au/Al ₂ O ₃	200	1.5% C ₃ H ₆ /4% O ₂ in He	22500	288	349	410	[117]
Au/Al ₂ O ₃	200	1% C ₃ H ₆ /9% O ₂ in He	219512	-	365	-	[118]
Ag/Al ₂ O ₃	50	3% C ₃ H ₆ /10% O ₂ in N ₂	12000	-	-	420	[119]
La _{1.7} Sr _{0.3} CuO ₄ S _{0.2}	200	0.1% C ₃ H ₆ /5% O ₂ in N ₂	30000	368	419	500	[120]
Non-coated mesh	-	1% C ₃ H ₆ /10% O ₂ in Ar	-	381	550	680	This work

Note: ^a WHSV is weight hourly space velocity; ^b T₁₀, T₅₀ and T₉₀ refer to the temperatures at which 10%, 50% and 90% propene is converted, respectively.

For the catalytic oxidation of hydrocarbons, two mechanisms have been widely accepted: a suprafacial mechanism, which involves interaction of surface oxygen with reactants, and an intrafacial one. This Mars van Krevelen mechanism (MvK) involves migration of bulk oxygen to the surface, where it participates in the reaction with the reactant, and replacement of bulk oxygen by oxygen from the gas phase [121]. Investigations have pointed out that this mechanism is active in the combustion of hydrocarbons over transition metal oxide catalysts [122]. Also, catalytic combustion of C₃H₆ over Co₃O₄ has been reported by Liotta et al [123]. to proceed according to the Mars van Krevelen mechanism. It is thus plausible that C₃H₆ combustion over α -Fe₂O₃ follows an intrafacial mechanism, which involves a redox cycle and is related to the mobility of the lattice oxygen.

In addition to the role played by the lattice oxygen in the catalytic performance, the differences observed in the catalytic properties may be also explained in correlation with the film morphology. In fact, it is well known that the sizes, shapes, and structures of catalyst materials are closely related to the catalytic performance [124]. Exposed planes containing

more iron atoms could provide more active sites for catalytic reactions and consequently higher catalytic performance. The catalytic performance can benefit from the exposed plate-like structures which could adsorb abundant gaseous molecules on the surface of the sample as an opportunity for their participation in the reaction sequence.

Further studies in which the effect of the preparation temperature, which is associated with the catalytic activities of different α -Fe₂O₃ thin films, will assist in the understanding of other catalyst nano-crystals and thus offer great opportunities to explore the dependence of a material's properties on the morphology and structure. The results highlight the validity of the PSE-CVD approach for the tailored synthesis of materials with specific morphology and good catalytic performance.

Summary

Thin films of hematite were successfully prepared via a PSE-CVD process. The obtained thin film was systematically characterized in terms of structure, composition, thermal stability, reducibility and catalytic properties. The study enables the following observations:

- ❖ The substrate temperature plays an important role on the crystalline shape evolution, therefore, determines the film morphology.
- ❖ The obtained α -Fe₂O₃ was found to be thermally stable up to 550 °C, attesting the stable status of hematite.
- ❖ The thin films of α -Fe₂O₃ exhibited good catalytic performance towards catalytic combustion of C₃H₆. Moreover, no trace of CO commonly observed in the catalytic oxidation of some volatile organic compounds by metal oxides was observed.
- ❖ The α -Fe₂O₃ maintained its activity and stability upon several consecutive heating and cooling cycles.

Here we show that the good performance for catalytic abatement of VOCs can be achieved with α -Fe₂O₃ thin film, prepared in the absence of any dopants, surfactant or capping agents. More importantly, the activity of the prominent catalytic behavior of the α -Fe₂O₃ catalyst is due to the concerted functions between the surface chemical composition, reducibility and film morphology. The lattice oxygen detected by XPS, the reduction property and the fine crystalline shape of samples prepared at low temperature played important roles in the catalytic oxidation process of C₃H₆.

3.3 PSE-CVD of catalytically active CuO thin film catalyst for CO and C₃H₆ oxidation

Cupric oxide (CuO) is a p-type semiconductor has been widely investigated for various applications such as solar energy conversion [125], electrochromic devices [126], biosensors [127], photocatalysis and catalysis [129,130]. Thanks to the non-toxicity of CuO and abundant availability of its constituents, CuO is an advantageous and promising material for diverse applications. In this work we provide an introduction of PSE-CVD to synthesize copper oxide under well-controlled conditions. Deposition pressures were optimized to obtain good growth rates. The deposited films were comprehensively characterized regarding structure, morphology, and thermal stability, very important in the comprehension of the films' properties. The catalytic performance of the grown copper oxide was investigated for the deep oxidation of C₃H₆.

3.3.1 Growth and phase dependence on deposition condition

To obtain fast and homogeneous deposition of CuO, the growth kinetics was investigated under variable pressure. At the pressure of 6 mbar, the CuO thin films were grown at a rate of 0.5 nm min⁻¹. This growth rate increased linearly with the pressure to reach 1.84 nm min⁻¹ at 24 mbar. However, further increase of the deposition pressure to 50 mbar seems not to influence the growth rate, as shown in Figure 3.10. The relatively low growth rate at lower pressure may result from the lower concentration of oxygen and precursor adsorbed or residing on the substrate. When the pressure reaches 24 mbar, the adsorption of the oxygen and precursor becomes saturated, which would lead to a similar growth rate with further increase of the deposition pressure. As 24 mbar gives a relatively high growth rate, all the characterization and tests in the following analysis were carried out with the samples obtained at 24 mbar.

The X-ray diffraction pattern of the deposited thin film is displayed in Figure 3.11. The substrate temperature was varied from 200 °C to 300 °C. Only Cu₂O was formed for substrate temperatures of 200-250 °C; a mixture of Cu₂O and CuO was observed at 275 °C, and a unique phase of CuO was formed at 300 °C with well-defined diffraction peaks. The lattice parameters of CuO are $a = 4.6883 \text{ \AA}$, $b = 3.4229 \text{ \AA}$, $c = 5.1319 \text{ \AA}$, which are in good agreement with the reported values in the literature [131].

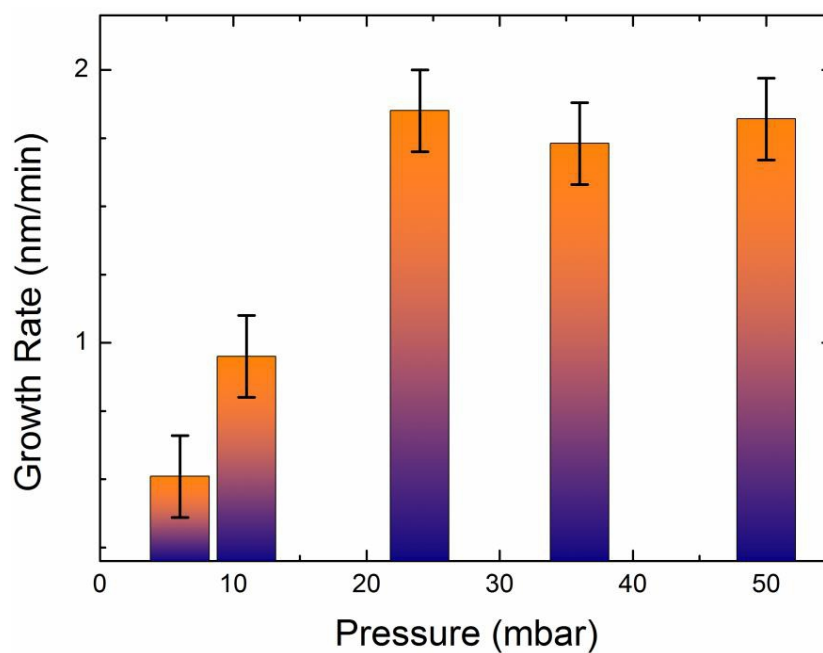


Figure 3.10 Growth kinetics of copper oxide as a function of deposition pressure [4].

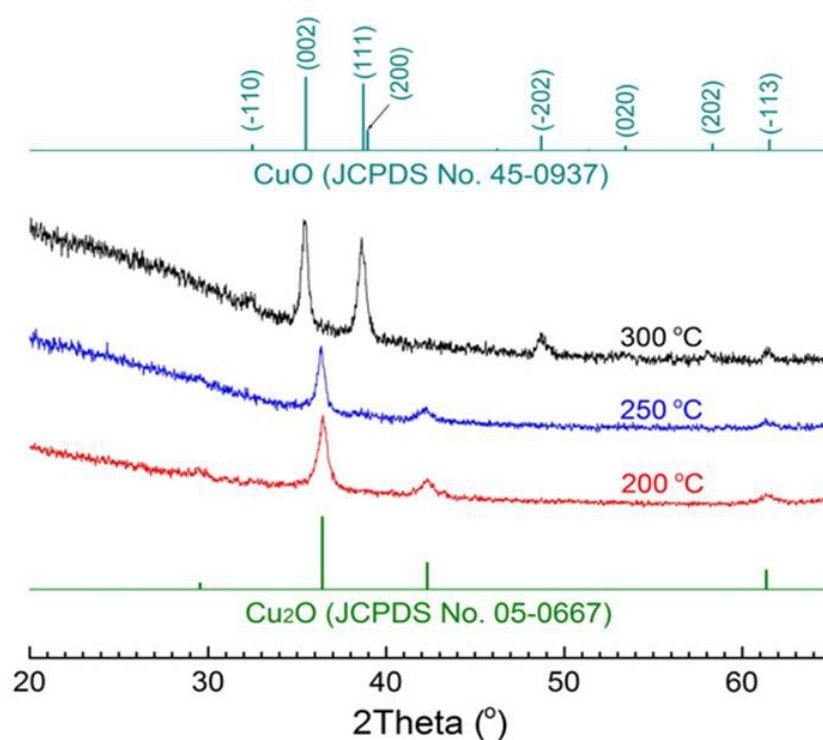


Figure 3.11 XRD pattern of copper oxide film showing phase dependence deposition temperature [4].

Starting from a liquid feedstock consisting of $\text{Cu}(\text{acac})_2$ dissolved in ethanol, the formation pathway of CuO during the PSE-CVD process can be illustrated with the combination of adsorption, dissociation and oxidation, as presented in Figure 3.12.

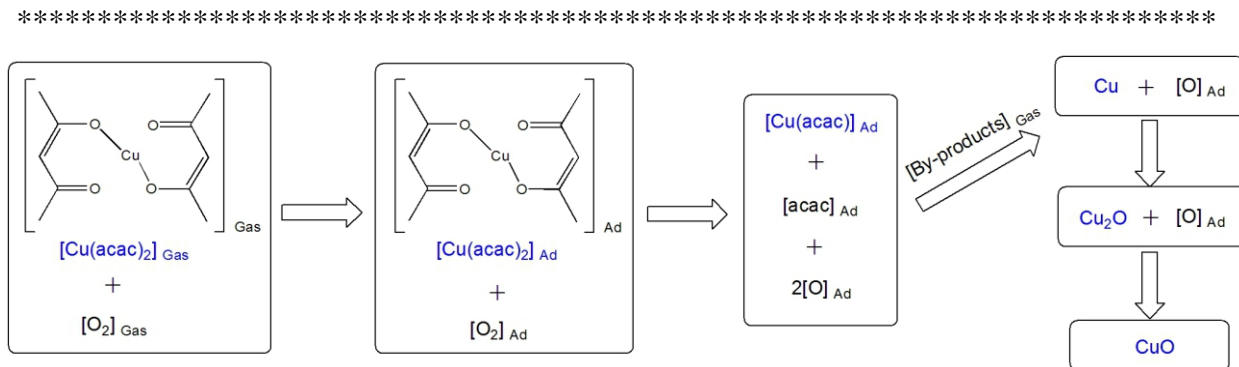


Figure 3.12 Formation pathway of CuO in the PSE-CVD process with $\text{Cu}(\text{acac})_2$ as precursor reproduced from [4].

3.3.2 Catalytic performance

The catalytic performance of the CuO was evaluated for the complete oxidation of C_3H_6 . The background effect of the mesh on the combustion process was examined by carrying out the oxidation of C_3H_6 respectively on non-coated mesh under the same gas inlet conditions. Figure 3.13 compares the conversion temperature of C_3H_6 production over CuO films and non-coated mesh. The conversion plots show clearly that CuO favors the total oxidation of CO and C_3H_6 at lower temperatures relative to the non-coated mesh. In the presence of CuO, the consumption of propene became observable at about 190 °C and complete conversion was reached within 310 °C, while these two values shift towards higher temperatures for the reaction on non-coated mesh. With CuO, no trace of CO was detected in the oxidation process. However, a significant amount of CO was formed in the reaction without catalyst, which can be assigned to the partial oxidation reaction. In the two cases, CO_2 was observed to be the final product. The temperatures T_{10} , T_{50} and T_{90} , corresponding to the C_3H_6 conversion during the temperature-programmed reaction, were selected to compare the catalytic performance of the deposited CuO as well as some representatives catalysts available in the literature (Table 3.2) toward C_3H_6 oxidation. CuO as shown in Table 3.2 exhibits excellent catalytic performance with $T_{50} = 272$ °C; this temperature is close to that of $\text{Cu}_{0.72}\text{Co}_{2.28}\text{O}_4$ (275 °C) and $\text{Au}/\text{BaO}/\text{A}_2\text{O}_3$ (290 °C), indicating that CuO features competitive activity to Co-Cu mixed oxides as well as to alkali-doped noble metals for the combustion of C_3H_6 . Based on the value of T_{50} , the performance is the following: $\text{CuO} \geq \text{Cu}_{0.72}\text{Co}_{2.28}\text{O}_4 > \text{Au}/\text{Rb}_2\text{O}/\text{A}_2\text{O}_3 > \text{Au}/\text{Rb}_2\text{O}/\text{A}_2\text{O}_3 > \text{Au}/\text{A}_2\text{O}_3 = \text{Au}/\text{MgO}/\text{A}_2\text{O}_3 > \text{La}_{1.7}\text{Sr}_{0.3}\text{CuO}_4\text{S}_{0.2} > > \text{non-coated mesh}$.

The catalytic oxidation of hydrocarbons employing metal oxides catalysts can proceed with the Mars-van Krevelen mechanism, and the C-H bond activation is related to the rate of oxidation for hydrocarbons [116]. In the current case, a redox mechanism consisting of three

steps: firstly, the reaction of C_3H_6 with the trapped or lattice oxygen leading to CuO reduction; secondly the release of oxygen from the Cu_2O on the surface, and finally the re-oxidation of Cu_2O by means of oxygen are involved. It is well known that the performance of copper oxides catalysts in the combustion process of hydrocarbons and CO were associated with the reducibility of the catalysts [132,133]. It might be applicable to the CuO obtained with PSE-CVD. However, further confirmations still remains.

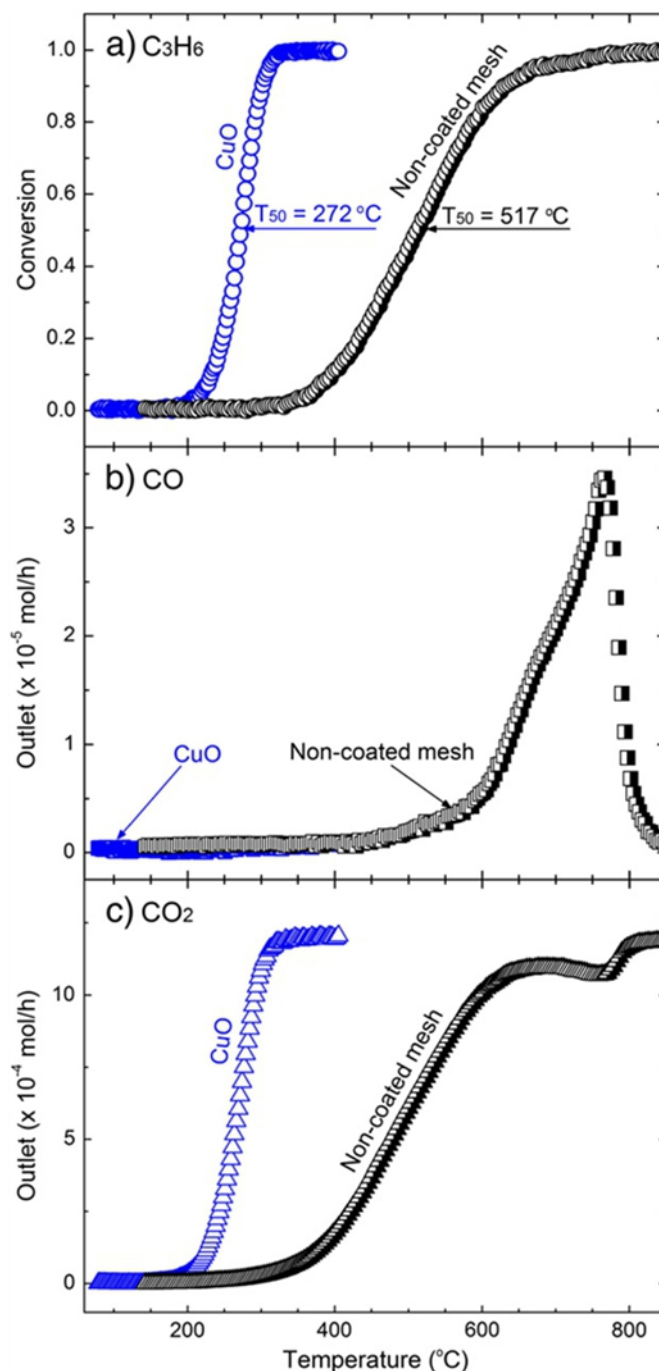


Figure 3.13 Light-off curves of CO and C_3H_6 conversion with CuO -coated and non-coated mesh [4].

Table 3.2 Comparison of the catalytic performance; reproduced from ESI [4].

Material	Gas composition	WHSV ^a (ml g ⁻¹ h ⁻¹)	T ₁₀ ^b (°C)	T ₅₀ ^b (°C)	T ₉₀ ^b (°C)	Ref.
CuO	1% C ₃ H ₆ /10% O ₂ in Ar	75000	229	272	301	This work
Co ₃ O ₄	2% C ₃ H ₆ /20% O ₂ in Ar	73000	293	327	356	[115]
Cu _{0.72} Co _{2.28} O ₄	13% C ₃ H ₆ /52% O ₂ in N ₂	15000	230	275	>400	[116]
Au/A ₂ O ₃	1.5% C ₃ H ₆ /4% O ₂ in He	22500	288	349	410	[117]
Au/A ₂ O ₃	1% C ₃ H ₆ /9% O ₂ in He	219512	-	365	-	[118]
Au/Rb ₂ O/A ₂ O ₃	1% C ₃ H ₆ /9% O ₂ in He	257143	-	307	-	
Au/MgO/A ₂ O ₃	1% C ₃ H ₆ /9% O ₂ in He	214286	-	359	-	
La _{1.7} Sr _{0.3} CuO ₄ S _{0.2}	0.1% C ₃ H ₆ /5% O ₂ in N ₂	30000	368	419	500	[120]
Non-coated mesh	1% C ₃ H ₆ /10% O ₂ in Ar	75000	398	517	629	This work

Note: ^a WHSV is weight hourly space velocity; ^bT₁₀, T₅₀ and T₉₀ refer to the temperatures at which 10%, 50% and 90% propene is converted, respectively.

Summary

PSE-CVD, which is a facile approach to achieve a tailored control over film composition and microstructure, has been used to deposit thin films of CuO. With XRD, emission FTIR, HIM and UV-Vis spectroscopy, the structure, morphology, band gap energy and thermal stability of the obtained thin film were systematically characterized.

- ❖ The structure study indicates that CuO was formed as the unique phase at 300 °C.
- ❖ The obtained CuO samples were found to be thermally stable up to 450 °C and exhibit a band gap energy of 1.81 ± 0.05 eV.
- ❖ The catalytic tests indicate that the as-deposited CuO is a very active catalyst in the oxidation of propene, with a performance comparable to that of supported noble metals.

3.4 PSE-CVD of Mn_3O_4 and investigation of its catalytic properties and thermal stability

Manganese oxides are of great importance in catalysis, electrochemistry, ion-exchange materials, magnetite, batteries, and catalysis among other areas [134,135]. In the recent past, controlled synthesis of MnO_x nano-materials has attracted considerable attention from both academia and industry [136,137]. Considering the availability and toxicity, Mn_3O_4 has captured great attention besides its unique physicochemical properties [138]. In view of these considerations, the synthesis of Mn_3O_4 thin films with the PSE-CVD process and an attempt to understand the physicochemical properties have been undertaken in the present work. Among the catalyst properties, the catalytic activity and the thermal stability are crucial in the catalytic oxidation, therefore require special attention in the design or selection of metal oxide catalysts. Growth kinetics with respect to the effect of the substrate temperature was optimized. The deposited films were comprehensively characterized and an analysis of the thermal properties, such as the stability and redox behavior, were investigated. Catalytic performance of the obtained samples was explored for the deep oxidation of CO and propene (C_3H_6) in a fixed-bed quartz reactor under atmospheric pressure.

3.4.1 Growth and characterization

The films obtained within the preparation temperature range of 350-500 °C were analyzed by XRD, to confirm the nature of the obtained phase. The XRD signature of all the prepared Mn_3O_4 films have been observed in the patterns, which have been perfectly attributed to the crystallographic planes of the tetragonal Mn_3O_4 (JCPDS No. 24-0734) structure (see Publication 5). As already noticed for all TMOs (Co_3O_4 , Fe_2O_3 , and CuO) successfully prepared in this thesis, no characteristic peaks of impurity phases or other MnO_x phases were detected in the XRD patterns, indicating the high purity of the final films. Moreover, the strong and sharp reflection peaks suggest that the as-prepared samples were well crystallized.

❖ Chemical composition and average oxidation states

To characterize the surface composition of the Mn_3O_4 films, ex situ XPS was used as indicated in Figure 3.14. It can be observed that the Mn 2p peak consists of two main spin-orbital lines. The Mn $2p_{3/2}$ peak is centered at 641.38 eV and the Mn $2p_{1/2}$ peak at 653.13 eV, with a splitting of 11.75 eV, which is in good agreement with literature values [80,139].

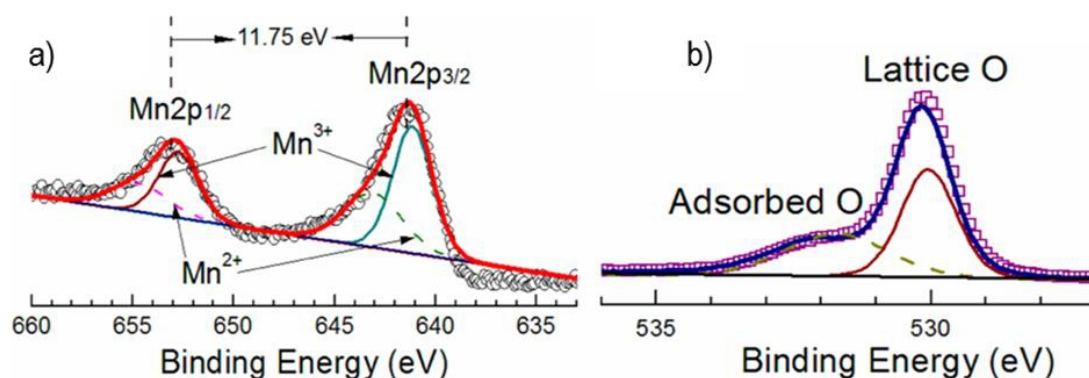


Figure 3.14 XPS analysis of the Mn_3O_4 samples: fitted Mn $2p_{1/2}$ and Mn $2p_{3/2}$ photoelectron peaks (a) and O $1s$ photoelectron peaks (b) [5].

The Mn $2p$ spectrum was deconvoluted as two pairs of doublets: 641.16 and 643.03 eV, 652.71 and 654.58 eV, corresponding to $\text{Mn}^{3+} 2p_{3/2}$ and $\text{Mn}^{2+} 2p_{3/2}$, $\text{Mn}^{3+} 2p_{1/2}$ and $\text{Mn}^{2+} 2p_{1/2}$, respectively. The calculated ratio of $\text{Mn}^{2+}/\text{Mn}^{3+}$ in Figure 3.14a is around 1:2, which is in line with a previously reported value [140]. An asymmetric two-band structure is observed in the O $1s$ spectra Figure 3.14b. It is resolved into two components, corresponding to the binding energies of 530.14 and 532.12 eV, respectively. The first peak is characteristic of the lattice oxygen of Mn_3O_4 , and the second peak is assigned to the physisorbed, chemisorbed, or dissociated oxygen or hydroxyl species in poor electrical contact with the surface [141,142]. On the basis of the XPS results, the O/Mn ratio is calculated to be 1.38. This ratio is slightly different than the value of 1.33 estimated from EDS studies, which is due to the strong contribution of the surface oxygen in the XPS measurement.

❖ Determination of Mn_3O_4 lattice stability limit

The lattice stability was evaluated by integrating the intensity of the characteristic peaks of the spinel as a function of the temperature which reflects the phase transformation. As depicted in Figure 3.15, the two bands centered at around 513 and 609 cm^{-1} were clearly seen at temperatures below 800 °C. These bands disappeared with further increase of the temperature, indicating that the as-prepared Mn_3O_4 is thermally stable up to 800 °C. This limit could be associated with the oxidation of Mn^{2+} ions under air condition [143]. Compared to other active transition metal oxides (Co_3O_4 , CuO and $\alpha\text{-Fe}_2\text{O}_3$) synthesized by PSE-CVD in this thesis, Mn_3O_4 thin films shows the highest potential for high-temperature catalytic application.

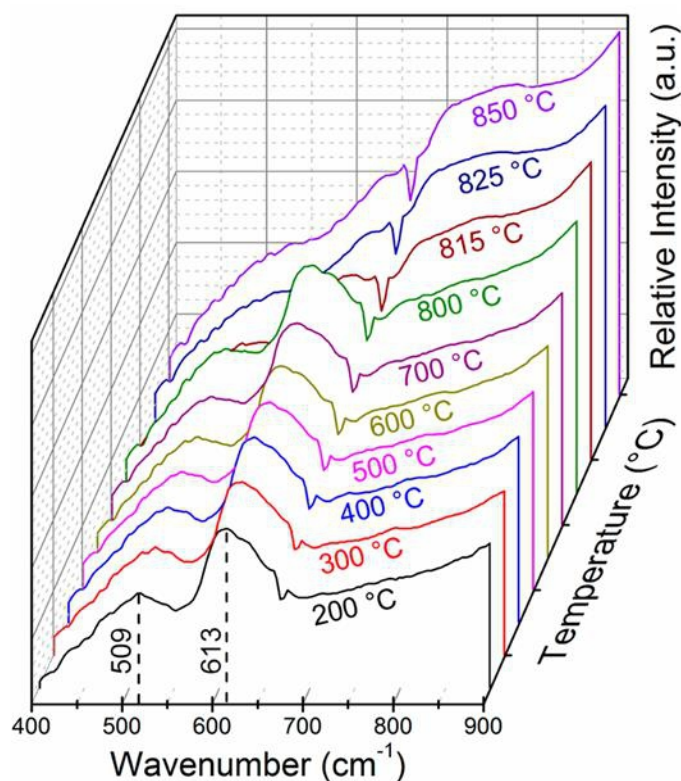


Figure 3.15 Thermal stability of the Mn_3O_4 film obtained on planar stainless steel with a thickness of 300 nm [5].

3.4.2 Catalytic performance

The catalytic performance was investigated with respect to the total oxidation of CO and C_3H_6 at atmospheric pressure. The full comparison of the reactants and products is given in Figure 3.16 and 3.17. The oxidation of CO over Mn_3O_4 becomes observable at 190 °C, and complete conversion occurs at 343 °C with a temperatures shift to 280 and 820 °C for an experiment without Mn_3O_4 . In this work, the temperature at 50 % (T_{50}) of CO conversion was observed at 271 °C demonstrating that Mn_3O_4 prepared by PSE-CVD in the present work is highly active in the deep oxidation of CO, compared to the CO oxidation over manganese oxides (MnO_x , and Mn_2O_3) prepared by precipitation [144], with T_{25} at 298 °C which is higher than the value (250 °C) obtained with Mn_3O_4 in the present work. The abundance of adsorbed oxygen, revealed in the XPS results, can play a key role in the oxidation process.

It is also observed that the conversion of C_3H_6 on Mn_3O_4 becomes detectable at 220 °C, and conversion of C_3H_6 approaches 100% at 433 °C. However, the oxidation of C_3H_6 on the non-coated mesh starts at ~ 290 °C, and a temperature as high as 821 °C (Figure 3.17) is required for complete conversion of C_3H_6 . More importantly, at low C_3H_6 conversions the main product is CO_2 , but a trace of CO peaking at 769 °C (Figure 3.17b) is formed on non-coated

 mesh, which results from partial oxidation. However, except CO₂ and water, no other byproducts were detected in the presence of Mn₃O₄, indicating that Mn₃O₄ is effective to reduce CO emission.

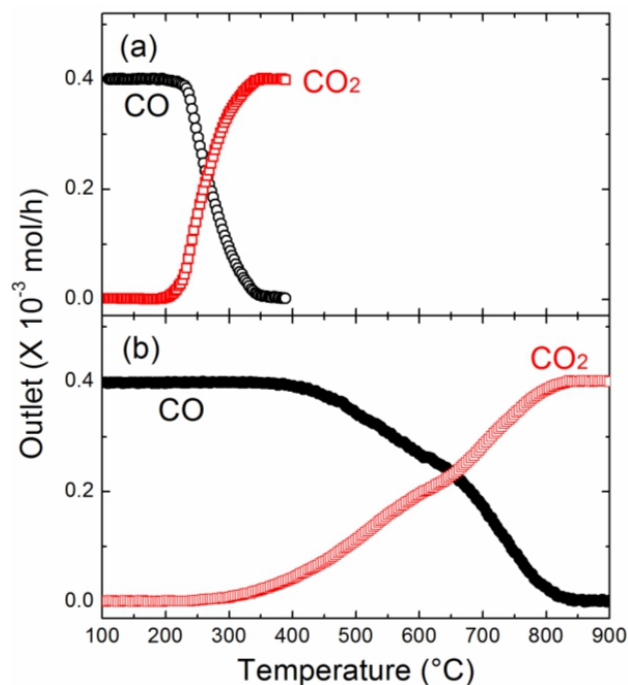


Figure 3.16 Catalytic test of CO oxidation with Mn₃O₄ (a) and a non-coated mesh (b). The WHSV is 75.000 mL/gcat·h for the reaction with Mn₃O₄ [5].

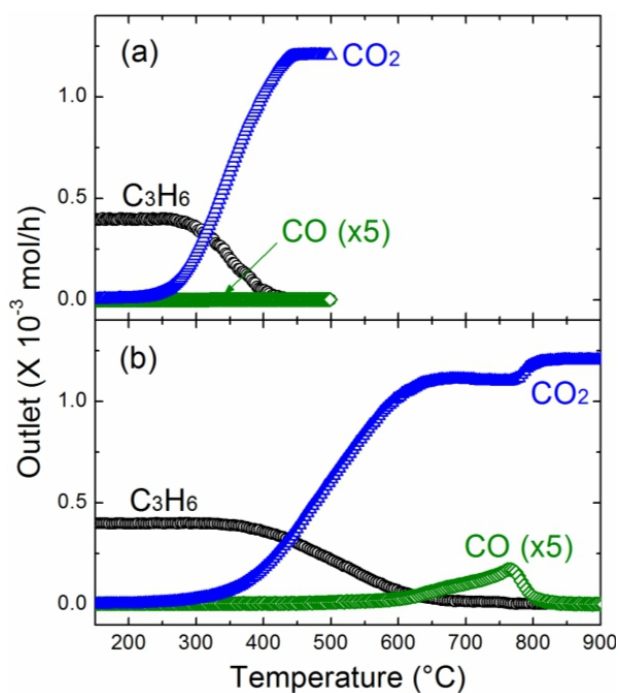


Figure 3.17 Catalytic test of C₃H₆ oxidation with Mn₃O₄ (a) and non-coated mesh (b). The WHSV is 75.000 mL/gcat·h for the reaction with Mn₃O₄ [5].

The catalytic oxidation of CO and C₃H₆ over Mn₃O₄ follows likely the Mars-van Krevelen (MvK) mechanism which involves reversible reduction-reoxidation steps of the lattice oxygen atoms. As reported, trapped oxygen is apparently released with the increase of the temperature, and Mn₃O₄ tends to be reduced through the subsurface oxidation of CO or C₃H₆ with the lattice or surface oxygen. Subsequently, the reduced metal oxide site is re-oxidized by the atmospheric O₂. According to the redox results, Mn₃O₄ is easier to be reoxidized than to be reduced, demonstrating that the reduction step could play a crucial role in the kinetics of the catalytic oxidation process.

Summary

Pure and fine thin film of hausmanite phase was deposited using PSE-CVD. The obtained samples were characterized in terms of structural, chemical composition. Moreover, the thermal properties were investigated with a newly developed in situ emission FTIR spectroscopy.

- ❖ According to the XRD, the entire prepared samples were tetragonal Mn₃O₄, irrespective of the substrate temperature within the range of 350-500 °C.
- ❖ The catalytic tests indicate that the use of Mn₃O₄ can initiate CO and C₃H₆ oxidation at lower temperatures, with higher selectivity toward CO₂ which may help prevent CO production during the oxidation of C₃H₆.
- ❖ Mn₃O₄ shows a high thermal stability up to 800 °C, high reducibility, and re-oxidative regeneration at low temperatures.

3.5 Active cobalt ferrite for low temperature catalytic combustion

Thin films based on spinel ferrites present numerous applications, including gas sensors [145], photocatalysis [146], adsorption technologies [147] and high-frequency transformer technology [148]. In the field of heterogeneous catalysis, spinel ferrites are effective catalysts for several industrial processes such as decomposition of alcohols and hydrogen peroxide, oxidation of CO [149], aerobic oxidation of monoterpene alkenes [150] and cyclohexane [151]. Among the transition metal oxides, cobalt ferrite owns an inverse cubic structure and has been widely investigated due to its high Curie temperature, high coercivity, excellent chemical stability and mechanical hardness [152]. Although cobalt ferrite exhibits attractive catalytic performance, the related studies concerning its catalytic application in the removal of VOCs [153] and deep oxidation of fuels [154] are scarce. Moreover, to the best of our knowledge, no reports correlate the redox properties of such materials with their band gap energies. The present work is devoted to synthesize Co-Fe-O thin films by PSE-CVD, the systematic characterization of their properties and finally their potential application as catalyst for low-temperature CO, C₃H₆, n-C₄H₈ and C₂H₆O oxidation by. The obtained samples were characterized in terms of structure, composition, morphology, optical and redox properties using X-ray Diffraction (XRD), Raman and X-ray Photoelectron Spectroscopy (XPS), Helium Ion Microscopy (HIM), Ultra-Violet Visible spectroscopy (UV-Vis) and in-situ emission FTIR. The effect of iron substitution by cobalt in the structure on the optical and redox properties was investigated. The catalytic performance of the Co-Fe oxides was discussed with respect to the participation of surface and lattice oxygen in the oxidation process. According to XPS and temperature-programmed reduction/oxidation (TPR/TPO) results, a suprafacial mechanism was the dominant mechanism for CO oxidation to CO₂; while C₃H₆, n-C₄H₈ and C₂H₆O were oxidized through an intrafacial process (Mark-van-Krevelen) .

3.5.1 Growth and characterization

For the preparation of the cobalt ferrite thin films, cobalt acetylacetonate (Co(acac)₃) and iron acetylacetonate (Fe(acac)₃) were weighed in the adequate molar ratios Co/Fe, dissolved in tetrahydrofuran and kept at respective concentrations of 5 mM. The single phase of Co_xFe_{3-x}O₄ of the respective stoichiometric relation was obtained by adjusting the molar ratio of the two metallic elements. After the synthesis, the structure of the deposited crystalline phases were analyzed using XRD and the phase were identified by referring to the powder XRD database (JCPDS-ICDD). Well-defined diffraction peaks presenting the same orientations as the CoFe₂O₄ inverse spinel (JCPDS Nr. 03-0864) were observed (see

Manuscript 1). According to the XRD result, a decrease of the lattice constant with the increases Co population in the matrix of CO-Fe-O was observed (see table 1 manuscript 1). The cationic distribution have been reported for similar composition as in this work to be $[\text{Co}^{2+}\text{Fe}^{3+}\text{Co}^{3+}]_{\text{T-site}}[\text{Fe}^{3+}\text{Co}^{2+}\text{Co}^{3+}]_{\text{O-site}}\text{O}_4$, $[\text{Co}^{2+}\text{Fe}^{3+}]_{\text{T-site}}[\text{Co}^{2+}\text{Fe}^{3+}\text{Co}^{3+}]_{\text{O-site}}\text{O}_4$, and $[\text{Co}^{2+}\text{Fe}^{3+}]_{\text{T-site}}[\text{Fe}^{3+}\text{Co}^{2+}]_{\text{O-site}}\text{O}_4$ for $\text{Co}_{2.01}\text{Fe}_{0.9}\text{O}_4$, $\text{Co}_{1.8}\text{Fe}_{1.2}\text{O}_4$ and $\text{Co}_{0.9}\text{Fe}_{2.1}\text{O}_4$ respectively. The observed decrease of the lattice constant with increasing Co content can be associated to this changing distribution. In fact, when the amount of cobalt increases, the cell parameter decreases and there is a gradual evolution toward a normal spinel structure as observed in our XRD patterns. This is due to the fact that the diamagnetic Co^{3+} cations replace the Fe^{3+} cations in the octahedral position and the octahedral preference of the Co^{2+} cations becomes less dominant.

A home-made Raman spectrometer, with spectral resolution of 4 cm^{-1} , was also used to confirm the phases of the obtained oxides. No other diffraction peaks corresponding to the formation of impurity phases were detected (see Manuscript 1), revealing the high purity of the synthesized thin films.

❖ Chemical composition

To identify the species involved in the catalytic oxidation ex-situ XPS was used to investigate the surface composition and chemical species of the cobalt ferrite thin films. XPS spectra of Fe 2p, Co 2p, and O1s are presented in Figure 3.18. The Fe $2p_{1/2}$ and Fe $2p_{3/2}$ spectra are visible in Figure 3.18a. The signals at 710.6 and 723.3 eV with the separation of 12.7 eV and a small satellite structure at ~ 734 eV have been reported to indicate the presence of Fe^{3+} [155]. Figure 3.18a shows the binding energies (BE) of Co $2p_{3/2}$ and Co $2p_{1/2}$ observed at 780.07 and 795.57 eV, respectively, corresponding to a normal spin-orbital splitting of Co2p [156]. The two satellites peaks with BE of 786.25 and 802.56 eV can be assigned to Co^{2+} ions in octahedral and tetrahedral sites, respectively [155]. The occupation of Co^{2+} in both the octahedral and tetrahedral sites in cobalt ferrite spinel has been reported previously by Nakagomi et al. [157] and Zhou et al. [158], which agree well with the present results. The high-spin Co^{2+} could allow for significant charge-transfer character between the cobalt 3d7 band structures with that of the neighboring O^{2-} lattice anions [159].

The core-level O1s spectra of the prepared film were recorded and the result is shown in Figure 2(c). The O1s spectra for all samples were deconvoluted in three peaks in the BE range of 530-533 eV. The peak at ~ 530 could be assigned to the lattice oxygen species O^{2-} . The two species at higher BE are generally assigned to “adsorbed oxygen” [158]. The highest peak at

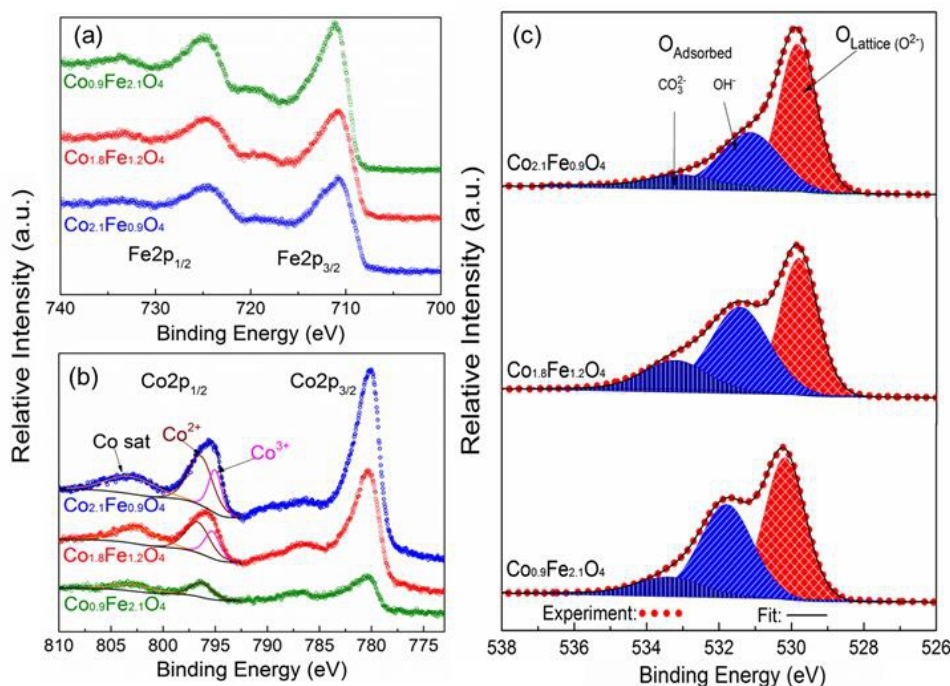


Figure 3.18 XPS spectra of the Co-Fe-O samples: (a) Fe2p; (b) Co2p; (c) O1s; reproduced from M1.

~531.4 eV is explained to be hydroxyl species (OH) or defective oxygen [160], whereas the peak at 533.2 eV probably comes from carbonate species, CO_3^{2-} or defects in the structure. In general lattice and adsorbed oxygen are observed for all samples. Both O_2^{2-} and O^- species are strongly electrophilic reactants, which play a crucial role in the degradation of the carbon skeleton [161]. For CO conversion over oxides, electrophilic oxygen species such as lattice and adsorbed oxygen are generally responsible for the total oxidation [162,163]. Thus, these O_2^{2-} or O^- detected by XPS measurement at the surface of Co-Fe-O oxides is expected to participate in the total oxidation of CO.

❖ Optical properties

It has been demonstrated that metal oxides with low band gap energy (E_g) can exhibit good catalytic performance [81,164]. The UV-Vis absorption spectra of Co-Fe-O samples were recorded and E_g was evaluated (see Figure 3.19). Typical UV-Vis spectra of the thin films are displayed in Figure 3.19a. Results for $\text{Co}_{0.9}\text{Fe}_{2.1}\text{O}_4$, $\text{Co}_{1.8}\text{Fe}_{1.2}\text{O}_4$ and $\text{Co}_{2.1}\text{Fe}_{0.9}\text{O}_4$ thin films have been calculated from the linear fit are 1.60, 1.90, and 2.09 eV, respectively. The E_g increases upon Fe substitution with Co. In this investigation, the increase of the grain size and the structural modification of the materials seem to be applicable to our deposited films. In addition, XRD revealed that the variation of the cobalt content in the matrix of the Co-Fe-O has modified the structural and cationic distribution and the lattice constant was decreased in

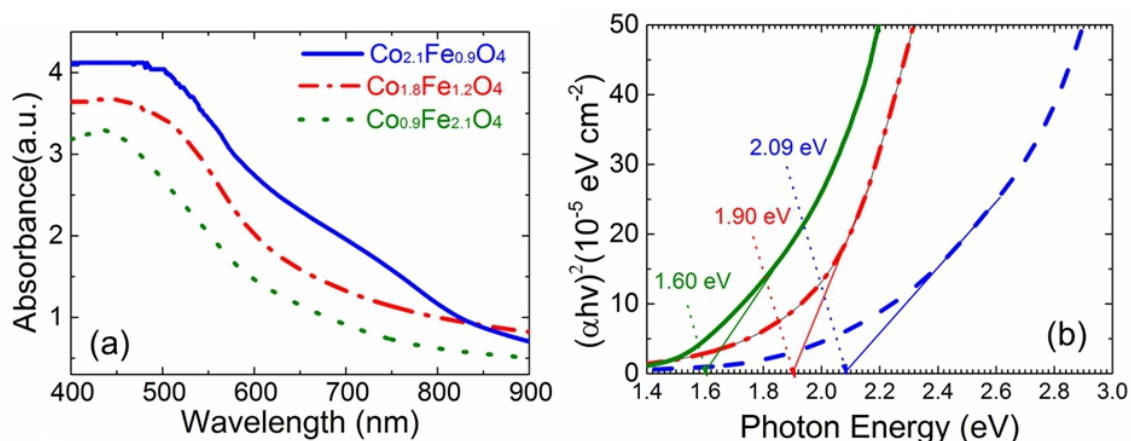


Figure 3.19 Optical absorption spectra (a) and Tauc's plot (b) resulting in an optical E_g for the different Co-Fe-O composites; reproduced from M1.

the material. This band structure perturbation together with the increases of the particles grain sized and cationic distribution might influence the band gap. This approach is consolidated by Nakagomi et al. who studied the influence of cobalt population on the structural properties of $\text{Co}_x\text{Fe}_{3-x}\text{O}_4$ [157]. These observations and concepts also seem useful with respect to the present composite oxides and their electronic, optical and photo-catalytic as well as catalytic applications. The obtained results highlight the validity of the PSE-CVD approach for the tailored synthesis of materials with specific control of the energy band gap.

❖ Redox behavior

To correlate the film composition and catalytic performance, the reduction (TPR) and re-oxidation (TPO) of the synthesized cobalt ferrite was evaluated with in-situ emission FTIR spectroscopy by integrating the intensity of the characteristic bands of the spinel as a function of the temperature, which reflects the loss or recovery of the spinel structure. The typical feature of the integrated IR band intensity of Fe-Co-O as a function of the temperature in the TPR is presented in Figure 3.20. As the temperature increases, a progressive red shift of the two observed bands at around 530 cm^{-1} and 628 cm^{-1} (Figure 3.20c) is observed. The reducibility order for the three samples is: $\text{Co}_{2.1}\text{Fe}_{0.9}\text{O}_4 < \text{Co}_{1.8}\text{Fe}_{1.2}\text{O}_4 < \text{Co}_{0.9}\text{Fe}_{2.1}\text{O}_4$. Figures 3.20b and 3.20d display the TPO profiles and the total recovery of the inverse spinel structure in the oxidation step, respectively. $\text{Co}_{2.1}\text{Fe}_{0.9}\text{O}_4$ (low lattice oxygen mobility) shows a high reduction and oxidation temperature, followed by $\text{Co}_{1.8}\text{Fe}_{1.2}\text{O}_4$, whereas the sample $\text{Co}_{0.9}\text{Fe}_{2.1}\text{O}_4$, with low cobalt content is reduced and re-oxidized at low temperature. It should be mentioned that the reduction and oxidation are notably shifted to higher temperatures, indicating that the increases of the Co content in the Co-Fe oxide can give rise to a significant

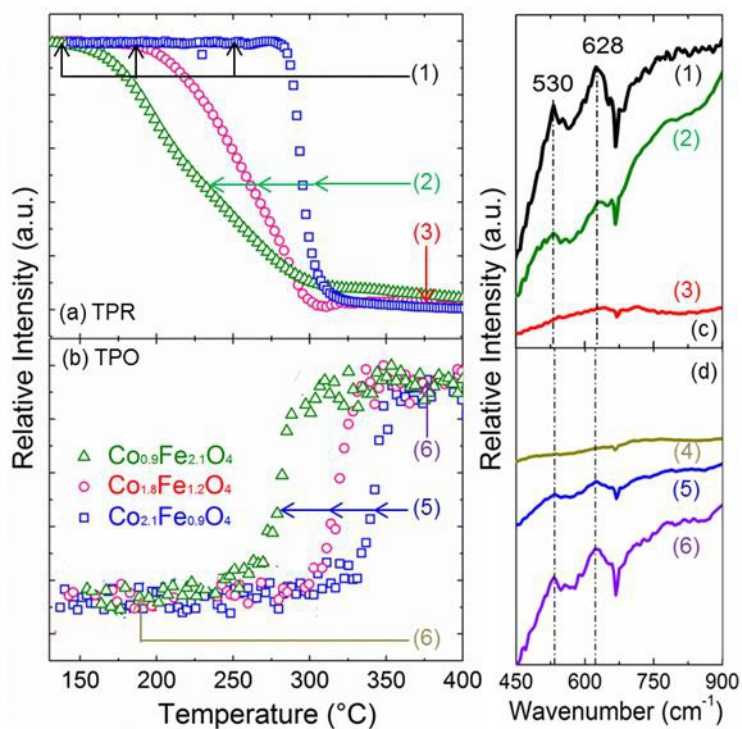


Figure 3.20 Redox behaviors of the selected Co-Fe-O oxides; (a) TPR, (b) TPO, (c) progressive loss of the spinel structure and (d) recover of Co-Fe-O IR vibration; reproduced from M1.

changes of its structure and thereby make it more difficult to be reduced. This weak reduction might be due to the generation of more intimate Fe-Co interactions in the cobalt ferrite structure. The presence of anionic vacancies in the lattice of Mn-doped [114] and Ce-doped Co_3O_4 [80] has been reported to also increase the reducibility temperature. In this study, this kind of vacancies can also be generated upon cobalt insertion and make the corresponding material less reducible. Nevertheless, since the samples with low cobalt content are reduced and re-oxidized at mild temperature consistently, it is expected that the lattice oxygen diffusion in $\text{Co}_{0.9}\text{Fe}_{2.1}\text{O}_4$ and $\text{Co}_{1.8}\text{Fe}_{1.2}\text{O}_4$ might become easier than $\text{Co}_{2.1}\text{Fe}_{0.9}\text{O}_4$ for CO oxidation if the process follows a redox mechanism.

3.5.2 Catalytic performance in the total oxidation of CO, C_3H_6 , $n\text{-C}_4\text{H}_8$ and $\text{C}_2\text{H}_6\text{O}$

The catalytic performance was investigated with respect to the total oxidation of CO, propene, n -butene and dimethyl ether at atmospheric pressure over the prepared cobalt ferrite referring to the non-coated mesh. The catalytic effect of the mesh has been excluded by the observation that no significant difference between the oxidation over non-coated mesh and in a blank system.

❖ CO catalytic oxidation

CO oxidation was investigated at atmospheric pressure over all samples. The results were thus compared with those obtained with pure α -Fe₂O₃ from previous work [3] and a blank sample of non-coated mesh, as shown in Figure 3.21. Single α -Fe₂O₃ become active in CO oxidation at around 230 °C and achieves complete CO conversion to CO₂ above 400 °C. Co-Fe-O composites exhibit lower temperatures for the initiation of CO oxidation than the single α -Fe₂O₃. The complete CO oxidation over Co_{0.9}Fe_{2.1}O₄, Co_{1.8}Fe_{1.2}O₄ and Co_{2.1}Fe_{0.9}O₄ occurs at 255, 275 and 325 °C, respectively. The results indicate that cobalt ferrites are more catalytically active than single α -Fe₂O₃. The performance order is the following: α -Fe₂O₃ < Co_{2.1}Fe_{0.9}O₄ < Co_{1.8}Fe_{1.2}O₄ < Co_{0.9}Fe_{2.1}O₄. The catalytic performance decreases with the increase of the Co content in the matrix of Co-Fe-O. The sample with low Co content (Co_{0.9}Fe_{2.1}O₄) exhibits the highest catalytic performance. An attempt to explain such behavior is made with respect to the redox property and the chemical composition as well as the ionic state at the surface the material.

The TPR and TPO result shows that Co-Fe-O samples were reduced at higher temperature, increasing the Co content. Generally for Co₃O₄, Co²⁺-Co³⁺ ion pairs are known to be very active in low-temperature CO oxidation [165]. Therefore, the presence in Co-Fe-O composites of both Co²⁺ and Co³⁺ together with Fe³⁺ in the O- and T-sites should enable a decrease of the reduction temperature and an improvement of the catalytic performance of CO conversion to CO₂ over samples with higher Co content (Co_{2.1}Fe_{0.9}O₄ and Co_{1.8}Fe_{1.2}O₄), which have the following cationic distribution in the O-site ([Co²⁺Fe³⁺Co³⁺]_{O-site}O₄). Surprisingly, the opposite behaviour is observed with Co_{0.9}Fe_{2.1}O₄ (the most active sample) in which only Fe³⁺ and Co²⁺ are present in the O-site: [Fe³⁺Co²⁺]_{O-site}O₄. It is thus suggested that the CO oxidation over Co-Fe-O catalyst does not proceed through a redox mechanism even if Co_{0.9}Fe_{2.1}O₄ presents the lowest reduction temperature. This hypothesis is strongly supported by the fact that CO oxidation of Co_{2.1}Fe_{0.9}O₄ is initiated at ~200 °C while the reduction (Fig. 3.20a) started at ~280 °C. Since the formation of carbonates on the cobalt surface has been suggested by Thormählen et al. to play an important role in the low-temperature oxidation of carbon monoxide [166], therefore, the earlier initiation of the reaction at low temperature can be assigned to the surface-adsorbed oxygen revealed by XPS analysis. It is thus proposed that CO oxidation over Co-Fe-O follows a suprafacial mechanism where CO molecules react with adsorbed oxygen, mainly as Co₃²⁻ and OH⁻, to form CO₂.

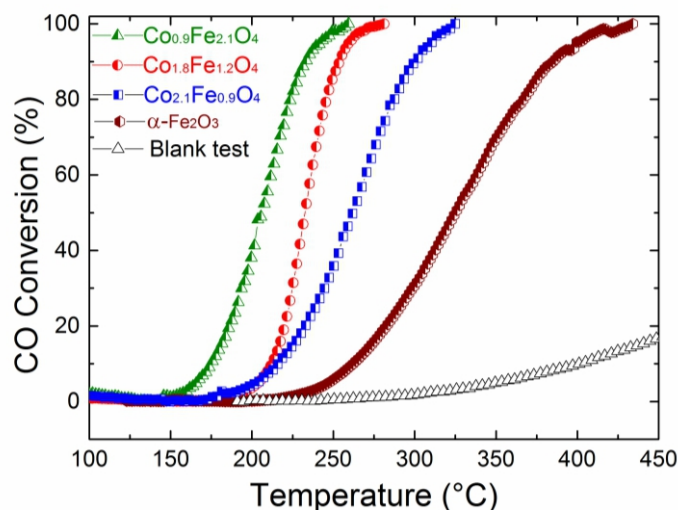


Figure 3.22 Light-off curves of CO conversion with the Co-Fe-O samples, α -Fe₂O₃ and non-coated mesh. The results obtained over α -Fe₂O₃ [3]; reproduced from M1.

❖ **Catalytic performance of C₃H₆, n-C₄H₈ and C₂H₈O over Cobalt ferrite and non-coated mesh**

The catalytic performance was investigated with respect to the total oxidation of propene, *n*-butene and DME at atmospheric pressure over cobalt ferrite (Co_{2.1}Fe_{0.9}O₄) referring to the non-coated mesh. The catalytic effect of the mesh has been excluded by the observation that no significant difference between the oxidation over non-coated mesh and in a blank system. Figure 3.22 depicts the outlet profiles as a function of the temperature during the oxidation. The results show that the cobalt ferrite films favor the complete conversion of the reactant gases at much lower temperatures relative to the non-coated mesh. Besides the reactant gas, CO₂ was detected as the unique product in the oxidation processes over cobalt ferrite, while additional CO was observed in the reaction on non-coated mesh. T₅₀ and T₉₀, corresponding to respective 50% and 90% conversion of the reactant gas, are used as parameters to compare the performance of the deposited samples. With cobalt ferrite, T₅₀ and T₉₀ of propene oxidation are 348 and 382 °C. These values shifted, respectively, to 578 and 691 °C for the experiment carried out with non-coated mesh (see Figures. 3.22a and 3.22b). Compared to the reaction over Co₃O₄ with E_a of 158.32 kJ/mol [80], the introduction of iron tends to initiate the oxidation of propene with lower E_a, which makes the cobalt ferrite more suitable for the catalytic applications. Figure 3.22c and 3.22d compare the results of *n*-C₄H₈ oxidation with and without cobalt ferrite. T₅₀ and T₉₀ of *n*-C₄H₈ oxidation over cobalt ferrite were observed at 358 and 402 °C, whereas these values shifted by respective 100 and 135 °C towards higher temperatures over non-coated mesh. It has been reported that a small quantity of 1,3-butadiene was selectively formed in the oxidation of *n*-C₄H₈ at temperature higher than

 350 °C over MnMoO₄-based catalysts with the C-H activation [167]. It should be noted that 1,3-butadiene was not detected in the present work such low temperature could result in negligible formation of 1,3-butadiene. Moreover, the insertion of Co in the ferrites could lead to scarce 1,3-butadiene.

For DME, cobalt ferrite also exhibits much better performance than the non-coated mesh, as revealed in Figure 3.22e and 3.22f. T₅₀ and T₉₀ of the reaction over cobalt ferrite are 356 and 409 °C. These values are observed to be 613 and 682 °C for the reaction without cobalt ferrite, respectively. According to Liu et al. [168], the reaction network for DME conversion consists of four pathways giving rise to CH₃OH, HCHO, HCOOCH₃ and CO_x. Low selectivity of CH₃OH and HCOOCH₃ was reported [168]. HCHO was not detected, which could be resulted either from the low concentration or its fast conversion to CO_x.

The good catalytic performance of cobalt ferrite could be correlated with the O_{adsorbed} on the surface, and attractive redox properties. It is widely accepted that the catalytic performance of ferrite-type catalysts depend on its oxygen mobility since the reaction follows Mars-van Krevelen mechanism [169]. The abundance of O_{adsorbed} could participate in the catalytic oxidation process, as proposed by Veleva and Trifirò [167]. The good reducibility and re-oxidability tend to enable the catalytic reactions at relatively low temperatures by involving various cations distributed in the octahedral and tetrahedral sites. Moreover, the slightly low band gap energy of cobalt ferrite could also indicate that the migration of O_{lattice} or O²⁻ from the bulk to the surface becomes easier and leads to good reducibility.

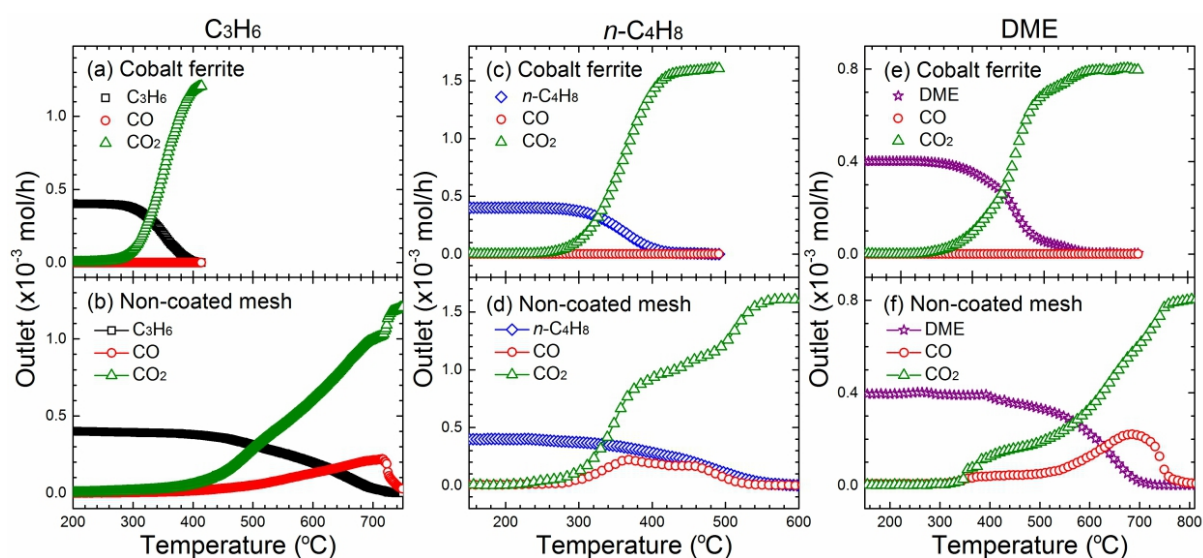


Figure 3.22 Outlet profiles of C₃H₆, n-C₄H₈ and DME oxidation over cobalt ferrite-coated and non-coated meshes. Reproduced from M2.

4 SUMMARY AND OUTLOOK

The present work reports the synthesis of functional transition metals oxides and investigation of their performance in catalytic combustion. This is an interesting topic which accounts the selective synthesis and systematic characterization of transition metal oxides (clean materials for emission control) and the investigation of their catalytic performance towards complete combustion of some representative fuels.

The general conclusion from this thesis is that the transition metal oxides (Co_3O_4 , Fe_2O_3 , CuO , Mn_3O_4 and CoFe_2O_4) catalysts were selectively synthesized using a dedicated pulsed spray evaporation chemical vapor deposition (PSE-CVD) approach, systematically characterized and tested as catalysts for the complete oxidation of carbon monoxide (CO), volatile organic compounds (C_3H_6 , $n\text{-C}_4\text{H}_8$), DME and biofuel ($n\text{-C}_4\text{H}_{10}\text{O}$). In this work, we show that the competitive performance for catalytic oxidation of selected fuels can be achieved with the deposited thin films obtained with PSE-CVD.

The PSE-CVD approach was used for the preparation of the TMOs catalysts. As a promising method to prepare catalytically active films, with its relatively low cost and simplicity, PSE-CVD has enabled the control of the thickness and morphology of the samples. Also, PSE-CVD was found to be particularly suitable for the selected precursors used in this study and was adapted for systematic synthesis of single-phase and mixed oxides on a number of relevant substrates.

The combined and systematic utilization of a number of adequate characterization techniques in terms of structure (XRD, Raman and FT-IR), morphology (SEM and HIM), composition (EDS and XPS), thermal stability, redox (TPO/TPR) and catalytic behavior have shed some light on the performance of the prepared catalysts and allowed a better understanding of the related catalytic processes.

Structure characterization using XRD was performed to identify the phase of the obtained film, and the obtained results were compared to the phase present in the XRD database. Raman spectroscopy was performed either to confirm the obtained phase or to distinguish the prepared films as in the case of Fe_2O_3 which could be present in different phases (α , β or γ) that cannot be distinguish by XRD. Emission FITR analysis was employed to visualize the metal-oxygen vibration band of the grown oxides.

The morphology was inspected by the means of SEM and HIM. The latter technique was

employed for the first time to the microstructure of the as-prepared TMOs thin films.

For the chemical composition analysis, both EDS and XPS were applied. EDS provides composition information in the bulk of the film, while XPS gives the chemical composition and ionic states at the surface of the materials (M2p (M = metal), O1s core shell and C1s core shell). These results have provided further understanding of the surface and bulk details of the obtained films what may be very important for the comprehension of the catalytic performance of the prepared materials. It is worth to mention that in spite of the care taken to optimize film growth, a typical deposition result of TMOs involve 30-40% of carbon, potentially as contamination. Carbon might be contamination products arising from the metal organic precursor decomposition. Nevertheless, the high-carbon content of the films still makes them useful and active in the respective catalyze processes. To avoid such high carbon ratio in the deposition, different (more refined) precursors or a more involved atomic layer deposition like process could be used, at the costs of a less facile process, however.

As important properties for metal oxide catalyst, the thermal properties were investigated. This experiment was performed to study the thermal stability and the redox properties of the prepared catalyst. TPO/TPR have provided information about the lattice oxygen mobility crucial in the catalytic oxidation. The thermal stability enables us to obtain the limit of the lattice stability of the prepared catalyst and the catalytic tests were performed within these stability limits.

Finally, the catalytic tests were made using flexible mesh grids as substrates on which the functional oxide were grown. Such structured catalytic beds were easily applied to the reactors shapes use in this study. The results show that the obtained samples exhibited high performance towards the deep oxidation of CO, C₃H₆ and *n*-C₄H₁₀O which served as representatives of VOCs and carbon monoxide. For all samples the complete oxidation of the fuel was obtained at relatively low temperature ($T \leq 400$ °C). Two different mechanisms were assumed to govern the catalytic oxidation in this study because they are consistent with the experimental results. The first one relies on the alternate reduction and oxidation of the oxide surface, favored by the bulk oxygen migration towards the surface, and replenishment of bulk oxygen by gas-phase oxygen. This suggests that the intrafacial mechanism (Mars van Krevelen) showed the dominant contribution to the complete oxidation of propene, *n*-butene and DME as well as *n*-butanol. For CO, the oxidation could follow a suprafacial mechanism in which the participation of adsorbed oxygen, mainly CO₃²⁻ and OH⁻ at the surface of the films were effectively crucial in the oxidation process.

The catalysts prepared and tested in this thesis present competitive activity to that reported for supported precious metals and confirm the status of TMOs as potential, viable and cheaper clean materials capable to replace noble metals generally used for catalytic combustion. The obtained performance was made possible by the selectively control of the film phase, morphology and chemical composition which are very sensitive to the deposition conditions and presented as key factors in the catalytic performance. The results obtained within this work highlight the validity of the PSE-CVD approach for the tailored synthesis of materials with specific morphology and good catalytic performance.

Further studies on the depositions conditions of catalytic activities of TMOs thin films will assist in understanding other catalyst nano-crystals and will offer great opportunities to explore the dependence of a material's properties on the composition, morphology and structure. Also the formulation of other binary mixed oxide such as Cu-Fe-O, Fe-Mn-O and ternary oxides like Co-Fe-Mn-O, Cu-Co-Fe-O and Co-Cu-Mn-O could be a potential technologically interesting solid-solution phases. The versatility of such composites might offer tunable structural composition, high thermal stability and might improve the physico-chemical properties and the catalytic performance of the materials. For such investigations, the use of inorganic precursors will be preferable in order to avoid carbone contamination observed with metal organic precursors in the present work.

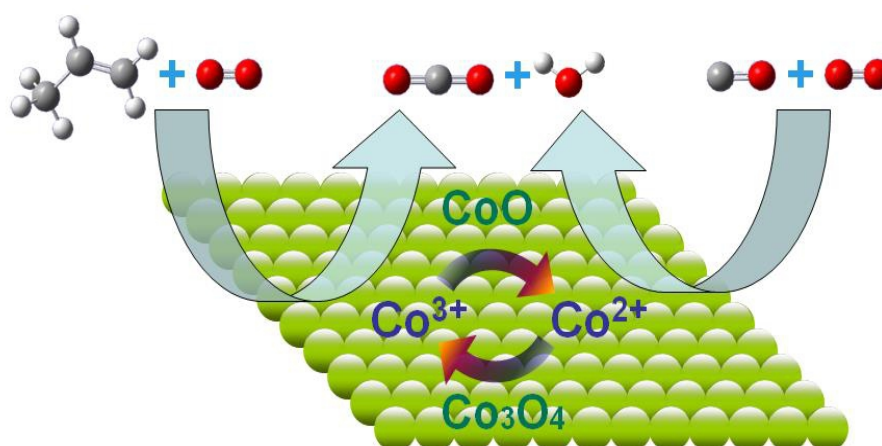
A) Publication 1

Patrick Mountapmbeme Kouotou, Zhen-Yu Tian, Udo Mundloch, Naoufal Bahlawane
and Katharina Kohse-Höinghaus

Controlled synthesis of Co_3O_4 spinel with $\text{Co}(\text{acac})_3$ as precursor

RSC Advances 2, 10809-10812, 2012

Graphical Abstract



Research Highlight

Co_3O_4 catalysts were controllably and systematically prepared with $\text{Co}(\text{acac})_3$ as precursor in different kinds of solvents by the PSE-CVD route.

Cite this: *RSC Advances*, 2012, 2, 10809–10812

www.rsc.org/advances

Controlled synthesis of Co_3O_4 spinel with $\text{Co}(\text{acac})_3$ as precursor†

Patrick Mountapmbeme Kouotou, Zhen-Yu Tian,* Udo Mundloch, Naoufal Bahlawane‡
and Katharina Köhse-Höinghaus

Received 25th June 2012, Accepted 1st September 2012

DOI: 10.1039/c2ra21277c

Cobalt(III) acetylacetonate ($\text{Co}(\text{acac})_3$) was used as a precursor to grow pure Co_3O_4 with pulsed-spray evaporation chemical vapor deposition (PSE-CVD). The effect of solvent and substrate temperature on the growth kinetics and morphology of the films was investigated. The obtained spinel exhibited good catalytic performance.

Among transition metal oxides, Co_3O_4 exhibits interesting electrical, magnetic, optical and catalytic properties.¹ In the last decade, the catalytic activity of Co_3O_4 and Co-based spinels has substantially increased the interest towards their technological application.² The promising ability of Co_3O_4 to exchange its lattice oxygen with the atmosphere sustains its high potential application in air pollution control *via* the oxidative abatement of CO ³ and organic pollutants from exhaust streams.⁴

Several methods have been reported previously to obtain Co_3O_4 thin films, including sol-gel,⁵ spray pyrolysis,⁶ atomic layer deposition,⁷ sputtering⁸ and chemical vapor deposition (CVD).^{9–11} Among these techniques, pulsed-spray evaporation CVD (PSE-CVD) is considered a promising method to prepare pure films due to its low cost, simplicity, high throughput and easy control of the thickness and morphology of the samples. Particularly, PSE-CVD is suitable for precursors with limited thermal stability and well adapted for systematic synthesis of single-phase spinel or perovskite oxides with tailored composition on various relevant substrates.

Most efforts to grow Co_3O_4 spinel by CVD involved several precursors (Table S1, ESI†). Metal-organic compounds (MOC) used as precursors are either commercially available or can be easily prepared in the laboratory. Of all the MOC, cobalt β -diketonates serve as non-toxic (environmentally friendly), volatile and inexpensive precursors. In the family of β -diketonates, cobalt acetylacetonates are the easiest to prepare, requiring no special atmosphere or environment.¹² Recent investigations reported the use of cobalt(II) acetylacetonate ($\text{Co}(\text{acac})_2$) for the synthesis of Co_3O_4 .^{13,14} However, this precursor shows instability in several solvents, and the selection

of alcohol presents a particularly complicated effect on the formed cobalt phase.¹³ In contrast to other solvents, alcohols exhibit certain reactivity with cobalt acetylacetonate under deposition conditions. This reactivity could lead to the formation of carbide phases at low temperature in the absence of oxygen.¹⁵ Therefore, an alternative may be needed.

The present work is focused on the controlled synthesis of Co_3O_4 spinel by PSE-CVD using cobalt(III) acetylacetonate ($\text{Co}(\text{acac})_3$) as precursor and the investigation of the effect of solvent and substrate temperature (T_s) on the growth kinetics and film morphology. Moreover, the catalytic performance of the sample obtained with tetrahydrofuran (THF) as the solvent was tested in terms of total oxidation of CO and propene (C_3H_6) in a flow reactor.

Special attention has been paid to the effect of aging on the stability and the ultraviolet-visible (UV-vis) absorption spectrum of the ethanol (EtOH) solution containing $\text{Co}(\text{acac})_2$ and $\text{Co}(\text{acac})_3$, respectively. The solutions were stored in a closed atmosphere for several days and the results are shown in Fig. 1. For $\text{Co}(\text{acac})_2/\text{EtOH}$ solution (A, C and E), the pink color transforms gradually into dark green, and a broad optical absorption band peaking at 590 nm is observed progressively after three days. However, neither color nor UV-vis spectra are changed for $\text{Co}(\text{acac})_3/\text{EtOH}$ solution (B, D and F). The absorption peak is characteristic of an octahedral Co(III)

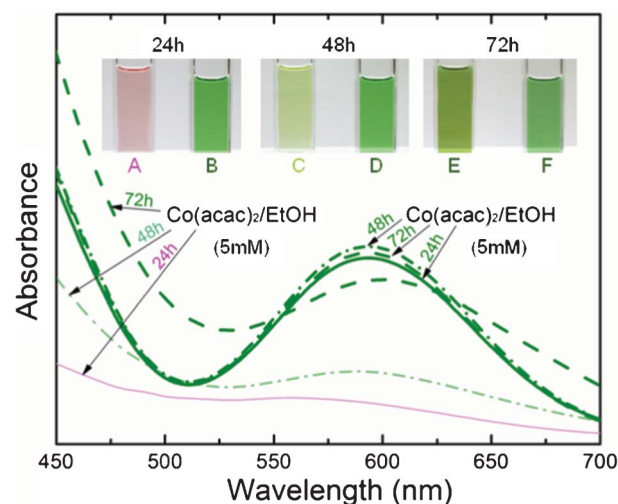


Fig. 1 UV-vis spectra of EtOH solution of $\text{Co}(\text{acac})_2$ (A, C and E) $\text{Co}(\text{acac})_3$ (B, D and F).

Department of Chemistry, Bielefeld University, Universitätsstraße 25, D-33615 Bielefeld, Germany. E-mail: zhenyu.tian@uni-bielefeld.de; Fax: +49-521 1066027; Tel: +49-521 1062199

† Electronic supplementary information (ESI) available: list of used cobalt precursor, experimental condition, solvent properties, comparison with other results, gas phase evolution of different solvents with and without $\text{Co}(\text{acac})_3$. See DOI: 10.1039/c2ra21277c

‡ Present address: Nanomaterials Research Unit, SAM Department, Centre de Recherche Public-Gabriel Lippmann, L-4422 Belvaux, Luxembourg.

species,¹⁶ which indicates that $\text{Co}(\text{acac})_3$ is more stable than $\text{Co}(\text{acac})_2$ and thus more suitable for the CVD processes with liquid-based feedstocks. Moreover, $\text{Co}(\text{acac})_3$ was reported to be more thermally stable than $\text{Co}(\text{acac})_2$.¹⁷ Even though studies on the development of CVD precursors (Co^{III} β -diketonates) have been reported,^{18,19} systematic and extensive investigation of the Co_3O_4 thin film synthesis starting from $\text{Co}(\text{acac})_3$ in several solvents system remains desirable. The $\text{Co}(\text{acac})_3$ precursor–solvent system was analyzed systematically with respect to the deposition results. The growth of cobalt oxide thin films was carried out in a cold-wall CVD reactor which is equipped with a home-built PSE unit for the precursor delivery. The description of the experimental setup can be found elsewhere.¹³ Further details of the experimental conditions are available (Table S2, ESI†).

The optimization of the Co_3O_4 growth was achieved using $\text{Co}(\text{acac})_3$ in EtOH as liquid feedstock. The thickness of the obtained films was estimated gravimetrically using a microbalance (Mettler ME30, digital resolution of 1 μg). The optimal growth rate, $\sim 1.6 \text{ nm min}^{-1}$ at 20 mbar and a substrate temperature of 350 to 500 $^\circ\text{C}$, was obtained using an O_2 flow rate of 0.5 SLM (standard liter per minute). In order to determine the effect of the agent in the synthesis of pure Co_3O_4 , different types of solvents were employed: EtOH (polar protic solvent), THF (polar aprotic solvent) and toluene (non polar solvent). The results indicate that the growth rate varies slightly depending on the solvents and a maximum value of $\sim 3 \text{ nm min}^{-1}$ was obtained with THF. With the investigation of the gas phase at lower temperatures (160–250 $^\circ\text{C}$) using molecular beam mass spectroscopy, the product pool is proven to be quite stable for a specific solvent with and without $\text{Co}(\text{acac})_3$, as shown in Figs. S1–S3, ESI†. However, the composition of the gas mixtures may evolve with oxidation reactions at higher temperatures (see Fig. S4, ESI†) and would vary the deposition process. The discussion of the detailed gas phase reaction is beyond of the current work and will be explained in a forthcoming study.

For characterization purposes, films were deposited on silicon, glass and stainless steel. The obtained films were subjected to XRD and SEM analyses, and the results are depicted in Fig. 2 and 3, respectively. As shown in Fig. 2, the films obtained at $T_s = 350/450 \text{ }^\circ\text{C}$ present different XRD patterns depending on both the deposition temperature and the nature of the solvent. The positions of the diffraction peaks fit well with the cubic spinel-type structure of Co_3O_4 (JCPDS Nr. 74-1656). No peaks associated to other crystalline forms could be detected, indicating that the obtained samples are of high purity and crystallinity.

The effect of T_s on the growth of the film was evaluated. The absence of some reflection planes is observed at $T_s = 350 \text{ }^\circ\text{C}$. The

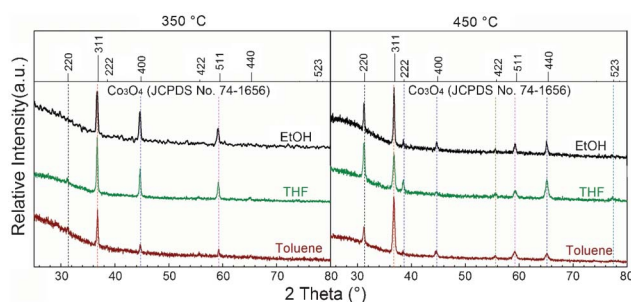


Fig. 2 XRD Patterns of the investigated Co_3O_4 spinels.

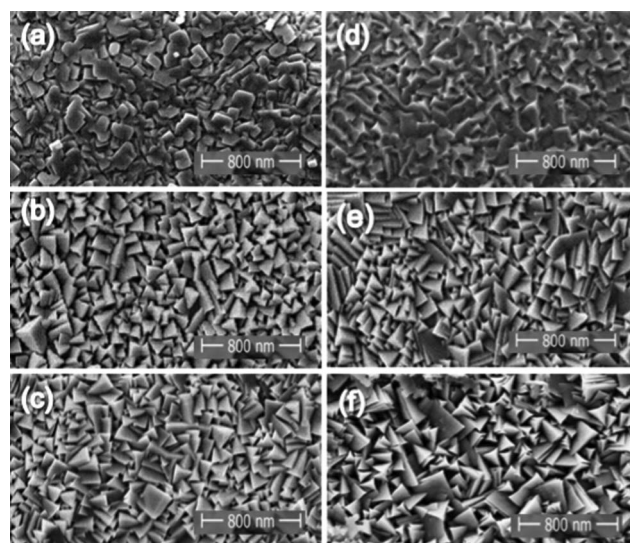


Fig. 3 SEM micrographs of Co_3O_4 obtain respectively at 350 and 450 $^\circ\text{C}$ (a, d) with ethanol; (b, e) with toluene; (c, f) with THF.

films grown at high temperature seem closer to a polycrystalline structure. However, all peaks fit well with the reference at 450 $^\circ\text{C}$ and no enhanced orientation can be claimed. EtOH, toluene and THF lead to the growth of films starting at a temperature of 350 $^\circ\text{C}$, and Co_3O_4 is the crystalline phase in the investigated T_s range (350–500 $^\circ\text{C}$). A clear identification of the spinel layer by XRD was obtained for the grown films at 350/450 $^\circ\text{C}$ with a thickness of $\sim 300 \text{ nm}$ over glass and silicon independent of the solvent. Increasing temperature from 350 to 450 $^\circ\text{C}$, the particles size increases by a few nanometers whereas the lattice parameter remains quite constant (see Table 1).

The behavior of different solvents with different physical properties (Table S3, ESI†) on the growth and morphology of the Co_3O_4 thin films was also investigated. Compared to a relatively slow solubility in EtOH, $\text{Co}(\text{acac})_3$ was observed to dissolve rapidly in both THF and toluene. Prolonged use of the precursor in the EtOH system causes crystallization of the precursor, which clogs of the spray nozzle and consequently limits its efficiency in the deposition experiments.

Besides the general effect of temperature and solvent on the growth rate and composition, it is demonstrated that the morphology of the formed Co_3O_4 can also be influenced by the choice of the solvents. As displayed in Fig. 3, the morphology of the deposited films indicates compact and geometrical particles, which differ with T_s and solvents. The coverage of the surface is homogeneous with THF and toluene as solvents, consisting of connected micrometer-sized agglomerates, whereas films are less defined with EtOH. Films deposited at 350 and 450 $^\circ\text{C}$ using EtOH as solvent, were randomly oriented with poorly crystallized grains. When THF and toluene

Table 1 Growth kinetics as a function of solvent and T_s

Solvents	T_s ($^\circ\text{C}$)	Growth (nm min^{-1})	$a/\text{\AA}$	Particle size (nm)
EtOH	350	1.55	8.10056	30.4
	450	1.52	8.10306	40.0
Toluene	350	1.91	8.08985	39.5
	450	2.17	8.09642	42.2
THF	350	2.16	8.09233	39.8
	450	2.89	8.08985	59.0

were employed, the obtained films are randomly oriented, well crystallized and present better defined facets. The Co_3O_4 crystallites showed trigonal pyramidal shape for films deposit at 350/450 °C with THF and toluene. In the explored temperature range, the increase of the growth rate as a function of the deposition temperature and the nature of the solvent can be explained in terms of variation of the surface diffusion with temperature and the co-adsorbed solvent. With EtOH at $T_s = 350/450$ °C, due to its reducing tendency (related to hydrogen from the alcohol function), the nucleation density becomes higher, giving rise to a fine-grained thin layer with low crystallinity. However, the surface diffusion was increased at the same T_s with THF/toluene, the chemical nature of which does not exhibit the reducing tendency. Consequently, the nucleation density was decreased, which could result in larger and well-crystallized particles. The temperature and the nature of the solvent dominate the film growth and affect its morphology. Various factors should be considered in understanding these complex processes, such as the solvent boiling point, vapour pressure, solubility, and polarity which have also considerable impact on the morphology of the final film.²⁰

Although the mechanisms involved in the development of the film morphology and the resultant microstructure are still speculative, the roles played by the T_s and solvent on the film morphology have been demonstrated. Such an influence could be caused by the reaction kinetics affecting the competitive nucleation and growth rates. For example, the inhomogeneous nucleation and rapid growth rates combined with low solubility of EtOH are responsible for non-effective dissolution, which could result in the formation of the observed amorphous morphology. On the other hand, a more homogeneous nucleation and slower growth combined with an effective separation of the particles in THF and toluene could lead to the fine particulate morphology.

With the deposition process optimized and properties analyzed using $\text{Co}(\text{acac})_3$ as the precursor, it is interesting to compare catalytic performance with that of previous systems using Co_3O_4 . In this work, no particular enhancement of the specific surface area and porosity can be noticed in all cases, which enables us to simplify the analysis of the catalytic activity. To assess the catalytic activity, oxidation of CO and C_3H_6 was performed over Co_3O_4 (12 mg, coated on mesh of stainless steel, SPW 40, 80×400) prepared using $\text{Co}(\text{acac})_3/\text{THF}$ at 350 °C. The total flow rate was kept at 15 ml min^{-1} with 1% fuel/10% O_2 dilute in Ar. A reflectron time-of-flight mass spectrometer (RTOFMS) was used for the analysis of the exhaust gas. The obtained Co_3O_4 catalysts exhibited excellent activity (see Fig. 4). Starting at around 230 °C, the total conversion of the investigated compounds to CO_2 is obtained at around 380 °C for C_3H_6 and 350 °C for CO, which gives an obvious temperature shift relative to the non-coated mesh. This result shows that Co_3O_4 is very active for total oxidation of CO, in line with the literature¹⁶ (see Table S3 ESI†). The excellent catalytic activity towards the oxidation of CO is attributed to the abundance of active Co^{3+} cations and oxygen vacancies on film surface. According to the assumption of Xie *et al.*²¹ and Hu *et al.*,²² Co^{3+} cations and oxygen vacancies acted as the active sites for CO oxidation and were key parameters governing the conversion rate of CO in the catalytic process. In fact, in the presence of CO and O_2 , CO can be adsorbed on the Co^{3+} sites of Co_3O_4 and react with the weakly bound surface oxygen species such as bridged $\text{Co}^{3+}-\text{O}_2-\text{Co}^{2+}$, leading to the production of CO_2 , and the resulting oxygen vacancy is subsequently filled by reaction with O_2 .²³

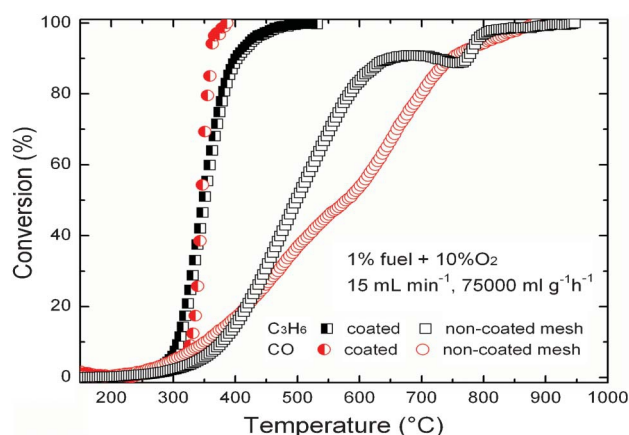


Fig. 4 Conversion of C_3H_6 and CO over Co_3O_4 .

Below 200 °C, Co_3O_4 exhibits no effect on the catalytic oxidation of C_3H_6 , but increasing the temperature, we obtained 90% conversion at 380 °C, which is in excellent agreement with our recent work,²⁴ and presents competitive activity to that reported for noble metals (Table S3 ESI†).^{25,26}

The catalytic activity of Co_3O_4 was explained in terms of formation of surface oxygen vacancies which are relevant to the C_3H_6 oxidation in the presence of gaseous oxygen. The surface lattice oxygen and adsorbed oxygen generally present on the transition metal oxides suggest that the C_3H_6 oxidation preferentially takes place on the surface lattice oxygen and adsorbed oxygen sites. Moreover, the presence of electrons in the neighbourhood of holes is necessary for the fission of the C=C bond in alkenes.²⁷

In summary, $\text{Co}(\text{acac})_3$ in both toluene and THF have been found to be suitable combinations for the deposition of pure Co_3O_4 spinel by PSE-CVD at a total pressure of 20 mbar. The morphology and growth rate have been found to be dependent on the solvent and substrate temperature. The obtained Co_3O_4 exhibits promising catalytic performance for the complete conversion of C_3H_6 as well as CO to CO_2 , comparable to noble metals.

Dr Tian and Mr. Mountapmbeme Kouotou thank the Alexander von Humboldt foundation and the Deutscher Akademischer Austausch Dienst (DAAD) respectively for their research stay at Bielefeld University in Germany. The authors acknowledge additional support by the Bielefelder Nachwuchsfonds and Prof. Thomas Hellweg for access to the SEM.

References

- H. Liang, J. M. Raitano, L. Zhang and S.-W. Chan, *Chem. Commun.*, 2009, **48**, 7569.
- R. Bashyam and P. Zelenay, *Nature*, 2006, **443**, 63.
- Y. J. Mergler, J. Hoebink and B. E. Nieuwenhuys, *J. Catal.*, 1997, **167**, 305.
- A. S. K. Sinha and V. Shankar, *Chem. Eng. J.*, 1993, **52**, 115.
- K. J. Kim and Y. R. Park, *Solid State Commun.*, 2003, **127**, 25.
- P. S. Patil, L. D. Kadam and C. D. Lokhande, *Thin Solid Films*, 1996, **272**, 29.
- A. Rautiainen, M. Lindblad, L. B. Backman and R. L. Puurunen, *Phys. Chem. Chem. Phys.*, 2002, **4**, 2466.
- H. Yamamoto, S. Tanaka and K. Hirao, *J. Appl. Phys.*, 2003, **93**, 4158.
- C. Guyon, A. Barkallah, F. Rousseau, K. Giffard, D. Morvan and M. Tatoulian, *Surf. Coat. Technol.*, 2011, **206**, 1673.
- N. Bahlawane, E. Fischer Rivera, K. Kohse-Höinghaus, A. Brechling and U. Kleineberg, *Appl. Catal., B*, 2004, **53**, 245.

-
- 11 E. Fischer Rivera, B. Atakan and K. Kohse-Höinghaus, *J. Phys. IV*, 2001, **11**, 629.
 - 12 T. T. Kodas, M. J. Hampden-Smith, *The Chemistry of Metal CVD*; VCH: Weinheim, Germany, 1994.
 - 13 P. A. Premkumar, N. Bahlawane and K. Kohse-Höinghaus, *Chem. Vap. Deposition*, 2007, **13**, 219.
 - 14 Z. Y. Tian, N. Bahlawane, F. Qi and K. Kohse-Höinghaus, *Catal. Commun.*, 2009, **11**, 118.
 - 15 P. A. Premkumar, A. Turchanin and N. Bahlawane, *Chem. Mater.*, 2007, **19**, 6206.
 - 16 S. Tanase, E. Bouwman, J. Reedijk, W. L. Driessen, M. Ferbinteanu, M. Huber, A. M. Mills and A. L. Spek, *Eur. J. Inorg. Chem.*, 2004, 1963.
 - 17 B. Atakan and M.A. Siddiqi, *Proc. Euro-CVD*, 2005, **15**, 229.
 - 18 H. Lee, C. H. Lee, I. S. Oh and I. M. Lee, *Bull. Korean Chem. Soc.*, 2010, **31**, 891.
 - 19 M. Burriel, G. Garcia, J. Santiso, A. N. Hansson, S. Linderöth and A. Figueras, *Thin Solid Films*, 2005, **473**, 98.
 - 20 L. M. Chen, Z. Hong, G. Li and Y. Yang, *Adv. Mater.*, 2009, **21**, 1434.
 - 21 X. W. Xie, Y. Li, Z. Q. Liu, M. Haruta and W. J. Shen, *Nature*, 2009, **458**, 746.
 - 22 L. Hu, K. Sun, Q. Peng, B. Xu and Y. Li, *Nano Res.*, 2010, **3**, 363.
 - 23 Y. Yu, T. Takei, H. Ohashi, H. He, X. Zhang and M. Haruta, *J. Catal.*, 2009, **267**, 121.
 - 24 Z. Y. Tian, P. H. Tchoua Nganou, V. Vannier, K. Kohse-Höinghaus and N. Bahlawane, *Appl. Catal., B*, 2012, **117-#x2013;118**, 125.
 - 25 R. Zhang, H. Alamdari and S. Kaliaguine, *Catal. Lett.*, 2007, **119**, 108.
 - 26 S. Ivanova, C. Petit and V. Pitchon, *Gold Bull.*, 2006, **39**, 3.
 - 27 M. Anpo, I. Tanahashi and Y. Kubokawa, *J. Chem. Soc., Faraday Trans. 1*, 1982, **78**, 2121.

Electronic Supplementary Information (ESI)

Controlled synthesis of Co_3O_4 spinel with $\text{Co}(\text{acac})_3$ as precursor

Patrick Mountapmbeme Kouotou, Zhen-Yu Tian*, Udo Mundloch, Naoufal Bahlawane[§],

Katharina Kohse-Höinghaus

Department of Chemistry 1, Bielefeld University, Universitätsstraße 25, D-33615 Bielefeld, Germany.

* Corresponding author. Tel: +49-521 1062199, Fax: +49-521 1066027; E-mail: zhenyu.tian@uni-bielefeld.de.

[§] Present address: Nanomaterials Research Unit, SAM Department, Centre de Recherche Public - Gabriel Lippmann, L-4422 Belvaux, Luxembourg.

Table S1: List of solvents and temperature range used for Co_3O_4 preparation

Precursor	Temperature (°C)	Preparation techniques	Solvents	Reference
$\text{Co}(\text{acac})_2$	230-440	PSE-CVD	EtOH	1
$\text{Co}(\text{acac})_2$	490-560	MOCVD	EtOH/chloroform	2
$\text{Co}_2(\text{CO})_8$	600, 650	PE-CVD	1-Hexene	3
$\text{Co}(\text{hfac})_2 \cdot 2\text{H}_2\text{O} \cdot \text{tetraglyme}$	65-180	MOCVD	CH_2Cl_2	4
$\text{Co}(\text{tmhd})_2$	350-500	CVD	-	5
	350-540	MOCVD	Monoglyme	6
CoCl_2	300	Spray pyrolysis	Distilled water	7-9
$\text{Co}(\text{CH}_3\text{CO}_2)_2 \cdot 4\text{H}_2\text{O}$	600	Sol-gel	2-Methoxyethanol	10
$\text{Co}(\text{NO}_3)_2$	400-480	Spray pyrolysis	-	11
$\text{Co}(\text{acac})_3$	360-540	MOCVD	Toluene	12

Note: PSE-CVD: pulsed spray chemical vapor deposition
MOCVD: metal organic vapor deposition
PE-CVD: pulsed evaporation
acac: acetylacetonate (2, 4-pentanedionate)
hfac: hexafluoroacetylacetonate (1,1,1,5,5,5-Hexafluoro-2,4-pentanedione)
tmhd: tetramethylheptanedionate (2,2,6,6-tetramethyl-3,5-heptanedionate)

Table S2: Experimental conditions for the preparation of Co_3O_4

Precursor	$\text{Co}(\text{acac})_3$
Solvent	EtOH; toluene or THF
Concentration of precursor	5 mM
Frequency and opening time	4 Hz, ~2 ms
Evaporation temperature	220 °C
Vaporizer temperature	240 °C
Substrate temperature range	350 °C; 400 °C; 450 °C and 500 °C
System pressure (mbar)	20
N_2 (SLM)	0.16
O_2 (SLM)	0.5
Substrates	Glass, silicon, planar or mesh of stainless steel

Table S3: Physical properties of the solvents

Physicals properties	Ethanol	Toluene	THF
Boiling point (°C) ^a	78.35	110.65	68.85
Density (g ml ⁻¹) ^b	0.790	0.866	0.880
Vapor pressure (bar, at 220 °C)	46.57 ^a	10.53 ^a	27.36 ^c
$\Delta_{\text{vap}}H^\circ$ (kJ/mol) ^a	42 ± 2	37 ± 3	32.16
Dipole moment (D, 20 °C) ^b	1.69	0.31	1.75
Hydrogen bonding ^b	19.4	2.0	8.0

Note: ^a data is from NIST chemistry webbook,¹³ ^b data is from Koehen and Smolders,¹⁴ ^c vapor pressure of THF is from Dortmund data bank.¹⁵

Table S4: Comparison with other results

Catalyst	Weight (mg)	Gas composition	Flow rate (ml min ⁻¹)	T ₉₀ ^a (°C)	GHSV ^b (ml g ⁻¹ h ⁻¹)	Reference
Co ₃ O ₄ thin film	12	1% CO/ 10% O ₂ /89% Ar	15	350	75000	This work
Co ₃ O ₄ bulk	50	1% CO/ 8% O ₂ in He	37	350	44400	¹⁶
CeO ₂	100	2% CO/ 2% O ₂ in N ₂	100	374	60000	¹⁷
Al ₂ O ₃	100	2% CO/ 2% O ₂ in N ₂	100	394	60000	
CeAlO ₃	100	2% CO/ 2% O ₂ in N ₂	100	465	60000	
Pt/H ₂ SO ₄ /ZrO ₂	50	3.5% CO/ 4% O ₂ in N ₂	100	290	120000	¹⁸
Co ₃ O ₄ thin film	12	1% C ₃ H ₆ /10% O ₂ /89% Ar	15	380	75000	This work
Co ₃ O ₄ thin film	12	2% C ₃ H ₆ / 20% O ₂ /78% Ar	15	385	75000	¹⁹
Au/Al ₂ O ₃	200	1.5% C ₃ H ₆ / 4% O ₂ in He	75	410	22500	²⁰
Ag/Al ₂ O ₃	50	3% C ₃ H ₆ / 10% O ₂ in N ₂	10	420	12000	²¹
La _{1.7} Sr _{0.3} CuO ₄ S _{0.2}	200	0.1% C ₃ H ₆ / 5% O ₂ / in He	100	500	30000	²²

Note: ^a T₉₀ refers to the temperature at which 90% of the fuel is converted; ^b GHSV is gas hourly space velocity.

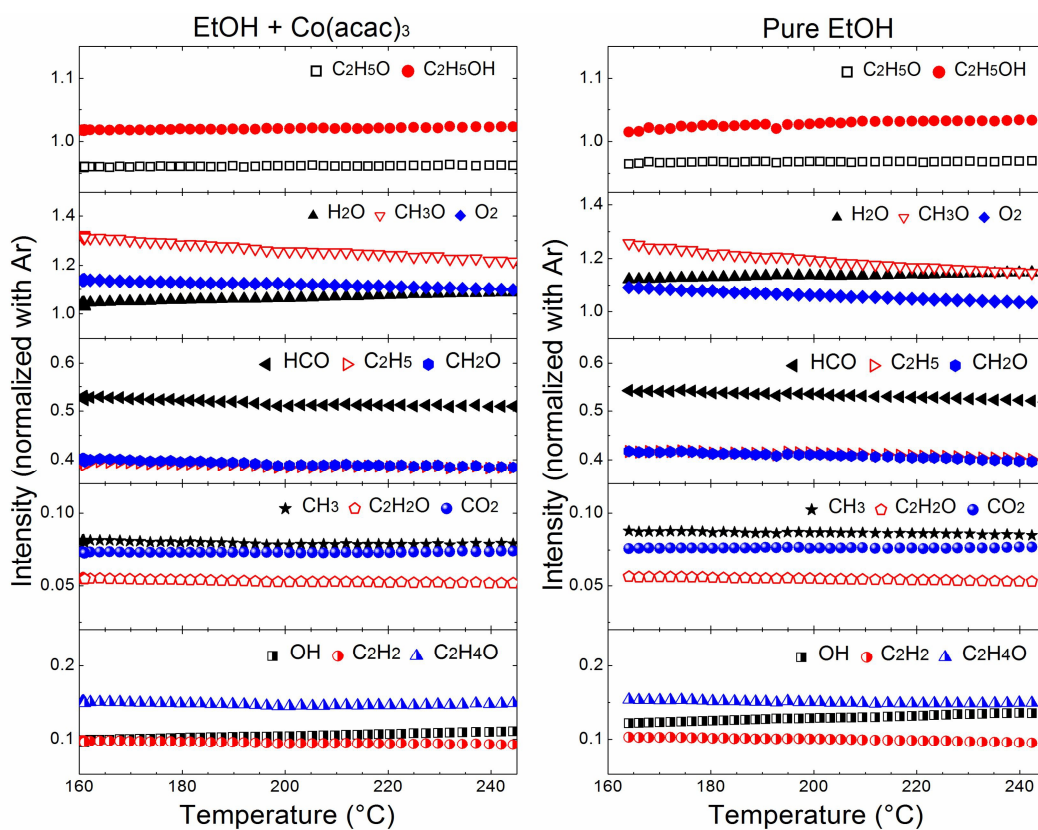


Fig. S1 Gas phase evolution of EtOH with and without $\text{Co}(\text{acac})_3$.

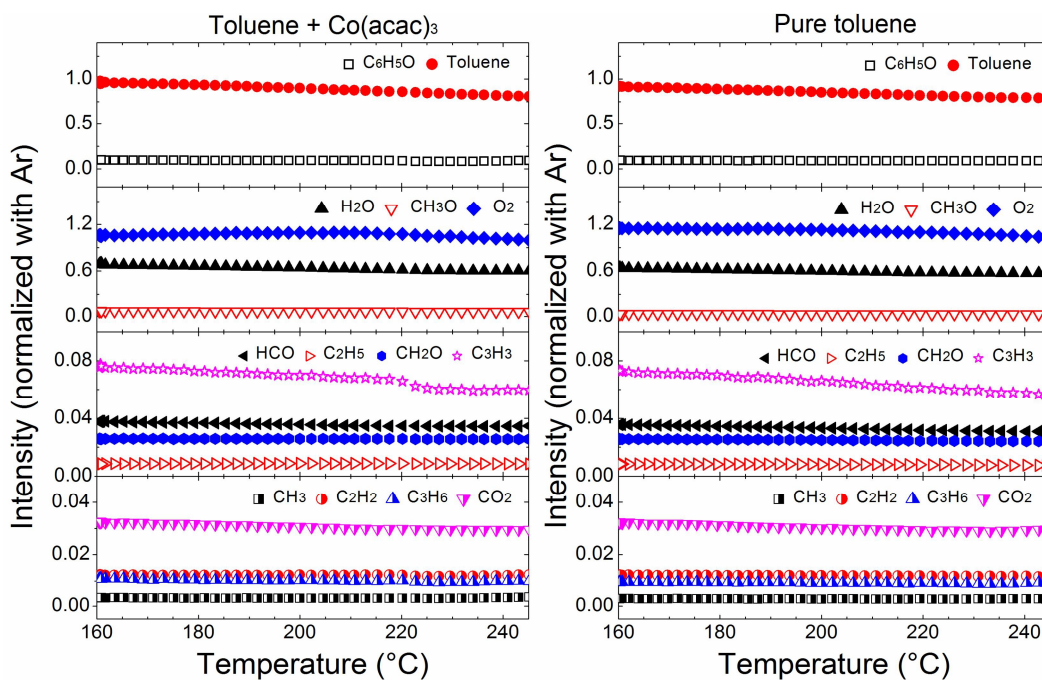


Fig. S2 Gas phase evolution of toluene with and without $\text{Co}(\text{acac})_3$.

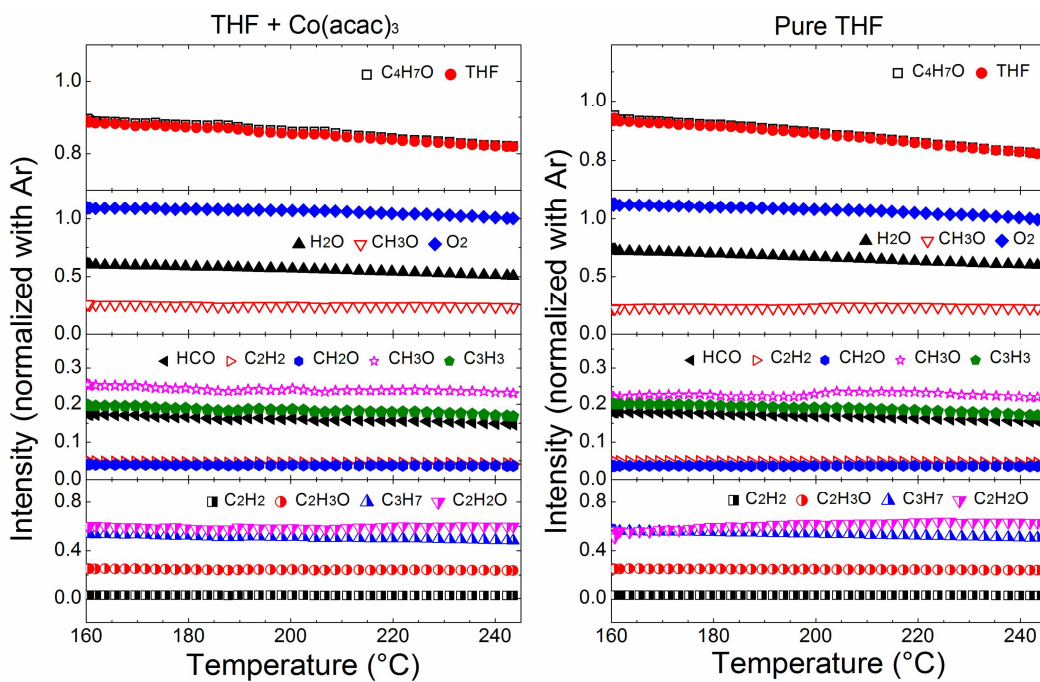


Fig. S3 Gas phase evolution of THF with and without Co(acac)₃.

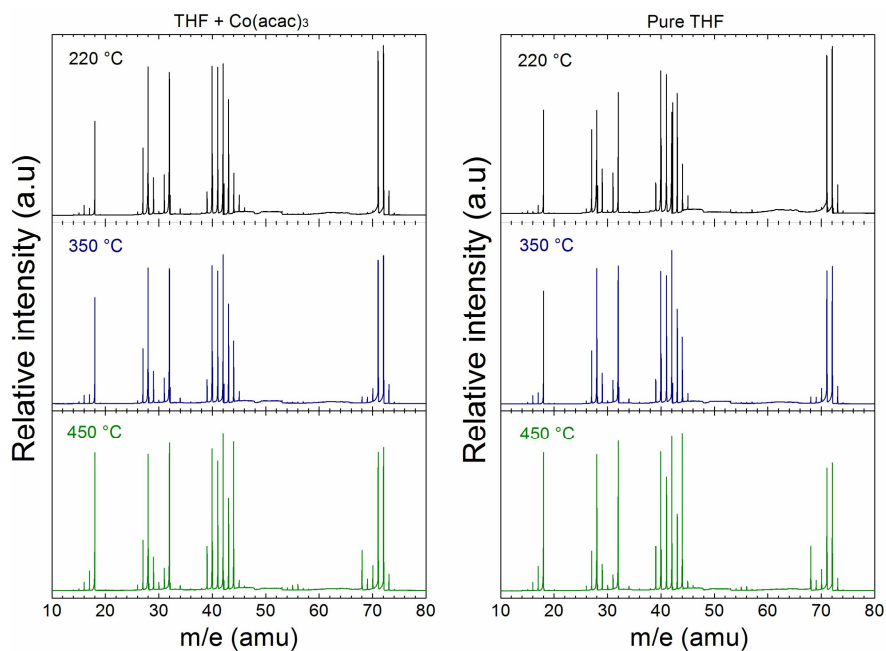


Fig. S4 Gas phase evolution of THF at 220, 350 and 450 °C with and without Co(acac)₃.

Notes to the figures: Electron impact with an energy of 25 eV was used as the ionization source to perform the experimental investigation. In addition to the fragments generated by the high electron energy, some products, such as C₂H₂ in Fig. S1 and CH₃O in Fig. S3 become detectable. At high temperatures (THF as an example, see Fig. S4), pyrolysis as well as oxidation of the solvent are observed by giving more water (m/e = 18), carbon dioxide (m/e = 44), furan (m/e = 68) and other products, which reveals the occurrence of the gas phase reaction. This is also the case for ethanol and toluene (not shown here). These may affect the kinetics of film growth and morphology.

References (ESI)

- 1 N. Bahlawane, E. Fischer Rivera, K. Kohse-Höinghaus, A. Brechling, U. Kleineberg, *Appl. Catal. B: Environ.*, 2004, **53**, 245.
- 2 S. M. Jogade, P. S. Joshi, B. N. Jamadar, D. S. Sutrave, *J. Nano- Electron. Phys.*, 2011, **3**, 203.
- 3 C. Guyon, A. Barkallah, F. Rousseau, K. Giffard, D. Morvan, M. Tatoulian, *Surf. Coat. Tech.*, 2011, **206**, 1673.
- 4 A. Gulino, P. Dapporto, P. Rossi, I. Fragala, *Chem. Mater.*, 2003, **15**, 3748.
- 5 D. Barreca, C. Massignan, *Chem. Mater.*, 2001, **13**, 588.
- 6 M. Burriel, G. Garcia, J. Santiso, A. Abrutis, Z. Saltyte, A. Figueras, *Chem. Vapor Depos.*, 2005, **11**, 106.
- 7 P. S. Patil, L. D. Kadam, C. D. Lokhande, *Thin Solid Films*, 1996, **272**, 29.
- 8 L. D. Kadam, P. S. Patil, *Mater. Chem. Phys.*, 2001, **68**, 225.
- 9 P. S. Patil, L. D. Kadam, C. D. Lokhande, *Solar Energy Materials and Solar Cells*, 1998, **53**, 229.
- 10 K. J. Kim, Y. R. Park, *Solid State Commun.*, 2003, **127**, 25.
- 11 M. Hamdani, J. F. Koenig, P. Chartier, *J. Appl. Electrochem.*, 2010, **18**, 556
- 12 M. Burriel, G. Garcia, J. Santiso, A. N Hansson, S. Linderoth, A. Figueras, *Thin Solid Films*, 2005, **473**, 98.
- 13 P. J. Linstrom, W. G. Mallard, Eds., NIST Chemistry WebBook, NIST Standard Reference database Number 69, June 2005, national Institute of Standards and Technology, Gaithersburg MD, 20899 (<http://webbook.nist.gov>).
- 14 D. M. Koenhen, C. A. Smolders, *J. Appl. Polym. Sci.*, 1975, **19**, 1163.
- 15 The Dortmund Data Bank for thermophysical properties of pure component and mixtures (<http://www.ddbst.com>).
- 16 Y. Ren, Z. Ma, L. Qian, S. Dai, H. He, P. G. Bruce, *Catal. Lett.*, 2009, **131**, 146.
- 17 P. A. Deshpande, S. T. Aruna, G. Madras, *Catal. Sci. Technol.*, 2011, **1**, 1683.
- 18 H. C. Wu, L. C. Liu, S. M. Yang, *Appl. Catal. A: Gen.*, 2001, **211**, 159.
- 19 Z. Y. Tian, P. H. Tchoua Nganou, V. Vannier, K. Kohse-Höinghaus, N. Bahlawane, *Appl. Catal. B: Environ.*, 2012, **117-118**, 125.
- 20 S. Ivanova, C. Petit, V. Pitchon, *Gold Bull.*, 2006, **39**, 3.
- 21 R. Zhang, H. Alamdari, S. Kaliaguine, *Catal. Lett.*, 2007, **119**, 108.
- 22 M. Machida, K. Ochiai, K. Ito, K. Ikeue, *J. Catal.*, 2006, **238**, 58.

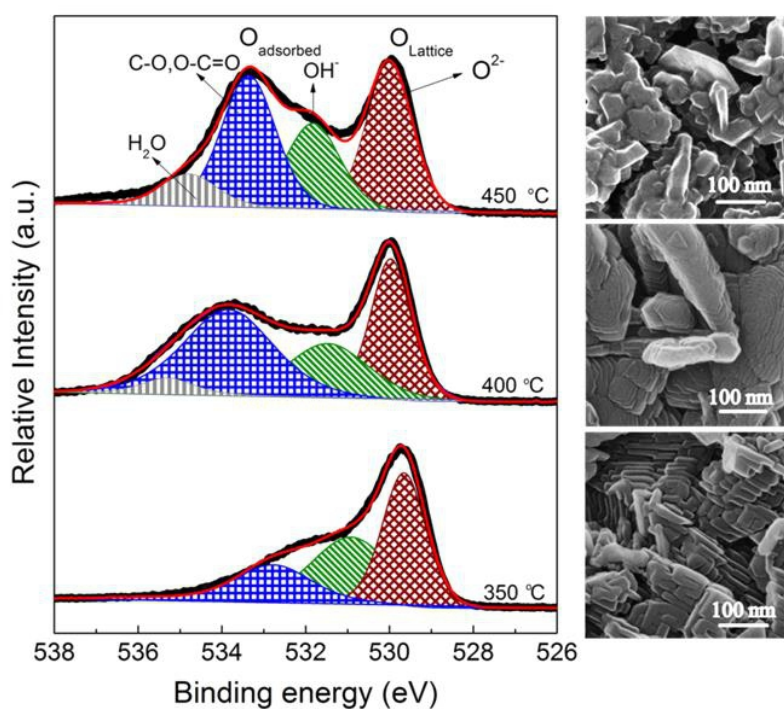
B) Publication 2

Patrick Mountapmbeme Kouotou, Zhen-Yu Tian, Henning Vieker, André Beyer, Armin Gölzhäuser and Katharina Kohse-Höinghaus

Selective synthesis of α -Fe₂O₃ thin films and effect of the deposition temperature and lattice oxygen on the catalytic combustion of propene

Journal of Materials Chemistry A 1, 10495-10504, 2013

Graphical Abstract



Research Highlight

Pulsed spray evaporation chemical vapor deposition (PSE-CVD), an elaborate CVD process, was employed to synthesize thin films of α -Fe₂O₃ for the catalytic combustion of propene.

Selective synthesis of α -Fe₂O₃ thin films and effect of the deposition temperature and lattice oxygen on the catalytic combustion of propene†

Cite this: *J. Mater. Chem. A*, 2013, **1**, 10495

Patrick Mountapmbeme Kouotou,^a Zhen-Yu Tian,^{*a} Henning Vieker,^b André Beyer,^b Armin Götzhäuser^b and Katharina Kohse-Höinghaus^a

Pulsed spray evaporation chemical vapour deposition (PSE-CVD), an elaborate CVD process, was employed to synthesize thin films of α -Fe₂O₃ for the catalytic combustion of propene. According to X-ray diffraction and Raman spectroscopy, the alpha structure type was presented as the unique phase. α -Fe₂O₃ with fine crystalline structure was revealed by scanning electron microscopy, and probed in depth for the first time by helium ion microscopy. Energy dispersive X-ray microscopy and X-ray photoelectron spectroscopy displayed an overview of the chemical composition of the samples. *In situ* emission FTIR spectroscopy was used for the accurate determination of the thermal stability of the samples at around 500 °C, and temperature-programmed reduction was performed to correlate the catalytic performance and reduction properties of the obtained α -Fe₂O₃ thin films. The results showed that the increase of the deposition temperature leads to significant changes of film morphology, chemical composition and reduction properties, with a direct consequence on the catalytic performance. α -Fe₂O₃ prepared at a low temperature (350 °C) exhibited high activity towards the deep oxidation of propene, which was attributed to its good reducibility and the plate-like structures. The alternate reduction and oxidation of the oxide surface (favored by the bulk oxygen migration towards the surface) and replenishment of bulk oxygen by gas-phase oxygen suggest that the oxidation of propene may proceed according to the Mars van Krevelen mechanism. The morphology and surface composition of the prepared samples remain the same before and after the catalytic test, demonstrating very good stability and reproducibility. We thus conclude that α -Fe₂O₃ effective in propene conversion can be selectively synthesized with PSE-CVD.

Received 3rd April 2013

Accepted 8th July 2013

DOI: 10.1039/c3ta11354j

www.rsc.org/MaterialsA

Introduction

Volatile organic compounds (VOCs) which are emitted from transportation and industrial activities are considered as an important class of air pollution.¹ VOCs are widespread chemicals commonly occurring in many commercial waste streams, and they have been linked to the increase in photo-chemical smog, the depletion in atmospheric ozone, the production of ground-level ozone, as well as the noxious effects on human health.²

Catalytic combustion is one of the most promising abatement technologies for VOCs regarding its flexibility and energy saving.¹ It presents the advantages of being operationally easy and allows unprecedentedly efficient reaction by specific ensembles of surface sites dependent on the crystal structures. Typical combustion catalysts are mainly noble metals such as Pt and Pd supported on alumina or other ceramic materials.^{3,4} However, due to noble metal's limited resources, high cost, low thermal stability and tendency to poisoning,⁵ transition metal oxides (TMOs) become suitable alternatives regarding their high thermal stability and low price.³ Thus, substantial efforts are currently made to develop TMO catalysts with a competitive activity.^{5–10}

Among TMOs extensively used, iron oxides have attracted considerable attention because of their interesting properties: they promise high stability at low cost and are environmentally benign and relatively non-toxic.¹¹ Hematite (α -Fe₂O₃), as the most stable iron oxide, features some unique properties: it is an n-type semiconductor, and it is magnetic and corrosion-resistant.¹² These properties have driven α -Fe₂O₃ in numerous promising applications, such as gas sensors,¹³ catalysts/photo-catalysts,^{12,14,15} and magnetic storage media.¹⁶

^aDepartment of Chemistry, Bielefeld University, Universitätsstraße 25, D-33615 Bielefeld, Germany. E-mail: zhenyu.tian@uni-bielefeld.de; Fax: +49-521 1066027; Tel: +49-521 106 2199

^bDepartment of Physics, Bielefeld University, Universitätsstraße 25, D-33615 Bielefeld, Germany

† Electronic supplementary information (ESI) available: Experimental conditions (Table ESI 1), comparison of the catalytic performance (Table ESI 2), a brief description of the PSE-CVD reactor, XPS spectra of C 1s core-shell present on α -Fe₂O₃ (Fig. ESI 1), surface morphology before and after catalytic tests (Fig. ESI 2), surface composition before and after catalytic tests (Fig. ESI 3), scheme of the PSE-CVD reactor (Fig. ESI 4) and setup for the catalyst test (Fig. ESI 5). See DOI: 10.1039/c3ta11354j

One of the prerequisites to achieve the above-listed properties relies on the synthesis of inorganic nanomaterials with ordered morphologies.¹⁷ Controlled synthesis of precise structures of active metal oxides on solid surfaces is one of the most important issues in designing high-performance heterogeneous catalysts. For instance, complex structures using nano-particles¹⁸ or surfactants¹⁹ as building blocks may be required for the synthesis of nano-devices for catalytic application. Such ordered structures often possess better mechanical strength and enable a lower pressure drop. They may thus permit higher reactant gas velocities than fine powder catalysts.¹⁸ Moreover, the surface morphology and bulk composition of the films depend upon the deposition methods and conditions,^{20,21} which may affect the films' properties. Thus a thin film of high purity and fine crystals is needed.

Preparation of catalysts with tunable morphology is an active research field. With respect to α -Fe₂O₃ thin films, several techniques have been employed for their synthesis including the hydro-thermal processes,²² aerosol-assisted CVD,²³ sol-gel methods,²⁴ thermolysis,²⁵ and atomic layer deposition.^{26,27} However, it remains a considerable challenge to selectively synthesize α -Fe₂O₃ thin films with a finely ordered crystal structure without using nano-subunits or surfactants as building blocks. Until now, most Fe₂O₃ nanomaterials have been synthesized in the presence of complicated structure-directing agents like surfactants to maintain specific shapes.^{25,28–31} Although the shapes were easily controlled, surfactants which were used to maintain the specific shapes may in part remain and their effect on the catalytic properties may be questionable in interpreting the catalytic properties. Therefore, more facile and efficient routes to prepare Fe₂O₃ nanomaterials with tunable morphology and without the presence of surfactants are highly expected.¹⁰ Herein, we report a facile synthesis route to prepare α -Fe₂O₃ thin films with complex geometrical structures and without any surfactants or capping agents. A pulsed spray evaporation chemical vapour deposition (PSE-CVD) approach was used for the preparation of the samples. PSE-CVD is considered as a promising method to prepare pure films regarding its relatively low cost, simplicity, high throughput and easy control of the thickness and morphology of the samples. It is particularly suitable for precursors with limited thermal stability and well adapted for systematic synthesis of single-phase/doped metals,³² spinels^{33,34} or perovskites³⁵ with tailored composition on a number of relevant substrates.

Thin films of α -Fe₂O₃ were thus synthesized at different deposition temperatures. A flexible mesh grid of stainless steel, which can be easily coated and rolled to adapt to different technical environments, was used as the substrate. All characterizations of the material detailed below were performed with stainless steel substrate, with the exception of X-ray diffraction (XRD) where silicon wafer had to be used under the same deposition conditions. The material properties of the obtained films were comprehensively characterized. Thermal properties of the catalysts were evaluated using *in situ* emission FTIR spectroscopy. The catalytic performance of the obtained α -Fe₂O₃ films towards the complete oxidation of propene was

investigated and special attention was focused on the effect of the substrate temperature on the film morphology, surface chemical composition as well as the reduction property and the catalytic performance.

Results and discussion

Structure

XRD analysis was performed to investigate the crystalline structure and the purity of the deposited thin films. The XRD patterns of the thin films coated on silicon wafer at different substrate temperatures (T_s) are presented in Fig. 1. All peaks fit well with the cubic spinel-type structure of Fe₂O₃ (JCPDS no. 39-0238), giving evidence to the existence of the Fe₂O₃ phase. The presence of one strongest peak at $2\theta = 33.16^\circ$ indicates that the (222) plane is the preferred growth direction. Successful deposition started at about 350 °C. By increasing the deposition temperature from 350 °C to 450 °C, the crystallinity of the deposited films improves as noticed by the sharpness of the peak corresponding to the (222) plane and the occurrence of the peak corresponding to the (211) plane. In the investigated deposition temperature range, the absence of peaks corresponding to other iron oxide structures such as FeO or Fe₃O₄ indicates the high purity of the deposited films. The preparation of single-phase iron oxide from Fe(acac)₃ was reported to be temperature-sensitive and it was hard to synthesize pure Fe₂O₃.^{36,37} However, in this study, Fe₂O₃ was observed to be the unique phase in the T_s range of 350–450 °C.

Since XRD cannot differentiate between the α - and γ -Fe₂O₃ phases, Raman spectroscopy was used to identify the phase of the prepared Fe₂O₃ oxide. As shown in Fig. 2, all samples exhibit similar spectral signatures, supporting the interpretation that the hematite (α phase) was observed. The bands at 226 and 492 cm⁻¹ are ascribed to the A_{1g} mode, whereas those observed at 246, 295, 412, 609 and 656 cm⁻¹ correspond to the E_g mode of α -Fe₂O₃. According to these results, the presence of peaks associated with maghemite (γ -phase) or magnetite (Fe₃O₄) can be definitively ruled out. Table 1 presents all observed peaks and assignments for different modes. The values related to the deposited α -Fe₂O₃ films are consistent with the previously

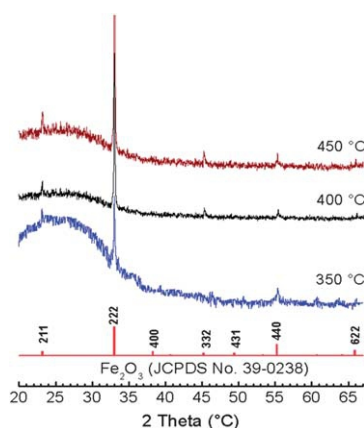


Fig. 1 XRD patterns of Fe₂O₃ thin films coated on silicon.

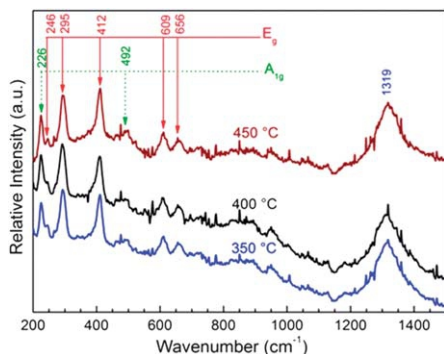


Fig. 2 Raman spectra of α -Fe₂O₃ thin films coated on stainless steel.

Table 1 Observed Raman active modes for iron oxide phases

Oxides	Structures	Raman shift (cm ⁻¹)	Assignment
Hematite ^a	α -Fe ₂ O ₃	226 and 492	A _{1g}
		246, 295, 412,	E _g
		609 and 656	
Hematite ^b	α -Fe ₂ O ₃	229 and 500	A _{1g}
		249, 295, 414,	E _g
		615 and 660	
Maghemite ^b	γ -Fe ₂ O ₃	700	A _{1g}
		511	E _g
		365	T _{2g}
Magnetite ^b	Fe ₃ O ₄	672	A _{1g}
		554	E _g
		310	T _{2g}

^a Frequency of the Raman shifts from this work. ^b Assignment from ref. 24, 25 and 36.

reported data of hematite.^{38–40} The strongest peak observed at 1319 cm⁻¹ is the characteristic band assigned to a two-magnon scattering feature resulting from the interaction of two magnons created on antiparallel close spin sites.^{41,42} The Raman spectrum has identified the prepared phase as α -Fe₂O₃ and further attests the purity of the films.

Morphology

Fig. 3 shows the surface morphology of the α -Fe₂O₃ thin films. The scanning electron microscopy (SEM) images are displayed in Fig. 3a–f. The film morphology obtained at 350 °C is composed of small grains embedded in the matrix, with an average crystalline size of ~50 nm. At 400 °C, the film presents a uniform densely packed microstructure with grains (~60 nm) in octahedral shape. It is well structured and composed of pallet shaped crystals superimposed on each other with precise orientation. At 450 °C, the film exhibits needle-like structures, each of which could result from the incorporation and agglomeration of small individual particles.

Helium ion microscopy (HIM), a newly developed imaging technique similar to SEM, was also used in this study, relying on a Carl Zeiss Orion Plus⁴³ instrument. With the involvement of a focused beam of helium ions, HIM exhibits superior resolution and outstanding performance on insulating samples.^{43–45} The

helium ion beam can be focused into a smaller probe size and provides a much smaller interaction volume at the sample surface than for typical electron microscopy. Thus it is possible to obtain superior resolution and depth of field. The HIM images of the synthesized α -Fe₂O₃ thin films present a morphology that varies with the T_S . As shown in Fig. 3g–l, the films are composed of ordered pallets with arrangement and orientation depending on the T_S from 350 to 400 °C. However, the film obtained at 450 °C is composed of continuous grains with poor structural shape in contrast to those observed at lower temperatures. This method enables us to probe the microstructure of the samples more in depth than the commonly used SEM. In general, the increase of the T_S from 350 °C to 450 °C gives rise to significant changes of α -Fe₂O₃ morphology. The films produced at 350 and 400 °C show fine geometric crystal structures. The grain size of the sample obtained at 350 °C is estimated to be 34 nm, which is much smaller than those prepared at 400 °C (56 nm) and 450 °C (60 nm). As the small grain size typically exhibits high specific surface area, the observation of temperature-dependent grain size may influence the physicochemical properties, and finally the catalytic performance.

Composition and ionic states

In order to determine the chemical composition of the synthesized α -Fe₂O₃ thin films, energy-dispersive X-ray spectroscopy (EDS) was performed. As shown in Fig. 4, only Fe and O peaks were observed. The atom ratios of O/Fe were about 60/40 for all samples in the investigated temperature range. No variation of the bulk composition was observed with the increase of the T_S . The ratios correspond well with the values calculated from the formula of hematite and are in good agreement with the literature.¹² The EDS analysis has confirmed the bulk composition of α -Fe₂O₃ samples.

A study of the catalyst surface by X-ray photoelectron spectroscopy (XPS) was carried out to obtain information of the species involved in the catalytic reaction. The results are depicted in Fig. 5. Fig. 5a shows the binding energies of Fe 2p_{3/2} and Fe 2p_{1/2} observed at 710.94 and 724.02 eV, respectively, which are characteristic of the Fe³⁺ state in the α -Fe₂O₃ thin film.^{46,47} The energy difference between the Fe 2p_{3/2} binding energy at 710.94 eV and that of the corresponding satellite peak is 8.2 eV, proving the presence of Fe³⁺.²² The spectra of the O 1s core-shell, as displayed in Fig. 5b, have been deconvoluted by means of four contributions with binding energies ranging from 529.0 to 536.0 eV. The lowest binding energy located at ~530 eV corresponds to the main lattice oxygen (O_L) contribution and is attributed to the oxygen present in the form of oxide (O²⁻). The other three bands expanded until 535.87 eV can be assigned to adsorbed oxygen (O_{ads}), including OH⁻, C–O, O–C=O and some moisture from air (H₂O). The obtained positions of all components are in reasonable accordance with the reported values in the literature.^{48,49} As can be seen from Fig. 5b, the intensity and the position of adsorbed oxygen are very sensitive to the T_S , while the peaks corresponding to the lattice oxygen are approximately at the same position with similar intensity for all the investigated deposition temperatures. It is generally

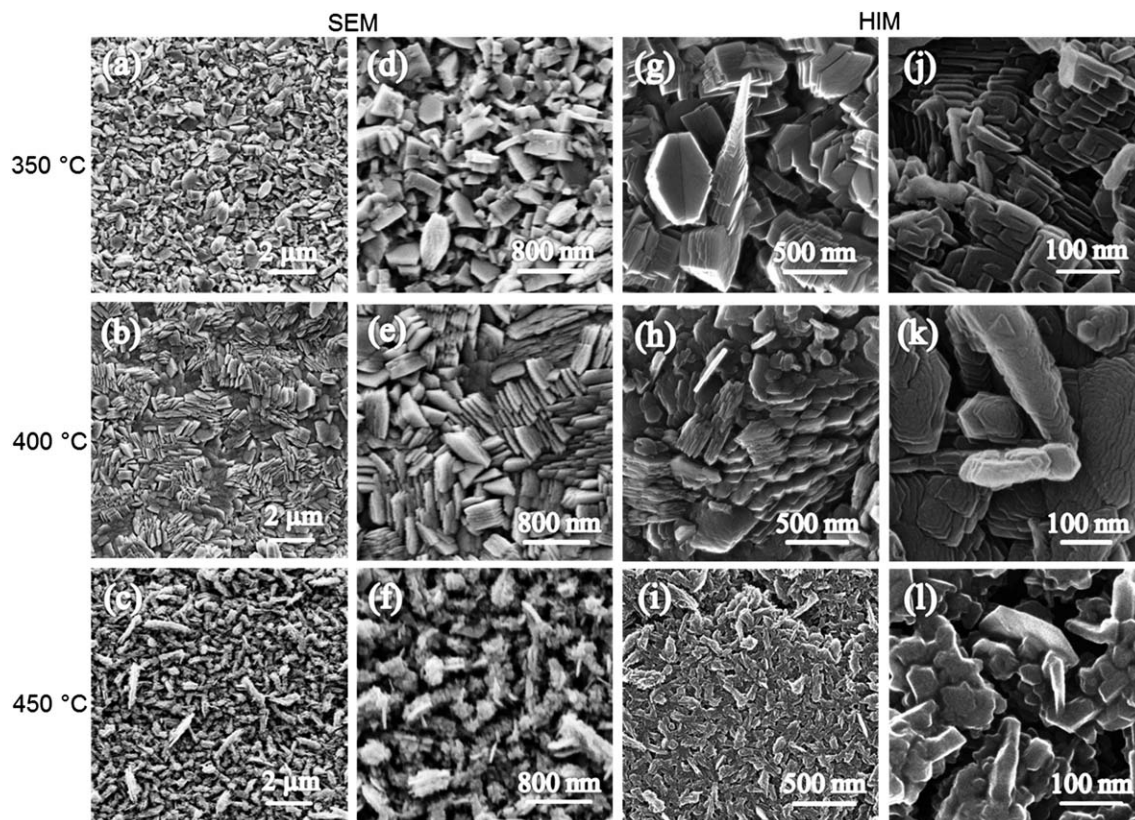


Fig. 3 SEM images of α -Fe₂O₃ thin films coated on stainless steel at: (a and d) 350 °C, (b and e) 400 °C and (c and f) 450 °C, and high vacuum HIM images of α -Fe₂O₃ thin films coated on stainless steel at: (g and j) 350 °C, (h and k) 400 °C and (i and l) 450 °C.

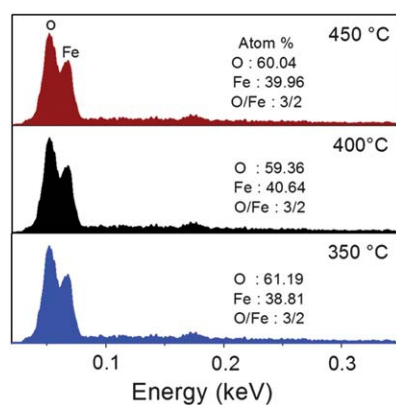


Fig. 4 EDS map of thin films of α -Fe₂O₃ with atomic percentage.

accepted that the catalytic combustion could occur upon the lattice and/or the adsorbed oxygen. Thus the observed differences of the adsorbed and lattice oxygen among samples synthesized at different deposition temperatures are expected to play significant roles in the catalytic reaction.

Temperature-programmed reduction

The reducibility of α -Fe₂O₃ was investigated by temperature-programmed reduction (TPR) with emission FTIR as an *in situ* monitoring technique. This method has been successfully used

to characterize the thermal properties of CVD-deposited oxide thin films before;^{9,34,50–52} for example, the reduction of Co₃O₄ to CoO has been clearly demonstrated in ref. 52. TPR was carried out with \sim 350 nm thick α -Fe₂O₃ films. Fig. 6 shows the TPR profiles of the samples obtained by integrating the two specific emission bands characteristic of the Fe–O–Fe stretching vibration mode of the Fe₂O₃. The decrease of the relative intensity indicates the consecutive loss of the α -Fe₂O₃ structure upon reduction. As shown in Fig. 6, complete reduction was observed at 306 °C, 345 °C and 375 °C for samples prepared at 350 °C, 400 °C and 450 °C, respectively. Above 375 °C, a plateau of complete reduction was observed for all samples; respective data points are shown up to 400 °C to illustrate the trends of the reduction process more clearly. Sample α -Fe₂O₃-350 °C exhibits the lowest temperature, and progressive shifts of the reduction towards higher temperatures are observed for α -Fe₂O₃-400 °C and α -Fe₂O₃-450 °C. Wyrwalski *et al.* have reported that the presence of anionic vacancies at higher temperatures was responsible for the lower reducibility in some metal oxides.⁵³ This could also occur in the current case for the films prepared at higher temperatures.

Thermal stability

In order to determine the stability limit of the prepared α -Fe₂O₃, *in situ* emission-FTIR spectroscopy was performed. As all samples exhibit similar behavior, only the sample obtained at

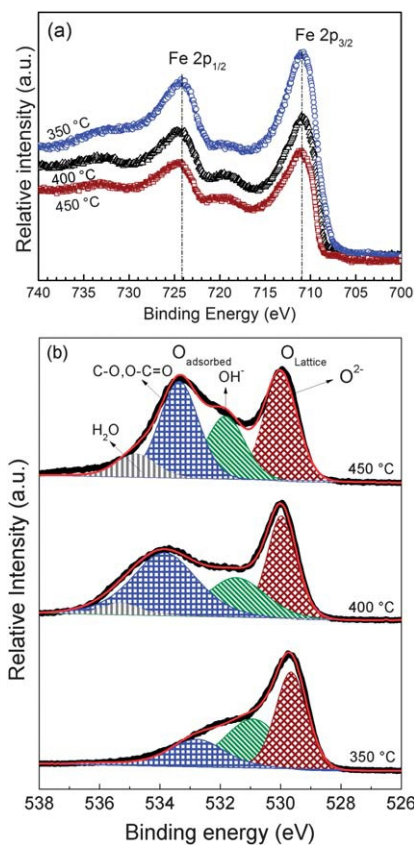


Fig. 5 XPS spectra of Fe 2p core-shell (a) and O 1s core-shell (b) of α -Fe₂O₃ thin films. Thin and thick lines are fitted and experimental results, respectively.

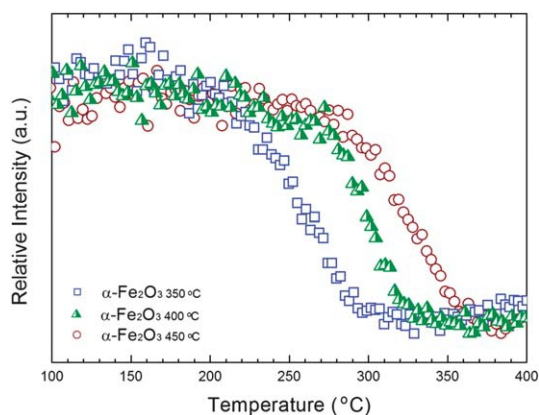


Fig. 6 TPR profiles of α -Fe₂O₃ thin films as a function of deposition temperature.

450 °C is presented as a representative. The thermal stability was analyzed in atmospheric air. In this test, the temperature of the catalyst was increased from 100 °C to 800 °C with a ramp of 5 °C min⁻¹. As shown in Fig. 7, typical features of the α -Fe₂O₃ spinels with characteristics bands at 421 and 515 cm⁻¹ disappear progressively with increasing temperature, indicating the gradual loss of its crystallinity. The sample gradually releases its lattice oxygen permitting an accurate determination of the limit of the lattice stability at \sim 550 °C. Above 550 °C, the plot shows a plateau which reflects the total loss of the α -Fe₂O₃ phase. The

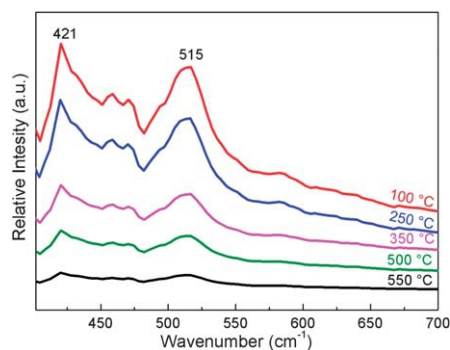


Fig. 7 Thermal stability of 430 nm α -Fe₂O₃ deposited on a stainless steel mesh at 400 °C.

obtained thermal stability temperature is in line with early reported values.^{54,55} Thus, the catalytic tests were performed within this stability limit.

Catalytic performance

To investigate the catalytic performance of the prepared films, stainless steel mesh grid (stainless steel, SPW 40, 80 × 400, micron-retention 36–45 μ m) substrates were coated with α -Fe₂O₃. Since the samples presented different morphology, oxygen states distribution (O_{ads} and O_{L}) and reducibility, the catalytic test was performed for all samples to investigate these effects on the catalytic properties. To analyze the catalytic behavior after re-oxidation as a prerequisite for application in consecutive cycles, the catalytic conversion of C₃H₆ was carried out both before and after pre-treatment of the catalyst under oxygen flow. This was done because the observed large amount of adventitious carbon, C–O, and O–C=O type moieties for the samples prepared at 400 and 450 °C (Fig. ESI †) would be expected to limit their performance. The presence of these carbonaceous species on the surface might lead to the formation of a barrier layer between the gas phase and the active solid phase on the catalyst surface, and thus reduce the interaction of gaseous oxygen with the surface. Bhargava *et al.*⁴⁸ reported that such intervening barrier layer, termed as the “native” surface film, was responsible for protecting the iron oxides from surface reactions. Consequently, the catalytic behavior of the prepared catalyst was compared with fresh samples and pre-treated samples under identical starting conditions. The catalytic tests on fresh samples were performed over catalysts prepared at 350 °C and 450 °C which present the lowest and the highest concentration of carbonaceous species, respectively. In addition, all pre-treated samples were used twice in the catalytic test to assess the reproducibility. Fig. 8 displays the light-off curves of C₃H₆ conversion obtained with α -Fe₂O₃ fresh samples (Fig. 8a) and with α -Fe₂O₃ pre-treated samples (Fig. 8b). With fresh samples, CAT_{350 °C} with lower adsorbed species presents better performance than CAT_{450 °C}. Starting at 100 °C, pre-treated samples exhibit no effect on the catalytic conversion of C₃H₆ up to 225 °C. For each sample, the conversion begins at around 250 °C. Temperatures for 10%, 50% and 90% C₃H₆ conversion are presented in Table 2 for fresh and pre-treated

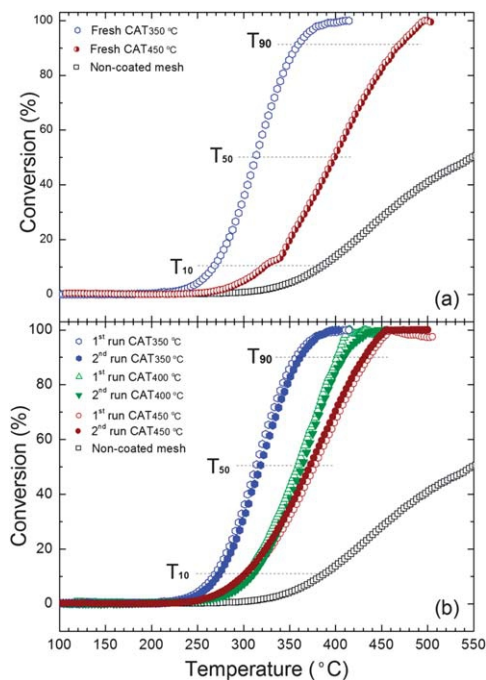


Fig. 8 Light-off-curves of C_3H_6 conversion over $\alpha\text{-Fe}_2O_3$ coated on the mesh of stainless steel and non-coated mesh.

samples. The film prepared at 350 °C is the most active one regarding the conversion profile as a function of temperature; followed by the films obtained at 400 °C and 450 °C, respectively. The experiments were repeated several times and the results were reproducible (Fig. 8b). Especially, the surface morphology and composition were detected to remain the same by measuring the samples before and after the catalytic tests with HIM/XPS (see Fig. ESI 2 and 3[†]). This observation further confirms that the adsorbed oxygen at the surface of the catalysts does not play a major role in the conversion of propene. $\alpha\text{-Fe}_2O_3$ presents competitive activity to that reported for supported noble metals^{56,57} as evident from Table ESI 2.[†] The table includes some recent examples for propene conversion given in the literature which were carefully selected to present approximately comparable conditions, if possible, with respect to weight hourly space velocity (WHSV) and weight of the catalyst sample. More details regarding the comparison can be found in the ESI.[†] In total, $\alpha\text{-Fe}_2O_3$ is active, reusable, and reproducible and no deactivation was observed after several times of use (Fig. 8b).

To identify clearly the phenomenon governing the difference in activity between the three catalytic films in Fig. 8 and Table 2, a correlation between the catalytic behavior and the $\alpha\text{-Fe}_2O_3$ characterization results was made. The XPS results revealed the presence of both adsorbed and lattice oxygen. The $O_{\text{ads}}/O_{\text{L}}$ ratio of $\text{CAT}_{350\text{ °C}}$ was the lowest for the three samples. The catalytic tests over fresh and pre-treated samples reveal the negligible role of the adsorbed oxygen, suggesting that the lattice oxygen plays a key role in the reaction sequence. This is corroborated by the TPR experiments. Based on these and the XPS results, the possible oxidation mechanism of C_3H_6 over the as-prepared catalysts can be discussed.

For the catalytic oxidation of hydrocarbons, two mechanisms have been widely accepted: a suprafacial mechanism, which involves interaction of surface oxygen with reactants, and an intrafacial mechanism. This Mars van Krevelen mechanism involves migration of bulk oxygen to the surface, where it participates in the reaction with the reactant, and replacement of bulk oxygen by oxygen from the gas phase.⁵⁸ Numerous investigations have pointed out that this mechanism is active in the combustion of hydrocarbon over transition metal oxide catalysts.^{59,60} In particular, Scirè *et al.*⁶¹ and Morales *et al.*⁶² studied catalytic combustion of VOCs over pure Fe_2O_3 , Au/Ag/Cu-supported Fe_2O_3 , and Mn_2O_3 , respectively. Both groups adopted a Mars van Krevelen type reaction mechanism to account for the reaction sequence. Also, catalytic combustion of C_3H_6 over Co_3O_4 has been reported by Liotta *et al.*⁶³ to proceed according to the Mars van Krevelen mechanism. From the comparison of the results regarding fresh and pre-treated samples, it is thus plausible that C_3H_6 combustion over $\alpha\text{-Fe}_2O_3$ follows an intrafacial mechanism, which involves a redox cycle and is related to the mobility of the lattice oxygen. The oxygen mobility associated with the catalyst reducibility is an important step in the mechanism. It is worth mentioning that the lower the reducibility temperature, the higher the mobility of lattice oxygen. Thus, a relationship between catalytic activity and reducibility may be established when the catalyst undergoes a redox cycle.⁵⁹ Considering the TPR results, it can be concluded that the mobility of the lattice oxygen in the samples is in the following order: $\text{CAT}_{350\text{ °C}} > \text{CAT}_{400\text{ °C}} > \text{CAT}_{450\text{ °C}}$. So it is reasonable that the $\text{CAT}_{350\text{ °C}}$ exhibits the highest catalytic activity due to its better reducibility. For the $\text{CAT}_{400\text{ °C}}$ and the $\text{CAT}_{450\text{ °C}}$ samples, their catalytic behavior also follows the reducibility order.

The catalytic oxidation of C_3H_6 by $\alpha\text{-Fe}_2O_3$ can be broken down into several steps as follows: C_3H_6 adsorption on the

Table 2 XPS peak deconvolution result in percentage, $O_{\text{ads}}/O_{\text{L}}$ ratio, T_{10} , T_{50} and T_{90} of $\alpha\text{-Fe}_2O_3$ at different T_s^a

	O_{L} (%)	OH^- (%)	$\text{O}-\text{C}=\text{O}$, $\text{C}=\text{O}$ (%)	H_2O (%)	$O_{\text{ads}}/O_{\text{L}}$	T_{10} (°C)		T_{50} (°C)		T_{90} (°C)	
						FS	PS	FS	PS	FS	PS
$\text{CAT}_{350\text{ °C}}$	46.52	25.87	22.76	—	1.05	264	260	326	315	405	350
$\text{CAT}_{400\text{ °C}}$	31.19	23.69	41.20	3.92	2.21	—	295	—	355	—	400
$\text{CAT}_{450\text{ °C}}$	27.31	25.47	43.82	3.41	2.66	326	302	405	380	470	435

^a Note: CAT refers to $\alpha\text{-Fe}_2O_3$; FS is fresh samples; PS is pre-treated samples.

catalyst surface, reduction of the catalyst accompanied by releasing the oxygen atom, and finally, the re-oxidation of the reduced iron cations by oxygen from the gas phase into Fe_2O_3 . Therefore, the redox tendency of $\alpha\text{-Fe}_2\text{O}_3$ plays an important role, which is related to the surface densities of the iron atoms in the prepared $\alpha\text{-Fe}_2\text{O}_3$ thin films.⁶³ The increased diffusion rate of oxygen in the lattice causes an increase of the catalytic activity. Again, $\alpha\text{-Fe}_2\text{O}_3$ thin films prepared in this work present competitive performance to that reported for supported noble metals (see Table ESI 2†).^{56,57}

In addition to the role played by the lattice oxygen in the catalytic performance, the differences observed in the catalytic properties may be also explained in correlation with the film morphology and preparation temperature. The $\alpha\text{-Fe}_2\text{O}_3$ thin films can favor the exposition of some reactive crystal planes, and hence promote their reaction efficiency. In fact, it is well-known that the sizes, shapes, and structures of catalyst materials are closely related to the catalytic performance.^{64,65} However, very little is known about the morphology-preparation temperature dependence of the catalytic activity of $\alpha\text{-Fe}_2\text{O}_3$ nano-crystals. In this investigation, the SEM/HIM results indicated that T_s was the principal factor controlling the film morphology, since only T_s was varied during the preparation process. The morphology variation with T_s was important in the catalytic activity of $\alpha\text{-Fe}_2\text{O}_3$. Therefore, we discuss the catalytic activity of $\alpha\text{-Fe}_2\text{O}_3$ thin films further in light of the different geometric structures imposed by the T_s variation. It can be seen that all the three $\alpha\text{-Fe}_2\text{O}_3$ samples show good reactivity compared to the test without catalyst. In detail, sample CAT_{350 °C} achieved a conversion of 90% at 350 °C, which is the most efficient catalyst of the three samples. Samples CAT_{400 °C} and CAT_{450 °C} gave 90% conversion at 400 °C and 435 °C. The different reactivity of the three samples may also be a result of the crystallization, morphology and structure of $\alpha\text{-Fe}_2\text{O}_3$. It has been reported that $\alpha\text{-Fe}_2\text{O}_3$ nanocatalysts showed apparent shape-dependent properties in CO and VOCs oxidation and the exposed facets have greatly modulated the reaction efficiency.^{66,67} Such morphology-dependent catalytic behavior of $\alpha\text{-Fe}_2\text{O}_3$ has been further verified in liquid-phase reactions⁶⁸ and photocatalysis.⁶⁹ The $\alpha\text{-Fe}_2\text{O}_3$ in the present work also exhibits a morphology-dependent catalytic performance. The ordered octahedral fine crystalline grains obtained at both 350 and 400 °C present better performance than the sample prepared at 450 °C with poor crystal structure. Three different planes exist in the hematite crystal structure on which the densities of active sites such as the iron atoms are different.⁷⁰ Exposed planes containing more iron atoms could provide more active sites for catalytic reactions and consequently higher catalytic performance. The catalytic performance can benefit from the exposed plate-like structures which could adsorb abundant gaseous molecules on the surface of the sample as an opportunity for their participation in the reaction sequence.

The grain size of a catalyst is one of the most important factors that determine the performance. In general, the smaller the grain size, the larger the specific surface area. As indicated by the SEM and HIM analysis, the grain size was found to be significantly dependent on the deposition temperature. The

increase of the preparation temperature leads to an increase of the grain size. It is thus assumed that CAT_{350 °C} with the smallest grain size (~34 nm) possesses the largest specific surface area. This argument is consistent with the experimental observation that CAT_{350 °C} presents the best performance.

Regarding the results obtained in this study, in addition to the fact that the shape of the metal oxides, through preferential exposure of reactive crystal planes, affects the catalytic reactivity as significantly as the traditionally considered parameters such as particle size and surface area,¹⁰ the observed catalytic performance of the iron oxide can also be related to the film morphology. Further studies on the preparation temperature-associated catalytic activities of different $\alpha\text{-Fe}_2\text{O}_3$ thin films will assist in the understanding of other catalyst nano-crystals and thus offer great opportunities to explore the dependence of a material's properties on the morphology and structure. The results highlight the validity of the PSE-CVD approach for the tailored synthesis of materials with specific morphology and good catalytic performance.

Experimental

Preparation of $\alpha\text{-Fe}_2\text{O}_3$ thin films

The growth of $\alpha\text{-Fe}_2\text{O}_3$ inverse spinel thin films was performed in a cold-wall stagnation point-flow CVD reactor, which is equipped with a homemade PSE unit for the delivery of liquid precursor feedstock. More details about the experimental setup are presented in Fig. ESI 4.† $\text{Fe}(\text{acac})_3$ dissolved in THF was used as the feedstock at a concentration of 5 mM. $\text{Fe}(\text{acac})_3$ was purchased from STREM Chemicals and was used as received. Metal acetylacetonates were selected in this study as precursors because of their stability and high solubility in THF.³³ The PSE delivery was achieved with a valve opening time of 2.5 ms and a frequency of 4 Hz. The evaporation of the injected feedstock takes place at 220 °C in the tubular vertical 30 cm long evaporation chamber, where a complete evaporation of the precursors in addition to THF takes place. The resulting vapour was transported to the deposition chamber with N_2/O_2 flow rates of 0.16/1.0 standard liter per minute (SLM). Stainless steel plates, steel mesh and silicon were used as substrates. The deposition temperature was varied (350–450 °C), while the total pressure in the reactor was kept constant at 25 mbar. The experimental condition for the preparation is summarized in Table ESI 1.†

Characterizations

The identification of the crystalline phase of the grown films was performed using several techniques, including X-ray diffraction (XRD), Raman scattering spectroscopy and energy dispersive spectroscopy (EDS). The XRD (PHILIPS X'Pert Pro MDR diffractometer with a PW 3830 X-ray generator) was carried out under ambient conditions. The crystalline phases were identified by referring to the powder XRD database (JCPDS-ICDD) and the crystallite sizes were calculated using the value of full width at half maximum (FWHM) for the highest intensity diffraction peak, by means of the following well known Debye-Scherrer equation:^{71,72}

$$D = \frac{0.9\lambda}{\beta \cos \theta} \quad (1)$$

where λ is the wavelength, β is the full width at half maximum (FWHM) of the peak and θ is Bragg's angle of the XRD peak. The thickness of the obtained films was estimated gravimetrically using a microbalance (Mettler ME 30, digital resolution of 1 μg). A home-built Raman spectrometer with respective spectral resolutions of 2 and 4 cm^{-1} was used to confirm the hematite spinel structure of the obtained oxides. Details related to the Raman measurements have been reported elsewhere.⁷³ The film composition (%) was determined by energy dispersive spectroscopy (EDS, S-450 Hitachi) and X-ray photoelectron spectroscopy (XPS, Multiprobe, Omicron Nanotechnology). XPS was done in a multi-technique UHV instrument using a monochromatic Al K α X-ray source (1486.7 eV, 250 W) and a hemispherical electron energy analyzer (Sphera) in the constant analyzer energy mode. The sample was at an angle of 13° from the surface normal to the electron detector. The chamber pressure was 5×10^{-10} mbar. CasaXPS was used for the analysis of the XP spectra, and a Shirley background subtraction procedure was employed. The peak shape was Gaussian-Lorentzian with 50% for O 1s and 30% for C 1s. The microstructure was examined using scanning electron microscopy (SEM, S-450 Hitachi) and helium ion microscopy (HIM, Carl Zeiss Orion Plus®). The helium ion beam was operated at 35 kV acceleration voltage at a current of 0.8 pA. We used a 5 μm Aperture at Spot Control 4. The working distance was 9 mm at a sample tilt of 0°. Secondary electrons were collected by an Everhart-Thornley detector at 500 V grid voltage. The samples were plasma-cleaned in the HIM Load-Lock for 8 minutes before measurement. The thermal stability was measured by means of an emission-FTIR spectrometer (Thermo Nicolet 5700). To illustrate the reduction properties of the $\alpha\text{-Fe}_2\text{O}_3$ films grown on stainless steel substrates, a temperature-programmed reduction (TPR) was performed in the temperature range of 100–500 °C with a temperature ramp of 3 °C min^{-1} , under an argon flow of 0.05 L min^{-1} containing 5 vol% of H_2 . During the TPR analyses, the IR emission spectra were recorded continuously and characteristic bands were integrated *versus* temperature to discuss the redox properties. With this technique, the sensitivity limited by detecting tiny changes in the dynamically renewed gas in the conventional method is substantially improved.⁹

Catalytic test

The catalytic performance for C_3H_6 combustion was carried out over $\alpha\text{-Fe}_2\text{O}_3$ in a quartz reactor. The catalytic tests were performed on the fresh samples and pretreated ones. The samples were treated by a flow of 10% O_2 stream diluted in Ar at 300 °C for 1 hour. The experimental setup is shown in Fig. ESI 5.† The total flow rate was kept at 15 ml min^{-1} with 1% of C_3H_6 and 10% of O_2 diluted in Ar. The weight hourly space velocity (WHSV) was controlled at 45 000 ml $\text{g}_{\text{cat}}^{-1} \text{h}^{-1}$. The gas flow rates were controlled by MKS mass-flow controllers, whereas the temperature inside the reactor was raised with a ramp of 3 °C min^{-1} using a HT60 controller (Horst). The temperature of the

mesh inside the reactor was recorded using a K-thermocouple and a digital thermometer (Greisinger GMH3250). The exhaust gases were analyzed using a homemade KBr transmission-FTIR cell coupled to a commercial FTIR spectrometer with a sensitivity of 0.1% (Thermo Nicolet 5700) in the wavelength range of 400–4000 cm^{-1} . This technique has been used to detect reactants, products and stable intermediates. Details of the data treatment were described elsewhere.⁹ Blank experiments were performed using a reactor filled with a non-coated mesh of stainless steel.

Conclusions

Thin films of $\alpha\text{-Fe}_2\text{O}_3$ were synthesized *via* a PSE-CVD process. The obtained thin film was systematically characterized in terms of structure, composition, thermal stability, reducibility and catalytic properties. The substrate temperature was found to play an important role in the crystalline shape evolution and, therefore, determined the film morphology. The obtained $\alpha\text{-Fe}_2\text{O}_3$ was shown to be thermally stable up to 500 °C, attesting to the most stable status of hematite. The thin film of $\alpha\text{-Fe}_2\text{O}_3$ exhibited good catalytic performance towards catalytic combustion of C_3H_6 . Moreover, no trace of carbon monoxide commonly observed in the catalytic oxidation of some volatile organic compounds by metal oxides was observed. The $\alpha\text{-Fe}_2\text{O}_3$ catalyst maintained its activity and stability upon several consecutive heating and cooling cycles. The lattice oxygen detected by XPS, the reduction property and the fine crystalline shape of samples prepared at low temperature played important roles in the catalytic oxidation process of C_3H_6 . Here we show that good performance for catalytic abatement of VOCs can be achieved with $\alpha\text{-Fe}_2\text{O}_3$ thin films with complex shapes, prepared in the absence of any dopants, surfactants or capping agents. The activity of the prominent catalytic behavior of the $\alpha\text{-Fe}_2\text{O}_3$ catalyst is due to the concerted functions between the surface chemical composition, reducibility and film morphology.

Acknowledgements

Mr Mountapmbeme Kouotou thanks Deutscher Akademischer Austausch Dienst (DAAD) for the financial support during his research stay at Bielefeld University in Germany. The authors are grateful to Prof. Thomas Hellweg for access to the SEM and EDS measurements, and Mr Harald Waterbör for his technical assistance in the laboratory.

Notes and references

- 1 J. J. Spivey, *Ind. Eng. Chem. Res.*, 1987, **26**, 2165.
- 2 M. Amann and M. Lutz, *J. Hazard. Mater.*, 2000, **78**, 41.
- 3 M. F. M. Zwinkels, S. G. Järås, P. G. Menon and T. A. Griffin, *Catal. Rev. Sci. Eng.*, 1993, **35**, 319.
- 4 E. M. Cordi and J. L. Falconer, *J. Catal.*, 1996, **162**, 104.
- 5 D. A. Peña, B. S. Uphade and P. G. Smirniotis, *J. Catal.*, 2004, **221**, 421.
- 6 L. H. Hu, Q. Peng and Y. D. Li, *J. Am. Chem. Soc.*, 2008, **130**, 16136.

- 7 Z. Y. Tian, N. Bahlawane, F. Qi and K. Kohse-Hoinghaus, *Catal. Commun.*, 2009, **11**, 118.
- 8 X. W. Xie, Y. Li, Z. Q. Liu, M. Haruta and W. J. Shen, *Nature*, 2009, **458**, 746.
- 9 Z. Y. Tian, P. H. Tchoua Ngamou, N. Bahlawane, V. Vannier and K. Kohse-Hoinghaus, *Appl. Catal., B*, 2012, **117–118**, 125.
- 10 X. L. Mou, X. J. Wei, Y. Li and W. J. Shen, *CrystEngComm*, 2012, **14**, 5107.
- 11 X. C. Jiang and A. B. Yu, *J. Mater. Process. Technol.*, 2009, **209**, 4558.
- 12 L. P. Zhu, N. C. Bing, L. L. Wang, H. Y. Jin, G. H. Liao and L. J. Wang, *Dalton Trans.*, 2012, **41**, 2959.
- 13 E. Comini, V. Guidi, C. Frigeri, I. Riccò and G. Sberveglieri, *Sens. Actuators, B*, 2001, **77**, 16.
- 14 P. S. Shind, G. H. Go and W. J. Lee, *J. Mater. Chem.*, 2012, **22**, 10469.
- 15 T. Ohmori, H. Takahashi, H. Mametsuka and E. Suzuki, *Phys. Chem. Chem. Phys.*, 2000, **2**, 3519.
- 16 H. Zeng, J. Li, J. P. Liu, Z. L. Wang and S. H. Sun, *Nature*, 2002, **420**, 395.
- 17 B. Xu, B. Huang, H. Cheng, Z. Wang, X. Qin, X. Zhang and Y. Dai, *Chem. Commun.*, 2012, **48**, 6529.
- 18 J. Ma, J. Teo, L. Mei, Z. Zhong, Q. Li, T. Wang, X. Duan, J. Lian and W. Zheng, *J. Mater. Chem.*, 2012, **22**, 11694.
- 19 Y. Sun and Y. Xia, *Science*, 2002, **298**, 2176.
- 20 C. J. Sartoretti, B. D. Alexander, R. Solarska, I. A. Rutkowska and J. Augustynski, *J. Phys. Chem. B*, 2005, **109**, 13685.
- 21 W. B. Jr Ingler, J. P. Baltrus and S. U. M. Khan, *J. Am. Chem. Soc.*, 2004, **126**, 10238.
- 22 H. G. Cha, J. Song, H. S. Kim, W. Shin, K. B. Yoon and Y. S. Kang, *Chem. Commun.*, 2011, **47**, 2441.
- 23 A. A. Tahir, K. G. Ubul Wijayantha, S. Saremi-Yarahmadi, M. Mazhar and V. McKee, *Chem. Mater.*, 2009, **21**, 3763.
- 24 W. Hamd, S. Cobo, J. Fize, G. Baldinozzi, W. Schwartz, M. Reymermier, A. Pereira, M. Fontecave, V. Artero, C. Laberty-Robert and C. Sanchez, *Phys. Chem. Chem. Phys.*, 2012, **14**, 13224.
- 25 N. S. Chaudhari, S. S. Warule, S. Muduli, B. B. Kale, S. Jouen, B. Lefez, B. Hannoyer and S. B. Ogale, *Dalton Trans.*, 2011, **40**, 8003.
- 26 B. Klahr, S. Gimenez, F. Fabregat-Santiago, J. Bisquert and T. W. Hamann, *Energy Environ. Sci.*, 2012, **5**, 7626.
- 27 Y. Lin, G. Yuan, S. Sheehan, S. Zhou and D. Wang, *Energy Environ. Sci.*, 2011, **4**, 4862.
- 28 S. B. Wang, Y. L. Min and S. H. Yu, *J. Phys. Chem. C*, 2007, **111**, 3551.
- 29 X. Liang, X. Wang, J. Zhuang, Y. Chen, D. Wang and Y. Li, *Adv. Funct. Mater.*, 2006, **16**, 1805.
- 30 Q.-X. Gao, X.-F. Wang, J.-L. Di, X.-C. Wu and Y.-R. Tao, *Catal. Sci. Technol.*, 2011, **1**, 574.
- 31 B. Lv, Z. Liu, H. Tian, Y. Xu, D. Wu and Y. Sun, *Adv. Funct. Mater.*, 2010, **20**, 3987.
- 32 N. Bahlawane, P. A. Premkumar, K. Onwuka, G. Reiss and K. Kohse-Hoinghaus, *Microelectron. Eng.*, 2007, **84**, 2481.
- 33 P. Mountapmbeme Kouotou, Z. Y. Tian, U. Mundloch, N. Bahlawane and K. Kohse-Hoinghaus, *RSC Adv.*, 2012, **2**, 10809.
- 34 Z. Y. Tian, N. Bahlawane, V. Vannier and K. Kohse-Hoinghaus, *Proc. Combust. Inst.*, 2013, **34**, 2261.
- 35 P. H. Tchoua Ngamou, K. Kohse-Hoinghaus and N. Bahlawane, *Catal. Commun.*, 2011, **12**, 1344.
- 36 T. Y. Ma and I. C. Lee, *J. Mater. Sci.: Mater. Electron.*, 2004, **15**, 775.
- 37 A. Martinez, J. Pena, M. Labeau, J. M. Gonzalez-Calbet and M. Vallet-Regi, *J. Mater. Res.*, 1995, **10**, 1307.
- 38 I. Chamritski and G. Burns, *J. Phys. Chem. B*, 2005, **109**, 4965.
- 39 P. P. Lottici, C. Baratto, G. Antonioli, A. Montenero and M. Guarneri, *Opt. Mater.*, 1998, **9**, 368.
- 40 L. V. Gasparov, D. B. Tanner, D. B. Romero, H. Berger, G. Margaritondo and L. Forro, *Phys. Rev. B: Condens. Matter Mater. Phys.*, 2000, **62**, 7939.
- 41 D. L. A. de Faria, S. V. Silva and M. T. de Oliveira, *J. Raman Spectrosc.*, 1997, **28**, 873.
- 42 D. Parras-Guijarro, M. Montejo-Gamez, N. Ramos-Martos and A. Sanchez, *Spectrochim. Acta, Part A*, 2006, **64**, 1133.
- 43 B. W. Ward, J. A. Notte and N. P. Economou, *J. Vac. Sci. Technol., B*, 2006, **24**, 2871.
- 44 R. Hill, J. A. Notte and L. Scipioni, Scanning Helium Ion Microscopy, in *Advances in Imaging and Electron Physics*, Elsevier, 2012, ch. 2, pp. 65–148.
- 45 D. C. Bell, *Microsc. Microanal.*, 2009, **15**, 147.
- 46 J. S. Xu and Y. J. Zhu, *CrystEngComm*, 2012, **14**, 2702.
- 47 S. Gandhi, S. Sethuraman and U. Maheswari Krishnan, *Dalton Trans.*, 2012, **41**, 12530.
- 48 G. Bhargava, I. Gouzman, C. M. Chun, T. A. Ramanarayanan and S. L. Bernasek, *Appl. Surf. Sci.*, 2007, **253**, 4322.
- 49 G. K. Pradhan and K. M. Parida, *ACS Appl. Mater. Interfaces*, 2011, **3**, 317.
- 50 Z. Y. Tian, P. Mountapmbeme Kouotou, N. Bahlawane and P. H. Tchoua Ngamou, *J. Phys. Chem. C*, 2013, **117**, 6218.
- 51 P. H. Tchoua Ngamou and N. Bahlawane, *Chem. Mater.*, 2010, **22**, 4158.
- 52 N. Bahlawane, P. A. Premkumar, J. Feldmann and K. Kohse-Hoinghaus, *Chem. Vap. Deposition*, 2007, **13**, 118.
- 53 F. Wyrwalski, J. M. Glaudon and J. F. Lamonier, *Catal. Lett.*, 2010, **137**, 141.
- 54 Ö. Özdemir and S. K. Banerjee, *Geophys. Res. Lett.*, 1984, **11**, 161.
- 55 X. H. Yey, D. H. Liny, Z. K. Jiaoz and L. Zhang, *J. Phys. D: Appl. Phys.*, 1998, **31**, 2739.
- 56 R. Zhang, H. Alamdari and S. Kaliaguine, *Catal. Lett.*, 2007, **119**, 108.
- 57 S. Ivanova, C. Petit and V. Pitchon, *Gold Bull.*, 2006, **39**, 3.
- 58 R. J. H. Voorhoeve, J. P. Remeika and D. W. Johnson, *Science*, 1973, **180**, 62.
- 59 C. Q. Hu, Q. S. Zhu, Z. Jiang, L. Chen and R. F. Wu, *Chem. Eng. J.*, 2009, **152**, 583.
- 60 B. Y. Jibril, S. M. Al-Zahrani, A. E. Abasaed and R. Hughes, *Chem. Eng. J.*, 2004, **103**, 59.
- 61 S. Scirè, S. Minicò, C. Grisafulli and S. Galvagno, *Catal. Commun.*, 2001, **2**, 229.
- 62 M. R. Morales, B. P. Barbero and L. E. Cadús, *Appl. Catal. B: Environ.*, 2007, **74**, 1.

- 63 L. F. Liotta, M. Ousmane, G. Di Carlo, G. Pantaleo, G. Deganello, G. Marci, L. Retailleau and A. Giroir-Fendler, *Appl. Catal., A*, 2008, **347**, 81.
- 64 T. Masui, Y. M. Peng, K. I. Machida and G. Y. Adachi, *Chem. Mater.*, 1998, **10**, 4005.
- 65 H. M. Chen, R. S. Liu, M. Y. Lo, S. C. Chang, L. D. Tsai, Y. M. Peng and J. F. Lee, *J. Phys. Chem. C*, 2008, **112**, 7522.
- 66 B. V. Reddy, F. Rasouli, M. R. Hajaligol and S. N. Khanna, *Chem. Phys. Lett.*, 2004, **384**, 242.
- 67 G. H. Qiu, H. Huang, H. Genuino, N. Opembe, L. Stafford, S. Dharmarathna and S. L. Suib, *J. Phys. Chem. C*, 2011, **115**, 19626.
- 68 A. Kanazawa, S. Kanaoka and S. Aoshima, *J. Am. Chem. Soc.*, 2007, **129**, 2420.
- 69 Z. H. Zhang, M. F. Hossain and T. Takahashi, *Appl. Catal. B: Environ.*, 2010, **95**, 423.
- 70 X. Liu, J. Liu, Z. Chang, X. Sun and Y. Li, *Catal. Commun.*, 2011, **12**, 530.
- 71 P. Scherrer, *Nachr. Ges. Wiss. Goettingen, Math.-Phys. Kl.*, 1918, **26**, 98.
- 72 J. I. Langford and A. J. C. Wilson, *J. Appl. Crystallogr.*, 1978, **11**, 102.
- 73 V. Vannier, M. Schenk, K. Kohse-Hoinghaus and N. Bahlawane, *J. Mater. Sci.*, 2012, **47**, 1348.

Electronic Supplementary Information (ESI)

Selective synthesis of α -Fe₂O₃ thin films and effect of the deposition temperature and lattice oxygen on the catalytic combustion of propene

Patrick Mountapmbeme Kouotou,^a Zhen-Yu Tian,^{a,*} Henning Vieker,^b André Beyer,^b Armin Gölzhäuser,^b
Katharina Kohse-Höinghaus^a

^aDepartment of Chemistry 1, Bielefeld University, Universitätsstraße 25, D-33615 Bielefeld, Germany

^bDepartment of Physics, Bielefeld University, Universitätsstraße 25, D-33615, Bielefeld, Germany

* Corresponding author. Tel: +49-521 106 2199, Fax: +49-521 106 6027; E-mail: zhenyu.tian@uni-bielefeld.de.

Table ESI 1 Experimental conditions for the preparation of α -Fe₂O₃

Precursor	Fe(acac) ₃
Solvent	Tetrahydrofuran
Concentration of precursor	5 mM
Frequency	4 Hz
Opening time	2 ms
Evaporation temperature	220 °C
Transportation temperature	220 °C
Substrate temperature	350 °C; 400 °C and 450 °C
Deposition pressure (mbar)	25
N ₂ (SLM)	0.16
O ₂ (SLM)	1.0
Substrates	Silicon, planar and mesh of stainless steel

Table ESI 2 Overview of the catalytic performance of the as-prepared α -Fe₂O₃ and some catalysts in the literature

Material	Weight (mg)	Gas composition	WHSV ^a (ml g ⁻¹ h ⁻¹)	T ₁₀ ^b (°C)	T ₅₀ ^b (°C)	T ₉₀ ^b (°C)	Ref.
α -Fe ₂ O ₃ 350 °C	20	1% C ₃ H ₆ /10% O ₂ in Ar	45000	260	313	350	This work
α -Fe ₂ O ₃ 400 °C				295	355	400	
α -Fe ₂ O ₃ 450 °C				302	380	435	
Co ₃ O ₄	12	1% C ₃ H ₆ /10% O ₂ in Ar	75000	306	347	396	[1]
Co ₃ O ₄	41.5	2% C ₃ H ₆ / 20%O ₂ in Ar	73000	293	327	356	[2]
Co ₃ O ₄	12	2% C ₃ H ₆ / 20%O ₂ in Ar	75000	325	354	385	[3]
Co _{2.66} Mn _{0.34} O ₄	12	2% C ₃ H ₆ / 20%O ₂ in Ar	75000	277	321	356	[3]
Cu _{0.72} Co _{2.28} O ₄	40	13% C ₃ H ₆ / 52%O ₂ in N ₂	15000	230	275	>400	[4]
Au/Al ₂ O ₃	200	1.5% C ₃ H ₆ / 4% O ₂ in He	22500	288	349	410	[5]
Au/Al ₂ O ₃	200	1% C ₃ H ₆ / 9% O ₂ in He	219512	-	365	-	[6]
Au/BaO/Al ₂ O ₃	200	1% C ₃ H ₆ / 9% O ₂ in He	250000	-	290	-	[6]
Au/Rb ₂ O/Al ₂ O ₃	200	1% C ₃ H ₆ / 9% O ₂ in He	257143	-	307	-	[6]
Au/Li ₂ O/Al ₂ O ₃	200	1% C ₃ H ₆ / 9% O ₂ in He	225000	-	327	-	[6]
Au/MgO/Al ₂ O ₃	200	1% C ₃ H ₆ / 9% O ₂ in He	214286	-	359	-	[6]
Ag/Al ₂ O ₃	50	3% C ₃ H ₆ / 10% O ₂ in N ₂	12000	-	-	420	[7]
La _{1.7} Sr _{0.3} CuO ₄ S _{0.2}	200	0.1% C ₃ H ₆ / 5% O ₂ in N ₂	30000	368	419	500	[8]
Non-coated mesh	-	1% C ₃ H ₆ /10% O ₂ in Ar	-	381	550	680	This work

Note: ^a WHSV is weight hourly space velocity; ^b T₁₀, T₅₀ and T₉₀ refer to the temperatures at which 10%, 50% and 90% propene is converted, respectively.

The table ESI 2 presents an overview of the catalytic performance of the as-prepared α -Fe₂O₃ and selected catalysts in the literature. Special attention is devoted to the comparison of the catalytic performance with noble metals and transition metals oxides. As crucial factors, the weights of the catalyst and the WHSV have been taken in account. Even though the experimental conditions are somewhat different, it can be seen from the table that both groups give similar results with the respect to the oxidation of propene. As pointed out in our recent work, Co₃O₄ and Co-based mixed oxide are very active. Up to now, only few studies involved iron oxide, especially hematite, for propene conversion. As mentioned in the introduction, iron compounds are abundantly available

and have attractive consideration attention because of their properties such as high thermodynamic stability and low cost; also, they are environmentally friendly. Therefore, α -Fe₂O₃ presents significant advantages over others transition metal oxides. In summary, as demonstrated here, hematite investigated in the present study can be successfully synthesized and is very active for VOCs conversion.

Carbon species analysis

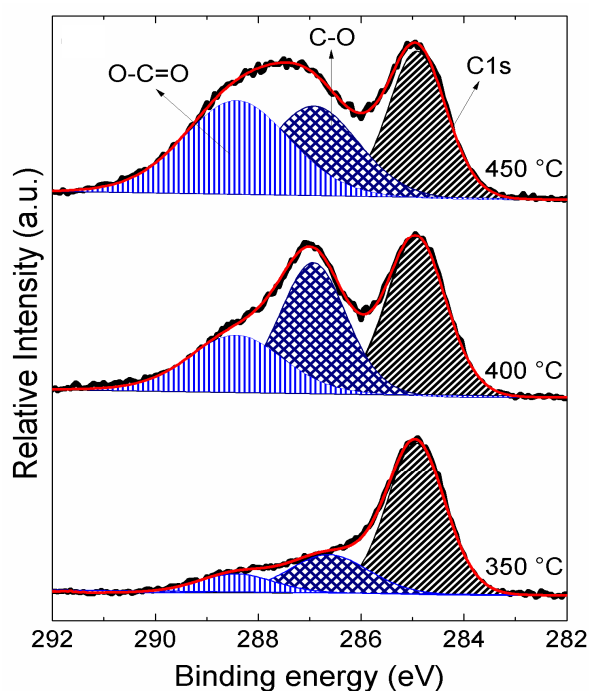


Fig. ESI 1 XPS spectra of C1s core shell present on α -Fe₂O₃. Thin and thick lines are fitted and experimental results, respectively.

Figure ESI 1 shows the C1s signal, in which three observed peaks are resolved into three components corresponding to adventitious carbon, C–O, and O–C=O moieties, respectively. The observed peaks confirmed the presence of a large amount amounting of carbonaceous species at the surface of the as-prepared α -Fe₂O₃, which are in excellent agreement with results of the oxygen signals.

Comparison of XPS results of hematite samples before and after the catalytic test

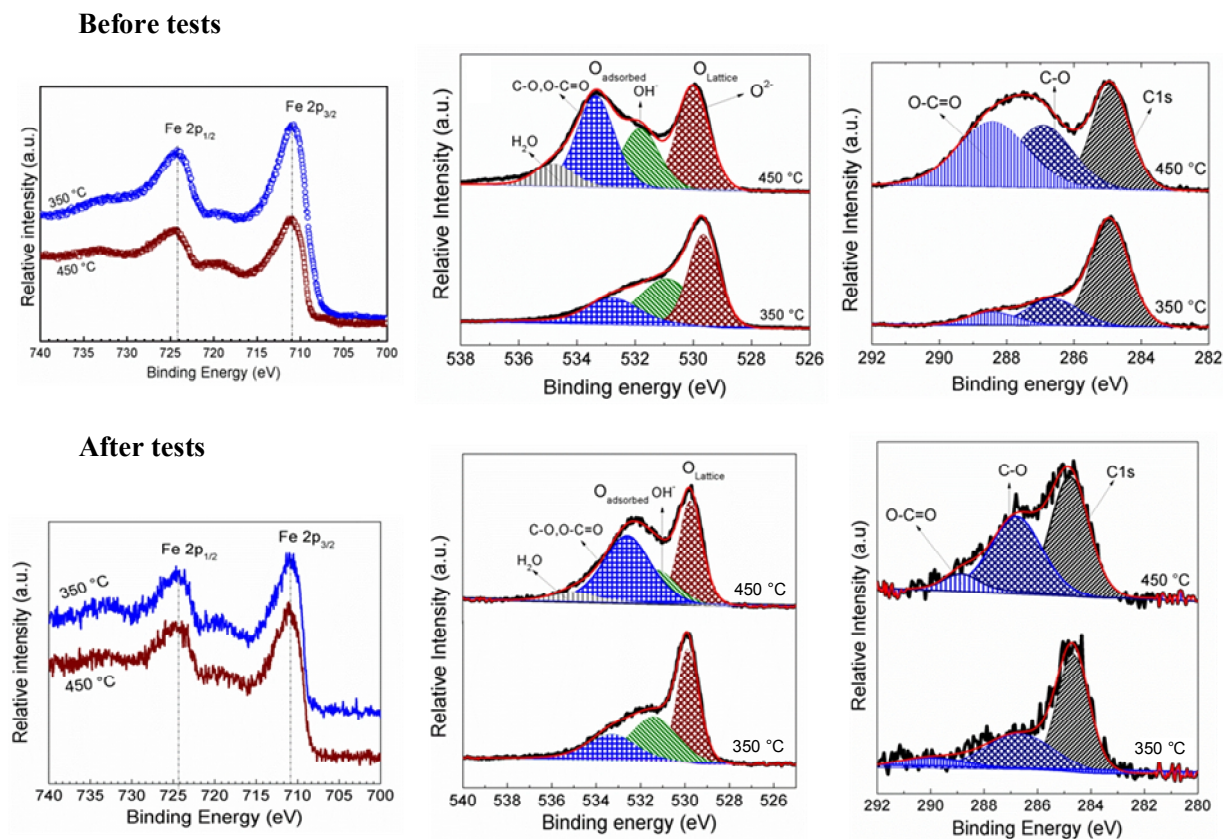


Fig. ESI 3 XPS spectra of hematite prepared at 350 °C and 450 °C before and after the catalytic tests. The high noise in the “after tests” measurements was due to a substantially lower X-ray source intensity.

As can be seen from Figs. ESI 2 and 3, the film morphology and surface composition remain quite similar for the samples before and after the catalytic test. Together with the reproducibility results in Fig. 8b, it can be predicted that the catalytic properties are not largely affected, which is also supported by the present morphology and composition results.

Brief description of the PSE-CVD reactor

The growth of α -Fe₂O₃ thin films was performed in a cold-wall stagnation point-flow CVD reactor, which is associated with a homemade PSE unit for the control delivery of liquid precursor feedstock. The reactor consists of three detachable parts: the evaporation zone (part I), carrier and transport gas zone (Part II) located above the cold-wall CVD chamber in which a flat heater (part III) is placed over the ceramic blocks. All parts were heated separately, and their temperatures were controlled by a temperature control unit (HT-60, Horst).

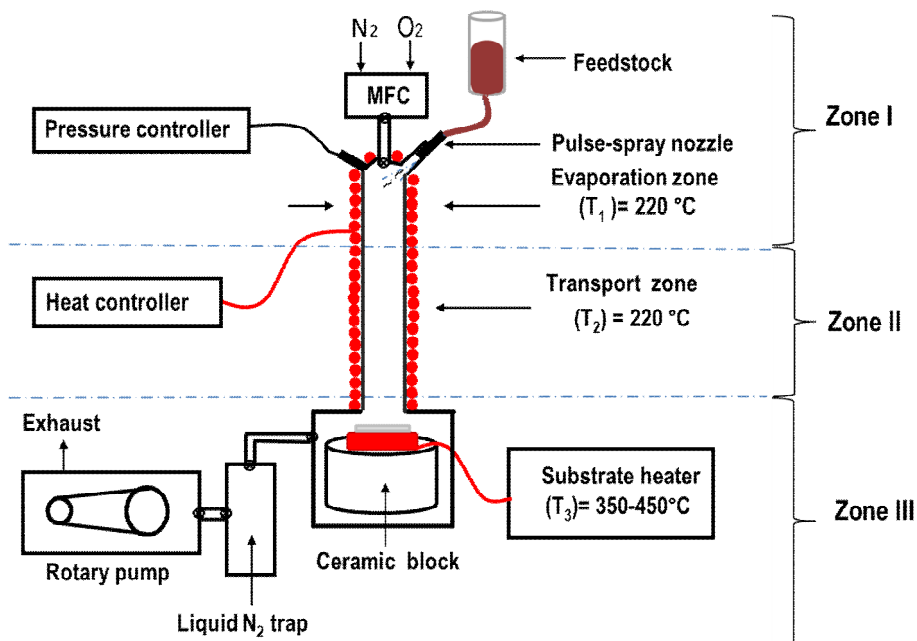


Fig. ESI 4 PSE-CVD reactor used for the synthesis of hematite.

Flow reactor use for the catalytic test

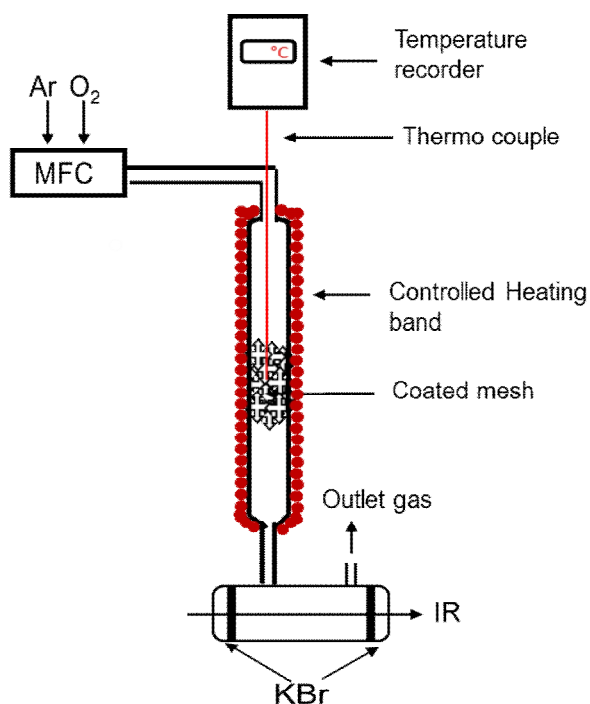


Fig. ESI 5 Schematic representation of the flow-reactor used for catalytic test.

References (ESI)

- [1] P. Mountapmbeme Kouotou, Z.Y. Tian, U. Mundloch, N. Bahlawane, K. Kohse-Höinghaus, *RSC Adv.*, 2012, **2**, 10809-10812.
- [2] Z. Y. Tian, N. Bahlawane, F. Qi, K. Kohse-Höinghaus, *Catal. Commun.*, 2009, **11**, 118-122.
- [3] Z. Y. Tian, P. H. Tchoua Ngamou, V. Vannier, K. Kohse-Höinghaus, N. Bahlawane, *Appl. Catal. B: Environ.*, 2012, **117-118**, 125-134.
- [4] H. Baussart, R. Delobel, M. Le Bras, J. M. Leroy, *J. Chem. Soc., Faraday Trans. I*, 1979, **75**, 1337-1345.
- [5] S. Ivanova, C. Petit, V. Pitchon, *Gold Bull.*, 2006, **39**, 3-8.
- [6] A. C. Gluhoi, N. Bogdanchikova, B. E. Nieuwenhuys, *J. Catal.*, 2005, **232**, 96-101.
- [7] R. Zhang, H. Alamdari, S. Kaliaguine, *Catal. Lett.*, 2007, **119**, 108.
- [8] M. Machida, K. Ochiai, K. Ito, K. Ikeue, *J. Catal.*, 2006, **238**, 58-66.

C) Publication 3

Patrick Mountapmbeme Kouotou, Zhen-Yu Tian, Henning Vieker, Katharina Kohse-Höinghaus

Pulsed-spray evaporation CVD synthesis of hematite thin films for catalytic conversion of CO

Surface & Coatings Technology 230, 59-65, 2013

Research Highlight

- PSE-CVD was applied to prepare pure hematite thin films.
- The structure, thermal and optical property of hematite was characterized.
- Hematite was thermally stable up to 500 °C and exhibited a band gap of 2.16 eV.
- Hematite showed competitive performance with reported catalysts for CO oxidation.
- A redox reaction mechanism was proposed based on the lattice and adsorbed oxygen.



Pulsed-spray evaporation CVD synthesis of hematite thin films for catalytic conversion of CO

Patrick Mountapmbeme Kouotou^a, Zhen-Yu Tian^{a,*}, Henning Vieker^b, Katharina Kohse-Höinghaus^a

^a Department of Chemistry, Bielefeld University, Universitätsstraße 25, D-33615 Bielefeld, Germany

^b Department of Physics, Bielefeld University, Universitätsstraße 25, D-33615 Bielefeld, Germany

ARTICLE INFO

Available online 14 June 2013

Keywords:

Hematite
Pulsed-spray evaporation CVD
Thin films
Catalytic oxidation
CO

ABSTRACT

Catalytically active thin films of hematite ($\alpha\text{-Fe}_2\text{O}_3$) were synthesized by pulsed-spray evaporation chemical vapor deposition (PSE-CVD) with $\text{Fe}(\text{acac})_3$ as the precursor. The obtained films were comprehensively characterized with X-ray diffraction (XRD), emission Fourier transform infrared (FTIR) and Raman spectroscopy, Scanning electron microscopy (SEM), Helium ion microscopy (HIM), Energy dispersive spectroscopy (EDS), X-ray photoelectron spectroscopy (XPS) and Ultraviolet–Visible (UV–Vis) spectrometry. The catalytic behavior of the prepared $\alpha\text{-Fe}_2\text{O}_3$ thin film towards total oxidation of CO was investigated in a plug-flow reactor. The structural analysis revealed that only the single-phase inverse spinel type $\alpha\text{-Fe}_2\text{O}_3$ was obtained at the deposition temperature of 300 °C. The optical band gap energy was estimated to be 2.16 ± 0.05 eV. The results showed that $\alpha\text{-Fe}_2\text{O}_3$ can initiate CO oxidation at 230 °C, enabling the production of CO_2 at much lower temperature compared to the reaction performed without catalyst. It also demonstrated that the hematite thin films prepared here can be competitive to catalysts described in the literature. Both the lattice and adsorbed oxygen detected by XPS were proposed to be consistent with the Eley–Rideal mechanism for CO conversion.

© 2013 Elsevier B.V. All rights reserved.

1. Introduction

In the last two decades, huge amounts of carbon monoxide (CO) were globally emitted (1.09 billion tons in 2000), mainly from transportation, power plants as well as industrial and domestic activities [1]. CO is a precursor gas of ground-level ozone, which can trigger serious respiratory problems [2]. On average, an exposure of CO at 50 ppm or greater is dangerous to human beings and animals. It is thus urgent to reduce CO emissions. One of the efficient methods of waste gas purification from CO and organic matter (C_xH_y , $\text{C}_x\text{H}_y\text{O}_z$) consists of their catalytic oxidation to non-toxic compounds, specifically carbon dioxide and water. Regarding the high price of noble metals on the one hand and the remarkable progress in active oxide syntheses on the other, catalytic oxidation of CO over oxides has captured increasing attention, and considerable effort has been devoted to the synthesis of transition metal oxides (TMOs) for such purposes [3–8].

Among these TMOs, hematite ($\alpha\text{-Fe}_2\text{O}_3$) has been extensively studied because of its excellent chemical stability, natural abundance and low cost. It has a wide range of applications, such as for catalysts [9,10], magnetic materials [11], gas sensors [12] and lithium-ion batteries [13]. In addition, as an important precursor, $\alpha\text{-Fe}_2\text{O}_3$ can be

converted into other functional materials such as maghemite ($\gamma\text{-Fe}_2\text{O}_3$) and magnetite (Fe_3O_4) [14].

Inspired by this diverse applicability of $\alpha\text{-Fe}_2\text{O}_3$, numerous approaches were employed for its synthesis, including hydrothermal methods [15], spray pyrolysis [16], magnetron sputtering [17], electrochemical deposition [18] and other techniques [19–24]. Chemical vapor deposition (CVD) has been found to be quite suitable for the preparation of metal oxide thin films. Especially, pulsed spray evaporation (PSE) CVD is considered as a promising method to prepare pure films given its relatively low cost and simplicity, high throughput and easy control of the thickness and morphology of the samples. It is particularly suitable for precursors with limited thermal stability and well adapted for systematic synthesis of single-phase/doped metals [25,26], spinels [27] or perovskites [28] with tailored composition and morphology on a number of relevant substrates.

The present work aims to report the facile synthesis and the comprehensive characterization of pure $\alpha\text{-Fe}_2\text{O}_3$ at low temperature (energy saving conditions) using a more elaborated CVD approach and the investigation of its catalytic performance towards CO conversion to CO_2 . The structure, chemical composition, morphology and optical properties of the prepared samples were investigated systematically with several dedicated characterization techniques. The catalytic property of the deposited thin film was investigated for the total oxidation reaction of CO in a tubular quartz flow reactor.

* Corresponding author. Tel.: +49 521 106 2199; fax: +49 521 106 6027.
E-mail address: zhenyu.tian@uni-bielefeld.de (Z.-Y. Tian).

2. Material and methods

2.1. Preparation of α -Fe₂O₃ thin films

The growth of α -Fe₂O₃ thin films was performed in a cold-wall stagnation point-flow CVD reactor, which is associated with a PSE unit for the controlled delivery of liquid precursor feedstock. A schematic representation of the setup is displayed in Fig. 1. The reactor consists of three zones: the evaporation zone (Zone I), the 30 cm long transportation zone (Zone II) and the deposition zone featured with a flat heater (Zone III). In the deposition process, commercially available iron acetylacetonate (Fe(acac)₃, Merck, 99%) was used as precursor and dissolved in tetrahydrofuran (THF, Prolabo HPCL 99%) to provide 5 mM concentration of liquid feedstock. The liquid feedstock was injected with a pulse frequency of 4 Hz and pulse width of 2.5 ms. The resulting spray passed through Zone I, giving rise to precursor vapor, which was then transported with a mixture of N₂ and O₂ (flow rates of 0.5 and 1.0 standard liter per minute, SLM, respectively) into Zone II. Finally, the deposition occurred on several types of heated substrates, including glass, silicon, planar stainless steel and grid mesh at 300 °C in Zone III. These substrates were selected to meet the requirements of the different characterization techniques. The temperatures were controlled by a heating controller (HT-60, Horst). Zones I and II were kept at 220 °C and the pressure was kept at 30 mbar during the deposition process. The thickness of the obtained films, which can be easily varied by adapting with different deposition parameters, was estimated gravimetrically using a microbalance (Mettler ME 30, digital resolution of 1 μ g).

2.2. Characterization

The obtained films were characterized in terms of structure, morphology, chemical composition, optical property with X-ray diffraction (XRD), emission Fourier transform infrared (FTIR) and Raman spectroscopy, Scanning electron microscopy (SEM), Helium ion microscopy (HIM), Energy dispersive spectroscopy (EDS), X-ray photoelectron spectroscopy (XPS) and Ultraviolet-Visible (UV-Vis) spectrometry. The XRD analysis (Philips X'Pert Pro MDR diffractometer with PW 3830 X-ray generator) was carried out under ambient conditions. The crystalline phase was identified by referring to the powder XRD database (JCPDS-ICDD). A Raman spectrometer with a spectral resolution of 4 cm⁻¹ was used to confirm the hematite structure of the sample. The chemical composition of the film was determined using EDS (S-450 Hitachi) and XPS (Multiprobe, Omicron Nanotechnology). The microstructure was examined using SEM (S-450 Hitachi) and HIM

(Zeiss, Orion plus). The optical property was evaluated using a UV-Vis spectrophotometer (Shimadzu UV-2501PC).

2.3. Catalytic test

The catalytic performance of the obtained α -Fe₂O₃ for CO conversion was investigated in a fixed-bed quartz reactor. Details of the setup were described in our recent work [29]. 20 mg of the catalyst supported on grid mesh of stainless steel (SPW 40, 80 × 400) was located inside the reactor. The total flow rate was kept at 15 ml min⁻¹ with 1% of CO and 10% O₂ diluted in Ar, corresponding to the weight hourly space velocity (WHSV) at 45,000 ml g⁻¹_{cat} h⁻¹. The gas flow rates were controlled by mass-flow controllers (MKS). The temperature of the reactor was raised with a ramp of 3 °C/min (Horst HT60 controller) and the temperature of the mesh inside the reactor was recorded using a K-thermocouple and a digital thermometer (Greisinger GMH3250). The exhaust gases were analyzed using a homemade KBr transmission cell equipped in an FTIR spectrometer (Nicolet FTIR 5700) over the wavelength range of 400–4000 cm⁻¹. Details about the data treatment were described elsewhere [29].

3. Results and discussion

3.1. Characterization of the structure

Fig. 2 presents the XRD pattern of a representative sample film (~300 nm) deposited at 300 °C. The diffraction peaks can be indexed to the inverse spinel phase of Fe₂O₃ (JCPDS 39-0238). No evidence of impurity phases such as FeO and Fe₃O₄ was observed, indicating that pure Fe₂O₃ products were obtained under the selected conditions. It is worth mentioning that negligible deposition was observed when the substrate temperature was lower than 300 °C. Emission FTIR analysis was employed to determine the nature of vibrational bands and functional groups of the prepared sample. As presented in Fig. 3, two strong peaks at 420 and 515 cm⁻¹ were observed, which can be attributed to the Fe–O–Fe stretching vibration mode of Fe₂O₃, in good agreement with the reported values [30].

Although XRD and emission FTIR confirmed that the obtained thin film was Fe₂O₃, they couldn't differentiate the four Fe₂O₃ phases. In this work, Raman spectroscopy was used to identify Fe₂O₃ phases. As shown in Fig. 4, the spectrum is indicative of the α -Fe₂O₃ phase exhibiting peaks at 225 and 491 cm⁻¹ due to the A_{1g} vibrational mode and at 245, 294, 411, 612 and 660 cm⁻¹ corresponding to the E_g vibrational mode. The observed peak values matched well with previously reported Raman data for hematite [31,32]. The Raman

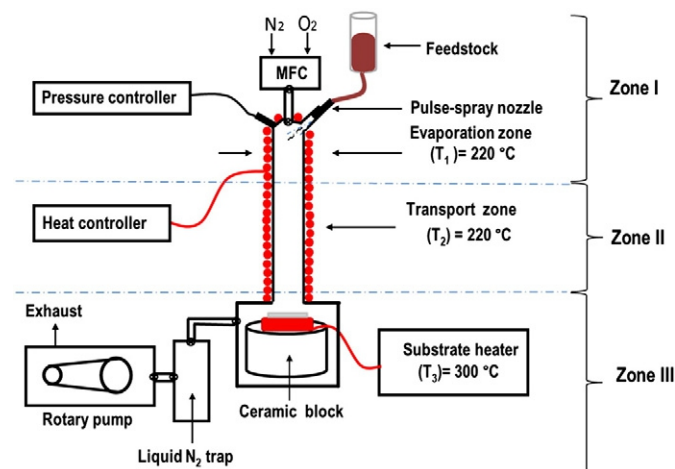


Fig. 1. Schematic PSE-CVD setup used for the preparation of α -Fe₂O₃ thin films.

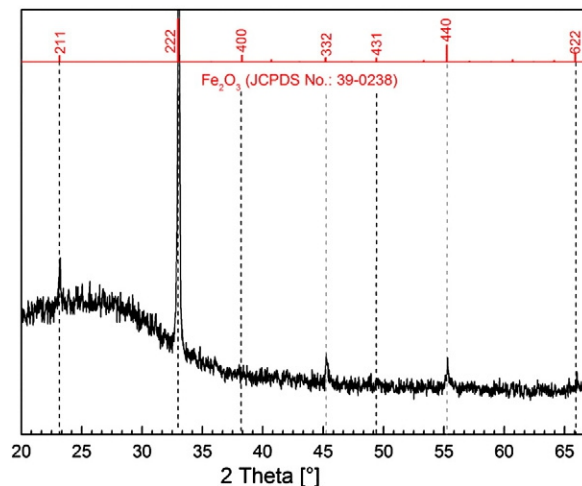


Fig. 2. XRD pattern of a representative α -Fe₂O₃ thin film.

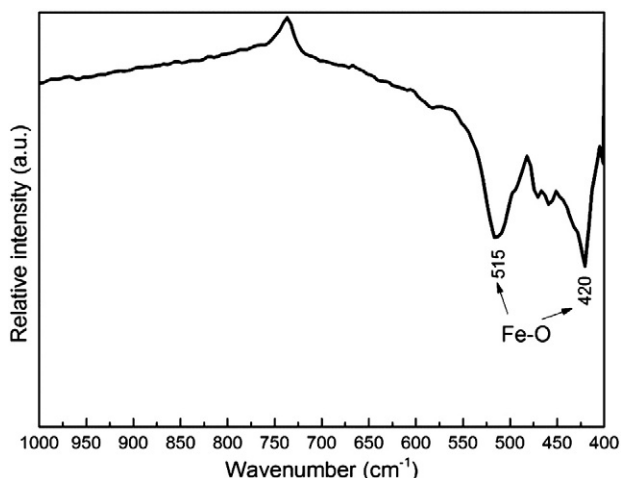


Fig. 3. Emission FTIR spectrum of a representative α - Fe_2O_3 thin film.

analysis reveals that α - Fe_2O_3 is the unique phase, which further clarifies the results obtained with XRD and FTIR.

Several CVD approaches have been used to prepare α - Fe_2O_3 previously [33–36]. However, in these cases, stringent conditions such as specific deposition temperatures and precursor vapor pressures were needed. For example, Tahir et al. [34] used $\text{Fe}(\text{CO})_5$, which is not environmentally friendly, as the precursor in atmospheric-pressure CVD because it has a relatively high vapor pressure. Also, numerous works reported that a further post-annealing step at high temperature was required to increase the crystallinity of the iron oxide films [9,35,37]. In the present work, $\text{Fe}(\text{acac})_3$ not only permits the deposition of pure α - Fe_2O_3 thin films by PSE-CVD but also allows the desired films to be obtained at relative low temperature (300 °C). The results highlight the validity of the PSE-CVD approach for the synthesis of single-phase materials at low temperature with easy control of deposition parameters.

3.2. Morphology and chemical composition

In this investigation, two different methods of morphology inspection, namely SEM and HIM, were utilized to probe the film morphology. In HIM, a finely focused beam of helium ions with a diameter down to 0.35 nm is scanned over the sample, and the secondary electrons (SE) generated by the He^+ impact are detected. In SE imaging, the topology of the sample produces more contrast as more electrons

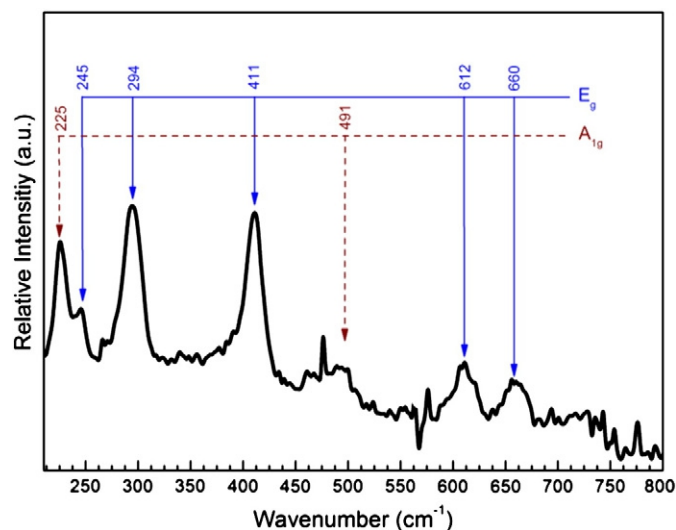


Fig. 4. Raman spectrum of a representative α - Fe_2O_3 thin film.

are ejected when the He^+ beam hits the sample at glancing incidence. Since the SE energy is very low, it leads to a higher surface sensitivity than typical electron microscopy. Fig. 5 shows representative SEM and HIM images of the hematite with different magnifications. The SEM images in Fig. 5(a–c) clearly reveal that the film is composed of a large quantity of plate-like geometric structures. It is also observed from HIM images in Fig. 5(d–f) that the α - Fe_2O_3 sample exhibits mainly nano-plate structures with random orientations. According to Ma et al. [38], such a morphology often possesses better mechanical strength and has a lower pressure drop, which allows for higher reactant gas velocities than fine powder catalysts. The observed morphology may thus be related with the catalytic performance of the deposited α - Fe_2O_3 .

EDS was performed to determine the chemical composition of α - Fe_2O_3 thin film. As shown in Fig. 6, only Fe and O peaks were observed. The atomic ratio of O/Fe was about 1.5 for the sample. This ratio corresponds well with the value calculated from the formula of hematite.

XPS results for the prepared α - Fe_2O_3 thin film are shown in Fig. 7. The binding energies of Fe $2p_{3/2}$ and Fe $2p_{1/2}$ were determined to be 711.03 and 725.2 eV, respectively, which is characteristic of the Fe^{3+} state in α - Fe_2O_3 [39,40]. The binding energies of O 1s were observed to be 530.3 and 532.4 eV, corresponding to lattice oxygen (O_L) and adsorbed oxygen (O_{ads}), respectively. Based on the XPS results, the atomic ratio of O/Fe was estimated to be 1.5, which is consistent with the XRD, FTIR, Raman and EDS analysis.

3.3. Optical properties

A correlation between catalytic performance and band gap energies of metal oxides has been reported by Jibril [41]. According to the author, metal oxides with a low energy band gap generally exhibit good catalytic performance [41]. A recent study by Tian et al. [25] on structure sensitivity of propene oxidation over Co-based spinel oxides confirmed the observation of Jibril [41]. The optical absorption spectrum and the Tauc plot showing the estimated band gap energy for the hematite thin films were investigated and the results are presented in Fig. 8. The absorption gradually decreases as the wavelength extends towards the visible region. From 400 to 600 nm, the absorption decreases significantly and becomes linear into the red region. The optical band gap energy from the optical absorption spectrum was estimated from the Tauc plot which uses the relationship between the incident photon energy ($h\nu$) and the absorption coefficient (α):

$$\alpha h\nu = A(h\nu - E_g)^n.$$

Here, A is a constant related to the refractive index, E_g is the band gap depending on the crystal structure and phase composition, and $n = 1/2$ for an allowed direct transitions. The band gap energy is estimated from the intercept of the extrapolated linear fit to the experimental data. The band gap energy was determined to be 2.16 ± 0.05 eV, which is consistent with previously reported data [39,42]. With a narrow band gap, the lattice oxygen mobility increases, and the migration of O^{2-} from the bulk to the surface becomes easier, favoring the catalyst's reducibility. It is therefore expected that the lower energy band gap obtained in this study for α - Fe_2O_3 will enhance its catalytic performance.

3.4. Catalytic properties

Catalytic oxidation of CO has attracted wide attention due to its applications in the purification of automotive exhaust. In this work, the catalytic performance was investigated for CO oxidation over α - Fe_2O_3 thin film. As a reference, the reaction was firstly performed on non-coated

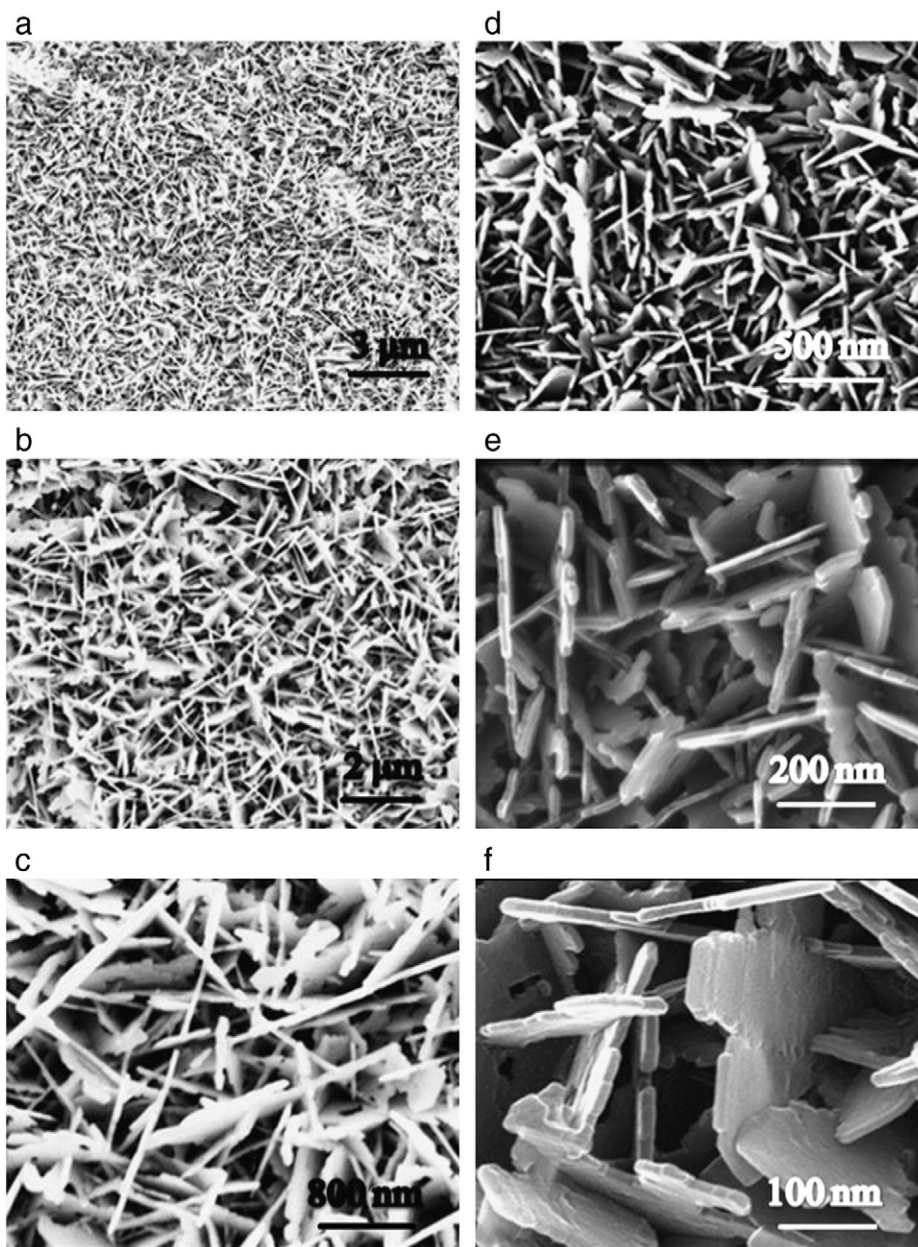


Fig. 5. SEM (a–c) and HIM (d–f) images at different magnifications of α -Fe₂O₃ thin films coated on stainless steel mesh at 300 °C.

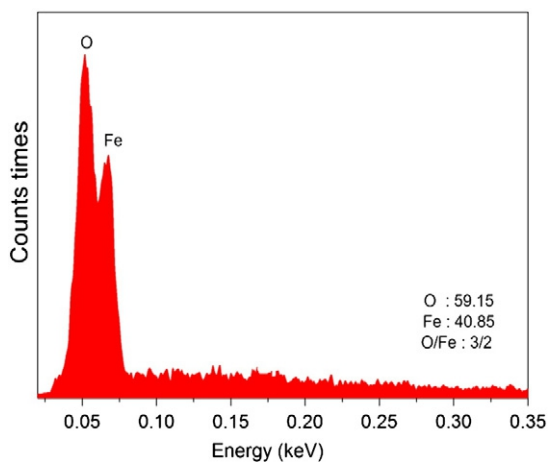


Fig. 6. EDX spectrum of a representative α -Fe₂O₃ thin film.

stainless steel mesh in the temperature range of 180 °C to 950 °C. An identical mesh coated with 20 mg α -Fe₂O₃ was then tested under the same inlet gas conditions, but raising the temperature only to 500 °C, the stability limit of α -Fe₂O₃. In the presence of α -Fe₂O₃, the conversion of CO started at ~220 °C and complete conversion occurred at 398 °C, while these values were shifted to ~300 and 930 °C on non-coated mesh, respectively, revealing the better catalytic performance of the deposited thin films. A systematic study was carried out by Walker et al. [43] to evaluate the possible application of iron catalysts for automotive emission control. Unsupported Fe₂O₃ and several supported catalysts were investigated in CO oxidation [43]. The authors reported the following order of activity in CO oxidation: Fe₂O₃/Al₂O₃ > Fe₂O₃/TiO₂ ≈ Fe₂O₃ > FeSbO₄ > FePO₄ > Fe₂(MoO₄)₃. The temperature at 10% and 50% of CO conversion, T_{10} and T_{50} , was found to be 327 and 398 °C with Fe₂O₃ as the catalyst [43]. In the present study, α -Fe₂O₃ thin films with plate-like structure obtained by PSE-CVD enabled the conversion of CO to CO₂ at T_{10} and T_{50} at 260 and 320 °C, respectively. As shown in Fig. 9, the second run of the catalytic test gave quite similar values for

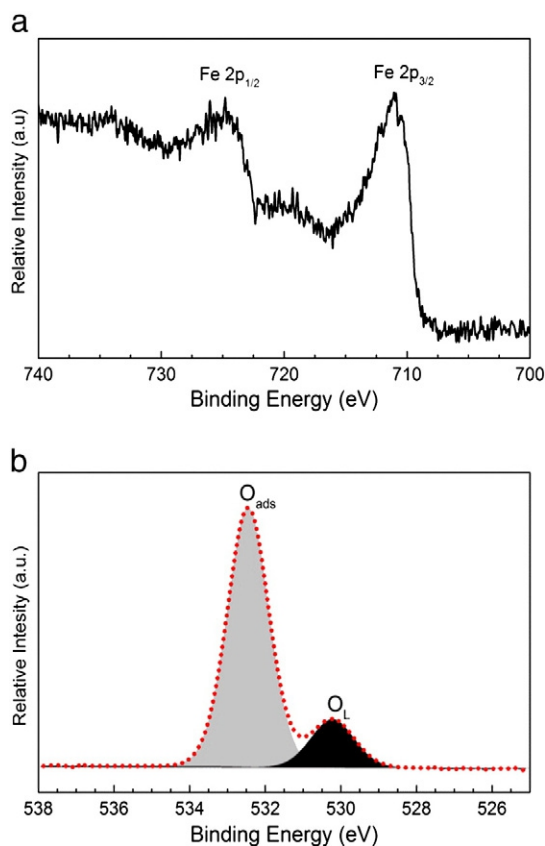


Fig. 7. XPS spectra showing Fe 2p (a) and O 1s signals (b) of a representative α -Fe₂O₃ thin film.

T_{10} and T_{50} . This result confirms the good performance of the prepared catalyst, also with respect to the literature [4,8,27,43–47]. Table 1 presents the comparison of CO conversion results over α -Fe₂O₃ thin films obtained in this study with other reported data. It should be mentioned that the reusability of the obtained α -Fe₂O₃ films and reproducibility of their catalytic performance in this work are satisfactory within experimental uncertainty (see Fig. 9). By comparing the XRD spectra measured before and after the catalytic test, the catalytic oxidation of CO under oxygen-rich condition is confirmed to have no obvious effect on the catalyst structure.

Two mechanisms can be involved in CO oxidation over hematite, namely the Eley–Rideal (ER) and the Langmuir–Hinshelwood (LH) mechanisms. The ER mechanism where an adsorbed species reacts with a gas-phase species has been discussed by Halim et al. [5] and Wagloehner et al. [48]. Bergermayer and Schweiger [49], in an *ab initio* thermodynamic study of Fe₂O₃, discussed the LH mechanism where both reacting species must first adsorb, followed by the conversion reaction. In 2007, Kandalam et al. [50] discussed both mechanisms for the oxidation of CO on various Fe₂O₃ surfaces. They suggested that a CO molecule first adsorbs onto hematite, weakening an Fe–O bond near the crystal surface and then, a second CO molecule adsorbs and forms CO₂ by breaking the weakened Fe–O bond [50]. As proposed by Grenfell et al. [51], hematite films are composed of a bulk and surface region on which active adsorption sites exist. Part of these sites could be occupied by trapped oxygen atoms, which can originate either *via* dissociation of adsorbed oxygen during the oxidation reaction or *via* diffusion from the lattice to the surface [50–52]. Due to the confinement of the adsorbed species to the active sites, the migration process across the surface is not favored for CO oxidation on hematite [51,52]. In addition, the number of surface iron atoms, with which the adsorbed O₂ can interact has been reported to play a significant role [51,53].

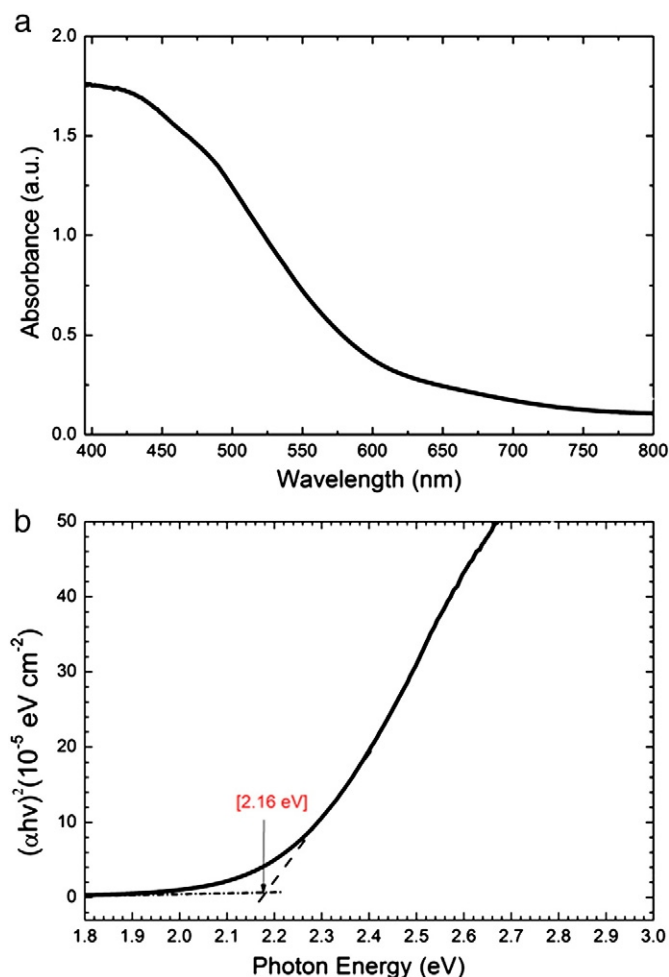


Fig. 8. Optical absorption spectrum (a) and Tauc's plot (b) resulting in an optical band gap of 2.16 eV for the α -Fe₂O₃ thin films (b).

It is known that three different planes exist in the hematite crystal structure on which the densities of the iron atoms are different [54]. According to Liu et al. [54], a catalyst with exposed planes containing

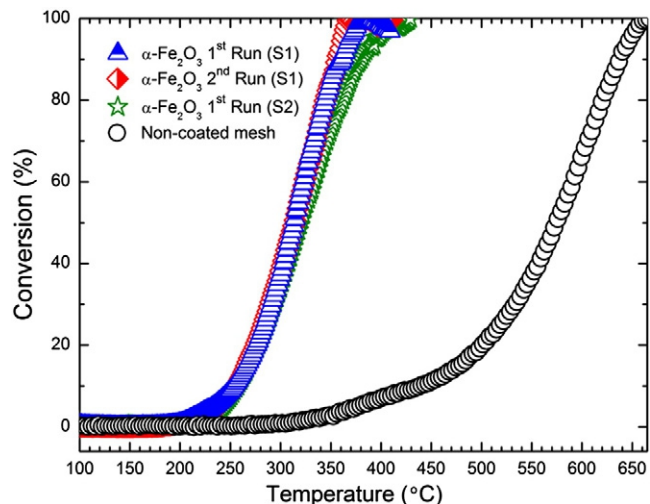


Fig. 9. CO conversion profiles over stainless steel grid meshes coated with α -Fe₂O₃ films at a WHSV of 45,000 g_{cat}⁻¹ h⁻¹. Two samples (S1 and S2) prepared at the same conditions were tested. 1st Run and 2nd Run are the catalytic tests performed for the first and second time, respectively. The performance for non-coated mesh is included as a reference.

Table 1
Comparison of the catalytic performance.

Catalyst	Weight (mg)	Gas composition	Flow rate (ml min ⁻¹)	T ₅₀ ^a (°C)	T ₉₀ ^a (°C)	WHSV ^b (ml g ⁻¹ h ⁻¹)	Ref.
α-Fe ₂ O ₃ thin film	20	1% CO/10% O ₂ /89% Ar	15	320	366	45,000	This work ^c
				319	364		This work ^d
				321	376		This work ^e
Fe ₂ O ₃	50	3.44% CO/20.6 O ₂ /85.96 He	1000	300	330	1,200,000	[4]
Fe ₂ O ₃	1000	2.5% CO/1.7% O ₂ /0.5% H ₂ /He	1000	367	397	60,000	[43]
Fe ₂ O ₃ /TiO ₂	1000	2.5% CO/1.7% O ₂ /0.5% H ₂ /He	1000	333	412	60,000	[43]
Fe ₂ O ₃ /Al ₂ O ₃	1000	2.5% CO/1.7% O ₂ /0.5% H ₂ /He	1000	327	377	60,000	[43]
Co ₃ O ₄ thin film	12	1% CO/10% O ₂ /89% Ar	15	335	350	75,000	[27]
Co ₃ O ₄ bulk	50	1% CO/8% O ₂ in He	37	–	350	44,400	[8]
CeO ₂	100	2% CO/2% O ₂ in N ₂	100	–	374	60,000	[44]
Al ₂ O ₃	100	2% CO/2% O ₂ in N ₂	100	–	394	60,000	[44]
CeAlO ₃	100	2% CO/2% O ₂ in N ₂	100	–	465	60,000	[44]
Pt/H ₂ SO ₄ /ZrO ₂	50	3.5% CO/4% O ₂ in N ₂	100	–	290	120,000	[45]
Pt/Al ₂ O ₃	2/200	1% CO/1.38% O ₂ in N ₂	–	333	430	90,000	[46]
Au/SiO ₂	100	1% CO/99% dry air	200	337	423	12,000	[47]

Note: ^aT₅₀ and T₉₀ refer to the temperatures at which 50% and 90% CO were converted, respectively; ^bWHSV is weight hourly space velocity; ^{c–e}These results are obtained in the first run with sample 1, the second run with sample 1 and first run with sample 2, respectively.

more Fe atoms could provide more active sites for catalytic reactions and consequently exhibit high catalytic activity. Based on the XPS results that confirmed the presence of iron and oxygenated species such as adsorbed oxygen at the catalyst surface, and the detailed kinetic data in the literature [48], the most probable mechanism in this investigation seems to be the ER mechanism which proceeds with three steps: O₂ adsorption, removal of the adsorbed oxygen by gaseous CO and desorption of CO₂. Different reactive anion intermediates such as O⁻ or O₂⁻ can result from the O₂ adsorption process, depending on how the O₂ approaches the surface e.g. sideways, perpendicularly or obliquely [49–51]. During desorption of CO₂, an active site occupied by an adsorbed oxygen atom can be formed for further reaction. Also, the catalytic performance can benefit from the exposed plate-like structures of α-Fe₂O₃ which present availability for abundant gaseous species at the surface as an opportunity for their participation in the catalytic reaction sequence.

4. Summary and conclusion

The PSE-CVD method was applied to prepare α-Fe₂O₃ thin films. The obtained samples were characterized in terms of structure, morphology, chemical composition, optical and catalytic properties with XRD, FTIR, Raman, EDS, SEM/HIM, XPS and UV–Vis spectroscopy. The obtained product was pure α-Fe₂O₃ at the stated deposition conditions. The structural analysis showed the deposited films to be constituted of randomly oriented plate-like elements with dimensions in the 100 nm regime. The optical properties of the thin films were investigated and the band gap energy of α-Fe₂O₃ was determined to be 2.16 ± 0.05 eV. Catalytic tests indicate that α-Fe₂O₃ thin film can initiate CO oxidation at lower temperature than non-coated substrates and that it is competitive with some materials from recent literature. Regarding plausible catalytic conversion mechanisms, it is assumed that the detection of both lattice and adsorbed oxygen at the surface of the catalyst by XPS may be consistent with the Eley–Rideal mechanism.

Acknowledgments

Dr. Tian would like to acknowledge the support of the Alexander von Humboldt Foundation for his research fellowship and additional support by the Bielefeld University Nachwuchsfonds. Mr. Mountapmbeme Kouotou thanks the Deutscher Akademischer Austausch Dienst (DAAD) for his research fellowship. The authors thank Prof. Thomas Hellweg for access to the SEM/EDX measurements and Prof. Armin Götzhäuser and Dr. André Beyer for access to the HIM/XPS facilities.

References

- [1] EarthTrends of the World Resources Institute, at http://earthtrends.wri.org/searchable_db/index.php?theme=3.
- [2] S. Royer, D. Duprez, ChemCatChem 3 (2011) 24–65.
- [3] X.W. Xie, Y. Li, Z.Q. Liu, M. Haruta, W.J. Shen, Nature 458 (2009) 746–749.
- [4] P. Li, D.E. Miser, S. Rabiei, R.T. Yadav, M.R. Hajaligol, Appl. Catal. B Environ. 43 (2003) 151–162.
- [5] M.H. Khedr, K.S.A. Halim, M.I. Nasr, A.M. El-Mansy, Mater. Sci. Eng., A 430 (2006) 40–45.
- [6] H.Y. Lin, Y.W. Chen, W.J. Wang, J. Nanopart. Res. 7 (2005) 249–263.
- [7] Y. Yu, T. Takei, H. Ohashi, H. He, X. Zhang, M. Haruta, J. Catal. 267 (2009) 121–128.
- [8] Y. Ren, Z. Ma, L. Qian, S. Dai, H. He, P.G. Bruce, Catal. Lett. 131 (2009) 146–154.
- [9] M.A. Gondal, A. Hameed, Z.H. Yamani, A. Al-Suwaiyan, Appl. Catal. A Gen. 268 (2004) 159–167.
- [10] Z. Zhong, J. Ho, J. Teo, S. Shen, A. Gedanken, Chem. Mater. 19 (2007) 4776–4782.
- [11] D. Jagadeesan, U. Mansoori, P. Mandal, A. Sundaresan, M. Eswaramoorthy, Angew. Chem. Int. Ed. 47 (2008) 7685–7688.
- [12] X.L. Hu, J. Yu, J.M. Gong, Q. Li, G.S. Li, Adv. Mater. 19 (2007) 2324–2329.
- [13] G. Jain, M. Balasubramanian, J.J. Xu, Chem. Mater. 18 (2006) 423–434.
- [14] F. Jiao, A. Harrison, J.C. Jumas, A.V. Chadwick, W. Kockelmann, P.G. Bruce, J. Am. Chem. Soc. 128 (2006) 5468–5474.
- [15] Y. Ling, G. Wang, D.A. Wheeler, J.Z. Zhang, Y. Li, Nano Lett. 11 (2011) 2119–2125.
- [16] C.J. Sartoretti, B.D. Alexander, R. Solarska, I.A. Rutkowska, J. Augustynski, J. Phys. Chem. B 109 (2005) 13685–13692.
- [17] J.A. Glasscock, P.R.F. Barnes, I.C. Plumb, N. Savvides, J. Phys. Chem. C 111 (2007) 16477–16488.
- [18] A. Kleiman-Shwarsstein, Y.S. Hu, A.J. Forman, G.D. Stucky, E.W. McFarland, J. Phys. Chem. C 112 (2008) 15900–15907.
- [19] J. Brillet, M. Grätzel, K. Sivula, Nano Lett. 10 (2010) 4155–4460.
- [20] S.K. Mohapatra, S.E. John, S. Banerjee, M. Misra, Chem. Mater. 21 (2009) 3048–3055.
- [21] P.M. Rao, X.L. Zheng, Nano Lett. 9 (2009) 3001–3006.
- [22] J.P. Yong, K.M.A. Sobahan, C.K. Hwangbo, Surf. Coat. Technol. 203 (2009) 2646–2650.
- [23] F. Le Formal, M. Grätzel, K. Sivula, Adv. Funct. Mater. 20 (2010) 1099–1107.
- [24] Y. Lin, S. Zhou, S.W. Sheehan, D. Wang, J. Am. Chem. Soc. 133 (2011) 2398–2401.
- [25] Z.Y. Tian, N. Bahlawane, V. Vannier, K. Kohse-Höinghaus, Proc. Combust. Inst. 34 (2013) 2261–2268.
- [26] N. Bahlawane, P.A. Premkumar, Z.Y. Tian, X. Hong, F. Qi, K. Kohse-Höinghaus, Chem. Mater. 22 (2010) 92–100.
- [27] P. Mountapmbeme Kouotou, Z.Y. Tian, U. Mundloch, N. Bahlawane, K. Kohse-Höinghaus, RSC Adv. 2 (2012) 10809–10812.
- [28] P.H. Tchoua Ngamou, N. Bahlawane, Chem. Mater. 22 (2010) 4158–4165.
- [29] Z.Y. Tian, P.H. Tchoua Ngamou, N. Bahlawane, V. Vannier, K. Kohse-Höinghaus, Appl. Catal. B Environ. 117–118 (2012) 125–134.
- [30] N. Du, Y.F. Xu, H. Zhang, C.X. Zhai, D. Yang, Nanoscale Res. Lett. 5 (2010) 1295–1300.
- [31] D. Bersani, P.P. Lottici, A. Montenero, J. Raman Spectrosc. 30 (1999) 335–360.
- [32] X. Fei, Z.Z. Shao, X. Chen, J. Mater. Chem. B 1 (2013) 213–220.
- [33] S. Dhar, K. Shalini, S.A. Shivashankar, Bull. Mater. Sci. 31 (2008) 723–728.
- [34] A.A. Tahir, K.G. Upul Wijayantha, S. Saremi-Yarahmadi, M. Mazhar, V. McKee, Chem. Mater. 21 (2009) 3763–3772.
- [35] S. Park, S. Lim, H. Choi, Chem. Mater. 18 (2006) 5150–5152.
- [36] A. Kay, I. Cesar, M. Grätzel, J. Am. Chem. Soc. 128 (2006) 15714–15721.
- [37] A. Martínez, J. Pena, M. Labeau, J.M. Gonzalez-Calbet, M. Vallet-Regi, J. Mater. Res. 10 (1995) 1307–1311.
- [38] J. Ma, J. Teo, L. Mei, Z. Zhong, Q. Li, T. Wang, X. Duan, J. Lian, W. Zheng, J. Mater. Chem. 22 (2012) 11694–11700.
- [39] H.G. Cha, J. Song, H.S. Kim, W. Shin, K.B. Yoon, Y.S. Kang, Chem. Commun. 47 (2011) 2441–2443.
- [40] J.S. Xu, Y.J. Zhu, CrystEngComm 14 (2012) 2702–2710.

- [41] B.Y. Jibril, *React. Kinet. Catal. Lett.* 86 (2005) 171–177.
- [42] D.A. Wheeler, G. Wang, Y. Ling, Y. Li, J.Z. Zhang, *Energy Environ. Sci.* 5 (2012) 6682–6702.
- [43] J.S. Walker, G.I. Straguzzi, W.H. Manogue, G.C.A. Schuit, *J. Catal.* 110 (1988) 298–309.
- [44] P.A. Deshpande, S.T. Aruna, G. Madras, *Catal. Sci. Technol.* 1 (2011) 1683–1691.
- [45] H.C. Wu, L.C. Liu, S.M. Yang, *Appl. Catal. A Gen.* 211 (2001) 159–165.
- [46] V.A. Törnroona, M. Skoglundh, P. Thormählen, E. Fridell, E. Jobson, *Appl. Catal. B Environ.* 14 (1997) 131–145.
- [47] K. Qian, W.X. Huang, Z.Q. Jiang, H.X. Sun, *J. Catal.* 248 (2007) 137–141.
- [48] S. Wagloehner, D. Reichert, D. Leon-Sorzano, P. Balle, B. Geiger, S. Kurerti, *J. Catal.* 260 (2008) 305–314.
- [49] W. Bergermayer, H. Schweiger, *Phys. Rev.* 69 (195409) (2004) 1–12.
- [50] A. Kandalam, P. Jena, S. Khanna, B. Chatterjee, B.V. Reddy, Oxidation of CO on various Fe₂O₃ surfaces a theoretical study, *Amer. Phys. Soc. Meeting*, March 13–17, 2007. (abstract W11.003).
- [51] J.L. Grenfell, J.W. Stock, A.B.C. Patzer, S. Gebauer, H. Rauer, *Planet. Space Sci.* 58 (2010) 1252–1257.
- [52] H. Randall, R. Doepper, A. Renken, *Ind. Eng. Chem. Res.* 36 (1997) 2996–3001.
- [53] N.N. Bulgakov, V.A. Sadykov, *React. Kinet. Catal. Lett.* 58 (1996) 397–402.
- [54] X. Liu, J. Liu, Z. Chang, X. Sun, Y. Li, *Catal. Commun.* 12 (2011) 530–534.

D) Publication 4

Zhen-Yu Tian, Hans Jakob Herrenbrück, Patrick Mountapmbeme Kouotou, Henning Vieker, André Beyer, Armin Gölzhäuser and Katharina Kohse-Höinghaus

Facile synthesis of catalytically active copper oxide from pulsed-spray evaporation CVD

Surface & Coatings Technology 230, 33-38, 2013

Research Highlight

- CuO thin films were prepared from $\text{Cu}(\text{acac})_2$ by PSE-CVD.
- The structures, chemical, thermal and optical properties of CuO were characterized.
- The obtained CuO samples are thermally stable up to 450 °C and exhibit a band gap of 1.81 ± 0.05 eV.
- CuO proved competitive activity to reactive non-noble transition metal oxides and some coated noble metals.
- The enhanced catalytic activity benefited from the decrease of the activation energy with CuO.



Facile synthesis of catalytically active copper oxide from pulsed-spray evaporation CVD

Zhen-Yu Tian^{a,*}, Hans Jakob Herrenbrück^a, Patrick Mountapmbeme Kouotou^a, Henning Vieker^b, André Beyer^b, Armin Gölzhäuser^b, Katharina Kohse-Höinghaus^a

^a Department of Chemistry, Bielefeld University, Universitätsstraße 25, D-33615 Bielefeld, Germany

^b Department of Physics, Bielefeld University, Universitätsstraße 25, D-33615 Bielefeld, Germany

ARTICLE INFO

Available online 19 June 2013

Keywords:

Copper oxide
Chemical vapor deposition
Helium ion microscopy
Catalytic oxidation

ABSTRACT

Copper oxide thin films were controllably synthesized by pulsed-spray evaporation chemical vapor deposition (PSE-CVD). The growth kinetics was investigated by considering the pressure effect. X-ray diffraction, in situ emission Fourier transform infrared spectroscopy, Helium ion microscopy (HIM) and ultraviolet-visible (UV-Vis) spectroscopy were employed to investigate the physicochemical properties of the deposited thin films. A pure phase CuO was confirmed by the structural investigations. The growth rate exhibited a linear increase when the deposition pressure was lower than 24 mbar, while further increase of the pressure to 50 mbar was observed to have a negligible effect on the growth rate. The optical bandgap energy was estimated to be 1.81 ± 0.05 eV. The catalytic performance of copper oxide was evaluated for the deep oxidation of propene with online FTIR as the monitoring technique. The catalytic tests show that CuO films prepared on flexible substrates such as stainless steel mesh exhibit advantages for the catalytic oxidation of propene.

© 2013 Elsevier B.V. All rights reserved.

1. Introduction

Cupric oxide (CuO) is a semiconducting compound and has been widely exploited for a broad field of applications including semiconducting sensors [1], catalytic combustion [2–5], diodes [6] and lithium-copper oxide electrochemical cells [7]. In recent years, CuO has attracted considerable interest because of its high solar absorptance and low thermal emittance [8]. Its suitable optical properties (bandgap of 1.2–1.9 eV) make it a promising semiconductor for solar cell production [9]. It is reported to possess unusual antiferromagnetic properties [10]. Among the available transition metal oxides, CuO is unique as it has square planar coordination of copper by oxygen in the monoclinic structure. Transition metal oxides, such as Co_3O_4 and Mn_3O_4 , are effective catalysts for the oxidative destruction of volatile organic compounds (VOCs) [11]. However, not much is known concerning the abatement of VOCs with CuO [12–14]. As CuO is non-toxic and its constituents are abundantly available, the synthesis of CuO is considered an important topic of research for catalytic processes.

CuO has been prepared by various strategies, including precipitation [15], sol-gel [12,16,17], wet impregnation [4], chelating method [2], electrospinning [18], activated reactive evaporation [19], thermal oxidation [20,21], pulsed laser deposition [22] and molecular beam

epitaxy [23]. Until now, only a few reports are available regarding synthesis of CuO thin films by chemical vapor deposition (CVD) [24–27]. Compared to other methods, CVD is very attractive due to its low cost and the facile deposition process to control thickness and morphology of thin films on different substrates. In our recent work, pulsed spray evaporation (PSE) chemical vapor deposition (CVD) has been successfully involved to prepare spinels [11]. It exhibits excellent potential to synthesize active oxides such as CuO.

The present work is to provide an introduction of PSE-CVD to synthesize copper oxide under well-controlled conditions. Deposition pressures were optimized to obtain good growth rates. The deposited films were comprehensively characterized regarding structure, morphology, bandgap energy and thermal stability. The catalytic performance of the grown copper oxide on mesh of stainless steel was investigated for the deep oxidation of C_3H_6 .

2. Materials and methods

Copper oxide thin films were synthesized in a cold-wall stagnation point-flow CVD reactor employing a PSE unit for the delivery of the precursor liquid feedstock [11,28]. The experimental setup is shown in Fig. 1. Copper acetylacetonate ($\text{Cu}(\text{acac})_2$) was dissolved with a concentration of 2.5 mM in ethanol solution. The PSE delivery of the feedstock was achieved with a frequency of 4 Hz and a valve opening time of 7.0 ms. The feedstock, with a feeding rate of 0.83 mL/min, was injected as a fine spray into a 30-cm long evaporation chamber kept at 180 °C. The resulting vapor was transported to the deposition

* Corresponding author at: Institute of Engineering Thermophysics, Chinese Academy of Sciences, Beijing 100190, China. Tel.: +49 521 106 2199; fax: +49 521 106 6027.

E-mail address: zhenyu.tian@uni-bielefeld.de (Z.-Y. Tian).

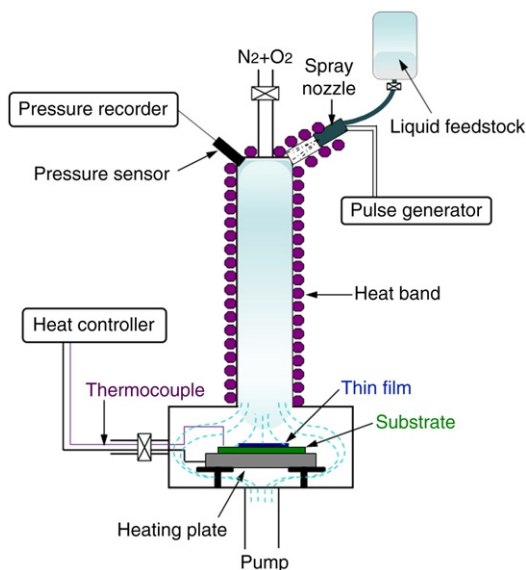


Fig. 1. Schematic diagram of the pulsed-spray evaporation chemical vapor deposition apparatus.

chamber kept at 200 °C, with N₂ and O₂ flow rates of 0.5 and 1.0 standard liter per minute (SLM), respectively. The total pressure in the reactor during deposition was 6–50 mbar. During the deposition process, planar glass, silicon, stainless steel and mesh of stainless steel substrates were heated to 300 °C using a flat resistive heater. The growth rate was estimated gravimetrically by measuring the weight change of the substrates with a microbalance (Mettler ME30).

The phase of the deposited films was identified by X-ray diffraction (XRD) using a Phillips X'Pert Pro MRD equipped with a Cu K α ($\lambda = 0.154056$ nm) radiation source and operated at 40 kV and 30 mA. Data were recorded in the 2θ range from 20° to 80°, with a step size of 0.05°. The thermal properties of the copper oxide films were also studied with emission FTIR spectroscopy under ambient atmosphere using a temperature-programmed mode. Helium ion microscopy (HIM) was used to examine the surface morphology of the obtained films. HIM was performed with a Carl Zeiss Orion Plus® instrument. The helium ion beam was operated at an acceleration voltage of 35 kV with a current between 0.3 and 1.7 pA and a 10- μ m aperture at Spot Control 4 to 5. Secondary electrons were collected by an Everhart-Thornley detector at 500 V grid voltage. The optical bandgap energies of the deposited samples were assessed using a Shimadzu UV-2501 PC UV-Vis spectrometer at room temperature.

The catalytic performance of the copper oxide films was investigated in a continuous-flow fixed-bed reactor at atmospheric pressure. The reactor was a quartz glass tube with 0.9 cm in diameter and 30 cm in length. The experimental setup has been described in detail elsewhere [29], and only a brief description is given here. A feed of argon gas containing 1% of C₃H₆ and 10% of O₂ was introduced into a tubular reactor at a total flow rate of 15 mL/min. The weight hourly space velocity (WHSV) of the feed gas was 90,000 mL/g_{cat} · h. Flow rates of gases were controlled by MKS mass-flow controllers, and the temperature of the reactor was raised with a ramp of 3 °C/min using an HT60 controller (Horst). The temperature of the mesh (with 10 mg coating or without coating) inside the reactor was measured with a K-type thermocouple and recorded by a digital thermometer (Greisinger GMH3250). The analysis of VOCs and products was conducted by online FTIR, and details of the data treatment are given in our recent work [11].

3. Results and discussion

3.1. Growth and structure

To obtain fast and homogeneous deposition of CuO, the growth kinetics was investigated by considering the effect of the deposition pressure. At 6 mbar, the CuO thin films were grown at a rate of 0.51 nm/min. This growth rate increased linearly with the pressure to reach 1.84 nm/min at 24 mbar. However, further increase of the deposition pressure to 50 mbar did not affect the growth rate, as shown in Fig. 2. The relatively low growth rate at lower pressure may result from lower amounts of oxygen and precursor adsorbing or residing on the substrate. The increase of the pressure may promote full surface coverage by adsorbing increasing amounts of Cu(acac)₂ and O₂, which could accelerate the nucleation step and result in a high growth rate. A similar pressure effect was observed by Condorelli et al. [27] who had investigated the kinetics of copper oxides films. Near 24 mbar, saturation of this adsorption is observed. All characterizations and tests in the following analysis were carried out with the samples obtained at 24 mbar.

The X-ray diffraction pattern of the as-synthesized thin film is displayed in Fig. 3. The well-defined diffraction peaks are observed at 2θ of 35.47°, 38.78°, 48.84°, 53.38°, 58.27° and 61.51°, which correspond to (002), (111), (-202), (020), (202) and (-113) orientations of CuO in the literature (JCPDS no. 45-0937). No characteristic peaks of any other impurities were observed in the XRD patterns, indicating the formation of monoclinic CuO phase. The lattice parameters of CuO determined here are $a = 4.6883$ Å, $b = 3.4229$ Å, $c = 5.1319$ Å, in good agreement with the literature [30]. The crystallite size and the micro-strain of CuO thin films were calculated to be 58 nm and 0.057 by applying Scherrer's formula: $D = 0.9\lambda/\beta \cos\theta$; and the equation $\varepsilon = \beta/2\cot\theta$ to the two most intense diffraction peaks, where $\lambda = 0.154056$ nm and where β and θ represent the full width at half maximum (FWHM) and diffraction angle of the observed peak, respectively.

To identify the formation mechanism of CuO in the PSE-CVD process, the substrate temperature was varied from 200 °C to 300 °C. Only Cu₂O was formed for substrate temperatures of 200 °C–250 °C; a mixture of Cu₂O and CuO was observed at 275 °C, and a unique phase of CuO was formed at 300 °C. Thus, the formation pathway of CuO in the current work can be illustrated with the combination of adsorption, dissociation and oxidation, as shown in Scheme 1. Firstly, both the evaporated Cu(acac)₂ and O₂ in the gas phase adsorb on the surface of the heated substrate, giving rise to adsorbed Cu(acac)₂ and O atoms. Secondly, the adsorbed Cu(acac)₂ dissociates and the adsorbed O atom reacts with the adsorbed ligands, producing surface Cu and by-products, respectively. Then, the surface Cu is oxidized to form Cu₂O and finally transformed to CuO. A similar adsorption

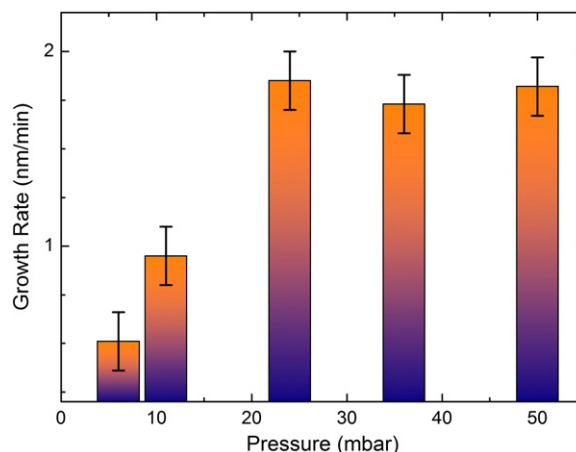


Fig. 2. Growth kinetics of copper oxide as a function of deposition pressure.

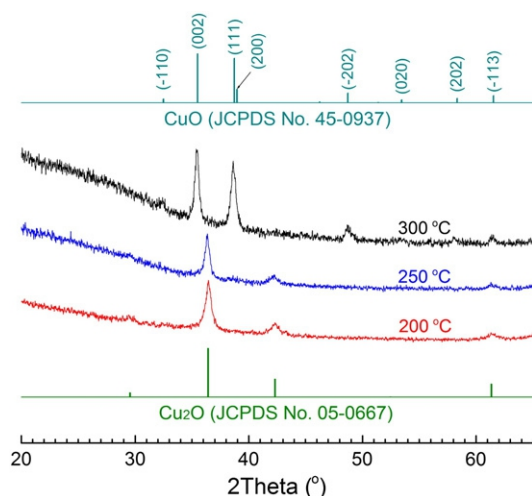


Fig. 3. XRD patterns of copper oxide films deposited on silicon at 200 °C, 250 °C and 300 °C.

process has been proposed previously [24,25]. However, a higher temperature (350 °C) was reported before for obtaining pure CuO [24]. According to Nair et al. [31], the Gibbs free energy of the conversion of Cu_2O to CuO is around $-3.73 \text{ kcal mol}^{-1}$. Moreover, Condorelli et al. [27] reported that Cu_2O could be formed at pressures lower than 6 mbar on substrates with 300 °C; pressures higher than 8 mbar would lead to the formation of CuO. It appears thus reasonable that CuO might be formed at 300 °C since the high oxygen pressure used in the present work could enhance the oxidation rate.

3.2. Morphology

To provide a deeper insight into the surface morphology and spatial organization of the obtained CuO thin film, HIM as a recently developed imaging technique that shares similarities with scanning electron microscopy (SEM) [32] was employed here. In HIM, a finely focused beam of helium ions with a diameter down to 0.35 nm is scanned over the sample, and the secondary electrons (SE) generated by the He^+ impact are detected. In SE imaging, the topology of the sample produces contrast as more electrons are ejected when the He^+ beam hits the sample at glancing incidence. The energy of the SE is very low, which results in a high surface sensitivity. HIM images of a representative CuO thin film are presented in Fig. 4. A smooth granular film with dome-top-shaped and loosely packed fine columnar grains was observed. The average size of grains observed with HIM is around 60 nm, which matches well with the calculation from Scherrer's equation utilizing XRD data. The HIM micrograph clearly shows the nanocrystalline nature of the CuO thin film prepared in the present work. Compared to the tightly packed columnar grains obtained with magnetron sputtering [33], the relatively loose surface structure may involve more oxygen vacancies, which would benefit its catalytic performance.

3.3. Optical properties

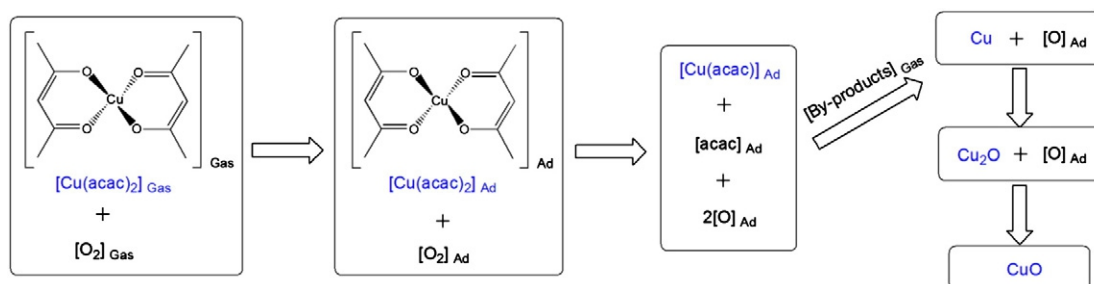
Fig. 5 displays the optical absorption spectrum of the deposited CuO thin film. As depicted in Fig. 5(a), a clear absorbance was observed in the region of 450–800 nm, which is consistent with the previous conclusion that CuO has a capability of absorbing light only below wavelengths of 400 nm [34]. The direct bandgap energy of the deposited CuO film can be calculated from the collected absorption spectra through Tauc's expression:

$$\alpha = \frac{A(h\nu - E_g)^{1/2}}{h\nu}$$

where E_g is the bandgap of the CuO film, α is the absorption coefficient, A is a constant relying on the refractive index and $h\nu$ is the photon energy. The corresponding plot of $(\alpha h\nu)^2$ as a function of $h\nu$ is shown in Fig. 5(b). The bandgap energy is estimated to be $1.81 \pm 0.05 \text{ eV}$ from extrapolation of the straight portion of this plot to the abscissa. This value is in good agreement with literature data for CuO thin films prepared via sol-gel techniques [17], chemical deposition [35], magnetron sputtering [36,37] and spray pyrolysis [38]. Table 1 compares the bandgap energy of CuO thin films in this work with those from other preparation methods. In the literature, CuO has been reported to exhibit both *p*-type (bandgap close to 2.1 eV, [19]) and *n*-type (bandgap between 1.3 and 1.5, [39]) properties. The presence of oxygen deficiencies in the preparation processes was proposed to play a significant role to endow the CuO with *n*-type conductivity [16,39]. Some values for the high bandgap of CuO were also reported, for example, 2.4 eV from reactive magnetron sputtering [40] and 2.1 eV from activated reactive evaporation [19]. According to Marabelli et al. [41], the bandgap is supposed to strongly depend on the sample preparation and on the measurement technique used. For instance, treatment at higher temperature may shift the bandgap energy to lower values [16,41]. The value reported here seems to be indicative of considerable *n*-type behavior, with potentially some contribution of *p*-type conductivity.

3.4. Thermal stability

A successful catalyst for high-temperature combustion should possess high thermal stability as well as high catalytic activity. To explore the potential application of the prepared CuO film in catalytic oxidation processes, the grown films were investigated in terms of their thermal stability. Emission FTIR spectroscopy was employed to perform the thermal stability test in air and at a rate of 5 °C/min. The stability was determined by integrating the intensity of the CuO peaks as a function of the temperature, a procedure from which the phase transformation is evident [11]. As displayed in the insert of Fig. 6, three bands centered at around 436, 495 and 596 cm^{-1} were distinguished at temperatures below 200 °C. Ethiraj and Kang [42] reported the same bands attributed to the A_u and B_u modes of CuO, with the latter two bands corresponding to the Cu-O stretching and vibration, respectively [43]. With the increase of the temperature to ~ 250 °C, another band located at



Scheme 1. Formation pathway of CuO in the PSE-CVD process with $\text{Cu}(\text{acac})_2$ as precursor.

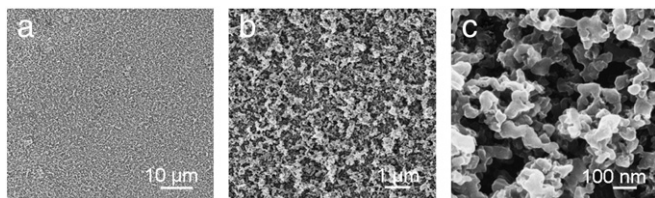


Fig. 4. HIM micrographs of representative CuO thin film deposited at 300 °C.

643 cm^{-1} appeared. This band has been attributed to the Cu(I)-O vibration mode in the Cu_2O phase by Iordanescu et al. [21]. In the temperature range of 250 °C–450 °C, a mixture of CuO and Cu_2O was observed. Up to a temperature of 450 °C, above which finally only a band of Cu_2O appears, CuO is thus thermally stable.

3.5. Catalytic performance

The catalytic performance of the CuO grown on mesh of stainless steel was evaluated for the complete oxidation of C_3H_6 in a flow reactor at atmospheric pressure. The background effect of the mesh element on the combustion process was examined by carrying out the oxidation of C_3H_6 on non-coated mesh under the same gas inlet conditions. Fig. 7 compares the temperature-dependent conversion of C_3H_6 to CO_2 as the final product and the associated CO production over CuO films and non-coated mesh. The conversion plots show clearly that CuO enables the total oxidation of C_3H_6 at lower temperatures relative to the non-coated mesh. In the presence of CuO, the consumption of propene became observable at about 190 °C and complete conversion was reached within 310 °C, while these two values are observed to shift by ~ 160 °C and ~ 440 °C, respectively, toward higher temperatures for the reaction on non-coated mesh. With CuO, no trace of CO was detected in the oxidation process. However, a significant amount of CO was formed in the reaction without catalyst, which

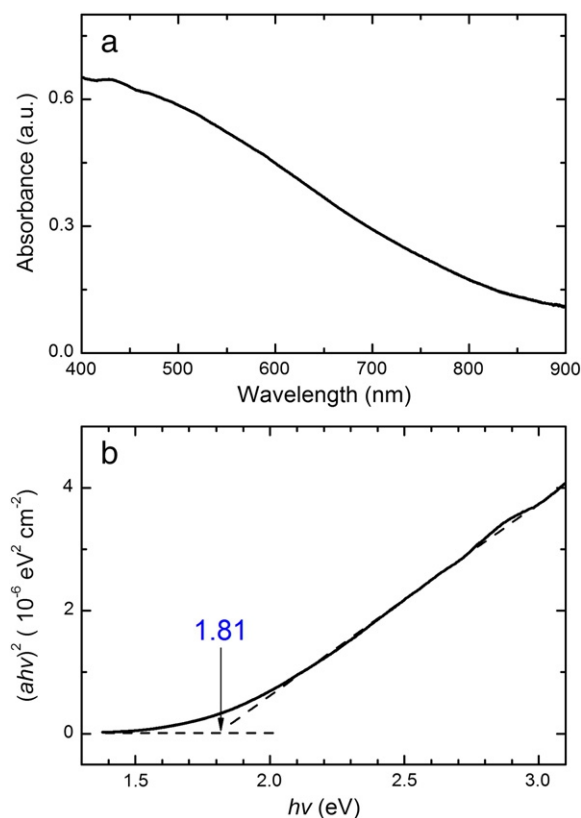


Fig. 5. UV-Vis absorption spectra (a) and $(\alpha h\nu)^2$ versus $h\nu$ of CuO films (b).

Table 1
Comparison of the bandgap energy (E_g) of CuO prepared with different methods.

Preparation method	E_g (eV)	Ref.
PSE-CVD	1.81	This work
Sol-gel	1.72–1.79	[17]
Sol-gel	1.46–1.64	[16]
Activated reactive evaporation	2.1	[19]
Reactive magnetron sputtering	2.4	[40]
Reactive magnetron sputtering	1.71–2.11	[36]
Chemical deposition	1.73	[35]
Chemical deposition	1.75	[31]
Spray pyrolysis	1.45–1.76	[38]
Radio frequency magnetron sputtering	1.96	[37]
Thermal oxidation	1.4–1.5	[20]

can be assigned to the partial oxidation reaction. It is worth noting that the catalytic oxidation of C_3H_6 under O_2 -rich conditions is tested to have no obvious effect on the catalyst structure by comparing the XRD spectra obtained before and after the catalytic tests.

The temperatures T_{10} , T_{50} and T_{90} , corresponding to the 10%, 50% and 90% C_3H_6 conversion, respectively, during the temperature-programmed reaction, were selected to compare the catalytic performance of the deposited CuO to that of other catalysts available in the literature for C_3H_6 oxidation. Table 2 summarizes the results and T_{50} is plotted in Fig. 8. As expected, all reactions with catalysts exhibit much higher activity than without catalyst. Compared to other active catalysts such as perovskites [44], Co_3O_4 [11,29,45] and Co-Mn binary oxides [11], CuO shows better performance for C_3H_6 oxidation, with a T_{50} of 272 °C. In contrast, T_{50} is observed to be 321 °C–354 °C for the reaction with Co_3O_4 /Co-Mn mixed oxides with different WHSV. $\text{La}_{1.7}\text{Sr}_{0.3}\text{CuO}_4\text{S}_{0.2}$ is also less active with T_{50} determined as 419 °C [44]. T_{50} for CuO in the present work is similar to that of $\text{Cu}_{0.72}\text{Co}_{2.28}\text{O}_4$ (275 °C) and $\text{Au}/\text{BaO}/\text{A}_2\text{O}_3$ (290 °C) [46–48], indicating that the as-prepared CuO features competitive activity to Co-Cu mixed oxides as well as to alkali-doped noble metals for the combustion of C_3H_6 . Based on the magnitude of T_{50} , the activity was found in an order of $\text{CuO} \geq \text{Cu}_{0.72}\text{Co}_{2.28}\text{O}_4 > \text{Au}/\text{BaO}/\text{A}_2\text{O}_3 > \text{Au}/\text{Rb}_2\text{O}/\text{A}_2\text{O}_3 > \text{Au}/\text{Rb}_2\text{O}/\text{A}_2\text{O}_3 \geq \text{Co}_{2.66}\text{Mn}_{0.34}\text{O}_4 > \text{Co}_3\text{O}_4 \geq \text{Au}/\text{A}_2\text{O}_3 = \text{Au}/\text{MgO}/\text{A}_2\text{O}_3 > \text{La}_{1.7}\text{Sr}_{0.3}\text{CuO}_4\text{S}_{0.2} > > \text{non-coated mesh}$.

With an Arrhenius expression for evaluation of the light-off profiles in the region where less than 15% of propene conversion was achieved, apparent activation energies (E_{appa}) were derived following [29]. Fig. 8 includes the comparison of these E_{appa} obtained in

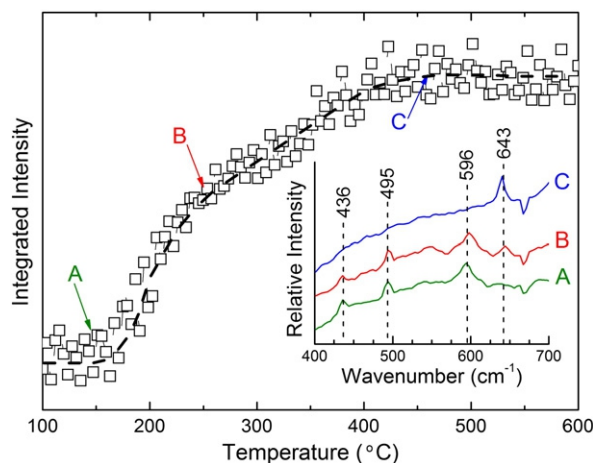


Fig. 6. Thermal stability of CuO with the emission FTIR spectroscopy. For example, spectra A, B and C were measured at 150 °C, 253 °C and 460 °C, respectively; integrated intensities from these spectra are plotted versus temperature, indicated by the arrows labelled A, B and C. Peaks from CuO are seen at 436, 495 and 596 cm^{-1} . The peak at 643 cm^{-1} , which is characteristic for Cu_2O , is the only feature remaining above 450 °C.

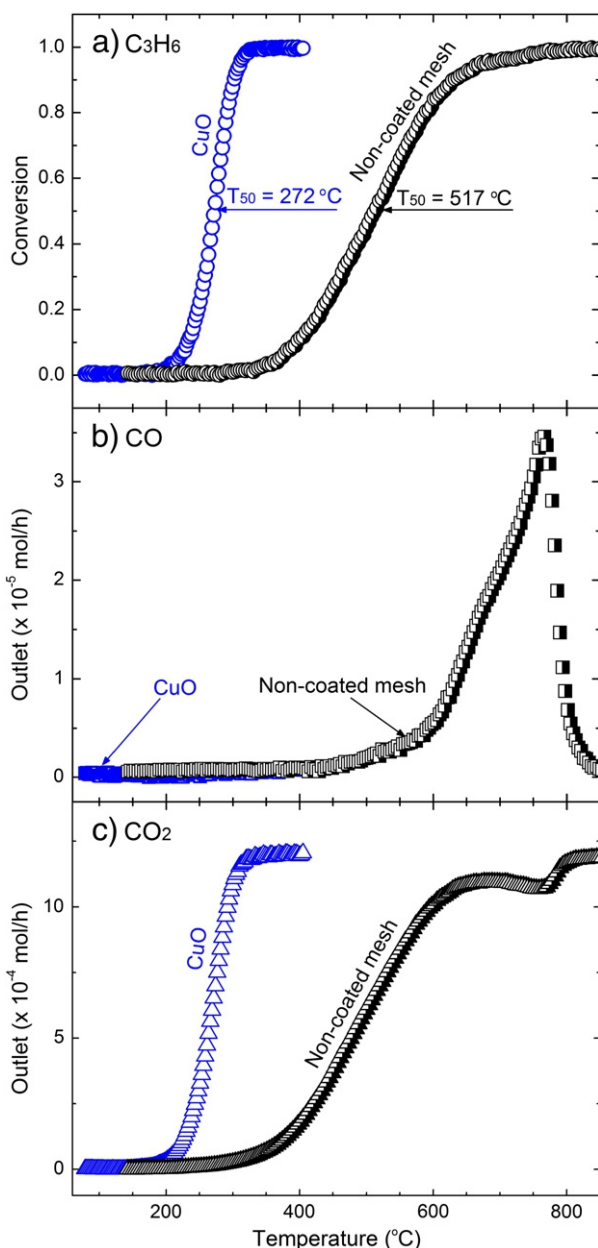


Fig. 7. Light-off curves for C_3H_6 oxidation: conversion of C_3H_6 (a); associated CO production (b) and CO_2 production (c) with CuO-coated and non-coated mesh.

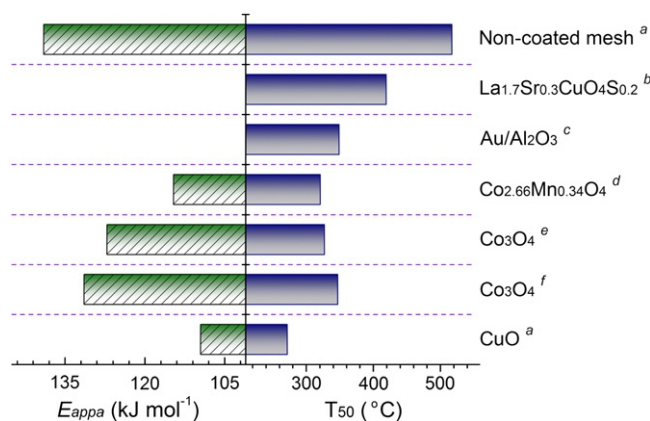


Fig. 8. T_{50} and apparent activation energy (E_{appa}) in the deep oxidation of C_3H_6 with different systems: ^a CuO and non-coated mesh in this work; ^b $La_{1.7}Sr_{0.3}CuO_4S_{0.2}$ [44]; ^c Au/ Al_2O_3 [46]; ^d $Co_{2.66}Mn_{0.34}O_4$ [11]; ^e Co_3O_4 [29]; ^f Co_3O_4 [45].

this work with our recent investigations of C_3H_6 oxidation with Co_3O_4 and Co-Mn mixed oxides. The reaction with CuO shows a relatively low activation energy ($109.5 \text{ kJ mol}^{-1}$). It increases to ~ 115 and $\sim 130 \text{ kJ mol}^{-1}$ for propene oxidation with $Co_{2.66}Mn_{0.34}O_4$ and Co_3O_4 , respectively. The non-catalyzed reaction gives an E_{appa} of $139.0 \text{ kJ mol}^{-1}$, which is higher than that with CuO.

According to Doornkamp and Ponc [49], the catalytic oxidation of hydrocarbons employing metal oxide catalysts such as CuO can proceed with the Mars–van Krevelen mechanism, and the C–H bond activation is related to the rate of oxidation for hydrocarbons. In the current case, a redox mechanism consisting of two steps, namely the reaction of C_3H_6 with the trapped or lattice oxygen, leading to CuO reduction and release of oxygen and formation of Cu_2O on the surface, and the re-oxidation of Cu_2O with oxygen to CuO can be assumed. It is well known that the performance of CuO catalysts in the combustion process of hydrocarbons and CO is associated with the reducibility of the catalysts [50–52]. This finding might be applicable to the CuO obtained with PSE-CVD, but further confirmation will be needed. Moreover, the catalytic activity could also benefit from the formation of oxygen-vacant sites in the redox mechanism, the importance of which was pointed out previously by Noller and Vinek [53], and the presence of which was confirmed in our previous work with PSE-CVD [11].

4. Conclusion

CuO thin films were prepared from $Cu(acac)_2$ by PSE-CVD, which is a facile approach to achieve a tailored control over film composition

Table 2
Comparison of the catalytic performance.

Material	Gas composition	WHSV ($\text{ml g}^{-1} \text{h}^{-1}$) ^a	T_{10} ($^{\circ}\text{C}$) ^b	T_{50} ($^{\circ}\text{C}$) ^b	T_{90} ($^{\circ}\text{C}$) ^b	Ref.
CuO	1% C_3H_6 /10% O_2 in Ar	75000	229	272	301	This work
Co_3O_4	1% C_3H_6 /10% O_2 in Ar	75000	306	347	396	[45]
Co_3O_4	2% C_3H_6 /20% O_2 in Ar	73000	293	327	356	[29]
Co_3O_4	2% C_3H_6 /20% O_2 in Ar	75000	325	354	385	[11]
$Co_{2.66}Mn_{0.34}O_4$	2% C_3H_6 /20% O_2 in Ar	75000	277	321	356	[11]
$Cu_{0.72}Co_{2.28}O_4$	13% C_3H_6 /52% O_2 in N_2	15000	230	275	>400	[48]
Au/ Al_2O_3	1.5% C_3H_6 /4% O_2 in He	22500	288	349	410	[46]
Au/ Al_2O_3	1% C_3H_6 /9% O_2 in He	219512	–	365	–	[47]
Au/BaO/ Al_2O_3	1% C_3H_6 /9% O_2 in He	250000	–	290	–	[47]
Au/Rb ₂ O/ Al_2O_3	1% C_3H_6 /9% O_2 in He	257143	–	307	–	[47]
Au/Li ₂ O/ Al_2O_3	1% C_3H_6 /9% O_2 in He	225000	–	327	–	[47]
Au/MgO/ Al_2O_3	1% C_3H_6 /9% O_2 in He	214286	–	359	–	[47]
$La_{1.7}Sr_{0.3}CuO_4S_{0.2}$	0.1% C_3H_6 /5% O_2 in N_2	30000	368	419	500	[44]
Non-coated mesh	1% C_3H_6 /10% O_2 in Ar	75000	398	517	629	This work

^a WHSV is weight hourly space velocity. ^b T_{10} , T_{50} and T_{90} refer to the temperatures at which 10%, 50% and 90% propene is converted, respectively.

and microstructure. With XRD, emission FTIR, HIM and UV-Vis spectroscopy, the structure, morphology, bandgap energy and thermal stability of the obtained thin film were comprehensively characterized. The structure study indicates that CuO was formed as the unique phase at 300 °C. The obtained CuO samples are thermally stable up to 450 °C and exhibit a bandgap of 1.81 ± 0.05 eV. The catalytic tests indicate that the as-deposited CuO is a very active catalyst in the oxidation of propene, with a performance comparable to that of supported noble metals. Compared to the reaction on non-coated substrate and on other transition metal oxides, the increased catalytic activity is attributed to the decrease of the activation energy with CuO.

Acknowledgment

The financial support from the Alexander von Humboldt Foundation and additional support from the Bielefeld University Nachwuchsfonds are gratefully acknowledged.

References

- [1] J.D. Choi, G.M. Choi, *Sensors Actuators B* 69 (2000) 120–126.
- [2] J.S. Yang, W.Y. Jung, W.K. Lee, K.T. Lim, M.S. Lee, S.S. Hong, *J. Nanosci. Nanotechnol.* 11 (2011) 1542–1546.
- [3] M. Haruta, H. Sano, *Int. J. Hydrogen Energy* 6 (1981) 601–608.
- [4] Y. Yang, X. Xu, K. Sun, *J. Hazard. Mater.* 139 (2007) 140–145.
- [5] S. Bennici, A. Gervasini, *Appl. Catal. B Environ.* 62 (2006) 336–344.
- [6] I.Y. Erdogan, O. Gullu, *J. Alloys Compd.* 492 (2010) 378–383.
- [7] L.B. Chen, N. Lu, C.M. Xu, H.C. Yu, T.H. Wang, *Electrochim. Acta* 54 (2009) 4198–4201.
- [8] A.N. Banerjee, K. Chattopadhyay, *Prog. Cryst. Growth Charact. Mater.* 50 (2005) 52–105.
- [9] S.C. Ray, *Sol. Energy Mater. Sol. Cells* 68 (2001) 307–312.
- [10] A.A. Eliseev, A.V. Lukashin, A.A. VCertegel, L.I. Heifets, A.I. Zhirov, Y.D. Tretyakov, *Mater. Res. Innovations* 3 (2000) 308–312.
- [11] Z.Y. Tian, P.H. Tchoua Ngamou, V. Vannier, K. Kohse-Höinghaus, N. Bahlawane, *Appl. Catal. B Environ.* 117–118 (2012) 125–134.
- [12] G.-H. Lee, M.S. Lee, G.-D. Lee, Y.-H. Kim, S.-S. Hong, *J. Ind. Eng. Chem.* 6 (2002) 572–577.
- [13] P.-O. Larsson, H. Berggren, A. Andersson, O. Augustsson, *Catal. Today* 35 (1997) 137–144.
- [14] E. Finocchio, R.J. Willey, G. Busca, V. Lorenzelli, *J. Chem. Soc. Faraday Trans.* 93 (1997) 175–180.
- [15] E. Koutsoukos, K. Nobe, University of California, Los Angeles, report No. 64-12, 1964.
- [16] D.M. Jundale, P.B. Joshi, S. Sen, V.B. Patil, *J. Mater. Sci: Mater. Electron.* 23 (2012) 1492–1499.
- [17] D. Chauhan, V.R. Satsangi, S. Dass, R. Shrivastav, *Bull. Mater. Sci.* 29 (2006) 709–716.
- [18] G.N.S. Vijayakumar, M. Rathnakumari, P. Sureshkumar, *Arch. Appl. Sci. Res.* 3 (2011) 514–525.
- [19] B. Balamurugan, B.R. Mehta, *Thin Solid Films* 396 (2001) 90–96.
- [20] G. Papadimitropoulos, N. Vourdas, V.Em. Vamvakas, D. Davazoglou, *Thin Solid Films* 515 (2006) 2428–2432.
- [21] C.R. Iordanescu, D. Tenciu, I.D. Feraru, A. Kiss, M. Bercu, D. Savastru, R. Notonier, C.E.A. Grigorescu, *Dig. J. Nanomater. Bios.* 6 (2011) 863–868.
- [22] W. Seiler, E. Millon, J. Perriere, R. Benzerga, C. Boulmer-Leborgne, *J. Cryst. Growth* 311 (2009) 3352–3358.
- [23] K.P. Muthe, J.C. Vyas, S.N. Narang, D.K. Aswal, S.K. Gupta, D. Bhattacharya, R. Pinto, G.P. Kothiyal, S.C. Sabharwal, *Thin Solid Films* 324 (1998) 37–43.
- [24] J. Medina-Valtierra, J. Ramirez-Ortiz, V.M. Arroyo-Rojas, F. Ruiz, *Appl. Catal. A Gen.* 238 (2003) 1–9.
- [25] G.G. Condorelli, G. Malandrino, I. Fragalà, *Chem. Mater.* 6 (1994) 1861–1866.
- [26] M. Ottosson, J.-O. Carlsson, *Surf. Coat. Technol.* 78 (1996) 263–273.
- [27] G.G. Condorelli, G. Malandrino, I.L. Fragalà, *Chem. Vap. Deposition* 5 (1999) 21–27.
- [28] N. Bahlawane, P.A. Premkumar, Z.Y. Tian, X. Hong, F. Qi, K. Kohse-Höinghaus, *Chem. Mater.* 22 (2010) 92–100.
- [29] Z.Y. Tian, N. Bahlawane, F. Qi, K. Kohse-Höinghaus, *Catal. Commun.* 11 (2009) 118–122.
- [30] A.Y. Oral, E. Mensur, M.H. Aslan, E. Basaran, *Mater. Chem. Phys.* 83 (2004) 140–144.
- [31] M.T.S. Nair, L. Guerrero, O.L. Arenas, P.K. Nair, *Appl. Surf. Sci.* 150 (1999) 143–151.
- [32] B.W. Ward, J.A. Notte, N.P. Economou, *J. Vac. Sci. Technol. B* 24 (2006) 2871–2874.
- [33] Y.-H. Chen, L.-C. Chang, M.-Y. Hsiao, J.-L. He, *Proc. Annu. Technol. Conf. Soc. Vac. Coaters* 54 (2011) 160–165.
- [34] D.A. Kumar, F.P. Xavier, J.M. Shyla, *Arch. Appl. Sci. Res.* 4 (2012) 2174–2183.
- [35] M.R. Johan, M.S.M. Suan, N.L. Hawari, H.A. Ching, *Int. J. Electrochem. Sci.* 6 (2011) 6094–6104.
- [36] J.F. Pierson, A. Thobor-Keck, A. Billard, *Appl. Surf. Sci.* 210 (2003) 359–367.
- [37] M.H.P. Reddy, J.F. Pierson, S. Ulthanna, *Phys. Status Solidi A* 7 (2012) 1279–1286.
- [38] A.S. Kumar, K. Perumal, P. Thirunavukkarasu, *Optoelectron. Adv. Mater.* 4 (2010) 831–833.
- [39] Y.S. Chaudhary, A. Agarwal, R. Shrivastav, V. Satsangi, S. Dass, *Int. J. Hydrogen Energy* 29 (2004) 131–134.
- [40] A.A. Ogwu, T.H. Darma, E. Bouquerel, *J. Achiev. Mater. Manuf. Eng.* 24 (2007) 172–177.
- [41] F. Marabelli, G.B. Parravicini, F. Salghetti-Drioli, *Phys. Rev. B* 52 (1995) 1433–1436.
- [42] A.S. Ethiraj, D.J. Kang, *Nanoscale Res. Lett.* 7 (2011) 70.
- [43] K. Kliche, Z.V. Popovic, *Phys. Rev. B* 42 (1990) 10060–10066.
- [44] M. Machida, K. Ochiai, K. Ito, K. Ikeue, *J. Catal.* 238 (2006) 58–66.
- [45] P. Mountapmbeme Kouotou, Z.Y. Tian, U. Mundloch, N. Bahlawane, K. Kohse-Höinghaus, *RSC Adv.* 2 (2012) 10809–10812.
- [46] S. Ivanova, C. Petit, V. Pitchon, *Gold Bull.* 39 (2006) 3–8.
- [47] A.C. Gluhoi, N. Bogdanichikova, B.E. Nieuwenhuys, *J. Catal.* 232 (2005) 96–101.
- [48] H. Baussart, R. Delobel, M. Le Bras, J.M. Leroy, *J. Chem. Soc. Faraday Trans.* 1 75 (1979) 1337–1345.
- [49] C. Doornkamp, V. Ponec, *J. Mol. Catal. A: Chem.* 162 (2000) 19–32.
- [50] V. Sánchez Escribano, C. del Hoyo Martínez, E. Fernández López, J.M. Gallardo Amores, G. Busca, *Catal. Commun.* 6 (2009) 861–864.
- [51] G. Sedmak, S. Hočevar, J. Levec, *J. Catal.* 222 (2004) 87–99.
- [52] H.H. Voge, C.R. Adams, *Catal. Relat. Subj.* 17 (1967) 151–221.
- [53] H. Noller, H. Vinek, *J. Mol. Catal.* 51 (1989) 285–294.

E) Publication 5

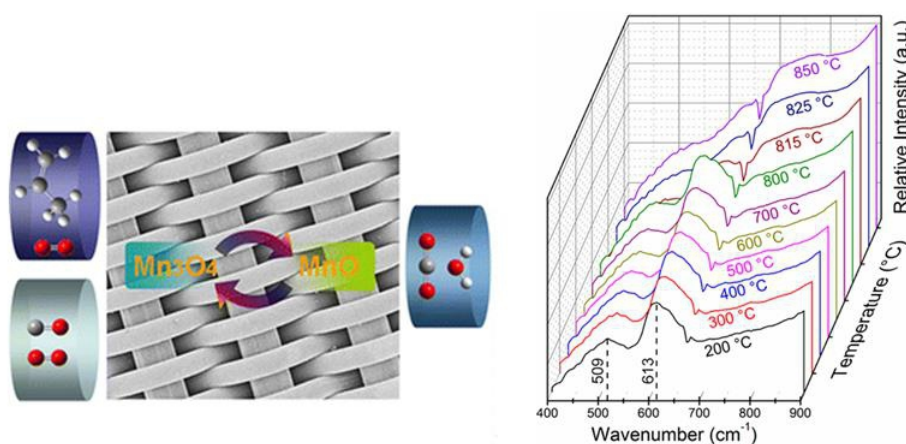
Zhen-Yu Tian, Patrick Mountapmbeme Kouotou, Naoufal Bahlawane, and Patrick Hervé

Tchoua Ngamou

Synthesis of the Catalytically Active Mn_3O_4 Spinel and Its Thermal Properties

Journal of Physical Chemistry C 117, 6218-6224, 2013

Graphical Abstract



Research Highlight

Tetragonal hausmannite (Mn_3O_4) was synthesized by pulsed-spray evaporation chemical vapor deposition (PSE-CVD) at moderate temperatures. The thermal properties of the obtained Mn_3O_4 thin films were evaluated with a newly developed in situ emission FTIR method. The performance of Mn_3O_4 grown on flexible stainless steel mesh substrates was investigated toward the oxidation of CO and C_3H_6 . X-ray diffraction (XRD) patterns, FTIR, and Raman spectroscopy reveal that only the single-phase tetragonal Mn_3O_4 spinel structure was obtained within the temperature range of 350-500 $^{\circ}\text{C}$. The as-deposited Mn_3O_4 is thermally stable up to 800 $^{\circ}\text{C}$, and its reduction plays a determinant role in the catalytic process. Compared to conventional powder catalysts, the combination of PSE-CVD, in situ emission FTIR, and the flexible substrate provides a novel tool for catalyst synthesis and the evaluation of the thermal properties and catalytic performance.

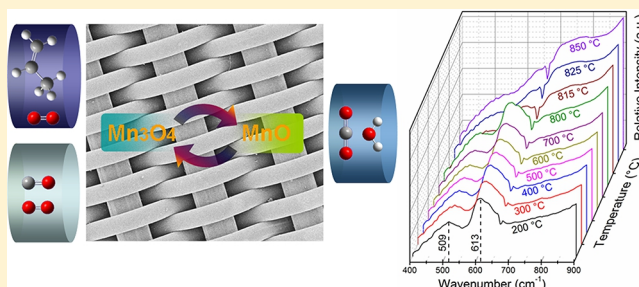
Synthesis of the Catalytically Active Mn_3O_4 Spinel and Its Thermal Properties

Zhen-Yu Tian,* Patrick Mountapmbeme Kouotou, Naoufal Bahlawane,[†]
and Patrick Hervé Tchoua Ngamou

Department of Chemistry, Bielefeld University, Universitätsstraße 25, D-33615 Bielefeld, Germany

S Supporting Information

ABSTRACT: Tetragonal hausmannite (Mn_3O_4) was synthesized by pulsed-spray evaporation chemical vapor deposition (PSE-CVD) at moderate temperatures. The thermal properties of the obtained Mn_3O_4 thin films were evaluated with a newly developed in situ emission FTIR method. The performance of Mn_3O_4 grown on flexible stainless steel mesh substrates was investigated toward the oxidation of CO and C_3H_6 . X-ray diffraction (XRD) patterns, FTIR, and Raman spectroscopy reveal that only the single-phase tetragonal Mn_3O_4 spinel structure was obtained within the temperature range of 350–500 °C. The as-deposited Mn_3O_4 is thermally stable up to 800 °C, and its reduction plays a determinant role in the catalytic process. Compared to conventional powder catalysts, the combination of PSE-CVD, in situ emission FTIR, and the flexible substrate provides a novel tool for catalyst synthesis and the evaluation of the thermal properties and catalytic performance.



1. INTRODUCTION

Transition metal oxides have been widely used in industrial applications as electrochemical, catalysis, magnetic cooling, optical, and recording devices.^{1–3} Among the transition metal oxides, Co_3O_4 , Mn_3O_4 , Fe_2O_3 , and CuO were identified as highly promising catalysts with good performances.^{4,5} Considering the availability and toxicity, Mn_3O_4 has captured a great deal of attention besides its unique physicochemical properties.^{6–8} Mn_3O_4 is known as a model spinel compound with tetragonal distortion, leading to the elongation of the cell along the c -axis ($a = b = 5.76 \text{ \AA}$, $c = 9.46 \text{ \AA}$) where Mn^{2+} ions occupy the tetrahedral sites and Mn^{3+} the octahedral sites. Mn_3O_4 has been implemented as a catalyst for the oxidation of methane and carbon monoxide (CO)^{10,11} and for the abatement of volatile organic compounds and waste gases.^{12–14}

Mn_3O_4 is commonly obtained by the high-temperature calcinations (>800 °C) of manganese powders or manganese oxides with a higher valence of Mn, hydroxides, and hydroxyoxides or oxysalts of Mn.^{15–17} Several attempts, i.e., solution-based methods relying on the precipitation of oxalate¹⁸ or nitrate,¹⁰ sol–gel with $\text{Mn}(\text{acac})_2$,¹⁹ ultrasonic-assisted route with $\text{MnCl}_2 \cdot 4\text{H}_2\text{O}$,²⁰ and atomic layer deposition with $\text{Mn}(\text{tmhd})_3$,²¹ have been performed to obtain Mn_3O_4 at moderate and low temperatures. It is worth mentioning that the literature cites only scarce attempts to investigate the comprehensive physicochemical properties including especially the thermal stability and redox behavior of Mn_3O_4 films²¹ that are highly relevant for catalytic applications. It is well-known that metal oxides such as spinel^{22,23} and perovskite oxides²⁴ can be easily prepared using pulsed-spray evaporation chemical

vapor deposition (PSE-CVD). With this method, the formation of solid film proceeds with liquid feedstock injection into an evaporation chamber, followed by the transportation and deposition on substrates. Compared to the above-mentioned methods, PSE-CVD shows many competitive advantages such as low cost, simplicity, high throughput, and accurate control of the thickness and morphology of the film. Moreover, PSE-CVD allows the use of a wide range of precursors and deposition of single-phase films with tailored composition on various kinds of supports. This deposition process is particularly useful to provide a catalytic activity to the inner walls of microreactors. In this contribution, flexible substrates such as mesh grids were coated with the catalytic thin films, which provide a catalytic bed that can be easily applied to any reactor shapes. This is particularly valuable as a model to evaluate the bulk contribution to the catalytic oxidation reactions.

In view of these considerations, the synthesis of Mn_3O_4 thin films with the PSE-CVD process and an attempt to understand the physicochemical properties have been undertaken in the present work. Growth kinetics with respect to the effect of the substrate temperature was optimized. The deposited films were comprehensively characterized by X-ray diffraction (XRD), FTIR, Raman, scanning electron microscopy (SEM), energy-dispersive spectrometry (EDS), and X-ray photoelectron spectroscopy (XPS). Thermal properties, such as the stability and redox behavior, were monitored with the in situ emission

Received: December 18, 2012

Revised: March 5, 2013

Published: March 6, 2013

FTIR technique. Catalytic performance of the obtained samples was explored for the deep oxidation of CO and propene (C_3H_6) in a fixed-bed quartz reactor under atmospheric pressure.

2. EXPERIMENTAL SECTION

2.1. Catalyst Preparation. The Mn_3O_4 CVD was performed in a cold-wall stagnation point-flow reactor employing a PSE unit for the delivery of the precursor liquid feedstock.^{24,25} $Mn(tmhd)_3$ was dissolved to a concentration of 5 mM in ethanol solution. The PSE delivery of the feedstock was achieved using a four-pinholes injector (Bosch) with a frequency of 4 Hz and an opening time of 2.5 ms. The feedstock was injected as a fine spray into a 30 cm long evaporation chamber kept at 180 °C. The resulting vapor was transported to the deposition chamber kept at 200 °C, with N_2/O_2 flow rates of 0.5/1.0 (11 mbar) slm. During the deposition process, planar glass, silicon, stainless steel, and mesh grid (stainless steel, SPW 40, 80 × 400, micrometer-retention 36–45 μm) substrates were heated to 350–500 °C using a flat resistive heater. The corresponding schematic diagram of the deposition process and typical deposition conditions are shown in Figure 1 and Table 1, respectively.

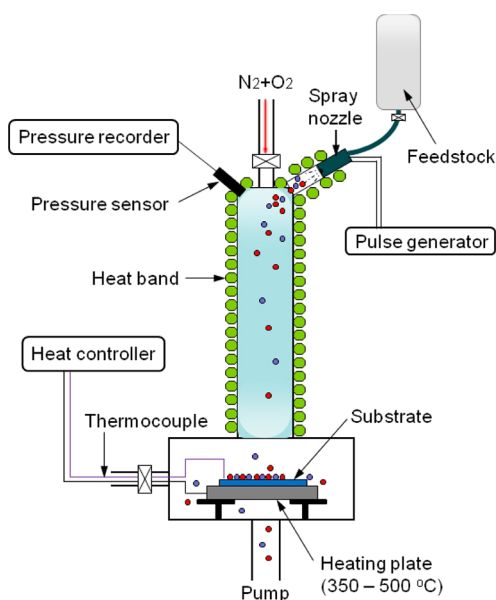


Figure 1. Schematic diagram of the pulsed-spray evaporation chemical vapor deposition apparatus.

2.2. Physicochemical Characterization. The deposited films obtained at different substrate temperatures were characterized by XRD using a Phillips XPert Pro MRD equipped with a $Cu K\alpha$ ($\lambda = 0.154056$ nm) radiation source and operated at 40 kV and 30 mA. The crystalline phases were monitored by referring to the powder XRD database (JCPDS). An FTIR spectrometer (Nicolet FTIR 5700) and a home-built Raman spectrometer,²⁶ both with spectral resolution of 4 cm^{-1} , were used to confirm the phases of the oxides. The morphology and composition of the deposited films were ascertained using SEM and EDS. The chemical states of the constituent elements were identified by XPS, using a Thermo Fisher Scientific apparatus with an $Al K\alpha$ line radiation source.

To investigate the thermal properties of the obtained films, a newly developed emission FTIR spectroscopy was adopted as

Table 1. Experimental Conditions for the Preparation of Mn_3O_4

precursor	$Mn(tmhd)_3$
solvent	ethanol
concentration	5 mM
delivery rate	0.83 $mL\ min^{-1}$
substrates	glass, silicon, planar/mesh of stainless steel
frequency and opening time	4 Hz, ~ 2 m/s
evaporation temperature	180 °C
transportation temperature	200 °C
substrate temperature	350–500 °C
system pressure (mbar)	11
carrier gas (N_2) (slm)	0.2
O_2 (slm)	1.0

an in situ analysis tool under temperature-programmed mode with a ramp of 5 °C/min.²⁷ A thermal emission (caused by gray body radiation) can be generated by heating a stainless steel sample with coated thin film. For spinels, these thermal emissions are superposed with characteristic bands, in the mid-infrared 500–700 cm^{-1} range. With emission FTIR, the changes of the materials' structures can be monitored by the integration of the intensity of their characteristic IR bands. In contrast to methods that rely on the detection of the tiny composition changes in the dynamically renewed gas, the emission FTIR relies on the in situ solid state analysis of the catalyst which enables a reliable characterization of samples with surfaces as small as 1 cm^2 .

2.3. Catalytic Test. The performance of the Mn_3O_4 film prepared at 400 °C was tested against the catalytic oxidation of CO and C_3H_6 at atmospheric pressure in a fixed-bed quartz reactor (9.0 mm inner diameter). The experimental setup is described in detail elsewhere,²² and a brief description is given here. A feed of argon gas containing 1% of CO or C_3H_6 and 10% of O_2 was introduced into a tubular reactor at a gas hourly space velocity (GHSV) of 75 000 $mL/g_{cat}\cdot h$. A flexible mesh grid was used as a structured catalytic bed. Flow rates of gases were controlled by MKS mass-flow controllers, whereas the temperature of the reactor was raised with a ramp of 5 °C/min using an HT60 controller (Horst). The temperature of the mesh inside the reactor was recorded using K-thermocouples and a digital thermometer (Greisinger GMH3250). The exhaust gas was analyzed by online FTIR, and details of the data treatment were described elsewhere.²⁷

3. RESULTS AND DISCUSSION

3.1. Phase Identification. The obtained films within the deposition temperature range 350–500 °C were analyzed by XRD, FTIR, and Raman spectroscopy. Figure 2 shows the XRD patterns of the Mn_3O_4 films grown on silicon. For all the prepared samples, diffraction peaks located at 29.05, 31.04, 32.5, 36.08, 36.5, 44.3, 51.1, 53.91, 58.5, 60.1, and 64.7° are observed in the patterns, which can be perfectly attributed to (112), (200), (103), (211), (202), (220), (105), (312), (321), (224), and (400) crystallographic planes of the tetragonal Mn_3O_4 (JCPDS Nr. 24-0734) structure. No characteristic peaks of impurity phases or other MnO_x phases are detected in the XRD patterns, indicating the high purity of the final films. The strong and sharp reflection peaks suggest that the as-prepared samples are well crystallized.

The crystallite size and microstrain of Mn_3O_4 thin films synthesized at different temperatures were estimated by

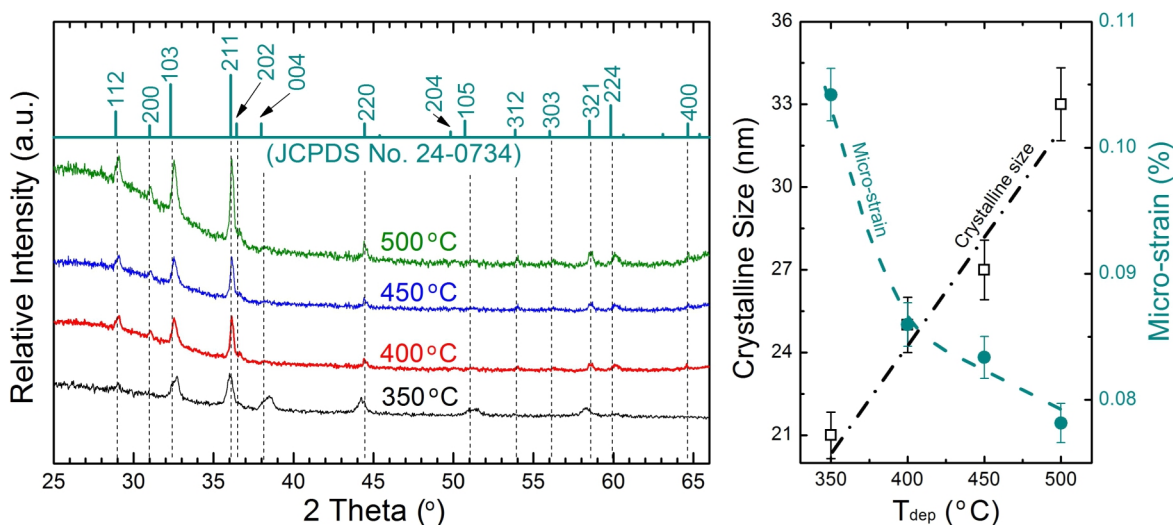


Figure 2. XRD patterns, crystalline sizes, and microstrains of Mn_3O_4 films (thickness of ~ 300 nm, corresponding to JCPDS card No. 34-0734) deposited on silicon at different substrate temperatures.

applying Scherrer's formula $D = 0.9\lambda/\beta \cos\theta$ and equation $\varepsilon = \beta/2 \cot\theta$ to the two most intense diffraction peaks, where $\lambda = 0.154056$ nm, and β and θ represent the full width at half-maximum (fwhm) and diffraction angle of the observed peak, respectively. As presented in Figure 2, with an increase of the deposition temperature from 350 to 500 °C, the average crystallite size increased from 21 to 33 nm, while the microstrain decreased from 0.104% to 0.078%. The larger crystallite size at higher deposition temperature could result from the faster growth of the crystallites, which is in agreement with the observed tendency of growth rate as a function of deposition temperature (see Table S1 in the Supporting Information (SI)). The decrease of the microstrain from 350 to 450 °C might be correlated with a decrease of the grain boundary density due to the increase in the crystallite size with increasing temperature. The strain may result from the presence of native imperfections such as vacancies and site disorders during the deposition process. It should be noted that the microstrain of the samples prepared at 400 °C is relatively smaller than that deposited at 350 °C. A further increase of the deposition temperature to 450 and 500 °C was not so sensitive to the decrease of microstrain. On the basis of this consideration the deposition at 400 °C was judged suitable for the synthesis of Mn_3O_4 thin film.

The lattice parameter and distortion parameter (D_p) of the Mn_3O_4 films are listed in Table S1 (see SI). The distortion variation is defined as the ratio of c/a . In general, all films have the lattice constants $a = b$ equal to 0.576 nm and $D_p = 1.64$ –1.65, demonstrating that the lattice constant and D_p are not sensitive to the substrate temperature within the temperature range of 350–500 °C. Comparison of the lattice constants and D_p with literature values for bulk Mn_3O_4 obtained by one-pot synthesis,²⁸ plasma-assisted molecular beam epitaxy,²⁹ and calcination³⁰ methods shows good agreement.

FTIR emission and Raman spectroscopy were also used to confirm the phase of hausmannite Mn_3O_4 . As shown in Figure 3, the IR and Raman spectra of the as-prepared Mn_3O_4 films reveal that the substrate temperature has a minor effect on the peaks. The FTIR spectra indicate two characteristic emission bands with maxima at 613 and 509 cm^{-1} , which are assigned to the coupling between Mn–O stretching modes of tetrahedral

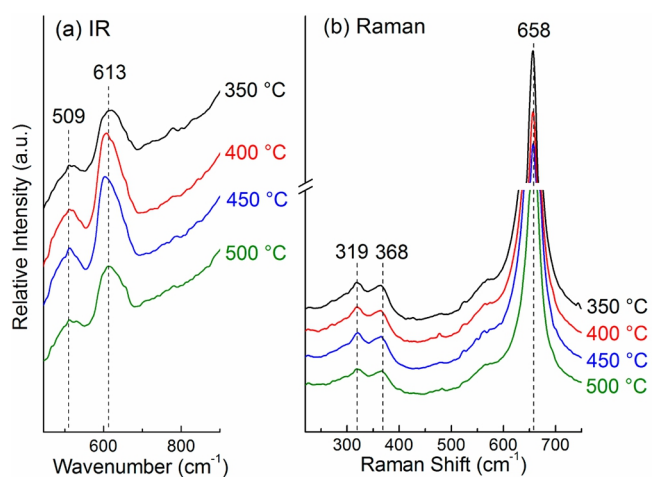


Figure 3. Effect of the growth temperature on the emission FTIR and Raman spectra.

and octahedral sites.^{31,32} Three strong peaks located at around 658, 368, and 319 cm^{-1} are observed in the Raman scattering spectra, which are consistent with the reported A_{1g} , T_{2g} , and E_g active modes of Mn_3O_4 .^{33,34} The strong peak at 658 cm^{-1} is characteristic of hausmannite with a spinel structure, corresponding to the Mn–O stretching vibration of divalent manganese ions in the tetrahedral coordination. These observations confirm that no secondary phase was formed, which further supports the XRD result. On the basis of the structural studies, Mn_3O_4 can be easily grown, irrespective of the substrate temperature in the 350–500 °C range. Deposition at 400 °C was indicated to be representative and was used for the following characterization and tests.

3.2. Microstructural Studies. SEM inspection was carried out to examine the morphology of the as-prepared samples. Figure 4 shows the representative micrographs recorded for the Mn_3O_4 spinels deposited on a mesh grid. The substrates are composed of a woven structure (Figure 4a), and the coating is homogeneous (Figure 4b). The surface area is estimated to be 3.65 m^2/g (see SI). The high-magnification micrograph of the grown films (Figure 4c) exhibits grain sizes of 25 nm, which agrees with the crystallite size obtained by XRD measurement.

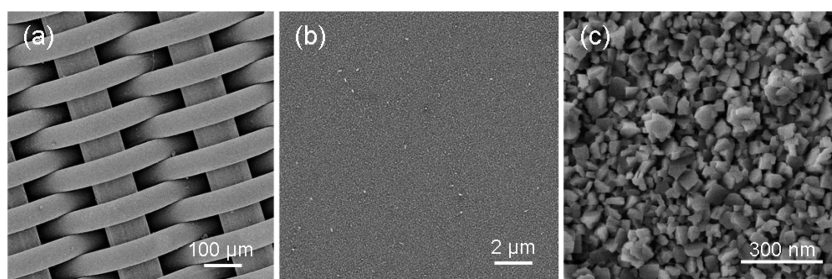


Figure 4. Typical SEM images of Mn_3O_4 thin film obtained at $400\text{ }^\circ\text{C}$ on a mesh grid.

Figure 4c also reveals the presence of some spherical particles, which could be due to Ostwald ripening.³⁵ EDS analysis (see Figure S1 in the SI) of the samples shows that the average O:Mn ratio is close to 4:3, which confirms the formation of Mn_3O_4 products in the deposition process.

Ex situ XPS was also used to characterize the surface composition of the Mn_3O_4 films, as indicated in Figure 5. The

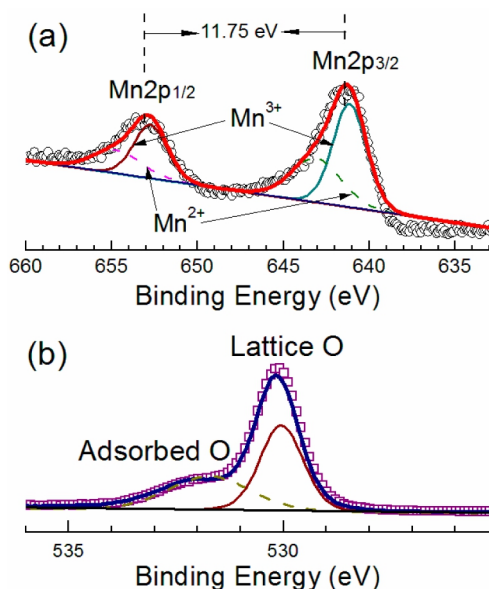


Figure 5. XPS analysis of the Mn_3O_4 samples: fitted Mn $2p_{1/2}$ and Mn $2p_{3/2}$ photoelectron peaks (a) and O_{1s} photoelectron peaks (b).

measurement was performed with reference to the C 1s binding energy (284.7 eV) as an internal standard. Elemental analysis was achieved with the same procedure as in our recent work.²⁷ It can be observed that the Mn 2p peak consists of two main spin-orbital lines. The Mn $2p_{3/2}$ peak is centered at 641.38 eV and the Mn $2p_{1/2}$ peak at 653.13 eV , with a splitting of 11.75 eV , which is in good harmony with literature values.^{27,36–38} The Mn 2p spectrum was deconvoluted as two pairs of doublets: 641.16 and 643.03 eV , 652.71 and 654.58 eV , corresponding to $\text{Mn}^{3+} 2p_{3/2}$ and $\text{Mn}^{2+} 2p_{3/2}$, $\text{Mn}^{3+} 2p_{1/2}$ and $\text{Mn}^{2+} 2p_{1/2}$, respectively. The calculated ratio of $\text{Mn}^{2+}:\text{Mn}^{3+}$ in Figure 6(a) is around 1:2, which is in good agreement with a previously reported value.³⁹ An asymmetric two-band structure is observed in the O 1s spectra. It is resolved into two components, corresponding to the binding energies of 530.14 and 532.12 eV , respectively. The first peak is characteristic of the lattice oxygen of Mn_3O_4 , and the second peak is assigned to the physisorbed, chemisorbed, or dissociated oxygen or hydroxyl species in poor electrical contact with the surface.^{40,41} On the basis of the XPS

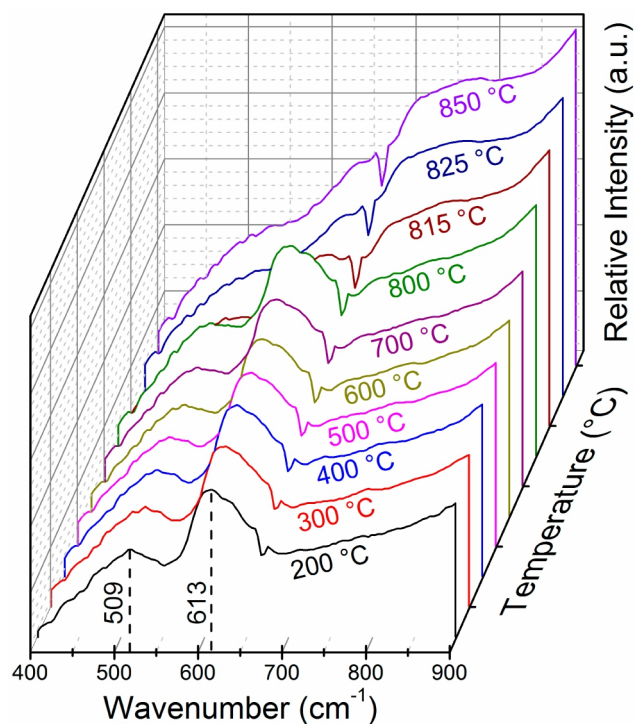


Figure 6. Thermal stability of the Mn_3O_4 film obtained on planar stainless steel with a thickness of 300 nm .

results, the O/Mn ratio is calculated to be 1.38. This ratio is a little larger than that estimated from EDS studies, which is due to the strong contribution of the surface oxygen in the XPS measurement.

3.3. Thermal and Redox Properties. To explore their potential application in catalytic oxidation processes, the grown films were investigated in terms of thermal stability. As the results are quite similar, only the sample prepared at $400\text{ }^\circ\text{C}$ is shown here as a representative. Emission FTIR spectroscopy was employed to perform the thermal stability test in air and at a rate of $5\text{ }^\circ\text{C}/\text{min}$. The lattice stability is determined by integrating the intensity of the characteristic peaks of the spinel as a function of the temperature which reflects the phase transformation.²⁷ As depicted in Figure 6, the two bands centered at around 513 and 609 cm^{-1} were clearly seen at temperatures below $800\text{ }^\circ\text{C}$. These bands disappeared with further increase of the temperature, indicating that the as-prepared Mn_3O_4 is thermally stable up to $800\text{ }^\circ\text{C}$. This limit could be associated with the oxidation of Mn^{2+} ions under air condition.⁴² Compared to other active transition metal oxides such as CuO ,⁴³ Co_3O_4 ,²⁷ and Fe_2O_3 ,^{44,45} the Mn_3O_4 film

synthesized by PSE-CVD shows the highest potential for high-temperature catalytic applications.

The temperature-programmed reduction (TPR) and re-oxidation (TPO) were carried out with emission FTIR as an in situ monitoring technique, using 5% of H₂ or O₂ in Ar (0.05 L/min). Figure 7a summarizes the redox behavior of the Mn₃O₄

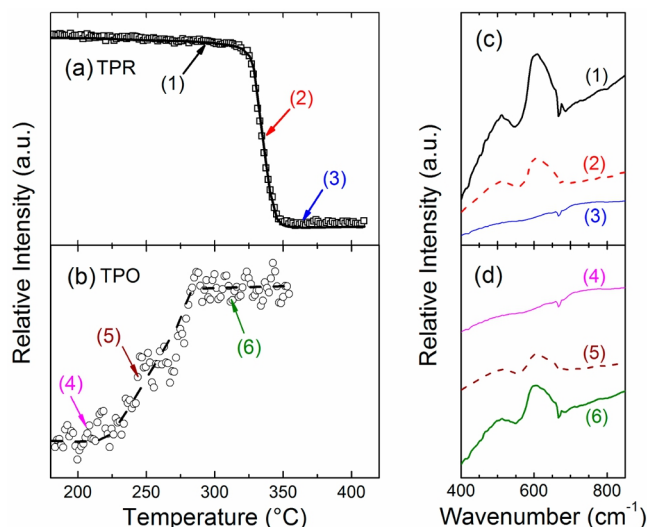


Figure 7. Redox behavior of the Mn₃O₄ film obtained on planar stainless steel with a thickness of 300 nm.

spinel. The integrated intensity of the typical feature of the Mn₃O₄ IR bands as a function of temperature in the TPR process is presented in Figure 7a. With the increase of the temperature (Figure 7b), the two bands tend to show a continuous redshift, and a weak band at around 711 cm⁻¹ is visible, consistent with the reduction scheme: Mn₃O₄ + H₂ → 3MnO + H₂O.⁴⁶ Figure 7c presents the TPO profile of Mn₃O₄, and Figure 7d demonstrates the recovery of the spinel structure in the reoxidation process. The results reveal that the reduction occurs at 315 °C, and the complete reduction happens at 350 °C. The reoxidation initiates at ~206 °C, and the films are completely recovered at 285 °C, indicating that the reduction step may play a limiting role in the catalytic oxidation process. Compared to the active Co₃O₄ reported in our recent work,²⁷ Mn₃O₄ is less reducible but is advantageously easier to reoxidize/recover. According to the magnitude of T₅₀, at which 50% of the catalyst is reduced or reoxidized, Mn₃O₄ is expected to be an active catalyst at lower temperature.

3.4. Catalytic Performance. As Mn₃O₄ films deposited at different temperatures showed a quite similar thermal stability, the catalytic properties were studied only for the sample prepared at relatively low temperature (400 °C). The catalytic performance was investigated with respect to the total oxidation of CO and C₃H₆ at atmospheric pressure in comparison with that of the noncoated mesh, as summarized in Figure 8. The full comparison of the reactants and products is given in Figures S3 and S4 in the SI. It is worth noting that the catalytic oxidation of CO and C₃H₆ under oxygen-rich conditions is observed to have no obvious effect on the catalyst or surface ionic states by checking the obtained XRD and XPS spectra before and after the catalytic tests.

The results of CO oxidation with and without Mn₃O₄ are presented in Figure 8a. In the presence of Mn₃O₄, the conversion of CO becomes observable at 190 °C, and complete

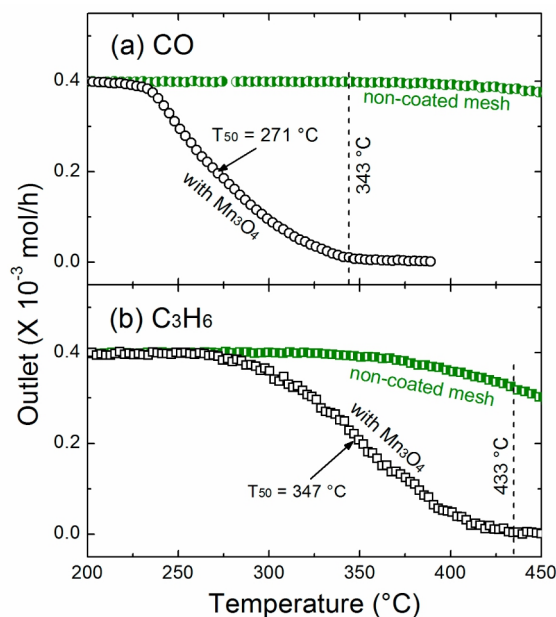


Figure 8. Catalytic test of CO (a) and C₃H₆ (b) oxidation with Mn₃O₄ at a GHSV of 75 000 mL/g_{cat}·h. Deep oxidation of CO and C₃H₆ was performed on noncoated mesh as a reference.

conversion occurs at 343 °C. These temperatures shifted, respectively, to 280 and 820 °C (see Figure S3, SI) for experiment without Mn₃O₄. In contrast, CO oxidation over manganese oxides (MnO_x, MnO₂, and Mn₂O₃) prepared by precipitation, as reported by Iablokov et al.,¹⁸ was found to present T₂₅ (temperature at 25% of CO conversion) at 298 °C over MnO_x,¹⁸ which is higher than the value (250 °C) obtained with Mn₃O₄ in the present work. Moreover, some other active metal oxides such as Co₃O₄,^{47,48} CeO₂,⁴⁹ and Al₂O₃⁴⁹ were reported to have T₉₀ (90% CO conversion) at 350, 374, and 394 °C, respectively, demonstrating that the obtained Mn₃O₄ in the present work is highly active in the deep oxidation of CO.

More reliable comparison of the catalytic performance of Mn₃O₄ with other manganese oxides reported in the literature was based on the reaction rate values corresponding to T₅₀ (50% CO conversion). In this work, T₅₀ is observed at 271 °C with a reaction rate of 4.17 μmol_{CO}/g·s. This rate is in good agreement with the literature values reported for those using Mn₂O₃^{50–52} and MnO₂.⁵³ However, T₅₀ is situated at about 130–170 °C lower temperatures than those reported before. The abundance of adsorbed oxygen, revealed in the XPS results, can play a key role in the oxidation process. Furthermore, the application of an Arrhenius equation at a low conversion range (<5%) allows the extraction of apparent activation energy values of E_a = 63.0 and 84.7 kJ/mol using light-off curves obtained in the presence and absence of Mn₃O₄ catalyst, respectively.

Figure 8b compares the outlet profiles of C₃H₆ in the oxidation of C₃H₆ with Mn₃O₄ and that of blank experiment carried out with noncoated mesh. The Mn₃O₄ sample exhibits much higher activity than the planar steel mesh without catalyst. It is observed that the conversion of C₃H₆ on Mn₃O₄ becomes detectable at 220 °C, and conversion of C₃H₆ approaches 100% at 433 °C. However, the oxidation of C₃H₆ on noncoated mesh starts at around 290 °C, and a temperature as high as 821 °C (see Figure S4, SI) is required for complete conversion of C₃H₆. Note that at low C₃H₆ conversions the

main product is CO₂, but a trace of CO peaking at 769 °C (Figure S4, SI) is formed on noncoated mesh, which results from partial oxidation. However, except CO₂ and water, no other byproducts were detected in the presence of Mn₃O₄, indicating that Mn₃O₄ is effective to reduce CO emission.

The obtained value of T_{50} (347 °C) in this work for the reaction with pure Mn₃O₄ was found to be quite similar to the T_{50} values reported for C₃H₆ oxidation with other systems, such as Mn₃O₄,¹² Co–Mn mixed oxides in our recent work,²⁷ and alkali-doped Au/Al₂O₃ catalysts.⁵⁴ Of interest, the relatively low E_a (62.8 kJ/mol) is obtained in this study as compared to those reported in the literature (80.3,¹² 114.59,²⁷ and 61–67 kJ/mol⁵⁴). It should be noted that without Mn₃O₄ coating 50% C₃H₆ conversion is reached at 606 °C with an activation energy of 109.1 kJ/mol.

The catalytic oxidation of CO and C₃H₆ over Mn₃O₄ follows likely the Mars–van Krevelen (MvK) mechanism which involves reversible reduction–reoxidation steps of the lattice oxygen atoms. As reported, trapped oxygen is apparently released with the increase of the temperature, and Mn₃O₄ tends to be reduced through the subsurface oxidation of CO or C₃H₆ with the lattice or surface oxygen. Subsequently, the reduced metal oxide site is reoxidized by the atmospheric O₂. According to the redox results, Mn₃O₄ is easier to be reoxidized than to be reduced, demonstrating that the reduction step could play a crucial role in the kinetics of the catalytic oxidation process. The performance of manganese catalysts in the oxidation process of volatile organic compounds has also been reported to be associated with their reducibility.^{55,56} Moreover, the surface oxygen revealed by the XPS results can also contribute to the activity of Mn₃O₄.

4. CONCLUSIONS

In summary, PSE-CVD was utilized to synthesize hausmannite (Mn₃O₄). The as-prepared samples were characterized in terms of thermal properties with a newly developed in situ emission FTIR spectroscopy. It was found that all obtained samples were tetragonal Mn₃O₄, irrespective of the substrate temperature within the range of 350–500 °C. The catalytic tests indicate that the use of Mn₃O₄ can initiate CO and C₃H₆ oxidation at lower temperatures, with higher selectivity toward CO₂ which may help prevent CO production during the oxidation of C₃H₆. Compared to our recent study of Co–Mn mixed oxides, Mn₃O₄ shows a high thermal stability up to 800 °C, high reducibility, and reoxidative regeneration at low temperatures.

■ ASSOCIATED CONTENT

Supporting Information

Characterization, catalytic test results, and temperature profiles. This material is available free of charge via the Internet at <http://pubs.acs.org>.

■ AUTHOR INFORMATION

Corresponding Author

*Tel.: +49 5211062199. Fax: +49 5211066027. E-mail: zhenyu.tian@uni-bielefeld.de.

Present Address

†Nanomaterials Research Unit, SAM Department, Centre de Recherche Public - Gabriel Lippmann, L-4422 Belvaux, Luxembourg.

Notes

The authors declare no competing financial interest.

■ ACKNOWLEDGMENTS

Dr. Tian would like to acknowledge the support of the Alexander von Humboldt Foundation for his research fellowship and additional support by the Bielefelder Nachwuchsfonds. Mr. Mountapbeme Kouotou thanks the Deutscher Akademischer Austausch Dienst (DAAD) for his research fellowship. The authors thank Prof. Katharina Kohse-Höinghaus for helpful discussion and Prof. Thomas Hellweg for access to the SEM and EDS measurements.

■ REFERENCES

- (1) Huang, Y. W.; Wu, C. H.; Aronstam, R. S. *Materials* **2010**, *3*, 4842–4859.
- (2) Tian, Z. R.; Tong, W.; Wang, J. Y.; Duan, N. G.; Krishnan, V. V.; Suib, S. L. *Science* **1997**, *276*, 926–930.
- (3) Li, Z. Q.; Liu, N. N.; Wang, X. K.; Wang, C. B.; Qi, Y. X.; Yin, L. W. *J. Mater. Chem.* **2012**, *22*, 16640–16648.
- (4) Xie, X. W.; Li, Y.; Liu, Z. Q.; Haruta, M.; Shen, W. J. *Nature* **2009**, *458*, 746–749.
- (5) Hu, L. H.; Peng, Q.; Li, Y. D. *J. Am. Chem. Soc.* **2008**, *130*, 16136–16137.
- (6) Li, Y.; Tan, H.; Yang, X.-Y.; Goris, B.; Verbeeck, J.; Bals, S.; Colson, P.; Cloots, R.; Tendeloo, G. V.; Su, B.-L. *Small* **2011**, *7*, 475–483.
- (7) Li, P.; Nan, C. Y.; Wei, Z.; Lu, J.; Peng, Q.; Li, Y. D. *Chem. Mater.* **2010**, *22*, 4232–4236.
- (8) Lv, H.; Yao, M. G.; Li, Q. J.; Li, Z. P.; Liu, B.; Liu, R.; Lu, S. C.; Li, D. M.; Mao, J.; Ji, X. L.; Liu, J.; Chen, Z. Q.; Zou, B.; Cui, T.; Liu, B. B. *J. Phys. Chem. C* **2012**, *116*, 2165–2171.
- (9) Xu, H. Y.; Xu, S. L.; Wang, H.; Yan, H. J. *Electrochem. Soc.* **2005**, *152*, C803–C807.
- (10) Stobbe, E. R.; Boer, B. A. de; Geus, J. W. *Catal. Today* **1999**, *47*, 161–167.
- (11) Zaki, M. I.; Hasan, M. A.; Pasupulety, L.; Kumari, K. *Thermochim. Acta* **1998**, *311*, 97–103.
- (12) Baldi, M.; Finocchio, E.; Milella, F.; Busca, G. *Appl. Catal. B: Environ.* **1998**, *16*, 43–51.
- (13) Baldi, M.; Finocchio, E.; Milella, F.; Busca, G. *Appl. Catal. A: Gen.* **1998**, *173*, 61–74.
- (14) Li, X.; Zhou, L.; Gao, J.; Miao, H.; Zhang, H.; Xu, J. *Powder Technol.* **2009**, *190*, 324–326.
- (15) Chang, Y. Q.; Xu, X. Y.; Luo, X. H.; Chen, C. P.; Yu, D. P. *J. Cryst. Growth* **2004**, *264*, 232–236.
- (16) Du, J.; Gao, Y. Q.; Chai, L. L.; Zou, G. F.; Li, Y.; Qian, Y. T. *Nanotechnology* **2006**, *17*, 4923–4928.
- (17) Sagheer, F. A. Al; Hasan, M. A.; Pasupulety, L.; Zaki, M. I. *J. Mater. Sci. Lett.* **1999**, *18*, 209–211.
- (18) Iablokov, V.; Frey, K.; Geszti, O.; Kruse, N. *Catal. Lett.* **2010**, *134*, 210–216.
- (19) Seo, W. S.; Jo, H. H.; Lee, K.; Kim, B.; Oh, S. J.; Park, J. T. *Angew. Chem., Int. Ed.* **2004**, *43*, 1115–1117.
- (20) Lei, S. J.; Tang, K. B.; Fang, Z.; Zheng, H. G. *Cryst. Growth Des.* **2006**, *6*, 1757–1760.
- (21) Nilsen, O.; Fjellvåg, H.; Kjekshus, A. *Thin Solid Films* **2003**, *444*, 44–51.
- (22) Tian, Z. Y.; Bahlawane, N.; Qi, F.; Kohse-Höinghaus, K. *Catal. Commun.* **2009**, *11*, 118–122.
- (23) Bahlawane, N. *Appl. Catal. B: Environ.* **2006**, *67*, 168–176.
- (24) Tchoua Ngamou, P. H.; Bahlawane, N. *Chem. Mater.* **2010**, *22*, 4158–4165.
- (25) Bahlawane, N.; Premkumar, P. A.; Tian, Z. Y.; Hong, X.; Qi, F.; Kohse-Höinghaus, K. *Chem. Mater.* **2010**, *22*, 92–100.
- (26) Vannier, V.; Schenk, M.; Kohse-Höinghaus, K.; Bahlawane, N. *J. Mater. Sci.* **2012**, *47*, 1348–1353.
- (27) Tian, Z. Y.; Tchoua Ngamou, P. H.; Vannier, V.; Kohse-Höinghaus, K.; Bahlawane, N. *Appl. Catal. B: Environ.* **2012**, *117–118*, 125–134.

- (28) Zhang, P. Q.; Zhan, Y. G.; Cai, B. X.; Hao, C. C.; Wang, J.; Liu, C. X.; Meng, Z. J.; Yin, Z. L.; Chen, Q. Y. *Nano Res.* **2010**, *3*, 235–243.
- (29) Guo, L. W.; Peng, D. L.; Makino, H.; Inaba, K.; Ko, H. J.; Sumiyama, K.; Yao, T. J. *Magn. Magn. Mater.* **2000**, *213*, 321–325.
- (30) Liu, Y.; Liu, Z.; Wang, G. *Appl. Phys. A: Mater. Sci. Process.* **2003**, *76*, 1117–1120.
- (31) Askarinejad, A.; Morsali, A. *Ultrason. Sonochem.* **2009**, *16*, 124–131.
- (32) Zapata, B.; Valenzuela, M. A.; Bosch, P.; Fetter, G.; Córdova, I.; Flores, S. O.; Vázquez, A. J. *Metastable Nanocryst. Mater.* **2004**, *20–21*, 163–168.
- (33) Kim, M.; Chen, X. M.; Fradkin, E.; Abbamonte, P.; Cooper, S. L. *Phys. Rev. Lett.* **2010**, *105*, 026402.
- (34) Yang, L. X.; Zhu, Y. J.; Tong, H.; Wang, W. W.; Cheng, G. F. J. *Solid State Chem.* **2006**, *179*, 1225–1229.
- (35) Braun, A.; Ilavsky, J.; Dunn, B. C.; Jemian, P. R.; Huggins, F. E.; Eyring, E. M.; Huffman, G. P. *J. Appl. Cryst.* **2005**, *38*, 132–138.
- (36) Todorova, S.; Kolev, H.; Holgado, J. P.; Kadinov, G.; Bonev, C.; Pereniguez, R.; Caballero, A. *Appl. Catal. B: Environ.* **2010**, *94*, 46–54.
- (37) Salavati-Niasari, M.; Davar, F.; Mazaheri, M. *Polyhedron* **2008**, *27*, 3467–3471.
- (38) Brabers, V. A. M.; Setten, F. M.; van Knapen, P. S. A. *J. Solid State Chem.* **1983**, *49*, 93–98.
- (39) Gillot, B.; Guendouzi, M.; El Laarj, M. *Mater. Chem. Phys.* **2001**, *70*, 54–60.
- (40) McIntyre, N. S.; Zetaruk, D. G. *Anal. Chem.* **1977**, *49*, 1521–1529.
- (41) Oku, M.; Hirokawa, K. *J. Electron Spectrosc. Relat. Phenom.* **1975**, *7*, 465–473.
- (42) Strohmeier, B. R.; Hercules, D. M. *J. Phys. Chem.* **1984**, *88*, 4922–4929.
- (43) Selim, M. M.; Youssef, N. A. *Thermochim. Acta* **1987**, *118*, 57–63.
- (44) Ye, X. S.; Lin, D. S.; Jiao, Z. K.; Zhang, L. D. *J. Phys. D: Appl. Phys.* **1998**, *31*, 2739–2744.
- (45) Özdemir, Ö.; Banerjee, S. K. *Geophys. Res. Lett.* **1984**, *11*, 161–164.
- (46) Burton, B. B.; Fabreguette, F. H.; George, S. M. *Thin Solid Films* **2009**, *517*, 5658–5665.
- (47) Ren, Y.; Ma, Z.; Qian, L.; Dai, S.; He, H.; Bruce, P. G. *Catal. Lett.* **2009**, *131*, 146–154.
- (48) Mountapmbeme Kouotou, P.; Tian, Z. Y.; Mundloch, U.; Bahlawane, N.; Kohse-Höinghaus, K. *RSC Adv.* **2012**, *2*, 10809–10812.
- (49) Wu, H. C.; Liu, L. C.; Yang, S. M. *Appl. Catal. A: Gen.* **2001**, *211*, 159–165.
- (50) Imamura, S.; Sawada, H.; Uemura, K.; Ishida, S. *J. Catal.* **1988**, *109*, 198–205.
- (51) Lin, R.; Liu, W. P.; Zhong, Y. J.; Luo, M. F. *Appl. Catal. A: Gen.* **2001**, *220*, 165–171.
- (52) Wang, L. C.; Huang, X. S.; Liu, Q.; Liu, Y. M.; Cao, Y.; He, H. Y.; Fan, K. N.; Zhuang, J. H. *J. Catal.* **2008**, *259*, 66–74.
- (53) Xu, R.; Wang, X.; Wang, D. S.; Zhou, K. B.; Li, Y. D. *J. Catal.* **2006**, *237*, 426–430.
- (54) Glulhoi, A. C.; Bogdanchikova, N.; Nieuwenhuys, B. E. *J. Catal.* **2005**, *232*, 96–101.
- (55) Aguilera, D. A.; Perez, A.; Molina, R.; Moreno, S. *Appl. Catal. B: Environ.* **2011**, *104*, 144–150.
- (56) Sidheswaran, M. A.; Destailats, H.; Sullivan, D. P.; Larsen, J.; Fisk, W. J. *Appl. Catal. B: Environ.* **2011**, *107*, 34–41.

Supplemental Material

Z.Y. Tian, P. Mountapmbeme Kouotou, N. Bahlawane, P.H. Tchoua Ngamou, Synthesis of catalytically active Mn_3O_4 spinel and its thermal properties, *Journal of Physical Chemistry C*, 2012.

Section 1: Characterization

Table S1 Characteristics of Mn_3O_4 thin films

T_s^a (°C)	Growth Rate (nm/min)	a (nm)	D_p^b	D^c (nm)	ε^d	E_g^e (eV)
350	0.75	0.576032	1.64	21	0.104%	3.05
400	0.79	0.576930	1.64	25	0.086%	3.03
450	0.81	0.576203	1.64	27	0.083%	3.0
500	0.84	0.575502	1.65	33	0.078%	2.82

Note: ^a T_s is the substrate temperature; ^b D_p is the distortion parameter, defining as lattice ratio c/a ; ^c D is the crystallite size; ^d ε is the micro-strain of the sample; ^e E_g is the bandgap energy.

The temperature dependence of the growth rate was investigated gravimetrically using a microbalance (Mettler ME30). The manganese oxide thin films were grown at a rate of 0.75 nm/min at 350 °C, and this growth rate increased slightly with the temperature to reach 0.84 nm/min at 500 °C. With increasing temperature, the crystallite size increased from 21 to 33 nm, while the micro-strain decreased from 0.104% to 0.078%. The lattice, distortion parameters and bandgap energy are not sensitive to the deposition temperature.

Estimation of specific surface area:

For each mesh substrate with a diameter of 6 cm, the surface area consists of three parts, top, side and inside area. The top surface area can be calculated as $\pi \cdot 0.03 \cdot 0.03 \cdot 2 \cdot 1.414$ (two sides and stretch of the mesh). The side area is estimated to be $\pi \cdot 0.06 \cdot (0.00004 + 0.0000006)$, considering the thickness of mesh as $\sim 40 \mu m$ and 300 nm thickness of deposition on both sides). The inside area is calculated as $0.00004 \cdot 0.053 \cdot 2 \cdot (0.053 \cdot 1.414 / 0.000036 + 0.053 / 0.000045)$, in which 0.053 is obtained by assuming that the mesh is in square shape so that the numbers of the mesh line could be deduced. In the catalytic test process, two meshes with total mass of 12 mg were used. The final specific surface area is estimated to be $3.65 \text{ m}^2/\text{g}$.

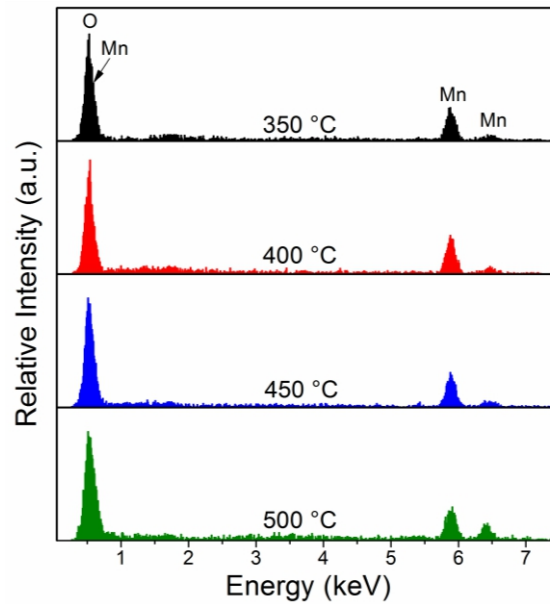


Fig. S1 The effect of substrate temperature on the EDS of Mn_3O_4 .

Figure S1 displays the Energy dispersive spectroscopy (EDS) of the Mn_3O_4 films. The elemental analysis was used to calculate the deposited amount of Mn_3O_4 . Three energy peaks at 5.90 and 6.49 KeV are characteristic peaks of metal manganese, which are in good agreement with previous results [K. Usha, C.K. Mahadevan, *Arch. Phys. Res.* 2 (2011) 75-80]. EDS analysis of the samples shows that the average O:Mn ratio is close to 4:3, which confirms the formation of stoichiometric Mn_3O_4 thin film.

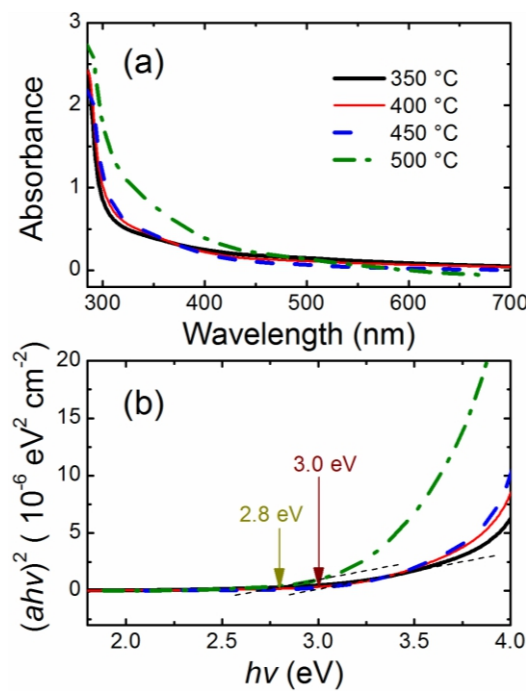


Fig. S2 UV-Vis absorption spectra (a) and $(ah\nu)^2$ versus $h\nu$ of Mn_3O_4 films (b) at different temperatures.

The UV-Visible absorption spectra of the Mn_3O_4 films deposited at different temperatures were measured to estimate the optical band gap energy by using a Shimadzu UV-2501 PC UV-Visible spectrometer. Figure S2 shows typical spectra of Mn_3O_4 films grown on planar glass. The direct band gap energy of the deposited Mn_3O_4 films can be calculated from the collected absorption spectra through Tauc's equation:

$$\alpha h\nu = A (h\nu - E_g)^n,$$

where α is the absorption coefficient, $h\nu$ is the photon energy, A is a constant relying on the refractive index, E_g is the band gap depending on the crystal structure and phase composition, and $n = 1/2$ for an allowed direct transitions. Plots of $(\alpha h\nu)^2$ versus $h\nu$ for Mn_3O_4 films are shown in Fig. S2(b). The extrapolation of the line to the abscissas at $(\alpha h\nu)^2 = 0$ gives the band gap energy for each sample. The E_g values for different film compositions are listed in Table 2. For substrate temperatures of 350 to 500 °C, the band gap was observed to be 3.05 to 2.82 eV. These values, assigned to the O^{2-} - Mn^{2+} charge transfer, are in good agreement with literature data [H.Y. Xu, S.L. Xu, H. Wang, H. Yan, J. Electrochem. Soc. 152 (2005) C803-C807]. These results show that, the band gap is not sensitive to the temperature, which is in accordance with the structural results.

Section 2: Catalytic test results

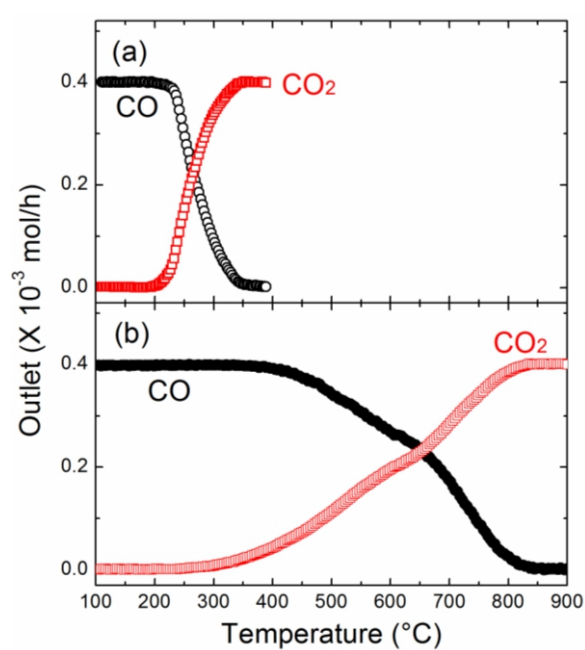


Fig. S3 Catalytic test of CO oxidation with Mn_3O_4 (a) and a non-coated mesh (b). The GHSV is 75,000 $\text{mL}/\text{g}_{\text{cat}}\cdot\text{h}$ for the reaction with Mn_3O_4 .

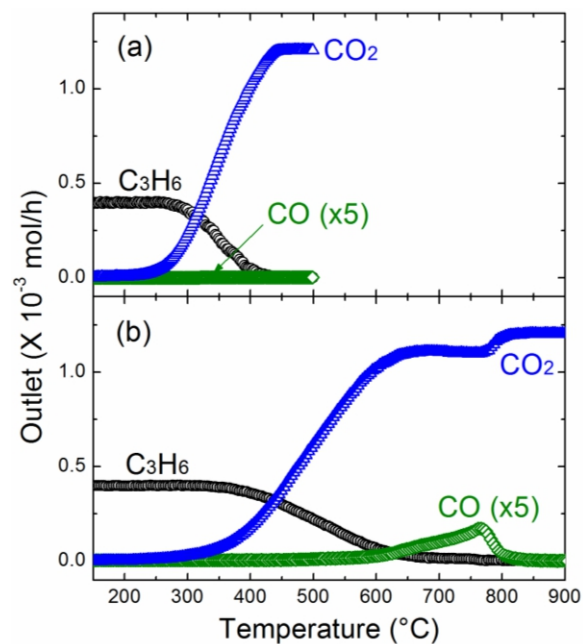


Fig. S4 Catalytic test of C_3H_6 oxidation with Mn_3O_4 (a) and non-coated mesh (b). The GHSV is 75,000 mL/ $g_{cat}\cdot h$ for the reaction with Mn_3O_4 .

Section 3: Temperature profiles

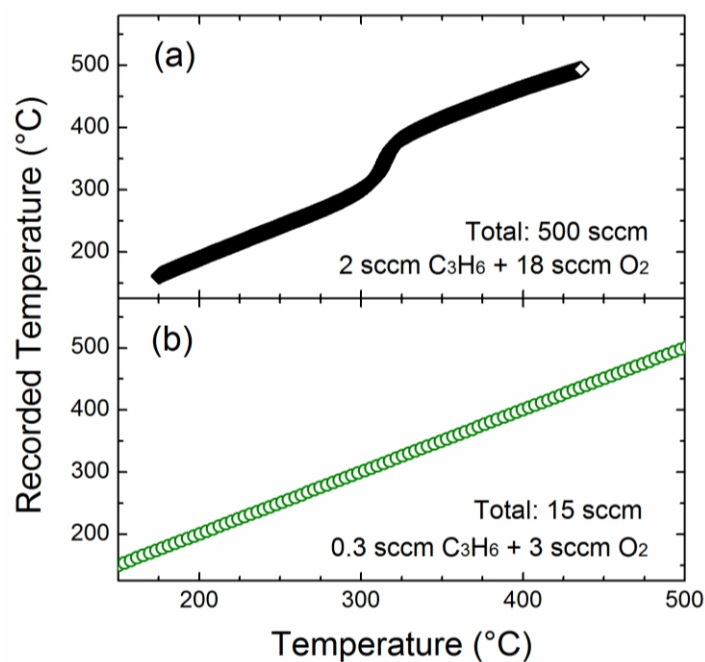


Fig. S5 Temperature profiles inside the coated meshes (Y-axis) as a function of the heating temperature outside of the flow reactor (X-axis): propene oxidation over Co_3O_4 (2 sccm C_3H_6 / 18 sccm O_2 / 480 sccm Ar) (a) and over Mn_3O_4 (0.3 sccm C_3H_6 / 3 sccm O_2 / 11.7 sccm Ar) (b).

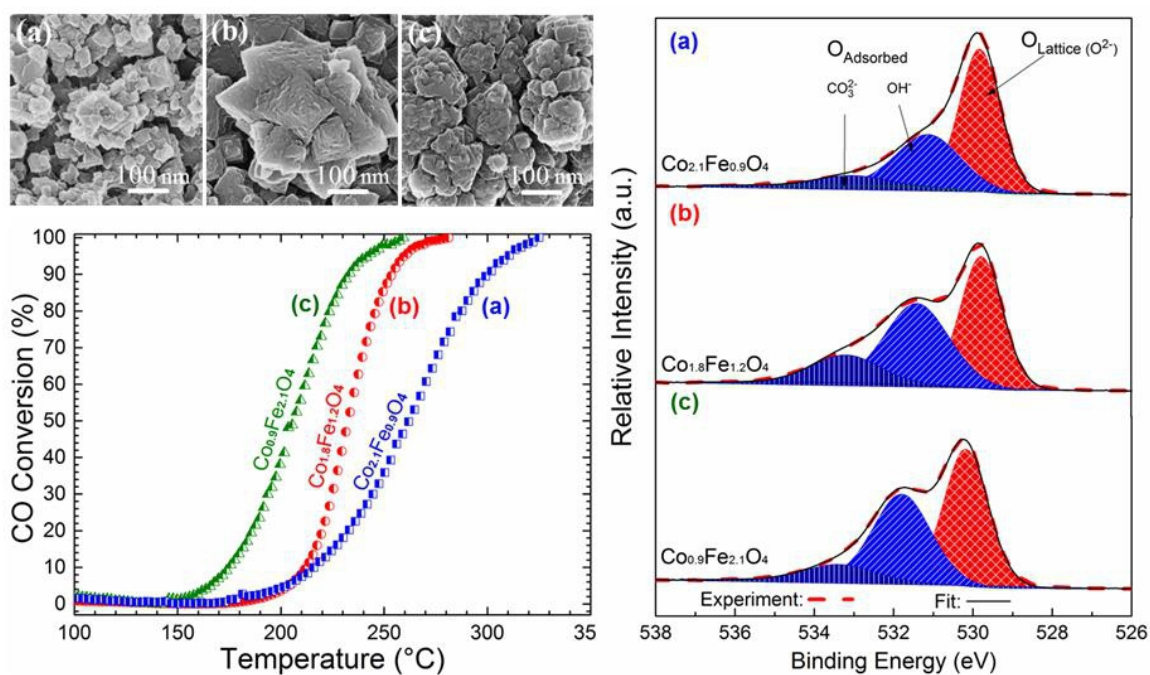
F) Manuscript 1

Patrick Mountapmbeme Kouotou, Z.Y. Tian, A. El Kasmi, H. Vieker, P. H. Tchoua Ngamou, A. Beyer, A. Götzhäuser, and K. Kohse-Höinghaus

Structure-activity relation of spinel-type Co-Fe oxides for low temperature CO oxidation

Catalysis Science & Technology (Revised)

Graphical Abstract



Research Highlight

Cobalt ferrite thin films were synthesized and systematically characterized for the catalytic oxidation of carbon monoxide. The optical and redox properties play decisive roles in the oxidation processes.

ARTICLE

Structure-activity relation of spinel-type Co-Fe oxides for low-temperature CO oxidation

Cite this: DOI: 10.1039/x0xx00000x

P. Mountapmbeme Kouotou,^{a,*} H. Vieker,^b Z.Y. Tian,^{a,c,*} P.H. Tchoua Ngamou,^a A. El Kasmi,^a A. Beyer,^b A. Gölzhäuser,^b and K. Kohse-Höinghaus^a

Received 00th January 2012,

Accepted 00th January 2012

DOI: 10.1039/x0xx00000x

www.rsc.org/

A series of cobalt ferrite thin films was prepared via Pulsed Spray Evaporation Chemical Vapour Deposition (PSE-CVD). The samples were comprehensively characterised in terms of structure, surface, morphology, optical and redox properties. Both X-ray diffraction (XRD) and Raman analysis show that all samples exhibited an inverse spinel structure. X-ray photoelectron spectroscopy (XPS) results indicate that the films were mainly composed of Co, Fe and O species, and an increase of the Co:Fe ratio with Fe substitution by Co was observed. Helium ion microscopy (HIM) images show film morphology depending on the Co:Fe ratio. The investigation of the optical property using ultra-violet visible spectroscopy reveals that the increase of the Co content results in an increase of the band gap energy. In-situ emission FTIR spectroscopy was used to evaluate the redox properties of the samples, and a shift of the redox temperature to higher values was observed upon increase of the Co content. The effect of Fe substitution by Co in the mixed oxide systems on their catalytic performance for CO oxidation was investigated. Co-Fe oxides exhibit substantially better catalytic performance than the single α -Fe₂O₃. The catalytic performance of the Co-Fe oxides towards CO oxidation was discussed with respect to the participation of surface and lattice oxygen in the oxidation process. According to XPS and temperature-programmed reduction/oxidation (TPR/TPO) results, a suprafacial mechanism where CO molecules react with surface-adsorbed oxygen functions to form CO₂ was proposed as the dominant mechanism.

Introduction

Catalytic oxidation has been recognized as one of the most efficient techniques for CO abatement [1]. Catalytic low-temperature combustion of CO is continuously developed as an important research topic in environmental emission control [2-4]. The advantages of this process include extensive applications in numerous fields such as automotive exhaust emission control [5], CO sensors [6], as well as traceable CO removal in enclosed atmospheres [7,8].

Currently, metal (e.g., Au) nanoparticles dispersed on solid supports and transition metal oxides (TMOs) have been found to be active catalysts for CO oxidation [9-11]. Although noble metals present high catalytic performance towards CO oxidation, they are generally costly, and easily deactivated due to the trend of particle agglomeration which causes the decrease of the surface area [2]. TMOs are relatively cheap and can be easily synthesized, possess high thermal stability [12] and may show comparable activity with precious metals. Therefore, special attention has been focused on TMOs with different structures [3,13]. Among the investigated TMOs, high interest has been devoted to iron oxides because of their abundant availability and attractive properties such as high thermodynamic stability [14,15], low cost, and environmentally friendly nature [16]. Several studies have shown the effectiveness of iron oxides and their composites towards the oxidation of CO [17-20]. However, compared to some catalytically active TMOs such as Co₃O₄ for CO oxidation [21-23], good performance of iron oxide is mainly observed at relatively high temperature.

Cobalt ferrite oxide (Co-Fe-O) with a spinel structure could thus be a potentially interesting material with combined properties. Because of the versatility of mixed-oxide spinels, which offer tuneable composition, structural stability and a possibility for bifunctional redox or acid/base behaviour [24], such combination could improve the physicochemical properties and the catalytic performance. Different cations with more than one oxidation state can be accommodated and distributed between the available octahedral and tetrahedral sites [25], to endow such interesting and tuneable properties. For instance, CoFe₂O₄ adopts an inverse spinel arrangement and is thermodynamically stable at around 900 °C [24,26-28]. The contrasting site occupation between iron and cobalt in the cobalt ferrite composite is expected to create a significant modification of its properties and activity.

Cobalt ferrite spinels have been intensively investigated as catalysts for various reactions [24,29,30]. A single cobalt ferrite with a composition of Co_{2.1}Fe_{0.9}O₄ (identical with one of the materials discussed in this article) has also recently been used as catalyst for DME, propene and *n*-butene oxidation [31]. Because it showed interesting catalytic behaviour against these compounds, it was used in this work to study the influence of the composition in a more systematic fashion. We have thus taken Fe₂O₃ as the starting material to improve its properties by Co addition. In fact, the activity of Co₃O₄ in the low-temperature conversion of CO has been systematically investigated and its high activity was reported to be due to the Co²⁺-Co³⁺ ion pairs [32,33]. In most cases, CO oxidation over Co₃O₄ follows a redox mechanism where Co³⁺ is reduced to Co²⁺ after CO adsorption

[32]. To improve the catalytic activity of α -Fe₂O₃, the aim here was to tailor the Co:Fe ratio and to deposit oxide composites in which both Co²⁺ and Co³⁺ are present with Fe³⁺ in the same phase.

The synthesis of Co-Fe-O thin films with varied composition for low-temperature CO oxidation was performed by Pulsed Spray Evaporation Chemical Vapour deposition (PSE-CVD) and their properties were systematically characterized. PSE-CVD is a synthesis approach which offers distinct advantages over conventional CVD and is considered as a promising method to prepare pure films regarding its relatively low cost, simplicity and high throughput [34]. The PSE precursor delivery system is advantageous as it allows using less stable precursors with good control of the process and thus permits to improve the reproducibility of the film properties [34]. It is well adapted to the deposition of metal oxides with tailored composition [35,36] to systematically study their properties. The obtained samples were characterised in terms of structure, composition, morphology, optical and redox properties using X-ray Diffraction (XRD), Raman and X-ray Photoelectron Spectroscopy (XPS), Helium Ion Microscopy (HIM), Ultra-Violet Visible spectroscopy (UV-Vis) and in-situ emission FTIR. It should be mentioned that part of this information is also provided in [31] for the composition Co_{2.1}Fe_{0.9}O₄. Upon variation of the cobalt content, the effect of the cobalt insertion in the iron oxide matrix on the optical and redox properties and the catalytic performance was investigated here and an attempt was made to correlate the observed effects with the characterized properties of the deposited thin films.

Experimental

The preparation and characterization procedures followed up on those presented in [31]. However, some detail is necessary to understand the correlations between physicochemical characteristics and catalyst behaviour addressed here, and a more in-depth analysis is given in the present paper.

Catalyst preparation

The Co-Fe-O thin films were prepared using a cold-wall stagnation-point flow CVD reactor, associated with a PSE system for the delivery of liquid precursor feedstock [20,31]. The PSE delivery was achieved with a valve opening time of 2.5 ms and a frequency of 4 Hz. Firstly, cobalt acetylacetonate (Co(acac)₃) and iron acetylacetonate (Fe(acac)₃) were weighed in the adequate molar ratios Co/Fe, dissolved in tetrahydrofuran (THF) and kept at respective concentrations of 5 mM. The single phase of Co_xFe_{3-x}O₄ of the respective stoichiometric relation was obtained by adjusting the volume molar ratio of the two metallic elements (Co%vol:Fe%vol=10:90, 30:70 and 50:50). The value *x* was calculated from the Co/Fe ratio obtained by XPS. The liquid delivery permits to overcome the inherent contrast between the sticking probabilities of different precursors in the dual-source strategy for the growth of multi-component films. The evaporation of the injected feedstock took place at 220 °C. The resulting vapour was transported to the deposition chamber with N₂/O₂ flow rates of 0.16/1.0 standard litres per minute (SLM). Stainless steel and bare glass were used as substrates, heated with a flat resistive heater. After optimization, the substrate temperature was fixed at 400 °C and the total pressure in the reactor was kept at 30 mbar during the deposition. The thickness of the obtained films was estimated gravimetrically using a microbalance, with resolution of 1 µg.

Characterization

A Philips X'Pert Pro MDR diffractometer with PW3830 X-ray generator was used to record the XRD patterns. The crystalline phases were identified by referring to the powder XRD database (JCPDS-ICDD), and the crystallite sizes were calculated using the Scherrer equation. Raman spectra were obtained with a home-made Raman spectrometer [37]. The surface microstructure was examined with a Carl Zeiss Orion Plus® helium ion microscope (HIM). The helium ion beam was operated at 35 kV acceleration voltage at a current of 0.5 pA. A 5 µm aperture at a setting of "spot control 4" was used. The working distance was 9 mm, and the sample tilt 0°. The samples were plasma-cleaned in the HIM load lock for 8 min before measurement. The chemical composition was determined by UHV-XPS (Multiprobe, Omicron Nanotechnology, base pressure about 10⁻¹⁰ mbar), using a monochromated Al K α X-ray source (1486.7 eV, 280 W) under an angle of 13° from the surface normal to the electron detector. CasaXPS was used to analyse the spectra with Shirley backgrounds and Scofield cross-sections. The evaluation of the Co and Fe spectra is not straightforward since an Auger peak from one metal overlays the 2p peak of the other metal. To overcome this effect, reference samples of cobalt and iron oxide were measured to calculate the 2p to Auger area ratio. With this, the areas used for the elemental composition were corrected (see details in the ESI).

The redox properties of the Co-Fe-O composites coated on stainless steel substrates were evaluated by Temperature-Programmed Reduction (TPR); this was followed by re-Oxidation (TPO). Both analyses were performed from 100 to 500 °C with a ramp of 3 °C/min, under an argon flow of 0.05 L/min containing 5 vol.% of H₂ (TPR) or O₂ (TPO), respectively. Emission FTIR spectra were recorded continuously during the TPR/TPO analyses and characteristic bands were integrated versus temperature. This technique allowed for substantial improvement of the sensitivity towards dynamic changes in the gas composition. UV-Vis spectra were recorded (UV-2501PC, SHIMADZU) to determine the optical properties.

Catalytic tests

The catalytic performance of the Co-Fe-O composites was evaluated using a 30 cm long quartz plug-flow reactor with a diameter of 0.9 cm. 20 mg catalyst (supported on grid mesh of stainless steel) were used. The reaction gas mixture consisted of 1% CO and 10% O₂ diluted in argon with a total flow rate of 15 mL/min, corresponding to a weight hourly space velocity (WHSV) of 45000 mL g⁻¹cat h⁻¹. The flow rates of gases were controlled by MKS mass flow controllers, and the temperature of the reactor was raised with a ramp of 3 °C/min using a HT60 controller (Horst). The temperature of the mesh inside of the reactor was recorded using K-type thermocouples and a digital thermometer (GMH3250, Greisinger). The composition of the effluent gas was detected in the wavelength range of 400-4000 cm⁻¹ with an online FTIR spectrometer equipped with a KBr transmission cell. Details of data treatment can be found in [38]. It should be noted that it was not the aim here to maximize surface area, but to investigate the effect of Co addition on the properties of Fe₂O₃ under well-defined conditions. The CVD synthesis approach offers, in principle, to coat structures with larger surface area by e.g., using washcoats or porous structures as templates.

Results and discussion

Structure

The structural investigation of the deposited thin films with a thickness of ~250 nm was performed using XRD and Raman spectroscopy, as shown in Fig. 1. The XRD patterns of the cubic Fd3m spinel Co₃O₄ [35] and hexagonal Ia3 hematite (α -Fe₂O₃) [20] from our

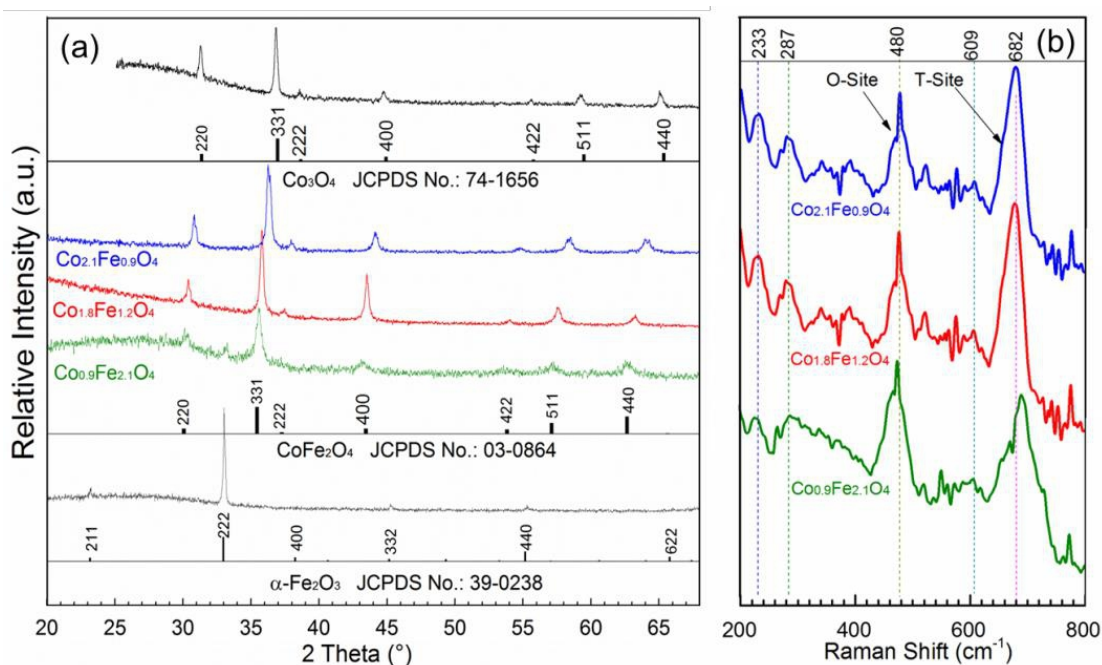


Fig. 1 (a) XRD patterns of Co-Fe-O oxides, pure Co_3O_4 [35] and $\alpha\text{-Fe}_2\text{O}_3$ [20]; (b) Raman spectra of the deposited Co-Fe-O films. The sample $\text{Co}_{2.1}\text{Fe}_{0.9}\text{O}_4$ is reproduced from [31].

recent work are presented as references. The deposited Co-Fe-O films exhibit a cubic $\text{Fd}3\text{m}$ inverse spinel structure like the reference CoFe_2O_4 inverse spinel (JCPDS Nr. 03-0864) and no extra diffraction peaks associated with the formation of other phases were detected. Starting from hematite ($\alpha\text{-Fe}_2\text{O}_3$), a non-spinel with hexagonal structure, Fe substitution by Co induces a structure transformation to an inverse spinel structure even at very low Co content. A decrease of the lattice constant from 8.39 to 8.21 Å (Table 1) was noted with increasing the cobalt content, which is visualized by the peak shift of diffraction peaks towards higher angles. The calculated values of the lattice constants vary from those of the reference materials CoFe_2O_4 (8.4 Å) and Co_3O_4 (8.1 Å). Hematite has a hexagonal close-packed structure with all Fe^{3+} ions in O-sites whereas Co_3O_4 has a normal spinel structure in which tetrahedral sites (T-sites) are occupied by Co^{2+} ions and octahedral sites (O-site) by Co^{3+} ions: $[\text{Co}^{2+}]_{\text{T-site}}[\text{Co}^{3+}\text{Co}^{3+}]_{\text{O-site}}\text{O}_4$. In contrast, CoFe_2O_4 has an inverse spinel structure in which Fe^{3+} , Co^{3+} and Co^{2+} ions are distributed in both T- and O-sites. A systematic analysis of a series of Co-Fe-O with similar compositions has been reported by Le Trong et al. using Mössbauer spectroscopy [39]. Following their analysis, we assigned the following distribution to our oxides upon increasing the Co content, i.e. $[\text{Co}^{2+}\text{Fe}^{3+}\text{Co}^{3+}]_{\text{T-site}}[\text{Fe}^{3+}\text{Co}^{2+}\text{Co}^{3+}]_{\text{O-site}}\text{O}_4$, $[\text{Co}^{2+}\text{Fe}^{3+}]_{\text{T-site}}[\text{Co}^{2+}\text{Fe}^{3+}\text{Co}^{3+}]_{\text{O-site}}\text{O}_4$, and $[\text{Co}^{2+}\text{Fe}^{3+}]_{\text{T-site}}[\text{Fe}^{3+}\text{Co}^{2+}]_{\text{O-site}}\text{O}_4$ for $\text{Co}_{2.01}\text{Fe}_{0.9}\text{O}_4$, $\text{Co}_{1.8}\text{Fe}_{1.2}\text{O}_4$ and $\text{Co}_{0.9}\text{Fe}_{2.1}\text{O}_4$, respectively. The observed decrease of the lattice constant with increasing Co content can be associated to this changing distribution. In fact, according to Le Trong et al. [39], when the amount of cobalt increases, the cell parameter decreases and there is a gradual evolution toward a normal spinel structure as observed in our XRD patterns. This is due to the fact that the diamagnetic Co^{3+} cations replace the Fe^{3+} cations in the octahedral position and the octahedral preference of the Co^{2+} cations becomes less dominant.

The particle size was evaluated by XRD analysis with the Scherrer equation. Increasing cobalt content tends to sharpen the peaks progressively. The Scherrer line-broadening analysis on the (331) plane reveals that the volume-averaged crystallite size increases

from 20 to 35 nm upon cobalt insertion. The agglomeration of small grain sizes to form larger particles may be one reason for the increase of the particle size.

Further structure information was obtained from Raman spectra of the deposited thin films, recorded at room temperature, and presented in Fig. 1b. Five Raman-active modes are observed: the modes at ~ 609 and ~ 682 cm^{-1} are related to the T-site mode; other peaks at ~ 233 , ~ 287 and ~ 480 cm^{-1} correspond to the O-site mode [40]. These assignments are in excellent agreement with the previously reported results for the Co-Fe-O system [24,41,42]. Thus, pure-phase Co-Fe-O spinel can be easily synthesized with PSE-CVD through the accurate adjustment of the feedstock composition.

Chemical composition

Ex-situ XPS was used to investigate the surface composition and chemical species of the cobalt ferrite thin films. Despite the presence of both metals and oxygen, carbon is found on all samples. Carbon and oxygen can be contamination products arising from the precursor decomposition and from ambient air. Therefore, the Fe/Co ratio was used to calculate the chemical compositions and the results are listed in Table 1. Details regarding XPS measurement and evaluation are collected in the ESI: Table ESI 1, Fig. ESI 1 and Fig. ESI 2.

High-resolution XPS spectra of Fe2p, Co2p, and O1s are shown in Fig. 2. To compare the metal spectra to the literature, the overlaying Auger peaks were directly subtracted from the data. It is worth mentioning that even for clear spectra, the identification and fitting of chemical species is not unique. This Auger correction gives an additional source of error whereas it is the best route in this study (see the original data in Fig. ESI 2). The Fe2p spectra are visible in Fig. 2a. The signals at 710.6 and 723.3 eV with the separation of 12.7 eV and a small satellite structure at ~ 734 eV have been reported to indicate the presence of Fe^{3+} [43]. Inspection of the measured Co2p peak (Fig. 2b) shows that it is composed of the main doublet with peaks at

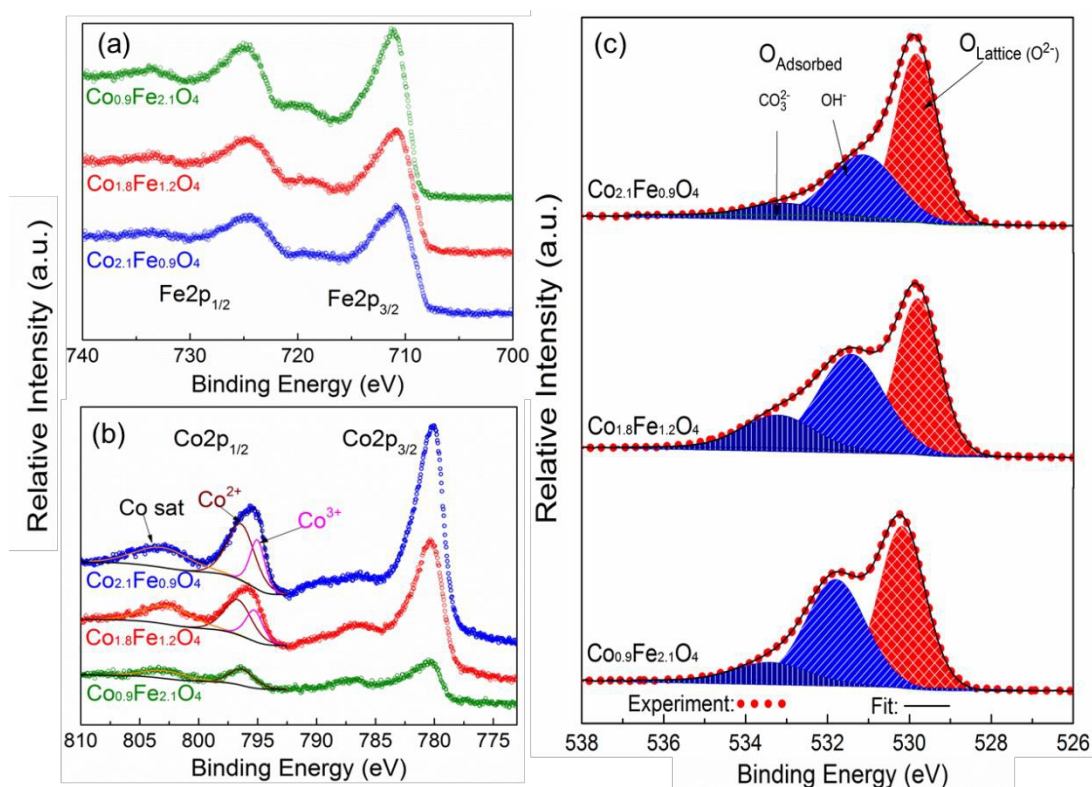


Fig. 2 XPS spectra of the Co-Fe-O samples: (a) Fe2p; (b) Co2p; (c) O1s. In case of the metals an overlaying Auger signal has been subtracted (see supplement for details). An offset is added for better visibility. The sample $\text{Co}_{2.1}\text{Fe}_{0.9}\text{O}_4$ is reproduced from [31].

around 780 and 795 eV, indicating the presence of oxidized species. Only the $2p_{1/2}$ parts of the spectra were fitted as it is less affected by the Auger correction. Here, the species interpretation according to Gautier et al [44] was used. The main peak consists of two species, one at ~ 795.2 eV for Co^{3+} and one at ~ 796.4 eV for Co^{2+} . A broad satellite peak at 802.8 eV is assigned to originate from Co^{2+} .

As shown in Fig. 2c, the O1s spectra for all samples were deconvoluted in three peaks in the BE range of 530-533 eV. The lower peak (~ 530 eV) could be assigned to the lattice oxygen species O^{2-} . The two species at higher BE are generally assigned to “adsorbed oxygen” [45]. The peak at ~ 531.4 eV is explained to be the hydroxyl species (OH^-) or defective oxygen [46], whereas the peak at 533.2 eV probably comes from carbonate species, CO_3^{2-} or defects in the structure. From the XPS spectra of all samples, lattice and adsorbed oxygen are observed. Both O^{2-} and O^- species are strongly electrophilic reactants, which can attack an organic molecule in the region of its highest electron density, and therefore result in the oxidation of the carbon skeleton [19]. For CO conversion over oxides, electrophilic oxygen species such as lattice and adsorbed oxygen are generally responsible for the total oxidation [10,47]. Thus, these electrophilic oxygen species (O^{2-} or O^-) present at the surface of Co-Fe-O oxides are expected to benefit the total oxidation of CO.

Morphology

The surface morphology of the thin films was studied with HIM and a few representative micrographs of the obtained films are shown in Fig. 3 (additional images can be found in Fig. ESI 3). The images revealed significant differences between the samples of different composition whereas sample $\text{Co}_{1.8}\text{Fe}_{1.2}\text{O}_4$ (Fig. 3b, 3e and 3h) shows

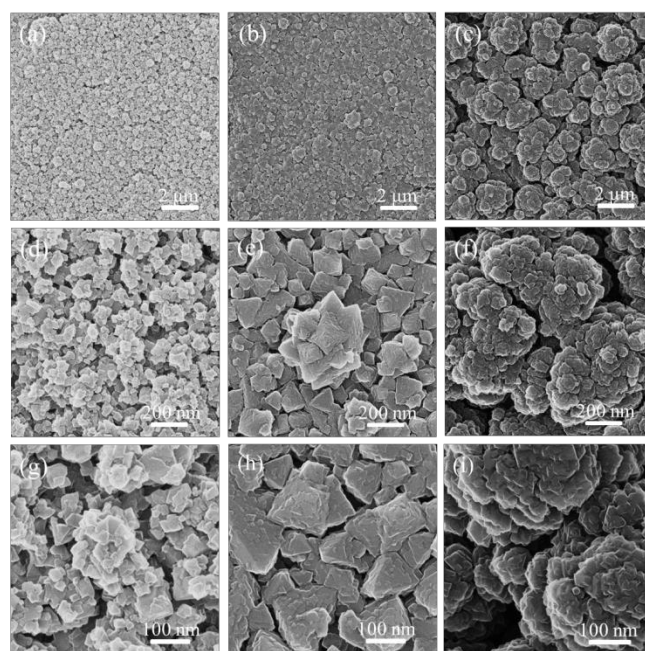


Fig. 3 High magnification HIM images of Co-Fe-O thin films coated on stainless steel at 400 °C, (a,d,g) $\text{Co}_{0.9}\text{Fe}_{2.1}\text{O}_4$, (b,e,h) $\text{Co}_{1.8}\text{Fe}_{1.2}\text{O}_4$ and (c,f,i) $\text{Co}_{2.1}\text{Fe}_{0.9}\text{O}_4$.

better defined crystals with a pyramidal shape embedded in a matrix consisting of small cubic grains. The sample $\text{Co}_{2.1}\text{Fe}_{0.9}\text{O}_4$ (Fig. 3c, 3f and 3i) shows films composed of large grains which exhibit a cauliflower structure; these films show apparent open porosity, thus no particular defined geometry is observed due to the complete loss

of the crystallinity. By increasing the Co content, the grain size apparently becomes larger due to the agglomeration of small grains with average values of about 20-35 nm. HIM images confirm visually that the increase of grain size upon Co addition is in accord with the estimation by XRD analysis. The grain size of $\text{Co}_{0.9}\text{Fe}_{2.1}\text{O}_4$ films is the smallest, followed by $\text{Co}_{1.8}\text{Fe}_{1.2}\text{O}_4$ and $\text{Co}_{2.1}\text{Fe}_{0.9}\text{O}_4$. Usually, the smaller the grain size, the larger the specific surface area [47,48]. Therefore, the difference in grain size may influence the physicochemical properties as well as the catalytic performance.

Optical properties

The controlled variation of the band gap energy (E_g) in catalyst materials could be used as a tool to reflect their performance. It has been demonstrated that metal oxides with low E_g can exhibit good catalytic performance [49,50]. To explore relationships between optical properties and the catalytic performance of Co-Fe-O, the UV-Vis absorption spectra were recorded and E_g was evaluated. It is worth mentioning that, to the best of our knowledge, the variation of the band gap energies and redox properties have not yet been correlated systematically.

Typical UV-Vis spectra of the thin films are display in Fig. 4a. The collected absorption spectra were then used to evaluate the direct E_g from the Tauc equation: $\alpha hv = A(hv - E_g)^n$, where α represents the absorption coefficient, $h\nu$ is the photon energy, A is the refractive index constant and n is a constant associated with the nature of the transition (1/2 for direct allowed transitions). E_g is estimated from the intercept of the extrapolated linear fit to the experimental data of $(\alpha hv)^2$ vs. $h\nu$, see Fig. 4b. Results for $\text{Co}_{0.9}\text{Fe}_{2.1}\text{O}_4$, $\text{Co}_{1.8}\text{Fe}_{1.2}\text{O}_4$ and $\text{Co}_{2.1}\text{Fe}_{0.9}\text{O}_4$ thin films calculated from the linear fit are 1.60, 1.90 and 2.09 eV, respectively. These values are larger than that of 1.44 eV reported by Rai et al. [51] and smaller than 2.61 eV by Ravindra et al. [52] for similar cobalt ferrites. It is important to note that E_g increases upon Fe substitution with Co. Several factors could influence the E_g of semiconductors: defects, charged impurities, disorder at the grain

boundaries, cationic distribution as well as three-dimensional quantum size effects. These influences have not been discussed in detail for our materials in the literature. The only pertinent studies reported the effect of grain size evolution and distribution on the optical properties of pure V_2O_5 thin films prepared by pulsed-laser deposition [53]. The decreases of E_g and changes in the spectral characteristics were attributed to the increase of the grain size, random grain distribution and the structural modification of the material [53]. This last assumption seems to be more applicable to our deposited films because the insertion of the cobalt in the matrix of the iron oxide is expected to create some structural disorder in the material and a perturbation of the band structure which can influence the band gap. The UV-Vis spectra of PSE-CVD-deposited Fe_2O_3 thin films exhibit one absorption band corresponding to an optical band gap energy of 2.16 eV [20] which is assigned to the ligand-metal charge transfer $\text{O}^{2-} \rightarrow \text{Fe}^{3+}$. The combination of two transition metals with variable oxidation states has caused a structural modification and perturbation of the band structure which is responsible for the shift of the optical band gap of the Co-Fe-O materials to lower values, which would also enable their application to photo-catalysis. The increase of the optical band gap of the deposited films with increasing the cobalt content can logically be associated to the structural modification arising with the cationic re-distribution in both the O- and T-sites which is in line with the XRD and XPS results. This approach is consolidated by Auvergne et al. [54] who reported that the band shift in oxides is due to Coulomb interaction between species which occurs as a result of doping. These observations and concepts also seem useful with respect to the present composite oxides and their electronic, optical and catalytic applications. It is well known that materials with narrow energy band gaps offer higher electron mobility, and the correlation of the electron availability and mobility with the redox activity of a respective catalyst has been reported [55]. According to Zaki et al. [55], the electron availability and mobility of lattice and surface oxygen species determine the redox activity of their catalysts. It is therefore crucial to investigate the influence of the optical band gap of the prepared sample in their redox properties.

Redox properties

To investigate the redox properties of the mixed oxides, TPR and TPO were carried out with emission FTIR as an in-situ monitoring technique, using 5% of H_2 or O_2 in Ar (0.05 L/min). Figure 5 displays the redox behaviour of the samples. The typical feature of the integrated IR band intensity of Fe-Co-O as a function of the temperature in the TPR is presented in Fig. 5a. As the temperature increases, a progressive red shift of the two bands at around 530 cm^{-1} and 628 cm^{-1} (Fig. 5c) is observed. The complete reduction is characterized by a plateau at $300\text{ }^\circ\text{C}$. Figures 5b and 5d display the TPO profiles and the total recovery of the inverse spinel structure in the oxidation step, respectively. The reducibility and the re-oxidation order for the three samples is: $\text{Co}_{2.1}\text{Fe}_{0.9}\text{O}_4 < \text{Co}_{1.8}\text{Fe}_{1.2}\text{O}_4 < \text{Co}_{0.9}\text{Fe}_{2.1}\text{O}_4$. The reduction and oxidation temperatures are notably shifted to higher values, indicating that the increase of the Co content can give rise to unexpected changes of the Co-Fe-O structure and thereby make it more difficult to be reduced. The presence of anionic vacancies in the lattice of Mn-doped [38] and Ce-doped Co_3O_4 [56] has been reported to also increase the reducibility temperature. In this study, this kind of vacancies can also be generated upon cobalt insertion and make the corresponding material less reducible. The sample $\text{Co}_{2.1}\text{Fe}_{0.9}\text{O}_4$ shows a high reduction and oxidation temperature

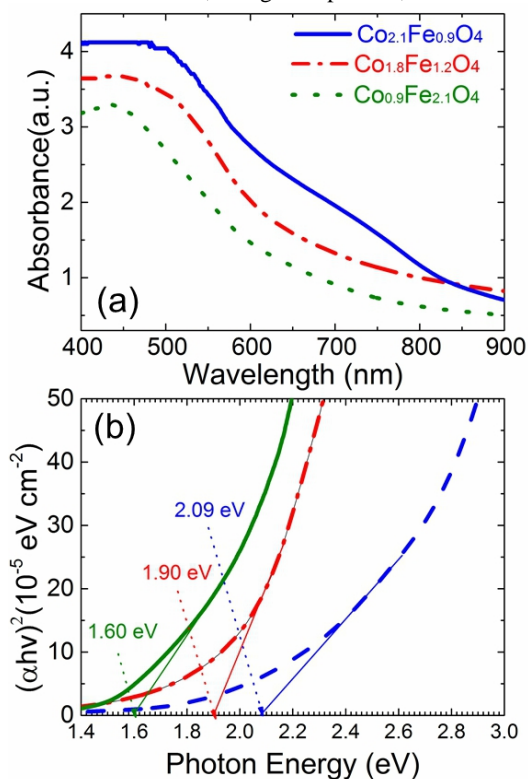


Fig. 4 (a) Optical absorption spectrum and (b) Tauc's plot resulting in an optical E_g for the different Co-Fe-O composites.

Table 1 Characteristics of Co-Fe-O thin films

Composition	<i>D</i> (nm)	<i>a</i> (Å)	<i>E_g</i> (eV)	T _{TPR} (°C)	T _{TPO} (°C)	T ₁₀ (°C)	T ₅₀ (°C)	T ₉₀ (°C)
Co _{0.9} Fe _{2.1} O ₄	20	8.39	1.60	295	309	170	205	230
Co _{1.8} Fe _{1.2} O ₄	33	8.36	1.90	300	338	210	232	250
Co _{2.1} Fe _{0.9} O ₄	35	8.21	2.09	317	350	215	260	300
α-Fe ₂ O ₃ [20]	-	-	2.16	-	-	262	325	384

D is the particle size; T_{TPR} and T_{TPO} refer to the temperature of complete reduction and re-oxidation, respectively; T₁₀, T₅₀ and T₉₀ stand for the temperatures corresponding to 10%, 50% and 90% CO conversion, respectively.

(low lattice oxygen mobility), followed by Co_{1.8}Fe_{1.2}O₄, whereas the sample Co_{0.9}Fe_{2.1}O₄, with low cobalt content, is reduced and re-oxidized at low temperature (high lattice oxygen mobility).

Taking also the optical properties into consideration, Co_{0.9}Fe_{2.1}O₄ and Co_{1.8}Fe_{1.2}O₄ samples might allow high electron mobility due to their narrow *E_g*, with the knowledge that the reduction/oxidation of oxide material can proceed with electron transfer [57,58]. Consistently, the redox behaviour of samples with low Co content (low *E_g*) can be explained in terms of easy migration of the O²⁻ to the surface due to the high electron mobility during the electron transfer process. It is thus reasonable to correlate the redox properties (lattice oxygen mobility) of the Co-Fe-O in this study also with the band gap energy (electron mobility) variation. Optical and redox properties can predict the behaviour of the catalytic activity if the redox mechanism is dominant in the CO oxidation to CO₂.

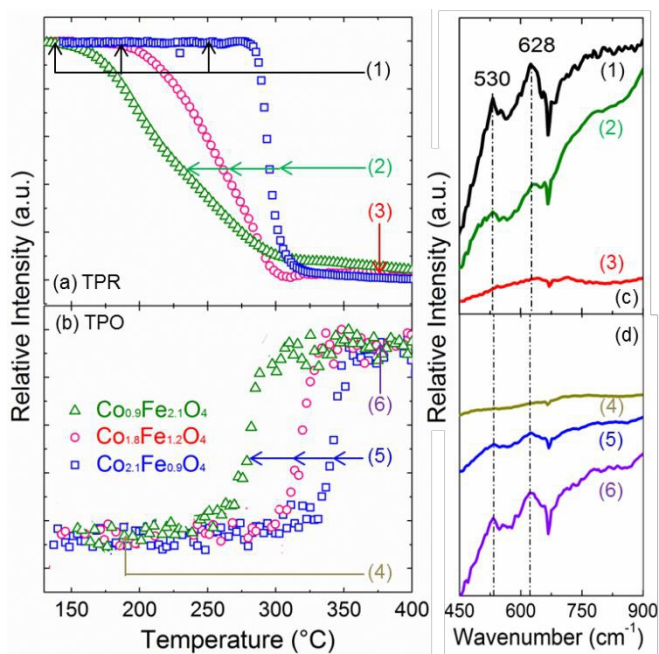


Fig. 5 Redox behaviour of the selected Co-Fe-O oxides: (a) TPR; (b) TPO; (c) progressive loss of the spinel structure and (d) recover of Co-Fe-O IR vibration. The sample Co_{2.1}Fe_{0.9}O₄ is reproduced from [31].

Catalytic performance

To evaluate the catalytic performance of the prepared cobalt ferrite mixed oxides, the oxidation of CO was investigated at atmospheric pressure over all samples. The results were thus compared with that obtained with pure α-Fe₂O₃ from previous work [20] and a blank sample of non-coated mesh, as shown in Fig. 6. Single α-Fe₂O₃ becomes active in CO oxidation at around 230 °C and achieves complete CO conversion to CO₂ above 450 °C. Co-Fe-O composites exhibit lower temperatures for the initiation of CO oxidation than single α-Fe₂O₃. The complete CO oxidation over Co_{0.9}Fe_{2.1}O₄, Co_{1.8}Fe_{1.2}O₄ and Co_{2.1}Fe_{0.9}O₄ occurs at 255, 275 and 325 °C, respectively. The catalytic performance of various catalysts can be more easily compared by T₅₀ (the reaction temperature corresponding to a 50% CO conversion), as presented in Table 1. The T₅₀ for single α-Fe₂O₃ is 350 °C. T₅₀ sharply decreases to ~232 °C for Co_{1.8}Fe_{1.2}O₄ and further decreases to 205 °C for Co_{0.9}Fe_{2.1}O₄. T₅₀ thus increases with the further substitution of Fe by Co in the Co-Fe composites. Only a small amount of Co is sufficient to shift the oxidation temperature of CO toward lower values. These results indicate that cobalt ferrite oxides are more catalytically active than the pure α-Fe₂O₃ single oxide. The performance order is the following: α-Fe₂O₃ < Co_{2.1}Fe_{0.9}O₄ < Co_{1.8}Fe_{1.2}O₄ < Co_{0.9}Fe_{2.1}O₄.

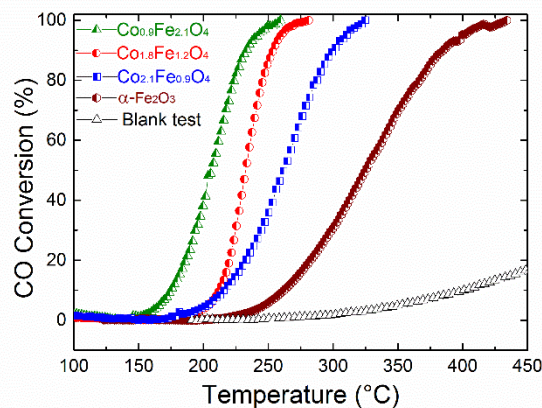
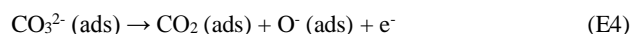
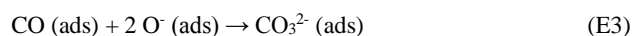
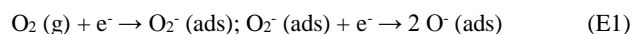


Fig. 6 Light-off curves of CO conversion with the Co-Fe-O samples and α-Fe₂O₃ as well as non-coated mesh. The results obtained over α-Fe₂O₃ [20].

To understand the difference observed in the catalytic performance upon Co addition, a study of the phenomena that govern the catalytic oxidation on the surface is needed. From a viewpoint of

oxygen species participating in the catalysis, adsorbed (and/or surface) oxygen and lattice oxygen are supposed to contribute to the suprafacial and intrafacial processes, respectively. XPS results revealed the presence of cations (Co^{3+} , Co^{2+} and Fe^{3+}) and anions (O^{2-} , OH^- as well as CO_3^{2-}) in the Co-Fe-O structure. The activity of Co-Fe-O composites should be dominated by the exposed fraction of the active species of the Co-Fe-O composite. We will therefore now discuss how either the redox properties or the adsorbed oxygen at the surface of Co-Fe-O may be involved in the CO catalytic oxidation process in this work.

It is generally accepted that CO oxidation over oxides follows a Mars van Krevelen-type mechanism [59,60], where the reactions involves alternate reduction and oxidation of the oxide surface with formation of surface oxygen vacancies (as the key step) and their replenishment by gas-phase oxygen. Thus, the density of surface oxygen vacancies in the solid oxide plays an important role in their catalytic activity in CO oxidation. Nevertheless, according to Tascón et al. [61] the CO oxidation reaction over mixed oxides may also follow a suprafacial mechanism in which lattice oxygen is not involved as presented in the following mechanism [62]:



In the present study, XPS analyses indicate the presence of both $\text{O}_{\text{Lattice}}$ and $\text{O}_{\text{Adsorbed}}$ species (Fig. 2c). As mentioned above, a shoulder of $\text{O}_{\text{Adsorbed}}$ at high BE is identified to be hydroxyl groups, mainly Fe-OH and Co-OH and CO_3^{2-} [63]. The catalyst with low Co content tended to have a larger amount of surface adsorbed oxygen in comparison with the sample with high Co content. It is therefore suggested that the adsorbed oxygenated species, mainly CO_3^{2-} and OH^- , could effectively participate in the oxidation of CO.

The TPR/TPO experiment reveals that the Co-Fe-O redox reaction is shifted to higher temperatures increasing the Co content. In an ideal state the reduction of Fe_2O_3 requires higher temperature than that of Co_3O_4 . The Co^{2+} - Co^{3+} ion pairs are known to be very active in low-temperature CO oxidation [33] over cobalt oxide; this higher activity is strongly dependent on the reduction of Co^{3+} to Co^{2+} after CO adsorption [32,64]. Therefore, the presence in Co-Fe-O composites of both Co^{2+} and Co^{3+} together with Fe^{3+} in the O- and T-sites should enable a decrease of the reduction temperature, accompanied with an improvement of the catalytic performance of CO over samples with higher Co content ($\text{Co}_{2.1}\text{Fe}_{0.9}\text{O}_4$ and $\text{Co}_{1.8}\text{Fe}_{1.2}\text{O}_4$), which have the following cationic distribution in the O-site ($[\text{Co}^{2+}\text{Fe}^{3+}\text{Co}^{3+}]_{\text{O-site}}\text{O}_4$). Surprisingly, the opposite behaviour is observed with $\text{Co}_{0.9}\text{Fe}_{2.1}\text{O}_4$ (the most active sample) in which only Fe^{3+} and Co^{2+} are present in the O-site: $[\text{Fe}^{3+}\text{Co}^{2+}]_{\text{O-site}}\text{O}_4$. A similar behaviour has been observed by Yu Yao [33] with CoAl_2O_4 spinel in which Co was stabilized as Co^{2+} , causing its inactivity in the CO oxidation through a redox mechanism. It can therefore be suggested here that the CO oxidation over Co-Fe-O catalyst does not proceed through a redox mechanism even if $\text{Co}_{0.9}\text{Fe}_{2.1}\text{O}_4$ presents the lowest reduction temperature. This hypothesis is strongly supported by the fact that CO oxidation of $\text{Co}_{2.1}\text{Fe}_{0.9}\text{O}_4$ is initiated at ~ 200 °C while the reduction (Fig. 5a)

started at ~ 280 °C. The earlier initiation of the reaction at low temperature can be assigned to the surface-adsorbed oxygen revealed by XPS analysis. Summarizing these observations, it is thus proposed that CO oxidation over Co-Fe-O follows a suprafacial mechanism where CO molecules react with adsorbed oxygen, mainly as CO_3^{2-} and OH^- , to form CO_2 . This is in excellent agreement with the results reported in the literature for the same material [30,65].

In this investigation, the results demonstrate that the combination of Fe and Co in the same phase intrinsically improves the redox properties and the catalytic performance of Co-Fe-O vs. Fe_2O_3 in CO oxidation and causes the shift of the optical band gap toward lower values. It is therefore likely that the controlled variation of the band gap energy (E_g) in catalyst materials could be used as a tool to reflect their redox properties. The sample possessing narrow E_g enables high mobility of electrons in the materials and consequently, the migration of O^{2-} from the bulk to the surface which occurs through electron transfer, will become easier as confirmed by the reduction of the catalyst with low E_g at low temperature.

In spite of the interesting observations in this study regarding the close interaction of the optical and redox properties and the consequent influence on the catalytic potential regarding the redox mechanism, we would still like to emphasize that the catalytic activity is mainly due to a surface mechanism in which mainly CO_3^{2-} and OH^- functions are involved.

Conclusions

Cobalt-iron mixed oxide thin films were prepared by Pulse Spray Evaporation Chemical Vapour Deposition and their properties were systematically characterized. The results show that the Co:Fe ratio in Co-Fe-O thin films strongly influences their physicochemical properties. In particular, the variation of the cobalt amount in the Co-Fe-O structure plays a decisive role in controlling both the band gap energies and the redox properties of Co-Fe-O films. Co-Fe mixed oxides exhibit better performance than pure α - Fe_2O_3 . The performance of Fe-Co mixed oxide catalysts for the CO oxidation reaction was significantly affected by the adsorbed oxygen species and the cobalt content. The XPS and TPR analyses suggest that the suprafacial mechanism is dominant in the CO oxidation over Co-Fe-O catalysts.

Acknowledgements

P. Mountapbeme Kouotou and A. El Kasmi kindly acknowledge the Deutscher Akademischer Austauschdienst (DAAD) for the financial support during their research stays at Bielefeld University. Z. Y. Tian is grateful for a fellowship of the Alexander von Humboldt Foundation, and P. H. Tchoua Ngamou acknowledges partial support by the DFG.

Notes and references

^a Department of Chemistry, Bielefeld University, Universitätsstraße 25, D-33615 Bielefeld, Germany.

^b Department of Physics, Bielefeld University, Universitätsstraße 25, D-33615 Bielefeld, Germany.

^c Present address: Institute of Engineering Thermophysics, Chinese Academy of Sciences, Beijing 100190, China.

* Corresponding authors.

Z.Y. Tian: Tel/Fax: +86-10 82483184. E-mail: tianzhenyu@iet.cn

P. Mountapbeme Kouotou. E-mail: patrick.mountap@uni-bielefeld.de

† Electronic supplementary information (ESI) available. Table ESI 1: estimated composition at the surface of the Co-Fe-O thin films; Fig. ESI 1: iron oxide and cobalt oxide reference; Fig. ESI 2: original spectra of Co2p and Fe2p; Fig. ESI 3: additional HIM micrographs. See DOI: 10.1039/b000000x/

- 1 W. Gac, *Appl. Catal. B: Environ.*, 2007, **75**, 107.
- 2 M. S. Chen and D. W. Goodman, *Science*, 2004, **306**, 252.
- 3 T. Cheng, Z. Fang, Q. Hu, K. Han, X. Yang and Y. Zhang, *Catal. Commun.*, 2007, **8**, 1167.
- 4 C. Jones, K. J. Cole, S. H. Taylor, M. J. Crudace and G. J. Hutchings, *J. Mol. Catal. A: Chem.*, 2009, **305**, 121.
- 5 M. Haruta, *Nature*, 2005, **437**, 1098.
- 6 S. Wicker, K. Großmann, N. Bârsan and U. Weimar, *Sensor Actuat. B: Chem.*, 2013, **185**, 644.
- 7 R. K. Kulkalekar and A. V. Salker, *Catal. Commun.*, 2010, **12**, 193.
- 8 J. Shao, P. Zhang, X. Tang, B. Zhang, W. Song, Y. Xu and W. Shen, *Chin. J. Catal.*, 2007, **28**, 163.
- 9 I. X. Green, W. Tang, M. Neurock and J. T. Yates Jr., *Science*, 2011, **333**, 736.
- 10 L. F. Liotta, H. Wu, G. Pantaleo and A. M. Venezia, *Catal. Sci. Technol.*, 2013, **3**, 3085.
- 11 W. Song and E. J. M. Hensen, *Catal. Sci. Technol.*, 2013, **3**, 3020.
- 12 M. F. M. Zwinkels, S. G. Järås, P. G. Menon and T. A. Griffin, *Catal. Rev. Sci. Eng.*, 1993, **35**, 319.
- 13 D. Barreca, D. Bekermann, E. Comini, A. Devi, R. A. Fischer, A. Gasparotto, M. Gavagnin, C. Maccato, C. Sada, G. Sberveglieri and E. Tondello, *Sensor Actuat. B: Chem.*, 2011, **160**, 79.
- 14 M. J. Aaron, C. A. Heather, *Appl. Mater. Inter.*, 2010, **2**, 2804.
- 15 X. C. Jiang and A. B. Yu, *J. Mater. Process. Technol.*, 2009, **209**, 4558.
- 16 X. Liu, J. Liu, Z. Chang, X. Sun and Y. Li, *Catal. Commun.*, 2011, **12**, 530.
- 17 W. K. Jozwiak, E. Kaczmarek, T. P. Maniecki, W. Ignaczak and W. Maniukiewicz, *Appl. Catal. A: Gen.*, 2007, **326**, 17.
- 18 S. C. Kwon, M. Fan, T. D. Wheelock and B. Saha, *Sep. Purif. Technol.*, 2007, **58**, 40.
- 19 P. Li, D. E. Miser, S. Rabiei, R. T. Yadav and M. R. Hajaligol, *Appl. Catal. B: Environ.*, 2003, **43**, 151.
- 20 P. Mountapbeme Kouotou, Z. Y. Tian, H. Vieker and K. Kohse-Höinghaus, *Surf. Coat. Technol.*, 2013, **230**, 59.
- 21 Y. Lou, L. Wang, Y. Zhang, Z. Zhao, Z. Zhang, G. Lu and Y. Guo, *Catal. Today*, 2011, **175**, 610.
- 22 S. Sun, L. Yang and G. Pang, S. Feng, *Appl. Catal. A: Gen.*, 2011, **401**, 199.
- 23 Z. Zhao, R. Jin, T. Bao and X. Lin, G. Wang, *Appl. Catal. B: Environ.*, 2011, **110**, 154.
- 24 N. Ballarini, F. Cavani, S. Passeri, L. Pesaresi, A. F. Lee and K. Wilson, *Appl. Catal. A: Gen.*, 2009, **366**, 184.
- 25 T. A. S. Ferreira, J. C. Waerenborgh, M. H. R. M. Mendonca, M. R. Nunes and F. M. Costa, *Solid State Sci.*, 2003, **5**, 383.
- 26 S. Kawano, N. Achiwa, N. Yamamoto and S. N. Higashi, *Mater. Res. Bull.*, 1976, **11**, 911.
- 27 G. D. Rieck and J. J. M. Thijssen, *Acta Crystallogr. Sect. B*, 1968, **24**, 982.
- 28 J. G. Na, T. D. Lee and E. C. Kim, S. J. Park, *J. Mater. Sci. Lett.*, 1993, **12**, 361.
- 29 V. Crocellà, F. Cavani, G. Cerrato, S. Cocchi, M. Comito, G. Magnacca and C. Morterra, *J. Phys. Chem. C*, 2012, **116**, 14998.
- 30 A. Biabani-Ravandi, M. Rezaei and Z. Fattah, *Chem. Eng. Sci.*, 2013, **94**, 237.
- 31 Z. Y. Tian, P. Mountapbeme Kouotou, A. El Kasmi, P. H. Tchoua Ngamou, H. Vieker, A. Beyer, A. Götzhäuser and K. Kohse-Höinghaus, *Proc. Combust. Inst.*, 2014 (revised).
- 32 M. Haruta, S. Tsubota, T. Kobayashi, H. Kageyama, M. J. Genet and B. Delmon, *J. Catal.*, 1993, **144**, 175.
- 33 Y.-F. Yu Yao, *J. Catal.*, 1974, **33**, 108.
- 34 J.-P. Sénateur, C. Dubourdieu, F. Weiss, M. Rosina and A. Abrutis, *Adv. Mater.*, 2000, **10**, 155.
- 35 P. Mountapbeme Kouotou, Z. Y. Tian, U. Mundloch, N. Bahlawane and K. Kohse-Höinghaus, *RSC Adv.*, 2012, **2**, 10809.
- 36 P. H. Tchoua Ngamou and N. Bahlawane, *Chem. Mater.*, 2010, **22**, 4158.
- 37 V. Vannier, M. Schenk, K. Kohse-Höinghaus and N. Bahlawane, *J. Mater. Sci.*, 2012, **47**, 1348.
- 38 Z. Y. Tian, P. H. Tchoua Ngamou, V. Vannier, K. Kohse-Höinghaus and N. Bahlawane, *Appl. Catal. B: Environ.*, 2012, **117-118**, 125.
- 39 H. Le Trong, L. Presmanes, E. De Grave, A. Barnabé, C. Bonningue, P. Tailhades, *J. Magn. Magn. Mater.*, 2013, **334**, 66.
- 40 T. Yu, Z. X. Shen, Y. Shi and J. Ding, *J. Phys. Condens. Mater.*, 2002, **14**, 613.
- 41 Y. Qu, H. Yang, N. Yang, Y. Fan, H. Zhu and G. Zou, *Mater. Lett.*, 2006, **60**, 3548.
- 42 N. Viart, G. Rebmann, G. Pourroy, J. L. Loison, G. Versini, F. Huber, C. Ulhaq-Bouillet, C. Meny, P. Panissod and L. Saviot, *Thin Solid Films*, 2005, **471**, 40.
- 43 C. Altavilla, E. Ciliberto and A. Aiello, *Chem. Mater.*, 2007, **19**, 5980.
- 44 J. L. Gautier, E. Rios, M. Gracia, J. F. Marco and J. R. Gancedo, *Thin Solid Films*, 1997, **311**, 51.
- 45 Z. Zhou, Y. Zhang, Z. Wang, W. Wei, W. Tang, J. Shi and R. Xiong, *Appl. Surf. Sci.*, 2008, **254**, 6972.
- 46 M. C. Biesinger, B. P. Payne, A. P. Grosvenor, L. W. M. Lau, A. R. Gerson and R. St. C. Smart, *Appl. Surf. Sci.*, 2011, **257**, 2717.
- 47 M. Arenz, K. J. J. Mayrhofer, V. Stamenkovic, B. B. Blizanac, T. Tomoyuki, P. N. Ross and N. M. Markovic, *J. Am. Chem. Soc.*, 2005, **127**, 6819.
- 48 E. Frackowiak and F. Béguin, *Carbon*, 2001, **39**, 937.
- 49 B. Y. Jibril, *React. Kinet. Catal. Lett.*, 2005, **86**, 171.
- 50 Z. Y. Tian, N. Bahlawane, V. Vannier and K. Kohse-Höinghaus, *Proc. Combust. Inst.*, 2013, **34**, 2261.

- 51 R. C. Rai, S. Wilser, M. Guminiak, B. Cai and M. L. Nakarmi, *Appl. Phys. A*, 2012, **106**, 207.
- 52 A. V. Ravindra, P. Padhan and W. Prellier, *Appl. Phys. Lett.*, 2012, **101**, 161902.
- 53 A. Bielański and J. Haber, *Catal. Rev.: Sci. Eng.*, 1979, **19**, 1.
- 54 D. Auvergne, J. Camassel and H. Mathieu, *Phys. Rev. B*, 1975, **11**, 2251.
- 55 M. I. Zaki, M. A. Hasan and L. Pasupulety, *Appl. Catal. A: Gen.*, 2000, **198**, 247.
- 56 F. Wyrwalski, J.-M. Giraudon and J.-F. Lamonier, *Catal. Lett.*, 2010, **137**, 141.
- 57 P. J. Gellings and H. J. M. Bouwmeester, *Catal. Today*, 1992, **12**, 1.
- 58 J. Y. Lee, S. P. Cho, S. H. Hong, S. H. Choi and S. C. Hong, *Proc. of 2nd Joint Int. Conf. on "Sustainable Energy and Environment"*, Nov. 21-13, 2006, Bangkok, Thailand, D-014 (P).
- 59 H. Bao, X. Chen, J. Fang, Z. Jiang and W. Huang, *Catal. Lett.*, 2008, **125**, 160.
- 60 E. Aneggi, J. Llorca, M. Boaro and A. Trovarelli, *J. Catal.*, 2005, **234**, 88.
- 61 J. M. D. Tascón, J. L. G. Fierro and L. G. Tejuca, *Z. Phys. Chem. NF*, 1981, **124**, 249.
- 62 W. Yang, R. Zhang, B. Chen, N. Bion, D. Duprez and S. Royer, *J. Catal.*, 2012, **295**, 45.
- 63 Q. Yang, H. Choi, S. R. Al-Abed and D. D. Dionysiou, *Appl. Catal. B: Environ.*, 2007, **74**, 170.
- 64 X. Xie, Y. Li, Z.-Q. Liu, M. Haruta and W. Shen, *Nature*, 2009, **458**, 746.
- 65 G. Evans, I. V. Kozhevnikov, E. F. Kozhevnikova, J. B. Claridge, R. Vaidhyanathan, C. Dickinson, C. D. Wood, A. I. Cooper and M. J. Rosseinsky, *J. Mater. Chem.*, 2008, **18**, 5518.

Electronic Supplementary Information (ESI)

Structure-activity relation of spinel-type Co-Fe oxides for low-temperature CO oxidation

P. Mountapmbeme Kouotou,^{a,*} H. Vieker,^b Z.Y. Tian,^{a,c,*} P.H. Tchoua Ngamou,^a A. El Kasmi,^a A. Beyer,^b A. Götzhäuser,^b and K. Kohse-Höinghaus^a

^a Department of Chemistry, Bielefeld University, Universitätsstraße 25, D-33615 Bielefeld, Germany

^b Department of Physics, Bielefeld University, Universitätsstraße 25, D-33615, Bielefeld, Germany

^c Present address: Institute of Engineering Thermophysics, Chinese Academy of Sciences, Beijing 100190, P.R. China

* Corresponding author.

Z.Y. Tian: Tel/Fax: +86-10 82483184; E-mail: tianzhenyu@iet.cn

P. Mountapmbeme Kouotou. E-mail: Patrick.mountap@uni-bielefeld.de

Table ESI 1: Estimated composition at the surface of the Co-Fe thin films.

	C1s	O1s	Co2p	Fe2p	Co/Fe	Co	Fe	O
Co _{0.9} Fe _{2.1} O ₄	43%	49%	3%	6%	0.43	0.9	2.1	4
Co _{1.8} Fe _{1.2} O ₄	37%	51%	7%	5%	1.47	1.8	1.2	4
Co _{2.1} Fe _{0.9} O ₄	35%	49%	11%	5%	2.23	2.1	0.9	4

Details about the XPS analysis

The surface composition was determined by the means of X-ray photoelectron spectroscopy (XPS). XPS was done in a multi technique ultra-high vacuum instrument (Multiprobe, Omicron Nanotechnology) using a monochromated Al K α X-ray source (1486.7 eV, 280 W) and a hemi-spherical electron energy analyzer (Sphera) in constant analyzer energy mode (25 eV) and a step size of 0.05 eV. The sample was located under an angle of 13° from the surface normal to the electron detector. The base pressure of the chamber is 2×10⁻¹⁰ mbar. CasaXPS was used to analyze the spectra, and a Shirley background subtraction procedure was employed. The elemental composition was calculated using the area of the Fe2p, Co2p, C1s and O1s peaks with the according Scofield cross-sections. The peak areas of the Fe2p and Co2p signals were corrected for Auger LMM peaks that each metal has in the 2p-area of the other metal. In both cases, mainly the 2p_{3/2} parts of the spectra are affected. To do the correction, 2 sputter-cleaned metal oxide samples made by PSE-CVD

were measured as references. The intensity correction of the peak area was done according to the following formula:

$$A(\text{Fe} - 2p) = \frac{M(\text{Fe}) - K(\text{Co})M(\text{Co})}{1 - (K(\text{Co})K(\text{Fe}))}$$

$$A(\text{Co} - 2p) = \frac{M(\text{Co}) - K(\text{Fe})M(\text{Fe})}{1 - (K(\text{Co})K(\text{Fe}))}$$

Definitions:

A = Area

K = [A(LMM) / A(2p)] (Correction factor)

Measured Areas:

M(Fe) = A(Fe-2p+Co-LMM)

M(Co) = A(Co-2p+Fe-LMM)

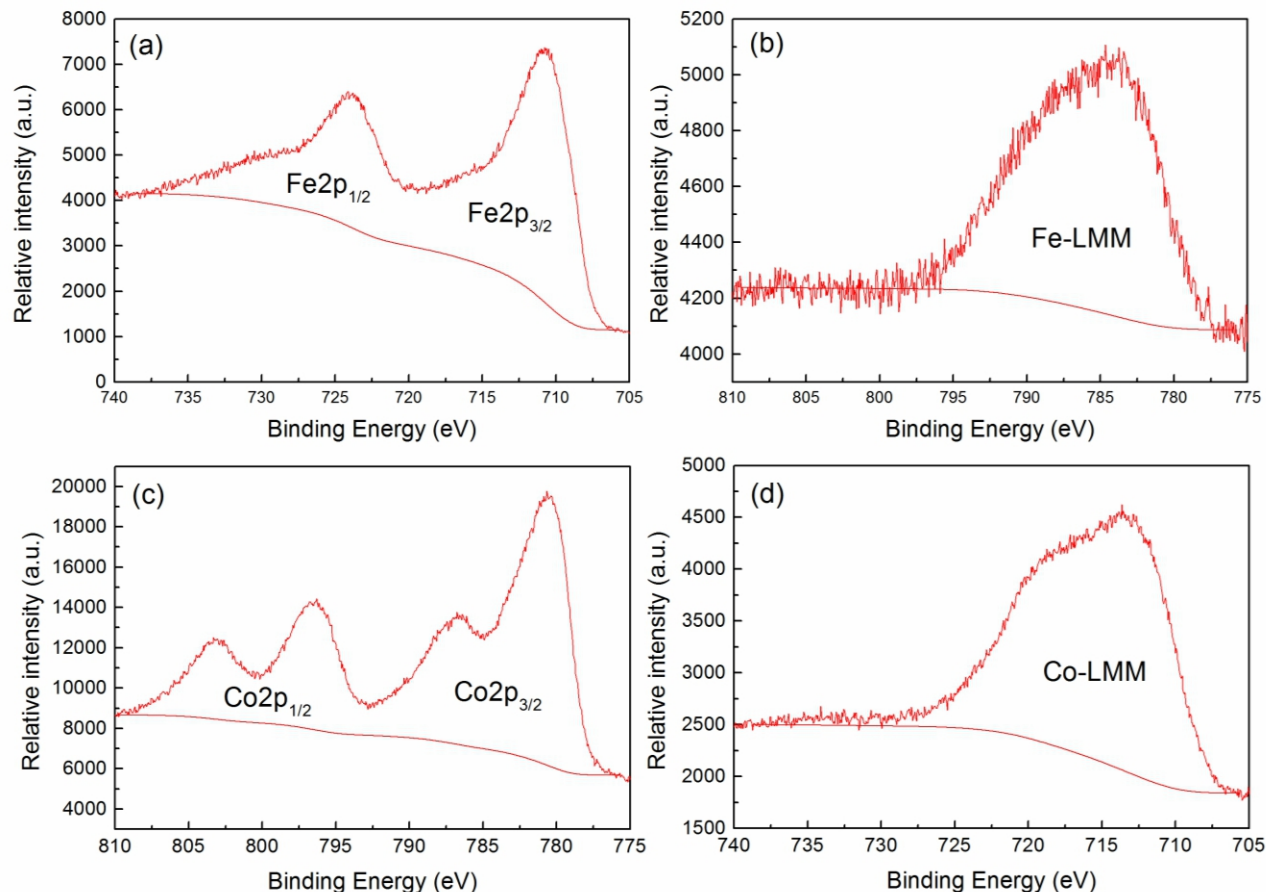


Fig. ESI 1 Pure iron oxide (a, b) and cobalt oxide (c, d) reference sample.

Area ratio K (Fe) = A(Fe-LMM) / A(Fe-2p) = 14.3 / 84.8 = 0.148

Area ratio K (Co) = A(Co-LMM) / A(Co-2p) = 41.1 / 206.8 = 0.210

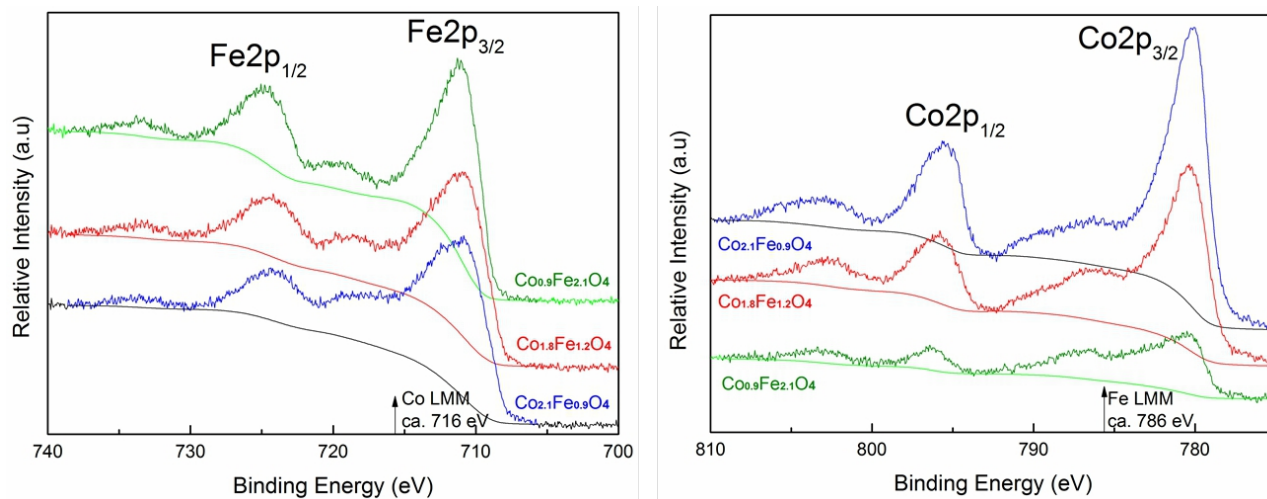


Fig. ESI 2 The original XPS spectra of Fe2p and Co2p with the corresponding Shirley backgrounds. In addition, the subtraction of the Auger signals was done to obtain less-disturbed iron and cobalt spectra. This was done with CasaXPS by subtracting the LMM references from the 2p data (see Fig 2a and 2b in the main text).

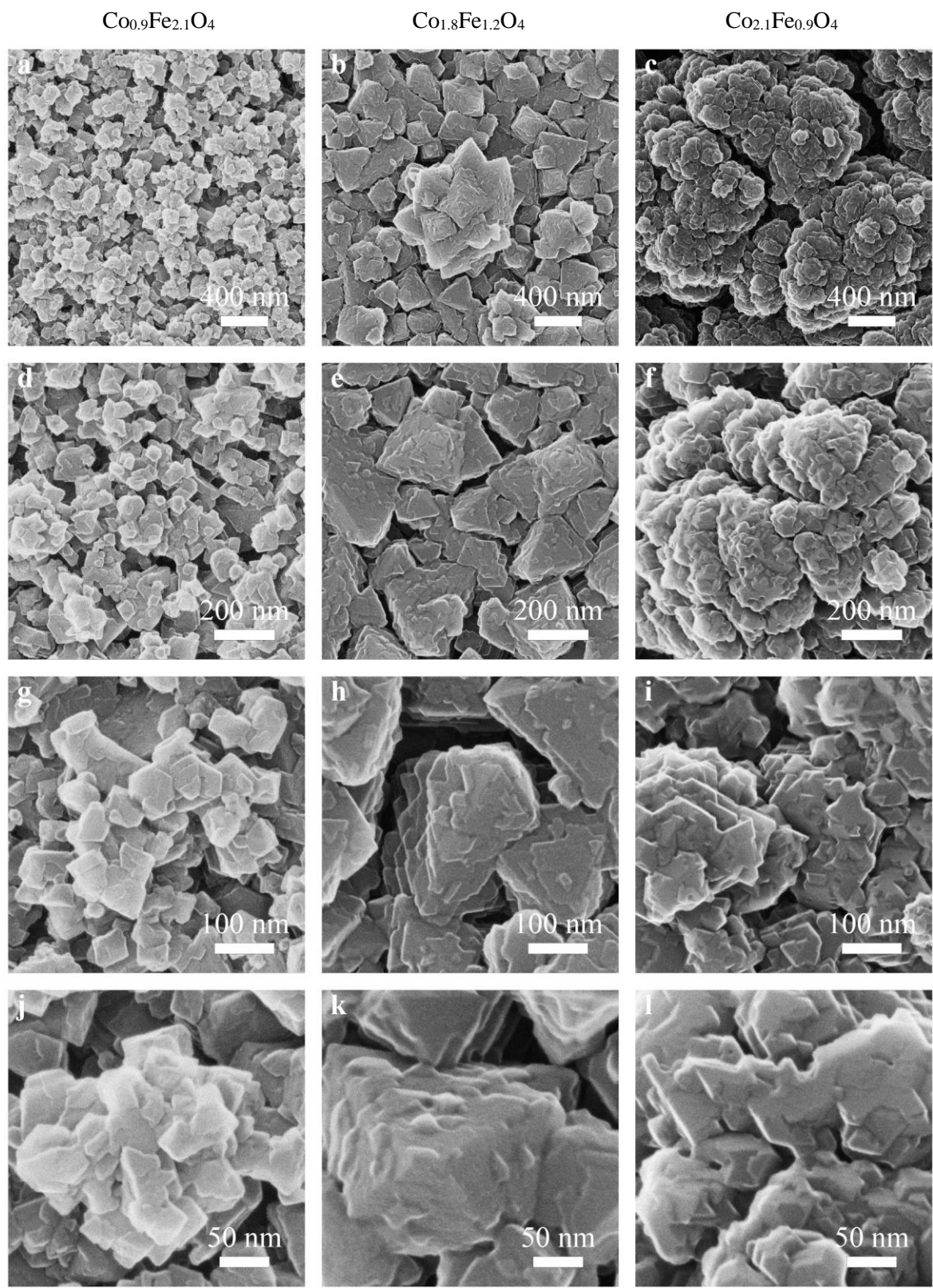


Fig ESI 3 Additional HIM micrographs.

G) Manuscript 2

Zhen-Yu Tian , Patrick Mountapmbeme Kouotou, Achraf El Kasmi, Patrick Hervé Tchoua Ngamou, Henning Vieker, André Beyer, Armin Gölzhäuser and Katharina Kohse-Höinghaus

Low-temperature deep oxidation of olefins and DME over cobalt ferrite

Proceeding of the Combustion Institute (Revised)

Low-temperature deep oxidation of olefins and DME over cobalt ferrite

Zhen-Yu Tian^{a,c,*}, Patrick Mountapmbeme Kouotou^a, Achraf El Kasmi^a, Patrick Hervé Tchoua Ngamou^a, Katharina Kohse-Höinghaus^a, Henning Vieker^b, André Beyer^b, Armin Götzhäuser^b

^a Department of Chemistry, Bielefeld University, Universitätsstraße 25, D-33615 Bielefeld, Germany

^b Department of Physics, Bielefeld University, Universitätsstraße 25, D-33615 Bielefeld, Germany

^c Present address: Institute of Engineering Thermophysics, Chinese Academy of Sciences, Beisihuanxi 11, 100190 Beijing, China

Corresponding author: Prof. Dr. Zhen-Yu Tian
Institute of Engineering Thermophysics
Chinese Academy of Sciences
Beisihuanxi 11
100190 Beijing, China
Fax: +86-8254 3052
E-mail: tianzhenyu@iet.cn

Colloquium: **HETEROGENEOUS COMBUSTION and MATERIAL SYNTHESIS**

Details of the words count (Method 1):

- Text: 3663
- References: $(33+2) \times 2.3 \times 7.6 = 612$
- Table: 0
- Figures and Captions: 1534 (Figure 1 = $(46+10) \times 2.2 + 11 = 134$, Figure 2 = $(51+10) \times 2.2 + 11 = 145$, Figure 3 = $(120+10) \times 2.2 + 17 = 303$, Figure 4 = $(108+10) \times 2.2 + 13 = 273$, Figure 5 = $(57.2+10) \times 2.2 + 28 = 176$, Figure 6 = $(50+10) \times 2.2 + 15 = 147$, Figure 7 = $(67.3+10) \times 2.2 \times 2 + 16 = 356$)

TOTAL = 5809

Supplemental Material is included in this paper.

* Corresponding author, Tel/Fax: +86-10 8254 3184, E-mail: tianzhenyu@iet.cn.

Low-temperature deep oxidation of olefins and DME over cobalt ferrite

Zhen-Yu Tian^{a,c,*}, Patrick Mountapmbeme Kouotou^a, Achraf El Kasmi^a, Patrick Hervé Tchoua Ngamou^a, Katharina Kohse-Höinghaus^a, Henning Vieker^b, André Beyer^b, Armin Götzhäuser^b

^a *Department of Chemistry, Bielefeld University, Universitätsstraße 25, D-33615 Bielefeld, Germany*

^b *Department of Physics, Bielefeld University, Universitätsstraße 25, D-33615 Bielefeld, Germany*

^c *Present address: Institute of Engineering Thermophysics, Chinese Academy of Sciences, Beisihuanxi 11, 100190 Beijing, China*

Abstract: This work reports the facile synthesis of cobalt ferrite catalysts by pulsed spray evaporation chemical vapor deposition (PSE-CVD) for low-temperature oxidation of dimethyl ether and olefin exhaust emission. To better understand the structure-performance relationship, the prepared thin films were comprehensively characterized in terms of phases, surfaces, and redox properties. A well-crystallized inverse spinel structure was revealed by both XRD and Raman analyses. Helium ion microscopy (HIM) images show that the obtained films have cauliflower structure with apparent open porosity. The catalytic performance of the as-prepared cobalt ferrite was evaluated with a fixed-bed quartz reactor-FTIR system. The results indicate that the cobalt ferrites were very active for the total oxidation of propene, *n*-butene, and DME at low temperature and no CO was observed during the oxidation processes. The attractive performance of cobalt ferrite catalysts is attributed to a redox mechanism which involves the synergistic effect of the morphology, reducibility, and lattice oxygen mobility.

Keywords: Catalytic oxidation; Olefins; Dimethyl ether; Cobalt ferrite; Chemical vapor deposition.

* Corresponding author, Tel/Fax: +86-10 8254 3184, E-mail: tianzhenyu@iet.cn.

1. Introduction

Catalytic combustion is generally known as one of the most efficient and promising technologies for the abatement of volatile organic compounds (VOCs) and deep oxidation of different fuels and exhaust emissions. Typical combustion catalysts involve noble metals such as Au, Pt, and Pd [1]. However, the use of such noble metals suffers from high cost, tendency to poisoning and low thermal stability. In recent years, transition metal oxides, especially binary oxides with bifunctional properties, have become suitable alternatives as catalysts for deep oxidation applications.

Among the transition metal oxides, cobalt ferrite has been widely investigated due to its high Curie temperature, high coercivity, excellent chemical stability and mechanical hardness [2]. Thin films of cobalt ferrite have covered a wide range of potential applications in high-density magnetic recording media, microwave devices, magnetic fluids, gas-sensing materials, catalytic materials as well as micro-electromechanical system devices [3,4]. Although cobalt ferrite exhibits attractive catalytic performance, the related studies concerning its catalytic application in the removal of VOCs [4] and deep oxidation of fuels [5] are scarce.

It has been reported that the properties of ferrites were governed by the choice of the cations and their distribution between tetrahedral and octahedral sites of the spinel lattice [6]. As the synthesis process can directly affect the properties, it is important to involve suitable methods. Many efforts have been made to prepare cobalt ferrite thin films, including sol-gel, pulsed laser deposition [2], multiple spin-coating [7], vacuum evaporation, sputtering, and chemical vapor deposition (CVD) [5]. Compared to other strategies that usually suffer from high cost of the precursors or organic solvents and their inherent toxicity, CVD with metal acetylacetonates and alcohols captures great attention. Recently, the application of pulsed spray evaporation (PSE) CVD has become a promising technique in synthesizing thin films of spinels [8,9] with the advantages of low cost, tailored

composition, and easy control of the thickness and morphology of the samples. PSE-CVD allows using a wide range of precursors and facile deposition of single-phase films with tailored composition on flexible substrates, which is very useful as a model to evaluate the surface contribution to the catalytic oxidation reactions. Thus, PSE-CVD exhibits the potential to prepare cobalt ferrite films as catalysts.

This work reports for the first time the catalytic performance of cobalt ferrite prepared by PSE-CVD towards the deep oxidation of olefins and DME. Several characterization techniques with respect to structure, surface, and thermal properties were used to reveal the structure-activity relationship. The catalytic performance of the prepared cobalt ferrite films towards low-temperature deep oxidation of olefins and DME was investigated in a fixed-bed quartz reactor under plug-flow conditions at atmospheric pressure.

2. Experimental

2.1 Catalyst preparation

Cobalt ferrite thin films were prepared using a cold-wall stagnation point-flow CVD reactor, which is associated with a PSE system for the delivery of liquid precursor feedstock [8]. The details of the experimental setup can be found elsewhere [8], and only a brief description is given here. Cobalt acetylacetonate ($\text{Co}(\text{acac})_3$) and iron acetylacetonate ($\text{Fe}(\text{acac})_3$) were dissolved with respective concentrations of 5×10^{-3} mol/L in tetrahydrofuran and then blended with a molar ratio of Co:Fe = 1:1 to obtain single-phase films. The PSE delivery was achieved with a frequency of 4 Hz and a valve opening time of 2.5 ms. The feedstock, with a feeding rate of 0.8 mL/min, was injected as a fine spray into the evaporation chamber kept at 220 °C. The resulting vapor was transported to the deposition chamber kept at 220 °C, with N_2/O_2 flow rates of 0.16/1.0 standard liter per minute

(SLM), respectively. During the deposition process, bare glass, stainless steel, and mesh grid (stainless steel, SPW 40, 80400, micron-retention 36-45 μm) were used as substrates and heated with a flat resistive heater. After optimization, the substrate temperature was fixed at 400 $^{\circ}\text{C}$ and the total pressure in the reactor was kept at 30 mbar. Flow rates of gases were controlled by mass-flow controllers (MKS). The thickness of the obtained films with an uncertainty of $\pm 2\%$ was estimated gravimetrically using a microbalance (Mettler ME 30). The experimental conditions are summarized in Table S1 in the Supplemental Material (SM).

2.2 Characterization

X-ray diffraction (XRD) analysis was carried out with a Phillips X'Pert Pro MRD (PW3830) instrument using Cu $K\alpha$ ($\lambda = 0.154056$ nm) radiation and operated at 40 kV and 30 mA. Data were recorded in the 2θ range from 20° to 80° , with a step size of 0.05° . The crystalline phase was monitored by referring to the powder XRD database (JCPDS-ICDD). A home-made Raman spectrometer, with spectral resolution of 4 cm^{-1} , was also used to confirm the phases of the obtained oxides. An Omicron Multiprobe X-ray photoelectron spectrometer (XPS) with an Al $K\alpha$ source was employed. Helium ion microscopy (HIM, Carl Zeiss Orion Plus $^{\circledR}$) was used to ascertain the morphology of the deposited films. To investigate the catalyst's redox properties, emission Fourier transform infrared (FTIR) spectroscopy was used in temperature-programmed mode with a ramp of $3\text{ }^{\circ}\text{C}/\text{min}$ using 5% of H_2/O_2 mixture in Ar (0.05 L/min). The detailed description of the XPS and HIM procedures can be found in the Supplemental Material.

2.3 Surface activity

The catalytic performance of cobalt ferrite films was investigated with a continuous-flow fixed-bed reactor (30 cm in length, 0.9 cm inner diameter) at atmosphere pressure. A feed of Ar gas

containing 1% of fuel and 10% of O₂ was introduced into a tubular reactor at a total flow rate of 15 mL/min, corresponding to a weight hourly space velocity (WHSV) of 45000 ml g⁻¹_{cat} h⁻¹. The temperature of the reactor was raised with a ramp of 3 °C/min using a temperature controller (Horst HT60). The temperature of the mesh (with 20 mg coating or without coating) inside the reactor was recorded using K-thermocouples and a digital thermometer (Greisinger GMH3250). The analysis of VOCs and products was conducted by online FTIR spectroscopy with an uncertainty of ± 5%, and details of the data treatment are given in our recent work [8].

3 Results and discussion

3.1 Phase identification

The phase of the deposited cobalt ferrite thin films with a thickness of ~300 nm was analyzed using XRD and Raman scattering spectroscopy, as displayed in Figs. 1 and 2, respectively. XRD patterns of Co₃O₄ (JCPDS Nr. 74-1656) and CoFe₂O₄ (JCPDS Nr. 03-0864) are shown as references (Fig. 1). The well-defined diffraction peaks are observed at 2θ of 30.73°, 36.27°, 44.15°, 58.44°, and 64.09°, which can be assigned to (220), (331), (440), (511), and (440) orientations of the cobalt ferrite. Moreover, two weak peaks observed at 38.04° and 54.67° can be attributed to (222) and (422) crystallographic planes. No other diffraction peaks corresponding to the formation of impurity phases were detected, revealing the high purity of the synthesized thin films. The cell parameter is determined to be $a = 8.388 \text{ \AA}$. The crystallite size (D) and the micro-strain (ϵ) were determined to be 35 nm and 0.05% from the XRD patterns by using the Scherrer line broadening analysis $D = 0.9\lambda/\beta\cos\theta$ and $\epsilon = \beta/2\cot\theta$ on the (311) plane, where λ is the wavelength of the X-ray radiation and β is the diffraction broadening of the peak at half height for Bragg's angle θ .

Figure 2 shows the Raman spectrum of a cobalt ferrite film recorded at room temperature. Five

well-defined peaks are located at 233, 287, 480, 609, and 682 cm^{-1} , whose positions and widths are in good agreement with previous reports for the spinel of cobalt ferrite [10]. In the frequency range of 200-700 cm^{-1} , the normal spinel structure of cobalt ferrite possesses two sets of Raman-active modes depicted as T_d and O_h . The high-frequency bands at 682 and 609 cm^{-1} , corresponding to the T_d -site mode, are attributed to the tetrahedral sub-lattice. The low-frequency bands at 480, 287, and 233 cm^{-1} are related to the O_h -site mode, reflecting the local lattice effect in the octahedral sub-lattice [11]. It is worth mentioning that the band peaking at 521 cm^{-1} could result from the plasma peaks of the laser or the Raman peak of the stainless steel substrate. These measurements indicate that all samples are single-phase cobalt ferrite, which further confirm the XRD results.

3.2 Composition

To identify the species involved in the catalytic oxidation, the actual surface composition of the prepared cobalt ferrite was determined by *ex-situ* XPS analysis. Details regarding the elemental compositions and ratios are collected in Table S2 (see SM). A certain amount of carbon was formed on the surface, which could be a result of contamination by precursor decomposition products during the synthesis processes. In addition, oxygen and carbon are known to adsorb from air. Based on the Co/Fe ratio, the prepared cobalt ferrite can be depicted as $\text{Co}_{2.1}\text{Fe}_{0.9}\text{O}_4$.

The spectra of Co 2p, Fe 2p, and O 1s are presented in Fig. 3. The interpretation of the Co and Fe spectra is not straightforward as an Auger peak from the other respective metal overlays mainly the 2p_{3/2} part. Figure 3a shows the spectra of Co 2p_{3/2} and Co 2p_{1/2} with peaks at binding energies (BE) observed at 780.1 and 795.6 eV, respectively, corresponding to a normal spin-orbital splitting of Co 2p [12]. The strong satellite peak at a BE of 803.2 eV is indicative of the presence of Co^{2+} ions, whereas the satellite at 786.3 eV is overlaid due to the Fe LMM line [13]. According to Gautier et al. [14], the Co 2p_{1/2} part was deconvoluted to 75% Co^{2+} and 25% Co^{3+} . Figure 3b displays the Fe 2p

spectrum with the Fe $2p_{3/2}$ peak at 711.3 eV and a doublet splitting of $\Delta E = 13.0$ eV. In addition, a satellite structure at 734 eV was observed. These BEs are due to the contributions from Fe^{3+} ions and are consistent with those reported for spin orbit components of Fe^{3+} [12,15]. The oxygen O 1s spectrum of the prepared film is shown in Fig. 3c. The deconvolution shows a dominant peak at 529.8 eV, which is attributed to the lattice oxygen (O_{Lat}). The other two components can be attributed to adsorbed oxygenates (O_{ads}) [13]. The peak at 531.1 eV is assigned to the possible defects and contaminations such as chemisorbed or dissociated oxygen, hydroxyl species, under-coordinated lattice oxygen, CoO/ Fe_2O_3 surface phases, or species intrinsic to the surface of the spinel [16]. The other peak at 533.3 eV probably results from the carbonate species CO_3^{2-} . O_{ads} has been reported to have a positive effect on the total oxidation of hydrocarbons [8,17], and the presence of O_{ads} is expected to affect the physicochemical property of the synthesized cobalt ferrite films and their catalytic applications.

3.3 Morphology

To obtain information on the surface morphology and spatial organization of the synthesized cobalt ferrite thin films, micrographs were measured by HIM. As a recently developed imaging technique, HIM provides deep insight into the surface structure based on secondary electrons (SE); it thus resembles scanning electron microscopy. In HIM, a finely focused beam of helium ions with a diameter down to 0.35 nm is scanned over the sample, and the SE generated by the He^+ impact are detected. In SE imaging, the topology of the sample produces contrast as more electrons are ejected when the helium ion beam hits the sample at glancing incidence. Since the energy of the SE is very low, it leads to a higher surface sensitivity than typical electron microscopy. Figure 4 depicts the representative HIM micrographs of cobalt ferrite films with different magnifications (see full-

resolution images in SM). A good homogeneity is observed. The films are composed of small grains and exhibit a cauliflower structure. Compared to our recent work on Fe_2O_3 [18], the obtained films in this work exhibit more open porosity, which could result from the competitive growth between cobalt and iron oxides during the preparation. The cauliflower structure with open porosity is expected to hold more oxygen and thus improve the catalytic performance.

3.4 Redox behavior

To correlate the film composition and catalytic performance, the reducibility and re-oxidability of the synthesized cobalt ferrite was evaluated with in-situ emission FTIR spectroscopy by integrating the intensity of the characteristic bands of the spinel as a function of the temperature which reflects the loss or recovery of the spinel structure. Figure 5 presents the temperature-programmed reduction (TPR) and re-oxidation (TPO) profiles. The typical behavior of the integrated IR band intensity of cobalt ferrite as a function of the temperature in the TPR process is shown in Fig. 5a. With the increase of the temperature (Fig. 5b), the two bands peaking at 531 cm^{-1} and 625 cm^{-1} exhibit a progressive red shift. The reduction occurs at around $278\text{ }^\circ\text{C}$ and the samples are completely reduced at $318\text{ }^\circ\text{C}$, corresponding to $\text{Co}^{3+} \rightarrow \text{Co}^{2+}/\text{Co}$ and $\text{Fe}^{3+} \rightarrow \text{Fe}^{2+}/\text{Fe}$ [19]. Figures 5c and 5d show the TPO profile and the recovery of the inverse spinel structure in the re-oxidation process. The re-oxidation initiates at around $306\text{ }^\circ\text{C}$ and is accomplished at $352\text{ }^\circ\text{C}$, demonstrating that the re-oxidation step may play a key role in the catalytic process. Compared to the reported redox behavior of Co_3O_4 [8] and Fe_2O_3 [18], cobalt ferrite exhibits a much better re-oxidability than Co_3O_4 and a better reducibility than Fe_2O_3 . According to our recent work on Co-Zn [20] and Co-Mn [8] binary oxides, Zn or Mn doping may lead to an insertion of hydrogen atoms into the lattice during deposition, which could refine the mobility of the oxygen atoms and make the samples less

reducible than Co_3O_4 . Moreover, the substitution of Co^{3+} by Fe^{3+} in the octahedral site could also contribute to the better redox property of cobalt ferrites. Since both the complete reduction and re-oxidation occur at relatively low temperature, cobalt ferrite is expected to be an active catalyst for low-temperature oxidation of different exhaust gases or fuels.

3.5 Catalytic performance

The catalytic performance was investigated with respect to the total oxidation of propene, *n*-butene, and DME at atmospheric pressure over the prepared cobalt ferrite referring to the non-coated mesh. The catalytic effect of the mesh has been excluded by the observation that no significant difference occurred between the oxidation over non-coated mesh and in a blank system, in accordance with previous conclusions [9]. Figure 6 compares the light-off curves under the same inlet conditions. In the presence of cobalt ferrite, the oxidation becomes detectable at around 250 °C for all three reactant gases; complete conversion occurs at 400, 425, and 446 °C for propene, *n*-butene, and DME, respectively. The reproducibility of the catalytic results and reusability of the cobalt ferrite catalysts were evaluated by carrying out tests over a series of samples with several runs. The results are reproducible and the prepared samples exhibit good reusability within the experimental uncertainty (see SM). Up to 400 °C, the conversion is negligible for the oxidation over non-coated mesh, demonstrating that cobalt ferrite is active towards the oxidation of the selected reactants. It is worth noting that the catalytic oxidation under oxygen-rich conditions is observed to have no obvious effect on the catalyst or surface ionic states by performing XRD and XPS analyses before and after the catalytic tests.

Figure 7 depicts the outlet profiles as a function of the temperature during the oxidation. The results show that the cobalt ferrite films favor the complete conversion of the reactant gases at much

lower temperatures relative to the non-coated mesh. Besides the reactant gas, CO₂ was detected as the unique product in the oxidation processes over cobalt ferrite, while additional CO was observed in the reaction on non-coated mesh. T₅₀ and T₉₀, corresponding to 50% and 90% conversion of the reactant gas, respectively, are used as parameters to compare the performance of the deposited samples. With cobalt ferrite, T₅₀ and T₉₀ of propene oxidation are 348 and 382 °C, which are quite close to values obtained with other active catalysts such as alkali-doped Au/Al₂O₃ [21] and Co-Mn oxides in our recent work [8]. These values are lower than those reported by Ivanova et al. [22] who obtained 355 and 410 °C by using 200 mg of 2% Au/Al₂O₃ catalyst in propene oxidation. Moreover, T₉₀ in this work is lower than that measured with Ag/Al₂O₃ (410 °C) [23] and La_{1.7}Sr_{0.3}CuO₄S_{0.2} (420 °C) [24], indicating that the prepared cobalt ferrites exhibit competitive activity. T₅₀ and T₉₀ shifted to 578 and 691 °C, respectively, for the experiment carried out with non-coated mesh (see Figs. 7a and 7b). With the light-off curves obtained with and without cobalt ferrite, application of the Arrhenius equation at less than 5% conversion allows extraction of apparent activation energy values of $E_a = 116.25$ and 119.86 kJ/mol, respectively. Compared to the reaction over Co₃O₄ with $E_a = 158.32$ kJ/mol [8], the introduction of iron tends to initiate the oxidation of propene with lower E_a , which makes cobalt ferrite more suitable for the catalytic applications.

Figure 7c and 7d compare the results of *n*-C₄H₈ oxidation with and without cobalt ferrite. T₅₀ and T₉₀ of *n*-C₄H₈ oxidation over cobalt ferrite were observed at 358 and 402 °C, which are slightly lower than those reported with pure Co₃O₄ [25]. These values shifted by 100 and 135 °C, respectively, toward higher temperatures over non-coated mesh. It has been reported that a small quantity of 1,3-butadiene was selectively formed in the oxidation of *n*-C₄H₈ at a temperature >350 °C over MnMoO₄-based catalysts upon C-H activation [26]. It should be noted that 1,3-butadiene was not detected in the present work. According to Veleva and Trifirò [26], the

initiation of $n\text{-C}_4\text{H}_8$ oxidation occurred at around 350 °C and O_{ads} is responsible for the oxidation of $n\text{-C}_4\text{H}_8$ to CO_x . However, $n\text{-C}_4\text{H}_8$ oxidation becomes measurable at relatively low temperature in this study. Such low temperature could result in negligible formation of 1,3-butadiene. Moreover, the insertion of Co into the ferrites could lead to scarce formation of 1,3-butadiene [27]. E_a was estimated to be 123.71 and 146.25 kJ/mol for the reaction with and without cobalt ferrite. Of interest, two turning points at 360 and 480 °C are observed in the reaction on non-coated mesh. These points correspond to the partial oxidation of $n\text{-C}_4\text{H}_8$ to CO, as can be seen from the two clear peaks in the product profile in Fig. 7d.

For DME, cobalt ferrite also exhibits a much better performance than the non-coated mesh, as revealed in Fig. 7e and 7f. T_{50} and T_{90} of the reaction over cobalt ferrite are 356 and 409 °C. These values are observed to be 613 and 682 °C for the reaction without cobalt ferrite, respectively. It has been established that the initiation of DME conversion happens at around 240 °C over Pd/Al₂O₃ [28], Pd/CeO₂ [28], ZrMo₂O₈ [29], Rh/Al₂O₃/Al [30], and SnO₂/MgO catalysts [31], which is quite close to the temperature obtained in this work. According to Liu et al. [29], the reaction network for DME conversion consists of four pathways giving rise to CH₃OH, HCHO, HCOOCH₃, and CO_x. Low selectivity of CH₃OH and HCOOCH₃ was reported [29]. HCHO was not detected, which could result from either the low concentration or its fast conversion to CO_x. E_a was calculated to be 114.31 and 168.62 kJ/mol for the reaction over cobalt-ferrite-coated and non-coated mesh. Similar to $n\text{-C}_4\text{H}_8$, two plateaus at around 355 and 700 °C are observed during the reaction in the absence of cobalt ferrite, which could result from the fast conversion of HCHO to CO_x. Such two-stage ignition behavior of DME has been reported and summarized for the homogeneous experiments [32].

Based on the characteristic observations, the good catalytic performance of cobalt ferrite could be correlated with the O_{ads} on the surface, the cauliflower morphology and attractive redox

properties. It is widely accepted that the catalytic performance of ferrite-type catalysts depends on their oxygen mobility, since the reaction follows the Mars-van-Krevelen mechanism [27]. The abundance of O_{ads} could support the catalytic oxidation process, as proposed by Veleva and Trifirò [26]. The obtained cauliflower surface structure with open porosity is expected to hold more oxygen and active sites and consequently could be beneficial for the catalytic reaction. The good reducibility and re-oxidability tend to enable the catalytic reactions at relatively low temperatures by involving various cations distributed in the octahedral and tetrahedral sites. The abundant Co^{2+} ions revealed by XPS could allow for significant charge-transfer character between the cobalt $3d^7$ band structure with that of the neighboring O^{2-} lattice anions [33] and thus enhance the catalytic performance of the cobalt ferrite. Moreover, the slightly lower bandgap energy of cobalt ferrite (see SM) could also indicate that the migration of O_{lat} or O^{2-} from the bulk to the surface becomes easier and leads to good reducibility.

Conclusion

Thin cobalt ferrite films were synthesized from $\text{Co}(\text{acac})_3$ and $\text{Fe}(\text{acac})_2$ by pulse spray evaporation chemical vapor deposition for low-temperature oxidation application. Structure, morphology, and elemental distribution of the deposited films were characterized by XRD, Raman, HIM, and XPS. Temperature-programmed reduction and re-oxidation by in-situ emission FTIR spectroscopy were used to elucidate the redox behavior of the prepared films. The catalytic performance of the obtained cobalt ferrite was tested against deep oxidation of olefins and dimethyl ether. The prepared samples were confirmed to be $\text{Co}_{2.1}\text{Fe}_{0.9}\text{O}_4$ and exhibited a cauliflower structure. The results indicate that the binary cobalt ferrite presents better redox properties than the individual oxide films, which leads to the easy mobility of oxygen species from the bulk to the surface.

Compared to the reactions on non-coated mesh for a specific reactant gas, the complete conversion is achieved at much lower temperatures with cobalt ferrite, and cobalt ferrite tends to prohibit the formation of CO. The oxygen mobility of cobalt ferrite catalysts is suggested to play a key role in determining the catalytic performance. This facile and inexpensive preparation method and correlation of the catalytic performance with the surface and thermal properties may be extended to investigate catalytic potential of other binary and multiple metal oxides in the abatement of exhaust emissions as well as unburned fuels.

Acknowledgements

PMK and AEK thank the Deutscher Akademischer Austauschdienst (DAAD) for the financial support during their research stay at Bielefeld University in Germany.

References

- [1] A. Wittstock, V. Zielasek, J. Biener, C.M. Friend, M. Bäumer, *Science* 327 (2010) 319-322.
- [2] R. Nongjai, S. Khan, H. Ahmad, I. Khan, K. Asokan, *AIP Conf. Proc.* 1451 (2012) 163-165.
- [3] M.J. Sharif, M. Yamauchi, S. Toh, S. Matsumura, S. Noro, K. Kato, M. Takata, T. Tsukuda, *Nanoscale* 5 (2013) 1489-1493.
- [4] F.X. Qin, S.Y. Jia, Y. Liu, X. Han, H.T. Ren, W.W. Zhang, J.W. Hou, S.H. Wu, *Mater. Lett.* 101 (2013) 93-95.
- [5] N. Bahlawane, P.H. Tchoua Ngamou, V. Vannier, T. Kottke, J. Heberle, K. Kohse-Höinghaus, *Phys. Chem. Chem. Phys.* 11 (2009) 9224-9232.
- [6] S. Xavier, S. Thankachan, B.P. Jacob, E.M. Mohammed, *J. Nanosci.* 2013 (2013) 524380.
- [7] X. Liu, S. Liu, S. O'Brien, *MRS Proceedings* 1507 (2013) mrsf12-1507-aa09-20.
- [8] Z.Y. Tian, P.H. Tchoua Ngamou, V. Vannier, K. Kohse-Höinghaus, N. Bahlawane, *Appl. Catal. B: Environ.* 117-118 (2012) 125-134.
- [9] Z.Y. Tian, N. Bahlawane, V. Vannier, K. Kohse-Höinghaus, *Proc. Combust. Inst.* 34 (2013) 2261-2268.
- [10] N. Ballarini, F. Cavani, S. Passeri, L. Pesaresi, A.F. Lee, K. Wilson, *Appl. Catal. A: Gen.* 366 (2009) 184-192.
- [11] Y. Qu, H. Yang, N. Yang, Y. Fan, H. Zhu, G. Zou, *Mater. Lett.* 60 (2006) 3548-3552.
- [12] NIST X-ray Photoelectron Spectroscopy Database, Version 4.1 (National Institute of Standards and Technology, Gaithersburg, 2012); <http://srdata.nist.gov/xps>.
- [13] M.C. Biesinger, B.P. Payne, A.P. Grosvenor, L.W.M. Lau, A.R. Gerson, R.St.C. Smart, *Appl. Surf. Sci.* 257 (2011) 2717-2730.
- [14] J.L. Gautier, E. Rios, M. Gracia, J.F. Marco, J.R. Gancedo, *Thin Solid Films* 311 (1997) 51-57.
- [15] T. Yamashita, P. Hayes, *Appl. Surf. Sci.* 254 (2008) 2441-2449.
- [16] Z. Zhou, Y. Zhang, Z. Wang, W. Wei, W. Tang, J. Shi, R. Xiong, *Appl. Surf. Sci.* 254 (2008) 6972-6975.
- [17] H.W. Zanthoff, S.A. Buchholz, A. Pantazidis, C. Mirodatos, *Chem. Eng. Sci.* 54 (1999) 4397-4405.
- [18] P. Mountapmbeme Kouotou, Z.Y. Tian, H. Vieker, A. Beyer, A. Gölzhäuser, K. Kohse-Höinghaus, *J. Mater. Chem. A* 1 (2013) 10495-10504.

- [19] A. Biabani-Ravandi, M. Rezaei, Z. Fattah, *Chem. Eng. Sci.* 94 (2013) 237-244.
- [20] N. Bahlawane J. Feldmann, K. Kohse-Höinghaus, *Electrochem. Proceedings of EUROCV-15*, The Electrochemical Society, 2005-09 (2005) 659-666.
- [21] A.C. Gluhoi, N. Bogdanchikova, B.E. Nieuwenhuys, *J. Catal.* 232 (2005) 96-101.
- [22] S. Ivanova, C. Petit, V. Pitchon, *Gold Bull.* 39 (2006) 3-8.
- [23] R. Zhang, H. Alamdari, S. Kaliaguine, *Catal. Lett.* 119 (2007) 108-119.
- [24] M. Machida, K. Ochiai, K. Ito, K. Ikeue, *J. Catal.* 238 (2006) 58-66.
- [25] Z.Y. Tian, N. Bahlawane, F. Qi, K. Kohse-Höinghaus, *Catal. Commun.* 11 (2009) 118-122.
- [26] S. Veleva, F. Trifirò, *Reac. Kinet. Catal. Lett.* 4 (1976) 19-24.
- [27] H. Lee, J.C. Jung, H. Kim, Y.M. Chung, T.J. Kim, S.J. Lee, S.H. Oh, Y.S. Kim, I.K. Song, *Catal. Lett.* 131 (2009) 344-349.
- [28] S. Colussi, A. Gayen, J. Llorca, C. de Leitenburg, G. Dolcetti, A. Trovarelli, *Ind. Eng. Chem. Res.* 51 (2012) 7510-7517.
- [29] H. Liu, P. Cheung, E. Iglesia, *J. Phys. Chem. B* 107 (2003) 4118-4127.
- [30] B.Y. Yu, K.H. Lee, K. Kim, D.J. Byun, H.P. Ha, J.Y. Byun, *J. Nanosci. Nanotechnol.* 11 (2011) 6298-6305.
- [31] L. Yu, J. Xu, M. Sun, X. Wang, *J. Nat. Gas Chem.* V16 (2007) 200-203.
- [32] F. Herrmann, P. Oßwald, K. Kohse-Höinghaus, *Proc. Combust. Inst.* 34 (2013) 771-778.
- [33] A.W. Moses, H.G. Garcia Flores, J.-G. Kim, M.A. Langell, *Appl. Surf. Sci.* 253 (2007) 4782-4791.

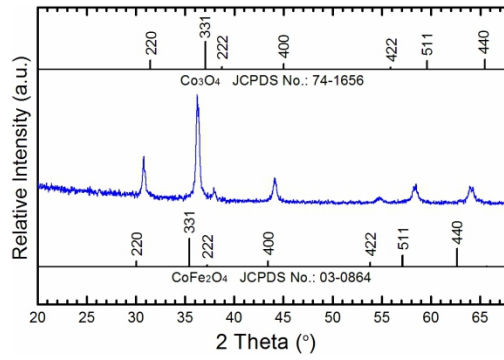


Fig. 1 Representative XRD pattern of the deposited cobalt ferrite films.

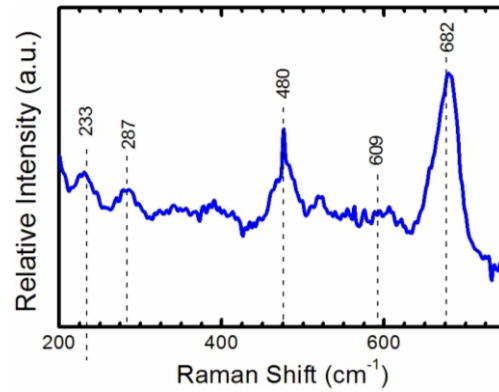


Fig. 2 Representative Raman spectrum of the deposited cobalt ferrite films.

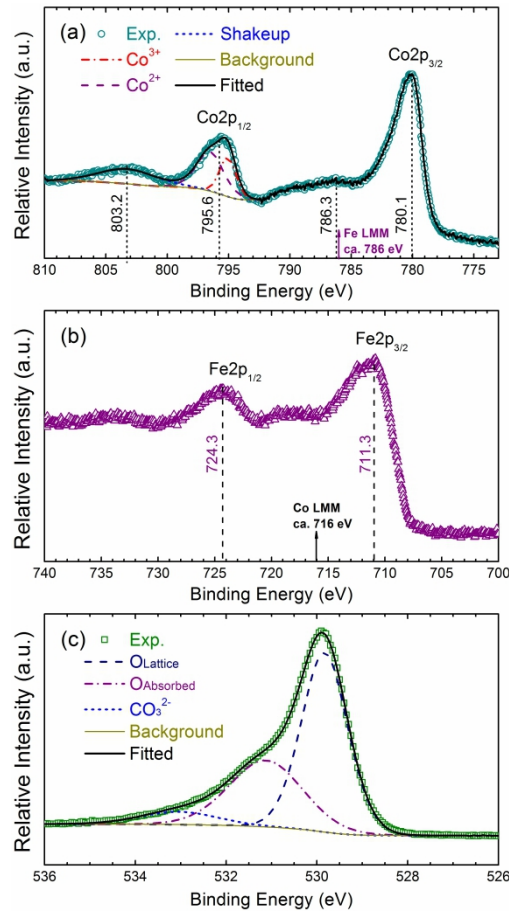


Fig. 3 XPS spectra of the cobalt ferrite films: Co 2p (a); Fe 2p (b); O1s (c).

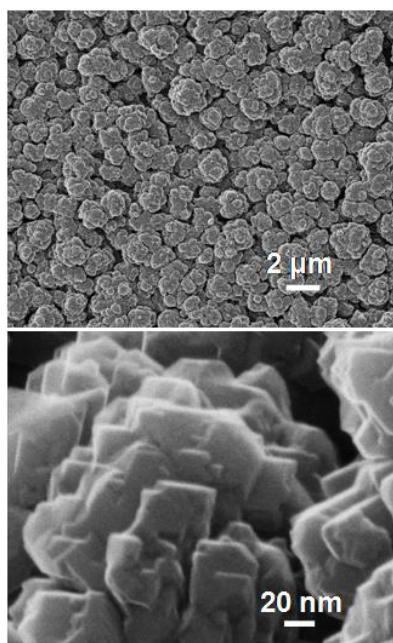


Fig. 4 HIM images of a representative cobalt ferrite film coated on stainless steel.

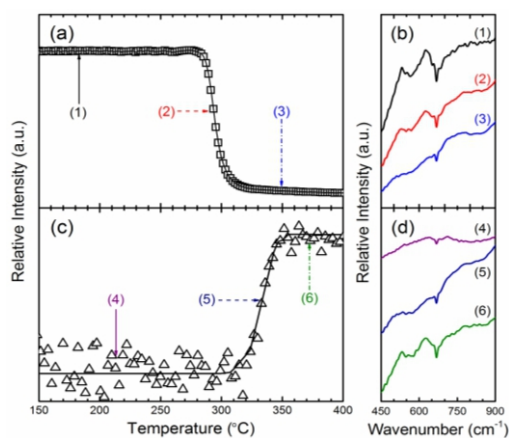


Fig. 5 Redox behavior of the cobalt ferrite oxides: TPR profile (a); progressive loss of the spinel structure (b); TPO profile (c); recovery of cobalt ferrite structure (d).

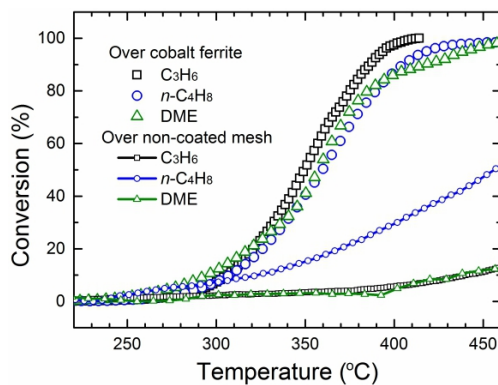


Fig. 6 Light-off curves of C_3H_6 , $n-C_4H_8$, and DME over cobalt ferrite-coated and non-coated meshes.

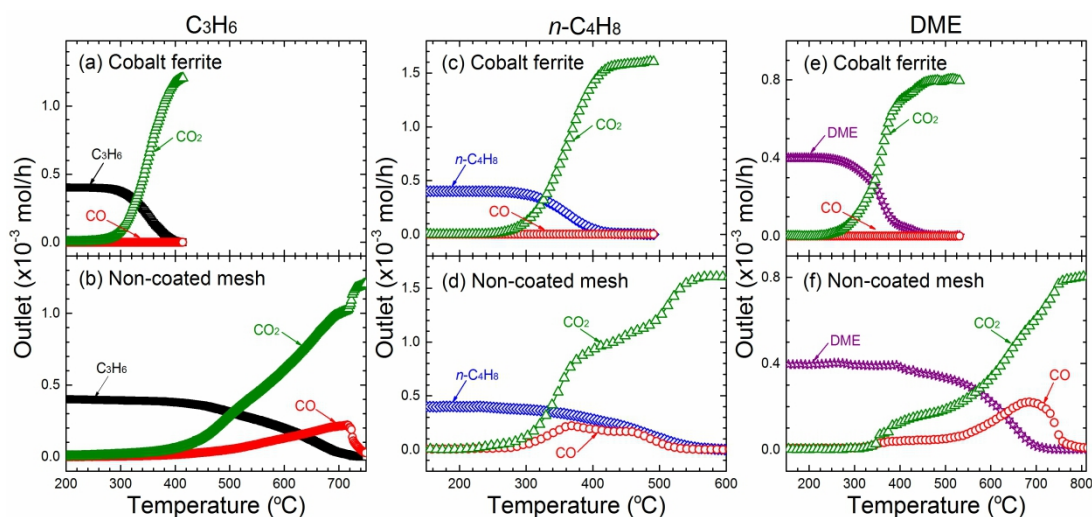


Fig. 7 Outlet profiles of C_3H_6 , $n-C_4H_8$, and DME oxidation over cobalt ferrite-coated and non-coated meshes.

Figure captions

Color figure in electronic versions only

Fig. 1 Representative XRD pattern of the deposited cobalt ferrite films.

Fig. 2 Representative Raman spectrum of the deposited cobalt ferrite films.

Fig. 3 XPS spectra of the cobalt ferrite films: Co 2p (a); Fe 2p (b); O 1s (c).

Fig. 4 HIM images of a representative cobalt ferrite film coated on stainless steel.

Fig. 5 Redox behavior of the cobalt ferrite oxides: TPR profile (a); progressive loss of the spinel structure (b); TPO profile (c); recovery of cobalt ferrite structure (d).

Fig. 6 Light-off curves of C_3H_6 , $n-C_4H_8$, and DME over cobalt ferrite-coated and non-coated meshes.

Fig. 7 Outlet profiles of C_3H_6 , $n-C_4H_8$, and DME oxidation over cobalt ferrite-coated and non-coated meshes.

SUPPLEMENTAL MATERIAL

TO

Low-temperature deep oxidation of olefins and DME over cobalt ferrite

Zhen-Yu Tian^{a,c,*}, Patrick Mountapmbeme Kouotou^a, Achraf El Kasmi^a, Patrick Hervé Tchoua Ngamou^a, Katharina Kohse-Höinghaus^a, Henning Vieker^b, André Beyer^b, Armin Gölzhäuser^b

^a *Department of Chemistry, Bielefeld University, Universitätsstraße 25, D-33615 Bielefeld, Germany*

^b *Department of Physics, Bielefeld University, Universitätsstraße 25, D-33615 Bielefeld, Germany*

^c *Present address: Institute of Engineering Thermophysics, Chinese Academy of Sciences, Beisihuanxi 11, 100190 Beijing, China*

* Corresponding author. Zhen-Yu Tian; E-mail: tianzhenyu@iet.cn; Fax: +86-8254 3052

Table of Contents

Section 1: Details of experimental conditions

Section 2: XPS details and surface composition

Section 3: Helium Ion Microscopy and full resolution images

Section 4: Optical property

Section 5: Reproducibility and reusability

Section 1: Details of experimental conditions

Table S1 Experimental conditions

Precursor	Co(acac) ₃	Fe(acac) ₃
Solvent	Tetrahydrofuran	
Concentration	5 mM	5 mM
Co/Fe ratio	1/1	
Delivery rate	0.80 mL min ⁻¹	
Substrates	Glass, stainless steel	
f^a , pulse width	4 Hz, 2.5 ms	
T_{evp} , T_{trs} , T_{sub}^b	220, 220, 400 °C	
P (mbar)	30	
N ₂ /O ₂ (SLM)	0.16/1.0	

Note: ^a f is the pulse frequency; ^b T_{evp} , T_{trs} and T_{sub} refer to the temperature of evaporation, transportation and substrate.

Section 2: XPS details and surface composition

The surface composition was determined by means of X-ray photoelectron spectroscopy (XPS). XPS was performed in a multi-technique ultra-high vacuum instrument (Multiprobe, Omicron Nanotechnology) using a monochromated Al K α X-ray source (1486.7 eV, 280 W) and a hemispherical electron energy analyzer (Sphera) in constant analyzer energy mode (25 eV) and a step size of 0.05 eV. The sample was located under an angle of 13° from the surface normal to the electron detector. The base pressure of the chamber was 2×10^{-10} mbar. CasaXPS was used to analyze the spectra, and a Shirley background subtraction procedure was employed. The elemental composition was calculated using the area of the Fe 2p, Co 2p, C 1s and O 1s peaks according to the Scofield cross-sections. The peak areas of the Fe 2p and Co 2p signals were corrected for Auger LMM peaks that each metal has in the 2p area of the other metal. In both cases, mainly the 2p_{3/2} parts of the

spectra are affected. For this correction, the full area of the 2p spectra (including the LMM area) was measured and then corrected with the intensity ratio of 2p to LMM (K) of a pure cobalt or iron oxide sample. The intensity correction of the peak area was done according to the following formula:

$$A(\text{Fe} - 2p) = \frac{M(\text{Fe}) - K(\text{Co})M(\text{Co})}{1 - (K(\text{Co})K(\text{Fe}))} \qquad A(\text{Co} - 2p) = \frac{M(\text{Co}) - K(\text{Fe})M(\text{Fe})}{1 - (K(\text{Co})K(\text{Fe}))}$$

Definitions:

A = Area

K = [A(LMM) / A(2p)] (Correction factor)

Measured Areas (M):

M(Fe) = A(Fe-2p+Co-LMM)

M(Co) = A(Co-2p+Fe-LMM)

Area ratio K (Fe) = A(Fe-LMM) / A(Fe-2p) = 14.3 / 84.8 = 0.148

Area ratio K (Co) = A(Co-LMM) / A(Co-2p) = 41.1 / 206.8 = 0.210

The representative XPS spectrum of C 1s is displayed in Fig. S1.

Table S2 Surface composition of the prepared films

Co 2p	Fe 2p	O 1s	C 1s	Co/Fe	Co	Fe	O
11	5.0	49.0	35.0	2.23	2.1	0.9	4.0

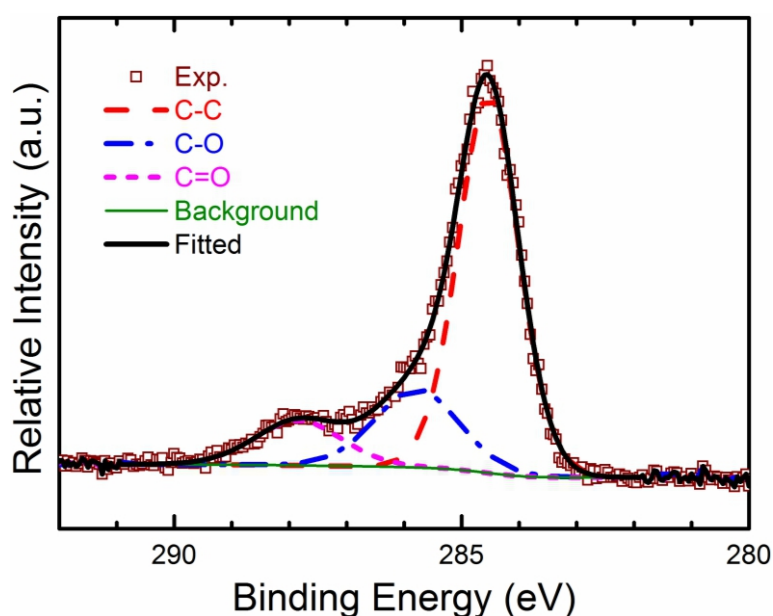


Fig. S1 XPS spectrum of C 1s.

Section 3: Helium Ion Microscopy and full resolution images

The high-resolution HIM micrographs were measured in a Carl Zeiss Orion Plus® Helium ion microscope. The helium ion beam was operated at 38.3 kV acceleration voltage at a current between 0.4 and 0.8 pA. A 10 μm aperture at Spot Control setting of 4-5 was used. The working distance was 9 mm at a sample tilt of 0° . Secondary electrons were collected by an Everhart-Thornley detector at 500 V grid voltage. The samples were plasma-cleaned in the HIM load lock for 8 minutes before measurement. The high-resolution HIM images with different magnifications are shown in Figs. S2 to S4.

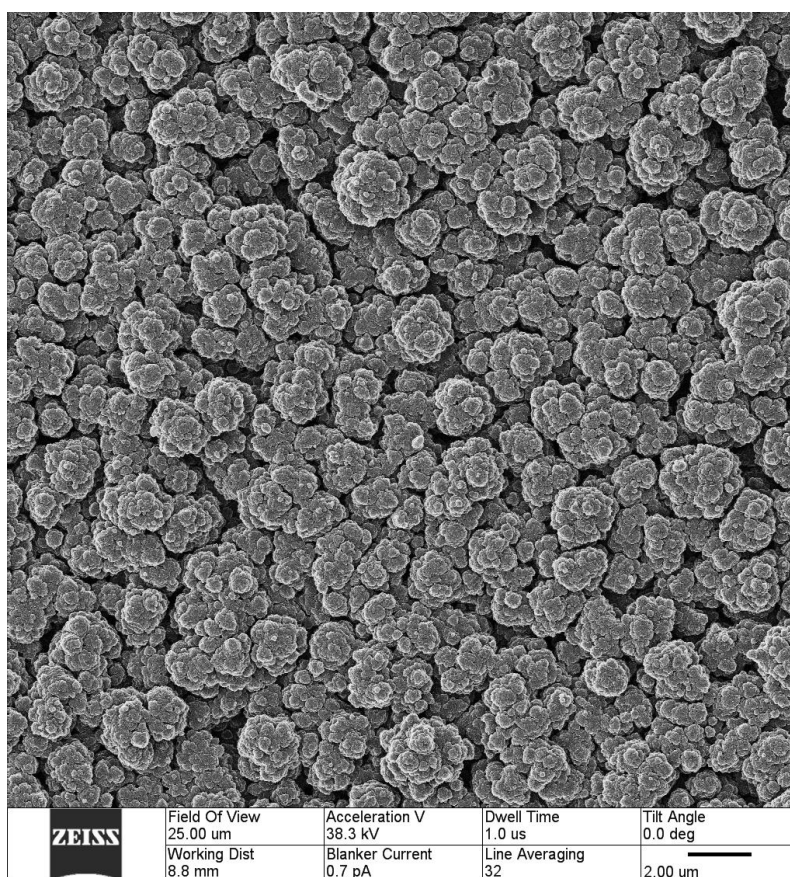


Fig. S2 Full-resolution HIM image, compare Fig. 4.



Fig. S3 High-resolution HIM image.

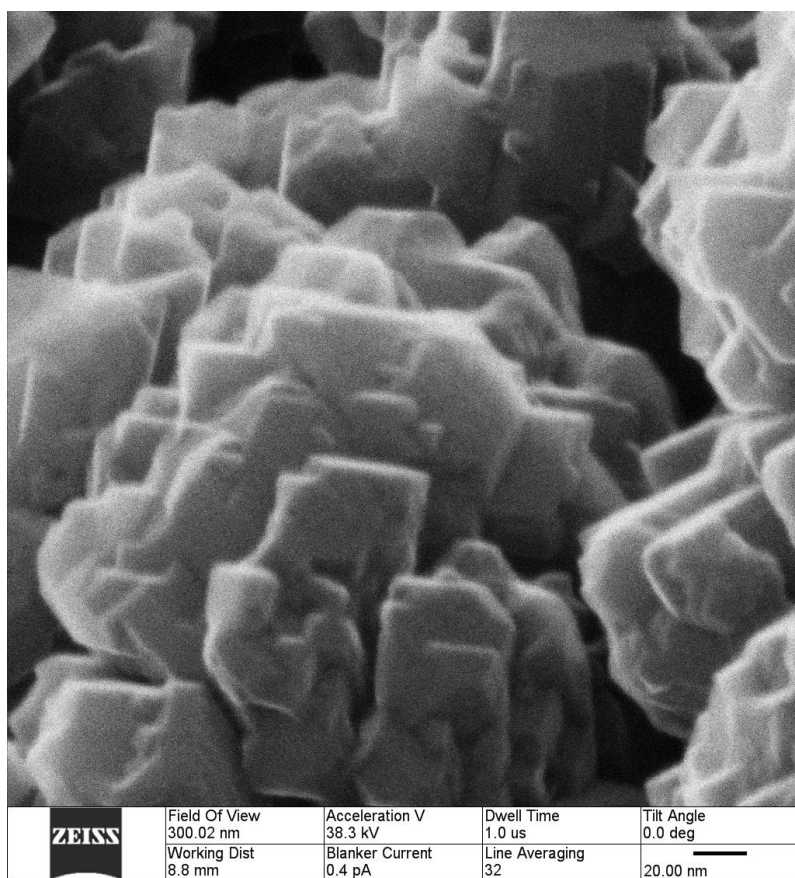


Fig. S4 High-resolution HIM image, compare Fig. 4.

Section 4: Optical property

According to Jibril [S1] and our recent work [S2], a strong correlation exists between the bandgap energy and the catalytic behavior of the catalysts. The direct bandgap energy of the prepared cobalt ferrite films can be estimated from the collected absorption spectra through Tauc's equation:

$$\alpha = \frac{A(h\nu - E_g)^{1/2}}{h\nu},$$

where A is a constant related to the refractive index, E_g is the bandgap energy of the cobalt ferrite film, n is a constant depending on the nature of the transition ($1/2$ for direct allowed transitions), α is the absorption coefficient and $h\nu$ is the incident photon energy. The corresponding plot of $(\alpha h\nu)^2$ versus $h\nu$ is shown in Fig. S5. E_g was determined to be 2.09 eV from extrapolation of the straight portion of this plot to the abscissa. Compared to the pure iron oxide [S3], the E_g value of cobalt ferrite is relatively smaller, which could be due to the presence of O^{2-} -octahedral ions associated with the surface basic sites. Moreover, the high content of Co^{2+} and oxygen vacancies as well as the possible charge transfer of O^{2-} - Co^{2+} may also contribute to the low E_g value. Therefore, the cobalt ferrite prepared in this work with low E_g is expected to possess high electron mobility character and exhibit good catalytic performance.

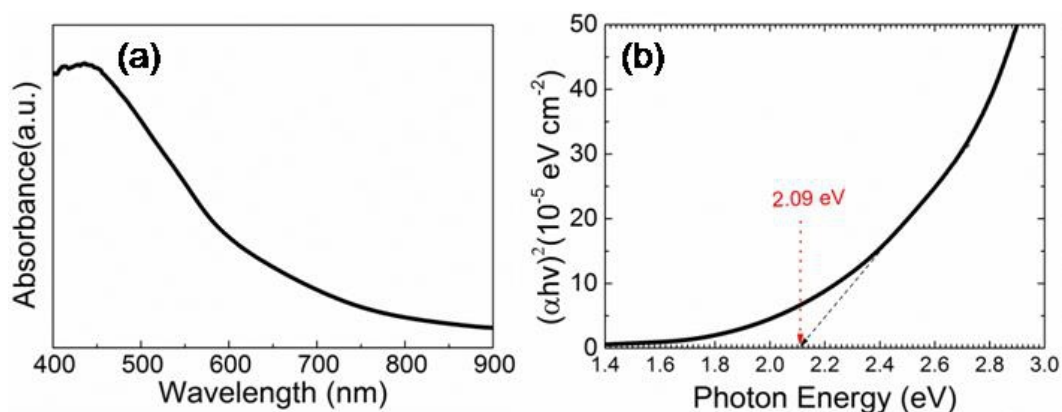


Fig. S5 UV-Vis absorption spectra and $(\alpha h\nu)^2$ versus $h\nu$ of cobalt ferrite films.

Section 5: Reproducibility and reusability

To test the reproducibility of the catalytic results and reusability of the cobalt ferrite catalysts, the catalytic tests were performed over a series of samples with several runs. As shown in Fig. S6a, the $n\text{-C}_4\text{H}_8$ conversion was well reproduced with the second and third cobalt ferrite sample within 3 °C. The catalytic tests of DME over the same cobalt ferrite (see Fig. S6b) reveal that the prepared sample exhibits a good reusability.

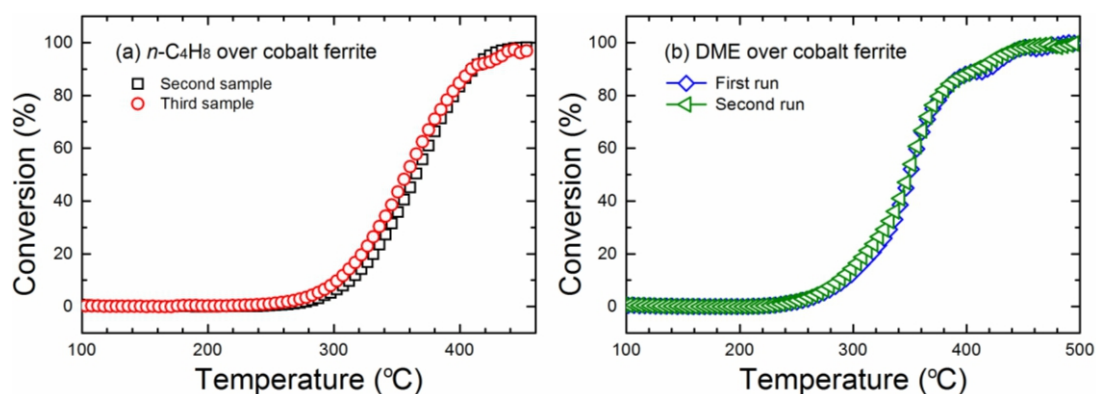


Fig. S6 Reproducibility and reusability: conversion profiles of $n\text{-C}_4\text{H}_8$ and DME over cobalt ferrite films.

References

- [S1] B.Y. Jibril, React. Kinet. Catal. Lett. 86 (2005) 171-177.
- [S2] Z.Y. Tian, N. Bahlawane, V. Vannier, K. Kohse-Höinghaus, Proc. Combust. Inst. 34 (2013) 2261-2268.
- [S3] P. Mountapmbeme Kouotou, Z.-Y. Tian, H. Vieker, K. Kohse-Höinghaus, Surf. Coat. Technol. 230 (2013) 59-65.

H) Publication 6

Zhen-Yu Tian, Tarik Chafik, Mhamed Asseban, Sanae Harti, Naoufal Bahlawane,
Patrick Mountapmbeme Kouotou and Katharina Kohse-Höinghaus

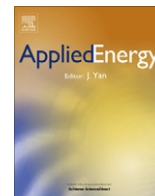
Towards biofuels combustion with an easily extruded clay as natural catalyst

Applied Energy 107, 149-156, 2013

Corrigendum to: *Towards biofuel combustion with an easily extruded clay as a natural catalyst* [Appl. Energy 107 (2013) 149-156] Appl. Energy 108, 528–529, 2013

Research Highlight

- Low-cost natural clay with three forms, powder, pellets and extruded monolith, was tested against biofuel combustion.
- The mineralogical, chemical thermal and textural properties of the clay were characterized.
- The effect of the equivalence ratio and of the total flow rate was investigated.
- The clay proved competitive activity to reactive non-noble transition metal oxides and some coated noble metals.
- The enhanced catalytic activity benefited from the abundance of Fe₂O₃ combined with some promoters.



Towards biofuel combustion with an easily extruded clay as a natural catalyst



Zhen-Yu Tian^{a,*}, Tarik Chafik^b, Mhamed Assebba^b, Sanae Harti^b, Naoufal Bahlawane^{a,1}, Patrick Mountapmbeme Kouotou^a, Katharina Kohse-Höinghaus^a

^a Department of Chemistry, Bielefeld University, Universitätsstraße 25, D-33615 Bielefeld, Germany

^b Laboratory LGCVR, Faculty of Sciences and Techniques, University Abdelmalek Essaadi, B.P. 416 Tangier, Morocco

HIGHLIGHTS

- ▶ Low-cost natural clay with three forms, powder, pellets and extruded monolith, was tested against biofuel combustion.
- ▶ The mineralogical, chemical thermal and textural properties of the clay were characterized.
- ▶ The effect of the equivalence ratio and of the total flow rate was investigated.
- ▶ The clay proved competitive activity to reactive non-noble transition metal oxides and some coated noble metals.
- ▶ The enhanced catalytic activity benefited from the abundance of Fe₂O₃ combined with some promoters.

ARTICLE INFO

Article history:

Received 30 April 2012

Received in revised form 6 October 2012

Accepted 6 February 2013

Available online 8 March 2013

Keywords:

Catalytic combustion

Biofuel

n-Butanol

Clay

Honeycomb monolith

ABSTRACT

The present work aims to investigate an innovative application of natural clay as a catalyst for biofuel combustion. The mineralogical, chemical, thermal and textural characterizations of the natural clay suggest an intrinsic catalytic potential without any prior treatment. The catalytic performance was studied with respect to the combustion of *n*-butanol as a representative biofuel using different forms of the natural clay: fine powder, pressed pellets and extruded honeycomb monoliths. No major difference was found among these forms regarding texture, morphology and stability. In terms of performance, this clay proved competitive relative to cobalt oxide spinel, which is one of the most reactive non-noble transition metal oxides. The significant amount of naturally occurring transition metals such as iron and some elements considered as promoters in the clay were proposed to account for the catalytic properties. A systematic investigation of the catalytic performance of the clay as a function of the equivalence ratio and of the total flow rate was performed using gas-phase FTIR spectroscopy. Increase of the equivalence ratio at a fixed flow rate yielded a lower catalytic performance toward *n*-butanol combustion producing a consequent fraction of carbon monoxide and ethylene. At a constant equivalence ratio of 0.6, the performance of the clay was not affected by increasing the total inlet flow rate up to 30 sccm. These findings may initiate the development of a new catalyst for biofuel combustion based on relatively low-cost and abundantly available raw materials such as the natural clay investigated here.

© 2013 Elsevier Ltd. All rights reserved.

1. Introduction

In the context of the energy transition to use renewable resources, biofuels like bio-diesel and bio-alcohol have attracted great attention in the last decade [1–4]. As an attractive alternative and additive to conventional gasoline, *n*-butanol has many superior

properties relative to ethanol, such as the higher energy density, lower vapor pressure, lower corrosivity, and higher hydrophobicity [5]. Moreover, *n*-butanol can be blended with diesel or gasoline at relatively high proportions, the use of which can reduce the amount of unwanted CO and hydrocarbon emissions. As *n*-butanol is regarded as one of the most promising biofuels in future applications, numerous investigations have focused on its combustion chemistry. These studies have predominantly addressed the experimental study [6–18] and kinetic modeling [5,8,15,16,19–23] of the homogeneous combustion. Considerably less work has been performed on its combustion involving heterogeneous catalysis. So far, only a few reports address this issue, where supported noble

* Corresponding author. Tel.: +49 521 106 2199; fax: +49 521 106 6027.

E-mail address: zhenyu.tian@uni-bielefeld.de (Z.-Y. Tian).

¹ Present address: Nanomaterials Research Unit, SAM Department, Centre de Recherche Public, Gabriel Lippmann, L-4422 Belvaux, Luxembourg.

metals [24–29] and $Zr_{0.4}Ce_{0.6-x}Mn_xO_2$ [30] were used with thermal activation, and TiO_2 with photo-activation [31].

Catalytic combustion usually proceeds at much lower temperatures than homogeneous combustion and is often carried out using honeycomb-shaped monoliths with open channels. These monoliths are made from metal or ceramic, such as the most popular cordierite three-way catalyst [32,33]. In recent years, clays received significant interest [34,35] as support of transition metal oxides [36,37] for efficient removal of contaminants from drinking water [38] as well as a layer to improve the performance of the air electrode for fuel cells [39,40]. Furthermore, clays served as catalysts because of their chemical composition: they contain mainly aluminosilicates and mixtures of several common minerals such as Fe_2O_3 , MgO , K_2O etc. [41–43]. However, to the best of our knowledge, the oxidation of biofuels, for example, *n*-butanol, over natural clay has never been investigated before.

The present work is oriented to evaluate the intrinsic catalytic performance of natural clay in terms of the catalytic combustion of biofuels. X-ray diffraction (XRD), Scanning electron microscopy (SEM) and Energy-dispersive spectroscopy (EDS) were used to characterize the clay. The clay was easily extruded into honeycomb monoliths without the need of chemicals as binder. The catalytic behavior of the clay was studied not only for extruded monolith but also for fine powder and pellet shapes. Moreover, the effect of equivalence ratio (Φ) and total flow rate on the catalytic performance was investigated. The objective is to evaluate the intrinsic catalytic potential of low-cost natural clay towards biofuel combustion.

2. Experimental

2.1. Clay samples preparation and mechanical test

Natural clay samples in three different forms, fine powder, pellet and extruded monolith, as shown in Fig. 1, were obtained from

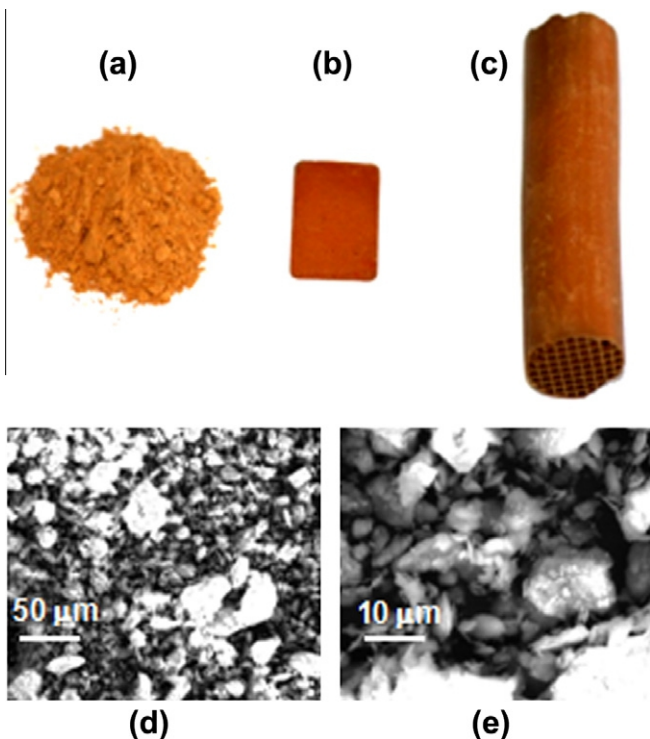


Fig. 1. Clay in powder (a), pellet (b) and extruded monolith form (c), and SEM micrographs obtained with the raw clay (d) and a piece from the corresponding extruded monolith (e).

northern Morocco. Firstly, the raw clays were ground and passed through a 180 μm sieve to obtain the fine powder. By mixing the fine powder with an appropriate amount of water, pellets and honeycomb monoliths (corning: 413 channels per square inch) were prepared with a thick paste mold and extrusion machine, respectively. The resulting samples were subsequently dried at 120 °C for two days. The mechanical properties were determined based on axial strength crush tests using a Shimadzu AG-IS universal machine, capable of working at a maximum pressure of 100 kN according to the standard procedure UNE-EN ISO 604 [34].

2.2. Characterization

XRD analysis was performed at room temperature using a Philips X'Pert Pro MRD (PW3830) equipped with a $Cu K\alpha$ ($\lambda = 0.154056$ nm) radiation and operated at 40 kV and 30 mA. Data were recorded in the 2θ range from 5° to 80°, with a step size of 0.05° and treated according to the Rietveld procedure using the Fullprof program [44]. The textural properties, BET surface area and pore size distribution of powder clay and pieces of the extruded monolith were estimated by measuring N_2 adsorption/desorption at –196 °C, using a Micromeritics ASAP 2020. SEM images and EDS results were obtained with a QUANTA-200 SEM (Philips) equipped with a Phoenix Microanalysis system.

2.3. Catalytic performance

Catalytic performance tests were carried out at atmospheric pressure in a quartz flow reactor, as shown in Fig. 2. The inlet gas consisted of 2 vol% of *n*-butanol in argon carrier flow gas containing 6–20 vol% of O_2 . The tubular glass reactor used for these tests has an inner diameter of 9 mm and a length of 180 mm, and the total flow rate was adjusted in the 15–50 sccm range. The clay samples (1 g) were loaded in the middle of the quartz reactor with quartz wool packed at the outlet side of the catalyst bed. As references, blank *n*-butanol oxidation experiments were carried out in the empty reactor and in a reactor containing a cordierite monolith (corning: 900 channels per square inch, 9 mm in diameter and 58 mm in length). Moreover, the catalytic performance of the clay was compared to that of Co_3O_4 or Fe_2O_3 thin film catalysts deposited on stainless steel meshes by pulsed-spray evaporation chemical vapor deposition [45,46]. The flow rates were controlled using MKS mass flow controllers, and the temperature of the clay inside the reactor was recorded using *K*-thermocouples and a digital thermometer (Greisinger, GMH3250). The experiments were carried out with a ramp of 5 °C/min using a HT60 controller (Horst). The gas phase composition at the outlet was monitored by FTIR spectroscopy for *n*-butanol, CO, CO_2 , C_2H_4

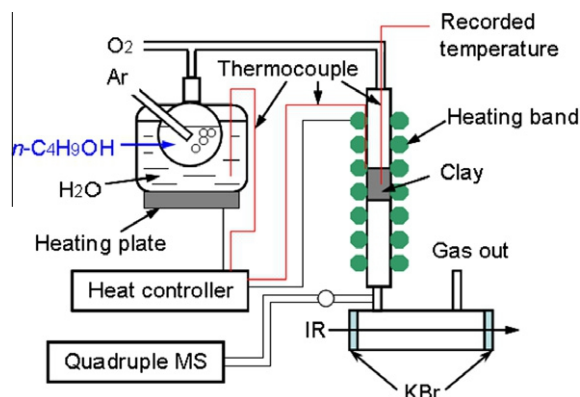


Fig. 2. Schematic illustration of the home-made flow reactor for the catalytic test.

Table 1
Experimental conditions of *n*-butanol oxidation.

System	Φ^a	Flow (sccm ^b)	<i>n</i> -C ₄ H ₁₀ O (%)	O ₂ (%)	Clay (g)
A	0.6	15	2.0	20	1.0
B	1.0	15	2.0	12	1.0
C	2.0	15	2.0	6	1.0
D	0.6	15	2.0	20	0.0
E ^c	0.6	15	2.0	20	0.0
F ^c	0.6	15	2.0	20	0.0
G ^c	0.6	15	2.0	20	0.0
H	0.6	30	2.0	20	1.0
I	0.6	50	2.0	20	1.0

^a Φ refers to the equivalence ratio.^b sccm is short for standard milliliter per minute.^c E, F and G are reactions with 10 mg Co₃O₄, 10 mg Fe₂O₃ on mesh of stainless steel and non-coated cordierite, respectively.

and C₂H₄O. Quadrupole mass spectrometry (QMS) was used to check the formation of *n*-butanal and butene, since some IR bands of these species might overlap with the detected IR bands of C₂H₄O and C₂H₄. The experimental conditions are compiled in Table 1, where the equivalence ratio (Φ) is defined as the ratio of the actual fuel/O₂ ratio to the stoichiometric fuel/O₂ ratio. The conversion of *n*-butanol is calculated as:

$$\text{Conversion}_{n\text{-butanol}}\% = \frac{[M_{n\text{-butanol}}(\text{inlet}) - M_{n\text{-butanol}}(\text{outlet})]}{M_{n\text{-butanol}}(\text{inlet})},$$

where $M_{n\text{-butanol}}(\text{inlet})$ and $M_{n\text{-butanol}}(\text{outlet})$ are the number moles of *n*-butanol in the inlet and outlet gases, respectively. The catalytic performance of the studied samples was analyzed based on the overall catalytic reaction rate, which is expressed as the ratio of the *n*-butanol conversion normalized to the mass or surface area of the catalyst:

$$r = \frac{M_{n\text{-butanol}}(\text{inlet})}{\text{Conversion}_{n\text{-butanol}}\% / \text{catalyst mass or surface area}}.$$

3. Results and discussion

3.1. Structural and chemical composition

The mineralogical composition of the raw clay was investigated by XRD spectroscopy, as presented in Fig. 3a. According to the International Centre for Diffraction Data (ICDD) database, the analysis of the diffractograms leads to the identification of phases listed

Table 2

Mineralogy information of the studied clay according to XRD analysis (ICCD database PDF code of the phase identified in parentheses).

Component	Mineralogical composition
1	Quartz (01-087-2096)
2	Muscovite (01-087-2042)
3	Kaolinite (01-0800885)
4	Vermiculite (01-077-0022)
5	Albite (00-019-1184)

Table 3

Elementary analysis (wt.%) of the investigated clay with EDS.

Elements	C	O	Na	Mg	Al	Si	K	Ca	Fe	Ti
Components	0.7	56.7	0.2	0.7	11.4	19.4	3.2	0.4	7.1	0.2

in Table 2. The studied clay displays a complex structural heterogeneity, containing quartz, muscovite, kaolinite, vermiculite as well as albite.

The EDS complementary microanalysis, as given in Table 3, confirms the existence of elements constituting the phases identified by XRD. The chemical analysis of the clay obtained here indicates a composition that is common to soils in other parts of the world as, for example, in the USA. [42], Spain [43], and Iran [41]. The low Si/Al ratio in the clay agrees well with the empirical phase composition suggested by the XRD analysis. It is worth pointing out that the clay's chemical composition reveals a strong potential for intrinsic catalytic properties, related to the presence of significant fraction of iron (7.1%) that might act as active phase. Silicon and aluminium oxides are also of interest because they are usually used as a catalyst support holding good structural properties at high temperature, whereas the alkali metals might play a significant role as electronic promoters.

3.2. Texture, morphology and stability

With N₂ adsorption/desorption isotherms, textural properties of the raw clay powder and monoliths were determined. The specific surface area (S_{BET}), total pore and micropore volumes were calculated to be 38.2 m²/g, 0.071, and 0.003 cm³/g for the powder versus 37.7 m²/g, 0.074, and 0.003 cm³/g for the monolith. This result confirms that the extrusion process does not affect the texture of the clay. The SEM micrographs (Fig. 1d and e) demonstrate an agglom-

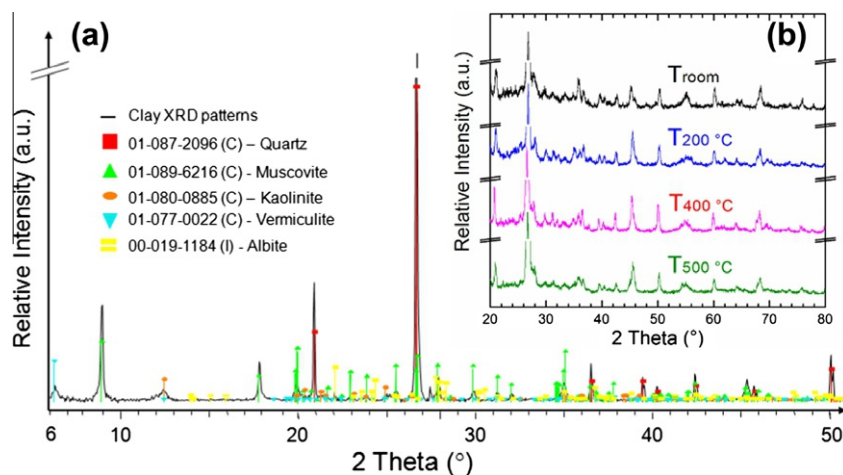


Fig. 3. Phase identification of raw clay at room temperature by XRD analysis (a) and the effect of temperature on the XRD patterns of raw clay (b).

erated and heterogeneous particle size distribution. An observation at high magnification also indicates the irregular shape of the constituent particles. Besides large voids, the observed smaller cavities might be associated with macroporosity.

The axial crush test of the extruded clay monolith reveals a mechanical resistance of 2.5 MPa. Although this value is lower than those reported for ceramic composites [47] and carbon-coated cordierite monoliths [48], it shows better performance than that for integral-type carbon monoliths extruded with binders [49] and is equivalent to the carbon-based monolith [50], demonstrating its potential for practical application. It is worth noting that the monolithic clay was extruded easily without any additives or binders.

To illustrate the thermal stability of the clay in the catalytic process, both pellets and extruded monoliths were studied with thermogravimetric analysis combined with temperature-programmed desorption mass spectrometry (TPDMS). The observed weight loss behavior (not shown) is similar to that reported previously for two other Moroccan clays [34]. Furthermore, the pellets and monoliths were exposed to the oxidation test conditions ($\Phi = 0.6$, 15 sccm) at different temperatures for 2 h. Since the pellets and monoliths show the same XRD pattern, only the spectra of pellet samples are compared in Fig. 3b. And increase of the temperature up to 500 °C does not yield any notable change in the relative intensities, which gives confidence that the clay is stable and can be used within this temperature range.

3.3. Catalytic performance

The catalytic performance and the effect of clay forms, equivalence ratio Φ and total flow rate on the oxidation process of *n*-butanol were investigated in this work. The gas phase composition at the outlet was monitored with online FTIR and QMS. Fig. 4a shows an illustrative example of selected IR spectra recorded as a function of temperature during the light-off test with 1 g of the clay powder and 15 sccm inlet flow and $\Phi = 0.6$. The IR bands at 2820–3050, 2240–2400, 2050–2230, 1690–1820, and 1380–1520 cm^{-1} are characteristic for *n*-butanol, CO_2 , CO, acetaldehyde, and ethylene, respectively [51]. Furthermore, the gas phase composition monitored with QMS indicate negligible formation of *n*-butanol and butene, in agreement with the flame study of *n*-butanol [11]. The existence of aldehydes was also observed in the oxidation of *n*-butanol over Pt/TiO₂ and Pt/x%Nb-TiO₂ catalysts reported by Finol et al. [28]. With the temperature increasing above 150 °C, the fraction of *n*-butanol decays gradually, and CO_2 is observed to be the unique carbonaceous species above 400 °C. CO, ethylene,

and acetaldehyde are the products of the catalytic oxidation at intermediate temperatures. According to Bouguer–Beer–Lambert's law, the intensities of the characteristic IR bands are proportional to the involved numbers of moles. With the known quantity of *n*-butanol, the amount of CO_2 was calculated according to the carbon balance of the reaction by calibrating the intensity of CO_2 when *n*-butanol was completely converted. The quantification of intermediates was obtained by comparison with CO_2 following the procedure given in the Supplemental Material, and the obtained composition profiles are shown in Fig. 4b.

3.3.1. Clay form

The aforementioned procedure was used to perform a preliminary investigation of the effect of the clay shapes on the catalytic performance. The light-off curves of *n*-butanol oxidation ($\Phi = 0.6$, 15 sccm) obtained with 1.0 g of the clay in three forms are presented in Fig. 5. These ignition curves were used to compare the catalytic performance on the basis of *n*-butanol consumption calculated as described in Section 2.3. In general, the three forms exhibit similar behavior since all the curves show complete oxidation at around 355 °C and only slight differences were observed at the low-temperature conversion rate. The temperatures, T_{10} , T_{50} , and T_{90} corresponding to 10%, 50%, and 90% of *n*-butanol conversion (Table S1) show that the *n*-butanol oxidation over pellets tends to begin at 10–20 °C (T_{10}) higher than over powder and

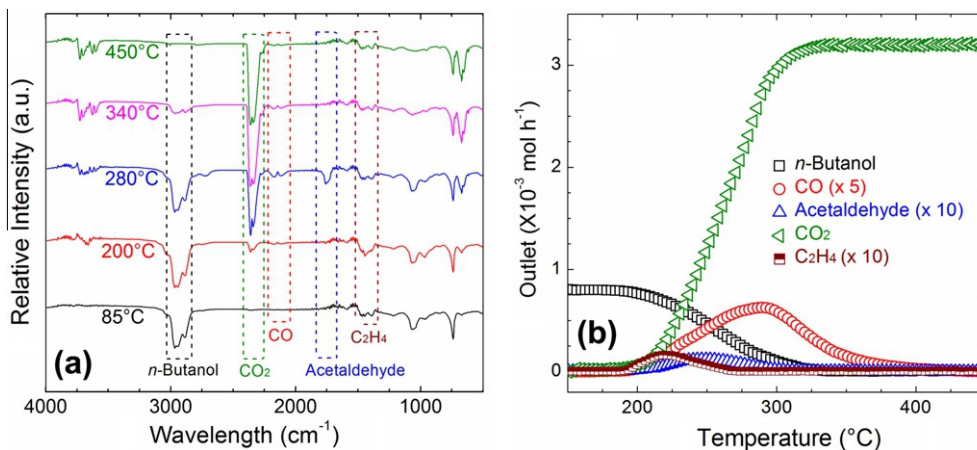


Fig. 4. FTIR spectra as a function of temperature (a) and production profiles for *n*-butanol oxidation at equivalence ratio of 0.6 and total flow rate of 15 sccm.

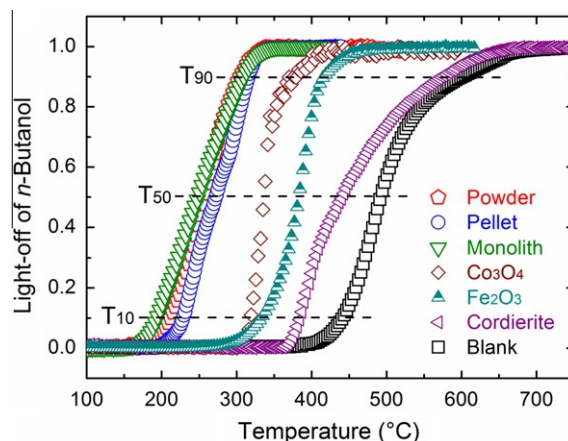


Fig. 5. Light-off curves of *n*-butanol as a function of reaction temperature with clay in powder, pellet, extruded monolith form, cobalt oxide (Co_3O_4), iron oxide (Fe_2O_3), cordierite and empty tube at equivalence ratio of 0.6 and total flow rate of 15 sccm.

monoliths. These results permit to establish the following catalytic performance order: monolith < powder < pellet based on T_{50} and T_{90} values. However, these differences are within the experimental uncertainties.

The catalytic performance of this clay was also compared to that of Co_3O_4 or Fe_2O_3 deposited on a mesh of stainless steel tested under similar conditions ($\Phi = 0.6$ and total flow rate of 15 sccm) after performing blank tests with empty reactor and with cordierite in order to check the existence of homogeneous reactions of n -butanol oxidation. As seen in Fig. 5, T_{10} obtained with clay shifts significantly by about 100, 110, 170, and 230 °C to higher temperatures for the reaction over Co_3O_4 , Fe_2O_3 , cordierite, and in the empty reactor, respectively. The same order is obtained for T_{50} and T_{90} . The reaction without catalyst or with cordierite doesn't start before 360 °C, a temperature at which n -butanol is already completely converted to CO_2 over the clay samples. This result shows clearly the high efficiency of the clay as a catalyst for the oxidation of n -butanol. Regarding the production of CO as a combustion intermediate, similar levels were observed with Co_3O_4 , Fe_2O_3 , and with the clay, while substantially higher CO concentration was found for homogeneous combustion (in the absence of catalyst, see Fig. S1).

To evaluate the potential application of the clay as a biofuel oxidation catalyst, the catalytic performance was investigated in terms of reaction rate. For this, we use a simple expression of the overall catalytic reaction rate that depends only on n -butanol conversion. This is justified by the fact that the oxygen concentration is generally larger than that of the fuel and usually remains constant under operating conditions. Although the adopted reaction rate does not provide insight into the catalytic act occurring on the surface, it permits a useful and quick comparison of the kinetic behavior of different samples. Hence, two types of reactions rates were calculated in this work: (1) r_m , normalized to the mass of the active catalyst (for clay, the active catalyst was considered as Fe_2O_3); (2) r_s , normalized to the surface area of the active catalyst. Table 4 presents the resulting reaction rates for Co_3O_4 , Fe_2O_3 , and clay in forms of powder, pellet and monolith at 200 and 300 °C. The r_m and r_s values obtained with both powder and monolith are larger than those obtained with pellet, which is due to the larger surface-to-volume ratios of powder and monolith. No reaction happens for Co_3O_4 and Fe_2O_3 at 200 °C. At 300 °C, the r_m values obtained with different forms of clay are generally several times larger than those of Co_3O_4 and Fe_2O_3 , because the clay forms have a higher conversion percentage of n -butanol. The reaction rates based on the surface area of catalyst yield similar values for clay and Fe_2O_3 . This is probably due to the lower dispersion of Fe_2O_3 on the clay area, as compared to the higher density of Fe_2O_3 sites on the stainless steel mesh. A similar explanation was given regarding mesh covered with catalytic copper oxide nanowires in methane oxidation [52]. Accordingly, the reaction rates indicate that the catalytic performance of clay with respect to n -butanol oxidation is better than that of Co_3O_4 and Fe_2O_3 .

Table 4
Reaction rates for Co_3O_4 , Fe_2O_3 and clay in forms of powder, pellet and monolith.

Catalysts	Reaction rate per unit mass of catalyst ($\times 10^{-6} \text{ mol g}^{-1} \text{ s}^{-1}$)		Reaction rate per unit surface area of catalyst ($\times 10^{-8} \text{ mol m}^{-2} \text{ s}^{-1}$)	
	200 °C	300 °C	200 °C	300 °C
Powder	0.39	7.78	0.11	2.08
Pellet	0.11	6.57	0.03	1.75
Monolith	1.30	7.46	0.35	1.99
Co_3O_4	–	0.50	–	0.44
Fe_2O_3	–	2.27	–	2.01

It is worth mentioning that the light-off profile of n -butanol over Fe_2O_3 obtained in this work is in agreement with literature result reported by Basińska et al. [29]. Although the introduction of Ru could lower that ignition temperature, the complete oxidation of n -butanol over Ru/ Fe_2O_3 needs 450 °C [29]. Compared to Pt/Pd and Zr-Ce-Mn catalysts permitting total conversion of n -butanol in the temperature range of 180–230 °C [26,28,30], the natural clay still shows potential in the catalytic removal of n -butanol.

According to the well-accepted Mars-van-Krevelen mechanism, the catalytic oxidation reaction requires a cyclic change of the oxidation state of the catalytic material. Note that Fe_2O_3 has been reported as an active catalyst for the oxidation of ethanol [53], n -butanol [29] and toluene [54]. Based on EDS results, Fe_2O_3 which is one of the main components of the studied clay, and also presents in some pillared [55] and vermiculite clays [56], might play an important role during the catalytic reaction investigated in the present work. The use of mixtures of silica, alumina and magnesia as structural stabilizers as well as Mg, K, Na and Ca as electronic promoters, is common practice in heterogeneous catalysis. Therefore, it is not surprising that the studied clay is more active than the catalyst based on iron oxide alone. Further evidence of the role of these promoters is beyond the scope of this work and will be the subject of future investigations.

3.3.2. Equivalence ratio

In the present work, the effect of Φ was investigated on the n -butanol conversion by fixing the inlet flow of n -butanol and the total flow at 15 sccm while varying the oxygen/ n -butanol ratio from 10 to 3 (Φ in the range of 0.6–2.0, conditions A to C in Table 1). As summarized in Fig. 6a, the increase of Φ shifts the light-off curve to higher temperatures. For $\Phi = 0.6$, the reaction begins at around 185 °C, while for $\Phi = 2.0$, this temperature is about 15 °C higher. A more profound shift (60 °C) was observed for the complete conversion temperature. As presented in Fig. 6, CO_2 production profiles coincide with the n -butanol depletion profiles, while CO, ethylene and acetaldehyde have intermediate-like profiles. The temperatures at which these intermediates are formed at maximal rates show also a clear shift to higher values with increasing Φ , following an order: $T_{\text{CO}} > T_{\text{acetaldehyde}} > T_{\text{ethylene}}$ at fixed Φ . The maximal CO formation rate was observed at 289 °C ($1.3 \times 10^{-4} \text{ mol h}^{-1}$) for $\Phi = 0.6$. This value shifts to 320 °C ($1.6 \times 10^{-4} \text{ mol h}^{-1}$) for $\Phi = 1.0$ and to 349 °C ($1.8 \times 10^{-4} \text{ mol h}^{-1}$) for $\Phi = 2.0$. Compared to CO, ethylene and acetaldehyde can be considered as minor products and the maximal production rate of acetaldehyde decreases significantly from lean to rich conditions. It should be noted that CO and acetaldehyde are completely depleted at 500 °C under lean and stoichiometric conditions, while they are still formed at a rate of 1.9×10^{-5} and $3.3 \times 10^{-6} \text{ mol h}^{-1}$ for $\Phi = 2$, respectively, which is a direct consequence of the oxygen deficiency under rich conditions. A comprehensive comparison of the effect of Φ on T_{10} and T_{50} of n -butanol conversion, maximum outlet and corresponding temperature of CO, ethylene and acetaldehyde is presented in Fig. S2 in the Supplemental Material.

3.3.3. Total flow rate

Concerning the influence of the total flow on n -butanol conversion, the experiments were carried out at a fixed catalyst weight and partial pressure of n -butanol, because high total flow rates lead to short residence time in the catalytic bed. Fig. 6b presents the reaction mixture containing 2% of n -butanol for flow rates 15–50 sccm at $\Phi = 0.6$. The oxidation of n -butanol starts significantly at 185 °C and complete conversion achieves at 320 °C for flow rates of 15 and 30 sccm. These temperatures shift to 200 and 350 °C for a total flow rate of 50 sccm. T_{10} and T_{50} (see Fig. S3) also give evidence that the oxidation of n -butanol with 50 sccm needs a higher temperature. Similar behavior was exhibited by CO_2 production,

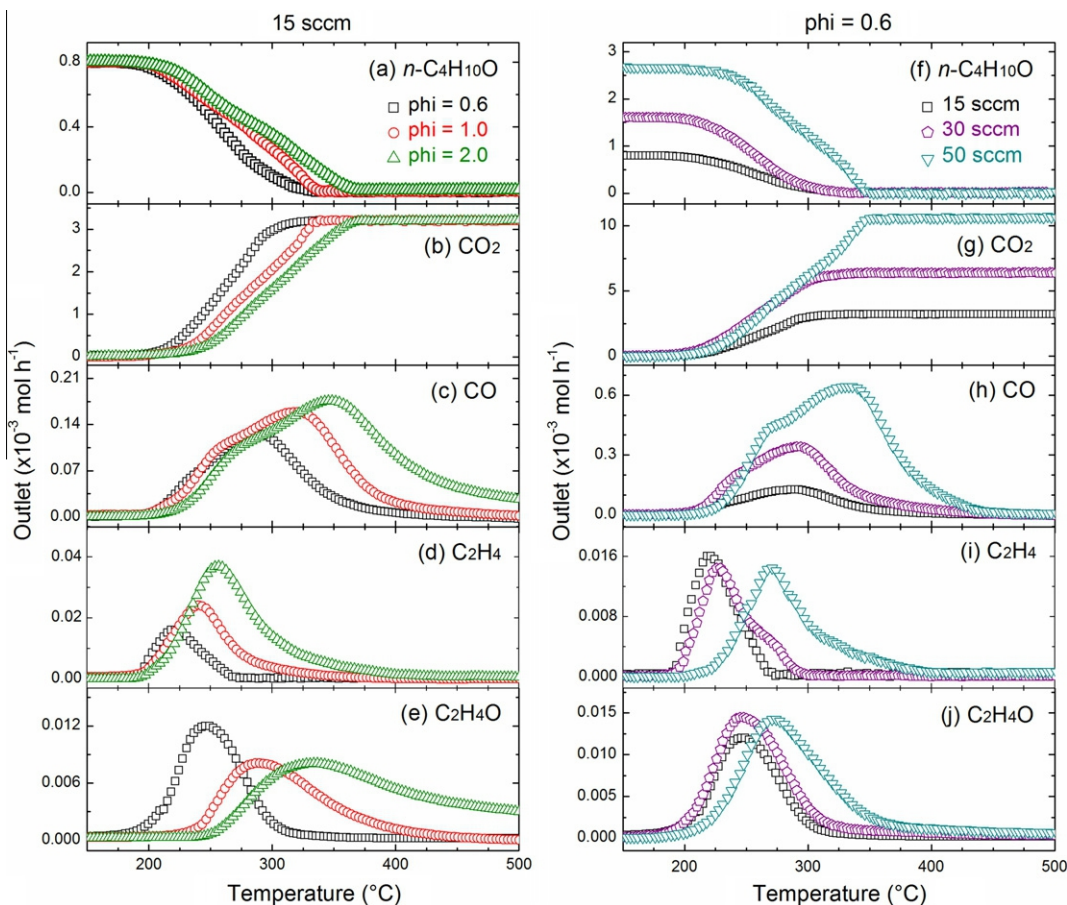


Fig. 6. The effect of equivalence ratio the mole fraction of n -butanol (a), CO $_2$ (b), CO (c), C $_2$ H $_4$ (d) and acetaldehyde (e) at a total flow rate of 15 sccm; effect of total flow rate on the outlet profiles of n -butanol (f), CO $_2$ (g), CO (h), C $_2$ H $_4$ (i) and acetaldehyde (j) at a fixed equivalence ratio of 0.6.

whereas CO was observed as an intermediate in all cases with an increased production at higher flow rate. Figs. 7g and S3 show the maximal CO formation rate at 290 $^{\circ}$ C for 15–30 sccm and at

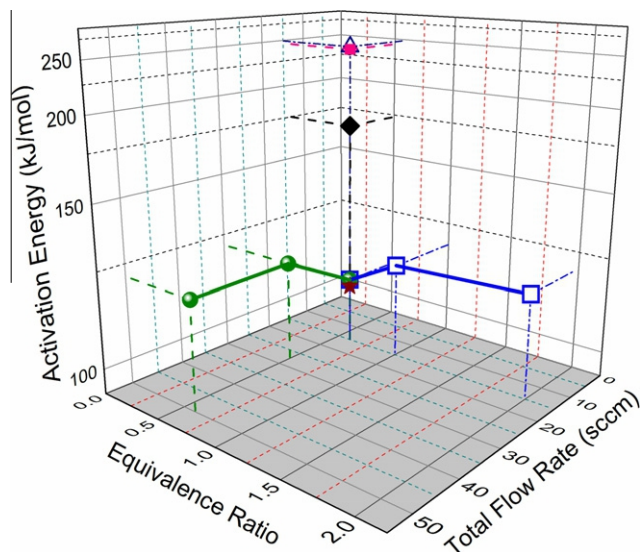


Fig. 7. The effect of equivalence ratio and flow rate on the apparent activation energy for n -butanol oxidation with clay (empty square and circular symbols), Co $_3$ O $_4$ (triangle symbol), Fe $_2$ O $_3$ (star), cordierite (solid square) and without catalyst (diamond symbol) at atmospheric pressure.

330 $^{\circ}$ C for 50 sccm. The reached maximal production rate shows a 5-fold increase when the total flow rate was increased from 15 to 50 sccm. Ethylene is also observed to peak toward higher temperatures when the total flow rate is increased. Concerning acetaldehyde, the maximum formation occurs at around 245 $^{\circ}$ C for 15 and 30 sccm and 270 $^{\circ}$ C for 50 sccm. The observed temperature shifts corresponding to the peak values remain within 10% for both ethylene and acetaldehyde, indicating that the total flow has a small impact on the production of ethylene and acetaldehyde.

3.4. Implications

In the present work, the comparison of the overall catalytic performance of the clay with that of Co $_3$ O $_4$ and Fe $_2$ O $_3$ catalyst was made assuming a simple model based on the rate of n -butanol conversion. The resulting apparent activation energies (E_{app} , see Table S2) were estimated from the light-off curves where less than 15% of the fuel was converted [32]. As the E_{app} in heterogeneous catalysis may result from a complex kinetic model, no control of the mass and heat transfer was considered for the E_{app} obtained in this work. As expected, no significant difference was observed for E_{app} values under different tested conditions, as summarized in Fig. 7. With clay, the E_{app} was 109.7 kJ mol $^{-1}$ at $\Phi = 0.6$ and a total flow rate of 15 sccm. With this value as a reference, E_{app} increased by 7.9 kJ mol $^{-1}$ for $\Phi = 1.0$ and further by 2.2 kJ mol $^{-1}$ for $\Phi = 2.0$. For a constant Φ , doubling the total flow rate from 15 to 30 sccm resulted in an 11.7 kJ mol $^{-1}$ increase of E_{app} . Further increase of the total flow to 50 sccm did not affect the apparent activation energy substantially. The light-off curves obtained with Fe $_2$ O $_3$ cata-

lyst gave similar E_{app} values to those obtained with the clay for the same conditions ($\Phi = 0.6$ and 15 sccm). In contrast, the values of E_{app} extracted from ignition curves obtained with empty reactor, cordierite and Co_3O_4 were significantly higher (176.5, 246.1 and 249.4 kJ mol⁻¹, respectively). Although the importance of the promoters remains unclear, these results indicate that the clay used in this work plays a significant role in the process of *n*-butanol oxidation and Fe_2O_3 is a good starting point to simulate the catalytic performance of the clay.

The experiment indicates that an appropriate Φ and total flow rate should be considered for the application of the clay as a natural catalyst. The extruded monolith exhibits similar catalytic behavior as the powder but presents increased practical application. It is known that supported noble metals on ceramic monolith leads to good catalytic performance. Recent results also show that non-noble metal oxide catalysts might be more attractive in terms of cost and efficiency as well as for suppressing CO formation [32]. In this sense, the studied clay may thus also present itself as a low-cost support to deposit some transition metal oxides.

4. Conclusion

Low-cost and easily available clay was used as a promising catalytic material for biofuel oxidation. Characterization data of the clay, carried out by specific surface area measurement, XRD and SEM revealed no significant differences when comparing the raw powder, pressed pellets and extruded monoliths. A structure study indicates that the clay is composed of different minerals. The catalytic performance of the clay was evaluated for the deep oxidation of *n*-butanol. With increasing equivalence ratio and total flow rate, higher temperatures were required to achieve full conversion. These conditions also led to higher CO production, while they had less impact on the formation of ethylene and acetaldehyde. In general, the natural clay exhibited better performance than some active transition metal oxides, such as Co_3O_4 and Fe_2O_3 . In view of the chemical composition of the studied clay mineral, the accessible active catalytic phases are probably associated with iron species. The better performance of the clay may benefit from the naturally present combination of mixed oxides and metals that are usually used as catalyst support and promoters. Our results indicate that the studied natural clay is a promising catalyst in the combustion of biofuels such as *n*-butanol, even though further fundamental research is still needed to understand the involved catalytic processes, particularly with respect to the nature of the active sites and related promoters.

Acknowledgements

Dr. Tian thanks the Alexander von Humboldt foundation for his research fellowship. The authors acknowledge the financial support by the Bundesministerium für Bildung und Forschung Project (BMBF 3681/Project 10/010/Morocco/Germany).

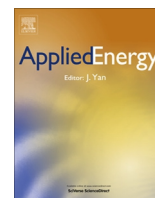
Appendix A. Supplementary material

Supplementary data associated with this article can be found, in the online version, at <http://dx.doi.org/10.1016/j.apenergy.2013.02.025>.

References

- [1] Kohse-Höinghaus K, Oßwald P, Cool TA, Kasper T, Hansen N, Qi F, et al. Biofuel combustion chemistry: from ethanol to biodiesel. *Angew Chem Int Ed* 2010;49:3572–97.
- [2] Demirbas A. Competitive liquid biofuels from biomass. *Appl Energy* 2011;88:17–28.
- [3] Qureshi N, Saha BC, Dien B, Hector RE, Cotta MA. Production of butanol (a biofuel) from agricultural residues: Part I – Use of barley straw hydrolysate. *Biomass Bioenergy* 2010;34:559–65.
- [4] Kannan GR, Karvembu R, Anand R. Effect of metal based additive on performance emission and combustion characteristics of diesel engine fuelled with biodiesel. *Appl Energy* 2011;88:3694–703.
- [5] Harper MR, Geem KMV, Pyl SP, Marin GB, Green WH. Comprehensive reaction mechanism for *n*-butanol pyrolysis and combustion. *Combust Flame* 2011;158:16–41.
- [6] McEnally CS, Pfefferle LD. Fuel decomposition and hydrocarbon growth processes for oxygenated hydrocarbons: butyl alcohols. *Proc Combust Inst* 2005;30:1363–70.
- [7] Yang B, Oßwald P, Li YY, Wang J, Wei LX, Tian ZY, et al. Identification of combustion intermediates in isomeric fuel-rich premixed butanol–oxygen flames at low pressure. *Combust Flame* 2007;148:198–209.
- [8] Sarathy SM, Thomson MJ, Togbé C, Dagaut P, Halter F, Mounaim-Rousselle C. An experimental and kinetic modeling study of *n*-butanol combustion. *Combust Flame* 2009;156:852–64.
- [9] Grana R, Frassoldati A, Faravelli T, Niemann U, Ranzi E, Seiser R, et al. An experimental and kinetic modeling study of combustion of isomers of butanol. *Combust Flame* 2010;157:2137–54.
- [10] Gu XL, Huang ZH, Wu S, Li QQ. Laminar burning velocities and flame instabilities of butanol isomers–air mixtures. *Combust Flame* 2010;157:2318–25.
- [11] Oßwald P, Gülkenberg H, Kohse-Höinghaus K, Yang B, Yuan T, Qi F. Combustion of butanol isomers – a detailed molecular beam mass spectrometry investigation of their flame chemistry. *Combust Flame* 2011;158:2–15.
- [12] Rakopoulos CD, Dimaratos AM, Giakoumis EG, Rakopoulos DC. Study of turbocharged diesel engine operation, pollutant emissions and combustion noise radiation during starting with bio-diesel or *n*-butanol diesel fuel blends. *Appl Energy* 2011;88:3905–16.
- [13] Agathou MS, Kyritsis DC. Experimental investigation of bio-butanol laminar non-premixed flamelets. *Appl Energy* 2012;93:296–304.
- [14] Zhang Y, Boehman AL. Oxidation of 1-butanol and a mixture of *n*-heptane/1-butanol in a motored engine. *Combust Flame* 2010;157:1816–24.
- [15] Yasunaga K, Mikajiri T, Sarathy SM, Koike T, Gillespie F, Nagy T, et al. A shock tube and chemical kinetic modeling study of the pyrolysis and oxidation of butanols. *Combust Flame* 2012;159:2009–27.
- [16] Dagaut P, Sarathy SM, Thomson MJ. A chemical kinetic study of *n*-butanol oxidation at elevated pressure in a jet stirred reactor. *Proc Combust Inst* 2009;32:229–37.
- [17] Szwaja S, Naber JD. Combustion of *n*-butanol in a spark-ignition IC engine. *Fuel* 2010;89:1573–82.
- [18] Valentino G, Corcione FE, Iannuzzi SE, Serra S. Experimental study on performance and emissions of a high speed diesel engine fuelled with *n*-butanol diesel blends under premixed low temperature combustion. *Fuel* 2012;92:295–307.
- [19] Moss JT, Berkowitz AM, Oehlschlaeger MA, Biet J, Warth V, Glaude PA, et al. An experimental and modeling study of the oxidation of the four isomers of butanol. *J Phys Chem A* 2008;112:10843–55.
- [20] Black G, Curran HJ, Pichon S, Simmie JM, Zhukov V. Bio-butanol: combustion properties and detailed chemical kinetic model. *Combust Flame* 2010;157:363–73.
- [21] Frassoldati A, Grana R, Faravelli T, Ranzi E, Oßwald P, Kohse-Höinghaus K. Detailed kinetic modeling of the combustion of the four butanol isomers in premixed low-pressure flames. *Combust Flame* 2012;159:2295–311.
- [22] Veloo PS, Wang YL, Egolfopoulos FN, Westbrook CK. A comparative experimental and computational study of methanol, ethanol, and *n*-butanol flames. *Combust Flame* 2010;157:1989–2004.
- [23] Sarathy SM, Vranckx S, Yasunaga K, Mehl M, Oßwald P, Metcalfe WK, et al. A comprehensive chemical kinetic combustion model for the four butanol isomers. *Combust Flame* 2012;159:2028–55.
- [24] Clair JGS, Behrens DA, Lee IC. Catalytic combustion of 1-butanol coupled with heat harvesting for compact power. *Combust Flame* 2011;158:1890–7.
- [25] Behrens DA, Lee IC, Waits CM. Catalytic combustion of alcohols for microburner applications. *J Power Sources* 2010;195:2008–13.
- [26] Papaefthimiou P, Ioannides T, Verykios XE. Combustion of non-halogenated volatile organic compounds over group VIII metal catalysts. *Appl Catal B: Environ* 1997;13:175–84.
- [27] Kruger JS, Chakrabarti R, Hermann RJ, Schmidt LD. Autothermal partial oxidation of butanol isomers. *Appl Catal A: Gen* 2012;411–412:87–94.
- [28] Finol MF, Rooke J, Su B-L, Trentesaux M, Giraudon J-M, Lamonier J-F. Additional effects of Pt and Nb on hierarchically porous titania in the catalytic removal of *n*-butanol. *Catal Today* 2012;192:154–9.
- [29] Basińska A, Klimkiewicz R, Domka F. Ru/Fe₂O₃ catalysts in *n*-butanol conversion. *Appl Catal A: Gen* 2001;207:287–94.
- [30] Azalim S, Franco M, Brahmib R, Giraudon J-M, Lamonier J-F. Removal of oxygenated volatile organic compounds by catalytic oxidation over Zr–Ce–Mn catalysts. *J Hazard Mater* 2011;188:422–7.
- [31] Kirchnerova J, Cohen M-LH, Guy C, Klvana D. Photocatalytic oxidation of *n*-butanol under fluorescent visible light lamp over commercial TiO₂ (Hombicat UV100 and Degussa P25). *Appl Catal A: Gen* 2005;282:321–32.
- [32] Tian ZY, Bahlawane N, Qi F, Kohse-Höinghaus K. Catalytic oxidation of hydrocarbons over Co₃O₄ catalyst prepared by CVD. *Catal Commun* 2009;11:118–22.

- [33] Zhang L, Zhang CB, He H. The role of silver species on Ag/Al₂O₃ catalysts for the selective catalytic oxidation of ammonia to nitrogen. *J Catal* 2009;261:101–9.
- [34] Chafik T, Harti S, Cifredo G, Gatica JM, Vidal H. Easy extrusion of honeycomb-shaped monoliths using Moroccan natural clays and investigation of their dynamic adsorptive behavior towards VOCs. *J Hazard Mater* 2009;170:87–95.
- [35] Harti S, Cifredo G, Gatica JM, Vidal H, Chafik T. Physicochemical characterization and adsorptive properties of some Moroccan clay minerals extruded as lab-scale monoliths. *Appl Clay Sci* 2007;36:287–96.
- [36] Caudo S, Centi G, Genovese C, Perathoner S. Copper- and iron-pillared clay catalysts for the WHPCO of model and real wastewater streams from olive oil milling production. *Appl Catal B: Environ* 2007;70:437–46.
- [37] Zuo SF, Huang QQ, Li J, Zhou RX. Promoting effect of Ce added to metal oxide supported on Al pillared clays for deep benzene oxidation. *Appl Catal B: Environ* 2009;91:204–9.
- [38] Srinivasan R. *Advances in materials science and engineering*. Hindawi Publishing Corporation 2011; 2011. p. 872531.
- [39] Huang YJ, Ye YS, Syu YJ, Hwang BJ, Chang FC. Synthesis and characterization of sulfonated polytriazole-clay proton exchange membrane by in situ polymerization and click reaction for direct methanol fuel cells. *J Power Sources* 2012;208:144–52.
- [40] Chao WK, Lee CM, Shieu SY, Chou CC, Shieu FS. Clay as a dispersant in the catalyst layer for zinc-air fuel cells. *J Power Sources* 2008;177:637–42.
- [41] Falamaki C, Ebadzadeh T. Kinetic investigation of the carbothermal reduction of an Iranian clay. *Ceram Int* 2002;28:887–92.
- [42] Herzig PM, Humphris SE, Miller DJ, Zierenberg RA. (Eds.); 1998.
- [43] Salerno P, Asenjo MB, Mendioroz S. Molybdenum species identification on pillared clays by temperature-programmed reduction. *Thermochim Acta* 2001;379:111–5.
- [44] Rodríguez-Carvajal J. Recent advances in magnetic structure determination by neutron powder diffraction. *Physica B* 1993;192:55–69.
- [45] Bahlawane N, Kohse-Höinghaus K, Weimann T, Hinze P, Röhe S, Bäumer M. Rational design of functional oxide thin films with embedded magnetic or plasmonic nanoparticles. *Angew Chem Int Ed* 2011;50:9957–60.
- [46] Tian ZY, Ngamou PHT, Vannier V, Kohse-Höinghaus K, Bahlawane N. Catalytic combustion of VOCs over mixed Co–Mn oxides. *Appl Catal B: Environ* 2012;117–118:125–34.
- [47] Yates M, Martin JA, Martin-Luengo MA, Blanco J. Study of the efficiency of monolithic activated carbon adsorption units. *Stud Surf Sci Catal* 2007;160:583–90.
- [48] Yu FD, Luo L, Grevillot G. Electrothermal swing adsorption of toluene on an activated carbon monolith: experiments and parametric theoretical study. *Chem Eng Process* 2007;46:70–81.
- [49] Gatica JM, Rodríguez-Izquierdo JM, Sánchez D, Chafik T, Harti S, Zaitan H, et al. Originally prepared carbon-based honeycomb monoliths with potential application as VOCs adsorbents. *C R Chimie* 2006;9:1215–20.
- [50] Vergunst T, Linders MJG, Kapteijn F, Moulijn JA. Carbon based monolithic structures. *Catal Rev* 2001;43:291–314.
- [51] Linstrom PJ, Mallard WG. NIST Chemistry Webbook, NIST Standard Reference Database Number 69, June 2005, National Institute of Standards and Technology, Gaithersburg, MD 20899; 2005. <<http://webbook.nist.gov/chemistry>>.
- [52] Feng YZ, Rao PM, Kim DR, Zheng XL. Methane oxidation over catalytic copper oxides nanowires. *Proc Combust Inst* 2011;33:3169–75.
- [53] Benvenuti EV, Gushikem Y. Comparative study of catalytic oxidation of ethanol to acetaldehyde using Fe(III) dispersed on Sb₂O₅ grafted on SiO₂ and on untreated SiO₂ surfaces. *J Braz Chem Soc* 1998;9:469–72.
- [54] Miki T, Tai Y. Catalytic oxidation of toluene over Fe₂O₃/Al₂O₃ catalyst. *Mater Sci Forum* 2011;695:101–4.
- [55] Molina CB, Casas JA, Zazo JA, Rodríguez JJ. A comparison of Al–Fe and Zr–Fe pillared clays for catalytic wet peroxide oxidation. *Chem Eng J* 2006;118:29–35.
- [56] Barshad I, Kishk FM. Chemical composition of soil vermiculite clays as related to their genesis. *Contr Mineral Petrol* 1969;24:136–55.



Corrigendum

Corrigendum to: Towards biofuel combustion with an easily extruded clay as a natural catalyst [Appl. Energy 107 (2013) 149–156]

Zhen-Yu Tian^{a,*}, Tarik Chafik^b, Mhamed Assebban^b, Sanae Harti^b, Hilario Vidal^c, José M. Gatica^c, Gustavo A. Cifredo^c, Naoufal Bahlawane^{a,1}, Patrick Mountapmbeme Kouotou^a, Katharina Kohse-Höinghaus^a

^a Department of Chemistry, Bielefeld University, Universitätsstraße 25, D-33615 Bielefeld, Germany,

^b Laboratory LGCVR, Faculty of Sciences and Techniques, University Abdelmalek Essaadi, B.P. 416 Tangier, Morocco

^c Departamento C.M., I.M. y Química Inorgánica, Universidad de Cádiz, Puerto Real 11510, Spain

The authors regret that the printed version of the above article contained a number of errors. The correct and final information follows. We would like to apologize for any inconvenience caused.

Results concerning the preparation and characterization of the natural clay monolith used in the article were obtained in the doctoral thesis of Sanae Harti under the direction of Prof. Tarik Chafik, University Abdelmalek Essaadi, Tangier, Morocco, with co-supervision by Prof. Hilario Vidal, University of Cádiz, Spain. It was brought to our attention that information regarding these results is incomplete and in part incorrect in the article.

The authors wish to clarify that the clay brought to the Bielefeld University laboratories for catalytic performance investigations and comparison with pulsed-spray chemical vapor deposition (PSE-CVD)-made catalytic materials is identical with the clay “FERA” in Ref. [34]. The mineralogical composition of this clay is given in Table 2; here, the phase label of muscovite should be corrected to muscovite (01-089-6216). Note also a typographical error in the phase label of kaolinite which should read (01-080-0885). This mineralogical composition of the clay matches that of FERA in Table 1 of Ref. [34] closely.

The elemental analysis of the clay in Table 3 is erroneously given in wt%; rather, the values reported correspond to mol%. They are comparable to those given in Table 2 of Ref. [34] for FERA.

The clay monolith was incorrectly stated in paragraph 2.1. on p. 150 as “(corning: 413 channels per square inch)”; here, the word “corning” should be eliminated.

The mechanical resistance of the extruded monolith is erroneously stated in paragraph 3.2. on p. 152 as 2.5 MPa. This resistance is characteristic of the FERA monolith with 3 × 3 channels and square cross section shown in Fig. 1 of Ref. [34]. Textural characteristics were investigated by means of adsorption/desorption of N₂ at –196 °C, using a Micromeritics ASAP 2020C instrument at the University of Cádiz. The experiments were performed with

samples which were, first, subjected to heating treatment under high vacuum at 200 °C for 4 h for both raw clay powder and pieces from the crushed extruded monoliths. The isotherms obtained were used to calculate the specific surface area and the porosity using the equipment’s software. These measurements were performed and processed by Sanae Harti with supervision of Dr. José M. Gatica, University of Cádiz.

The corresponding paragraph on p. 152 should thus read:

“The axial crush test of extruded clay monoliths with square cross section and around 14 cells cm^{–2} in Ref. [34] reveals a mechanical resistance of 2.5 MPa. Although this value is lower than those reported for ceramic composites [47] and carbon-coated cordierite monoliths [48], it shows better performance than that for integral-type carbon monoliths extruded with binders [49] and is equivalent to the carbon-based monolith [50], demonstrating its potential for practical application. It is worth noting that the monolithic clay was extruded easily without any additives or binders. Moreover, according to previous experience working with carbon honeycomb monoliths [49] and results demonstrated in [57], the mechanical resistance of the clay honeycomb monoliths studied here should improve as a consequence of their higher cell density”.

The authors wish to report that the micrographs in Fig. 1d and 1e were obtained during Sanae Harti’s thesis in the Central Service of Science and Technology of the University of Cádiz using its SEM facilities. SEM images were obtained with a QUANTA-200 scanning electron microscope (Philips) equipped with a Phoenix Microanalysis System using a nominal resolution of 3 nm. Both acquisition and interpretation of SEM images as well as EDS results were carried out by Dr. Hilario Vidal, University of Cádiz. Note that both micrographs show a raw clay sample at different magnification; the result in Fig. 1e thus does not represent a piece from the extruded monolith as erroneously reported in the caption of Fig. 1.

Further, the XRD results shown in Fig. 3a were also obtained during Dr. Sanae Harti’s thesis in the Central Service of Science and Technology of the University of Cádiz using its XRD facilities. The diffractogram was registered at room temperature using a Bruker D8-500 powder diffractometer operating with Cu K α radiation. The 2 Θ angle ranged from 6° to 65° with a step of 0.03°/5 s,

DOI of original article: <http://dx.doi.org/10.1016/j.apenergy.2013.02.025>

* Corresponding author. Tel.: +49 521 106 2199; fax: +49 521 106 6027.

E-mail address: zhenyu.tian@uni-bielefeld.de (Z.-Y. Tian).

¹ Present address: Nanomaterials Research Unit, SAM Department, Centre de Recherche Public, Gabriel Lippmann, L-4422 Belvaux, Luxembourg.

from 65° to 105° with a step of 0.05° during a counting time of 7 s, and from 105° to 145° with a step of 0.07° and a counting time of 9.5 s. The results were mainly interpreted by Dr. Gustavo A. Cifredo, University of Cádiz.

Regarding their involvement in the corresponding experiments and their interpretation, specified above, Drs. Hilario Vidal, José M. Gatica, and Gustavo A. Cifredo, Departamento C.M., I.M. y Química Inorgánica, Universidad de Cádiz, Puerto Real 11510, Spain are now included as authors of the present article. The team at the University of Cádiz wishes to thank the Ministry of Science and Innovation of Spain/FEDERProgram of the EU (Project MAT2008-00889/NAN), the Junta de Andalucía (FQM-110 group) and the International Cooperation Spanish Agency (AECI Project A/8880/

07) for their financial support. The Central Service of Science and Technology of the University of Cádiz is gratefully acknowledged for use of their SEM and XRD facilities.

The conclusions of the above article are not affected.

References

- [34] Chafik T, Harti S, Cifredo G, Gatica JM, Vidal H. Easy extrusion of honeycomb-shaped monoliths using Moroccan natural clays and investigation of their dynamic adsorptive behavior towards VOCs. *J Hazard Mater* 2009;170:87–95.
- [57] Gatica JM, Harti S, Vidal H. Changing the adsorption capacity of coal-based honeycomb monolith for pollutant removal from liquid streams by controlling their porosity. *Appl Surf Sci* 2010;256:7111–7.

Bibliographic References

- [1] P. Mountapmbeme Kouotou, Z.-Y. Tian, U. Mundloch, N. Bahlawane and K. Kohse-Höinghaus, Controlled synthesis of Co_3O_4 spinel with $\text{Co}(\text{acac})_3$ as precursor. *RSC Advances* **2**, 10809-10812, 2012.
- [2] P. Mountapmbeme Kouotou, Z.-Y. Tian, H. Vieker, A. Beyer, A. Götzhäuser and K. Kohse-Höinghaus, Selective synthesis of $\alpha\text{-Fe}_2\text{O}_3$ thin films and effect of the deposition temperature and lattice oxygen on the catalytic combustion of propene. *Journal of Materials Chemistry A* **1**, 10495-10504, 2013.
- [3] P. Mountapmbeme Kouotou, Z.-Y. Tian, H. Vieker and K. Kohse-Höinghaus, Pulsed-spray evaporation CVD synthesis of hematite thin films for catalytic conversion of CO. *Surface Coating Technology* **230**, 59-65, 2013.
- [4] Z.-Y. Tian, H. J. Herrenbrück, P. Mountapmbeme Kouotou, H. Vieker, A. Beyer, A. Götzhäuser, and K. Kohse-Höinghaus, Facile synthesis of copper oxide from alcohol-assisted CVD. *Surface Coating Technology* **230**, 33-38, 2013.
- [5] Z.-Y. Tian, P. Mountapmbeme Kouotou, N. Bahlawane, and P. H. Tchoua Ngamou, Synthesis of catalytically active Mn_3O_4 spinel and its thermal properties. *Journal of Physical Chemistry C* **117**, 6218-6224, 2013.
- [6] Z.-Y. Tian, T. Chafik, M. Assebban, S. Harti, N. Bahlawane, P. Mountapmbeme Kouotou and K. Kohse-Höinghaus, Towards biofuel combustion with an easily extruded clay as a natural catalyst. *Applied Energy* **107**, 149-156, 2013. Corrigendum to: Towards biofuel combustion with an easily extruded clay as a natural catalyst [Applied Energy **107** 149-156, 2013] *Applied Energy*, **108**, 528-529, 2013.
- [7] B. Bhatta, Analysis of urban growth and sprawl from remote sensing data. *Springer Heidelberg Dordrecht* (London New York) 2010.
- [8] A. J. McMichael, R. E. Woodruff and S. Hales, Climate change and human health: present and future risks. *The Lancet* **367**, 11-17, 2006.
- [9] M. Haruta, The chemical industry would be transformed if selective oxidation of hydrocarbons could be achieved efficiently using cheap and clean oxygen from the air. Doing that with gold as a catalyst is a method gaining in allure. *Nature* **437**, 1098-1099, 2005.
- [10] H. H. Kung. Transition metal oxides: surface chemistry and catalysis. *Elsevier* (Amsterdam-Oxford-New-York-Tokyo) 1989.
- [11] J. D. Spengler, P. Koutrakis, D. W. Dockery, M. Raizenne and F. E. Speizer, Health effects of acid aerosols on North American children: air pollution exposures. *Environmental Health Perspectives* **104**, 492-499, 1996.

Bibliographic References

- *****
- [12] S. Holgate, J. Samet, H. Koren and R. Maynard, Air pollution and health. *Academic Press* (London-California) 1999.
- [13] K. Katsouyanni, G. Touloumi and C. Spix, Short-term effects of ambient sulphur dioxide and particulate matter on mortality in 12 European cities: results from times series data from the *APHEA project*. *British Medical Journal* **314**, 1658-63, 1997.
- [14] D. W. Dockery, C. A. Pope, X. Xu, J. D. Spengler, J. H. Ware, M. E. Fay, B. G. Ferris and F. E. Speizer, An association between air pollution and mortality in six US cities. *The New England Journal of Medicine* **329**, 1753-1759, 1993.
- [15] C. A. Pope III, M. J. Thun, M. M. Namboodiri, D. W. Dockery, J. S. Evans, F. E. Speizer and C. W. Heath Jr., Particulate air pollution as a predictor of mortality in a prospective study of US adults. *American Journal of Respiratory and Critical Care medicine* **151**, 669-674, 1995.
- [16] H. Meixner, J. Gerblinger, U. Lampe and M. Fleischer, Thin-film gas sensors based on semiconducting metal oxides. *Sensors and Actuators B* **23**, 119-125, 1995.
- [17] Y. S. H. Najjar, Gaseous pollutants formation and their harmful effects on health and environment. *Innovative Energy Policies* **1**, 2011. Article ID E101203
- [18] A. Foster and N. Kumar, Health effects of air quality regulations in Delhi, India. *Atmospheric Environment* **45**, 1675-1683, 2011.
- [19] C. A. Pope III, D. W. Dockery and J. Schwartz, Review of epidemiological evidence of health effects of particulate air pollution. *Inhalation Toxicology* **7**, 1-18, 1995.
- [20] T. Bell, The impact of nanoscience on heterogeneous catalysis. *Science* **299**, 1688-1691, 2003.
- [21] M. Bowker, The basis and applications of heterogeneous catalysis, *Oxford University Press* (New York) 1998.
- [22] J. Hagen, Industrial Catalysis: A Practical Approach; 2nd Edition, *WILEY-VCH Verlag GmbH & Co. KGaA* (Weinheim, Germany) 2006.
- [23] J. J. Berzelius, Einige Ideen über eine bei der Bildung organischer Verbindungen in der lebenden Natur wirksame, aber bisher noch nicht bemerkte Kraft. *Jahres-Bericht über die Fortschritte der Physischen Wissenschaften* **15**, 237-245, 1835.
- [24] W. Ostwald, Über die Katalyse. *Zeitschrift für Physikalische Chemie* **3**, 313-322, 1901.
- [25] G. Ertl, Reactions at surfaces: from atoms to complexity. *Nobel Lecture*, December 8, 2007.
- [26] G. C. Bond, Heterogeneous catalysis principles and applications, 2nd Edition, *Oxford University Press* (United Kingdom) 1987.

Bibliographic References

- *****
- [27] I. Chorkendroff and J. W. Niemantsverdriet, Concepts of modern catalysis and kinetics. *Wiley-VCH Verlag GmbH & Co* (Weinheim, Germany) 2007.
- [28] R. Burch, Knowledge and know-how in emission control for mobile applications. *Catalysis Reviews: Science and Engineering* **46**, 271-334, 2005.
- [29] Z. Kowalczyk, J. Sentek, S. Jodzis, M. Muhler and O. Hinrichsen, Effect of potassium on the kinetics of ammonia synthesis and decomposition over fused iron catalyst at atmospheric pressure. *Journal of Catalysis* **169**, 407-414, 1997.
- [30] Z. Kowalczyk, M. Krukowski, W. Rarog-Pilecka, D. Szmigiel and J. Zielinski, Carbon-based ruthenium catalyst for ammonia synthesis: Role of the barium and caesium promoters and carbon support. *Applied Catalysis A: General* **248**, 67-73, 2003.
- [31] D. Szmigiel, H. Bielawa, M. Kurtz, O. Hinrichsen, M. Muhler, W. Rarog, S. Jodzis, Z. Kowalczyk, L. Znak and J. Zielinski, The kinetics of ammonia synthesis over Ruthenium-based catalysts: The role of Barium and Cesium. *Journal of Catalysis* **205**, 205-212, 2002.
- [32] R. A. van Santen and J. W. Niemantsverdriet, Chemical kinetics and catalysis. *Plenum Press* (New York) 1995.
- [33] Y. Sun and Y. Xia, Shape-controlled synthesis of gold and silver nanoparticles. *Science* **298**, 2176-2179, 2002.
- [34] M. Hermanek, R. Zboril, I. Medrik, J. Pechousek, and C. Gregor, Catalytic efficiency of iron(III) oxides in decomposition of hydrogen peroxide: Competition between the surface area and crystallinity of nanoparticles. *Journal of American Chemical Society* **129**, 10929-10936, 2007.
- [35] S. Colussi, A. Gayen, J. Llorca, C. de Leitenburg, G. Dolcetti, and A. Trovarelli, Catalytic performance of solution combustion synthesized alumina- and ceria-supported Pt and Pd nanoparticles for the combustion of propane and dimethyl ether (DME). *Industrial & Engineering Chemistry Research* **51**, 7510-7517, 2012.
- [36] V. Idakiev, T. Tabakova, K. Tenchev, Z.-Y. Yuan, T.-Z. Ren and B.-L. Su, Gold nanoparticles supported on ceria-modified mesoporous titania as highly active catalysts for low-temperature water-gas shift reaction. *Catalysis Today* **128**, 223-229, 2007.
- [37] T. Barakat, J. C. Rooke, E. Genty, R. Cousin, S. Siffert and B.-L. Su, Gold catalysts in environmental remediation and water-gas shift technologies. *Energy & Environmental Science* **6**, 371-391, 2013.
- [38] J. M. Jones, V. A. Dupont, R. Brydson, D. J. Fullerton, N. S. Nasri, A. B. Ross and A. V. K. Westwood, Sulphur poisoning and regeneration of precious metal catalyzed methane combustion. *Catalysis Today* **81**, 589-601, 2003.
- [39] N. Dimitratos, J. A. Lopez-Sanchez and G. J. Hutchings, Selective liquid phase oxidation with supported metal nanoparticles. *Chemical Science* **3**, 20-44, 2012.

- [40] A. O. Rusu and E. Dumitriu, Destruction of volatile organic compounds by catalytic oxidation. *Environmental Engineering and Management Journal* **2**, 273-302, 2003.
- [41] J. Ludvíková, K. Jiráková and F. Kovanda, Mixed oxides of transition metals as catalysts for total ethanol oxidation. *Chemical Papers* **66**, 589-597, 2012.
- [42] Z. Guo, B. Liu, Q. Zhang, W. Deng, Y. Wang and Y. Yang, Recent advances in heterogeneous selective oxidation catalysis for sustainable chemistry. *Chemistry Society Reviews* **43**, 3480-3524, 2014.
- [43] S. Royer and D. Duprez, Catalytic oxidation of carbon monoxide over transition metal oxides. *ChemCatChem* **3**, 24-65, 2011.
- [44] A. J. Zarur and J. Y. Ying, Reverse micro-emulsion synthesis of nanostructured complex oxides for catalytic combustion. *Nature* **403**, 65-67, 2000.
- [45] W. B. Ingler Jr., J. P. Baltrus and S. U. M. Khan, Photo-response of p-type zinc-doped iron(III) oxide thin films. *Journal of American Chemical Society* **126**, 10238-10239, 2004.
- [46] H. Tanaka and M. Misono, Advances in designing perovskite catalysts. *Current Opinion in Solid State and Materials Science* **5**, 381-387, 2001.
- [47] A. Civera, M. Pavese, G. Saracco and V. Specchia, Combustion synthesis of perovskite-type catalysts for natural gas combustion. *Catalysis Today* **83**, 199-211, 2003.
- [48] B. Xu, B. Huang, H. Cheng, Z. Wang, X. Qin, X. Zhang and Y. Dai, α -Fe₂O₃ hollow structures: formation of single crystalline thin shells. *Chemical Communication* **48**, 6529-6531, 2012.
- [49] K. Ralphs, C. Hardacre and S. L. James, Application of heterogeneous catalysts prepared by mechanochemical synthesis. *Chemistry Society Reviews* **42**, 7701-7718, 2013.
- [50] M. Sun, B. Lan, T. Lin, G. Cheng, F. Ye, L. Yu, X. Cheng and X. Zheng, Controlled synthesis of nanostructured manganese oxide: crystalline evolution and catalytic activities. *CrystEngComm* **15**, 7070-7018, 2013.
- [51] W. Oelerich, T. Klassen and R. Bormann, Metal oxides as catalysts for improved hydrogen sorption in nanocrystalline Mg-based materials. *Journal of Alloys and Compounds* **315**, 237-242, 2001.
- [52] M. C. Álvarez-Galvána, B. Paweleca, V. A. de la Peña O'Shea, J. L. G. Fierro and P. L. Arias, Formaldehyde/methanol combustion on alumina-supported manganese-palladium oxide catalysts. *Applied Catalysis B: Environmental* **51**, 83-91, 2004.
- [53] X. Wang, W. Tian, T. Zhai, C. Zhi, Y. Bando and D. Golberg, Cobalt(II,III)oxide hollow structures: fabrication, properties and applications. *Journal of Materials Chemistry* **22**, 23310-23326, 2012.

Bibliographic References

- [54] L. F. Liotta, H. Wu, G. Pantaleo and A. M. Venezia, Co_3O_4 nanocrystals and Co_3O_4 - MO_x binary oxides for CO, CH_4 and VOC oxidation at low temperatures: a review. *Catalysis Science Technology* **3**, 3085-3102, 2013.
- [55] H. Zhang, J.-L. Cao, G.-S. Shao and Z.-Y. Yuan, Synthesis of transition metal oxide nanoparticles with ultrahigh oxygen adsorption capacity and efficient catalytic oxidation performance. *Journal of Materials Chemistry* **19**, 6097-6099, 2009.
- [56] J. Ma, J. Teo, L. Mei, Z. Zhong, Q. Li, T. Wang, X. Duan, J. Lian and W. Zheng, Porous platelike hematite mesocrystals: synthesis, catalytic and gas-sensing applications. *Journal of Material Chemistry* **22**, 11694-11700, 2012.
- [57] P. O. Larsson and A. Andersson, Oxides of copper, ceria promoted copper, manganese and copper manganese on Al_2O_3 for the combustion of CO, ethyl acetate and ethanol. *Applied Catalysis B: Environmental* **24**, 175-192, 1996.
- [58] C. J. Heyes, J. G. Irwin, H. A. Johnson and R. L. Moss, The catalytic oxidation of organic air pollutants, Part 1: Single metal oxide catalyst. *Journal of Chemical Technology Biotechnology* **32**, 1025-1033, 1982.
- [59] P. Martin, Introduction to surface engineering and functionally engineered materials. *John Wiley & Sons, Inc. Hoboken (New Jersey) and Scrivener Publishing LLC, (Salem, Massachusetts)* 2011.
- [60] K. L. Choy, Chemical vapor deposition of coatings. *Progress in Materials Science* **48**, 57-170, 2003.
- [61] J.-P. Sénateur, C. Dubourdieu, F. Weiss, M. Rosina and A. Abrutis, Pulsed injection MOCVD of functional electronic oxides. *Advanced Materials for Optics and Electronics* **10**, 155-161, 2000.
- [62] J.-P. Sénateur, F. Weiss, O. Thomas, R. Madar and A. Abrutis, *Patent No 93/08838*, 1993.
- [63] F. Felten, J.-P. Sénateur, F. Weiss, R. Madar and A. Abrutis, Deposition of oxide layers by computer controlled "Injection-LPCVD". *Journal de Physique IV France* **5**, C5-1079-C5-1086, 1995.
- [64] S. Pasko, A. Abrutis, L. G. Hubert-Pfalzgraf and V. Kubilius, Cobalt (II)-diketonate adducts as new precursors for the growth of cobalt oxide films by liquid injection MOCVD. *Journal of Crystal Growth* **262**, 653-657, 2004.
- [65] M. Burriel, G. Garcia, J. Santiso, A. Abrutis, Z. Saltyte and A. Figueras, Growth kinetics, composition, and morphology of Co_3O_4 thin films prepared by pulsed liquid injection MOCVD. *Chemical Vapor Deposition* **11**, 106-111, 2005.
- [66] G. Garcia, J. Caro, J. Santiso, J. A. Pardo, A. Figueras and A. Abrutis, Pulsed injection MOCVD of YSZ thin films onto dense and porous substrates. *Chemical Vapor Deposition* **9**, 279-284, 2003.

- [67] C. Dubourdieu, M. Rosina, H. Roussel, F. Weiss, J.-P. Sénateur and J. L. Hodeau, Pulsed liquid-injection metalorganic chemical vapor deposition of $(\text{La}_{0.7}\text{Sr}_{0.3}\text{MnO}_3/\text{SrTiO}_3)_{15}$ superlattices. *Applied Physics Letters* **79**, 1246-1248, 2001.
- [68] W. Massa, Kristallstrukturbestimmung, 5th Edition, *Teubner* (Stuttgart) 2007.
- [69] P. Scherrer, Bestimmung der Größe und der inneren Struktur von Kolloidteilchen mittels Röntgenstrahlen. *Nachrichten von der Gesellschaft der Wissenschaften zu Göttingen Mathematisch-Physikalische Klasse* **2**, 98-100, 1918.
- [70] U. Holzwarth and N. Gibson, The Scherrer equation versus the Debye-Scherrer equation. *Nature Nanotechnology* **6**, 534-534, 2011.
- [71] V. Vannier, Deposition and characterization of complex metal and metal oxide Structures synthesized by chemical vapor deposition, *Dissertation*, Bielefeld 2012.
- [72] N. B. Colthup, L. H. Daly and S. E. Wiberly, Introduction to infrared and Raman spectroscopy, 2nd Edition, *Academic press* (New York San Francisco-London) 1975.
- [73] B. W. Ward, J. A. Notte and N. P. Economou, Helium ion microscope: A new tool for nanoscale microscopy and metrology. *Journal of Vacuum Science Technology B* **24**, 2871-2874, 2006.
- [74] R. Hill and F. H. M. Faridur Rahman, Advances in helium ion microscopy. *Nuclear Instruments and Methods in Physics Research Section A: Accelerators, Spectrometers, Detectors and Associated Equipment* **645**, 96-101, 2011.
- [75] J. I. Goldstein, D. E. Newbury, D. C. Joy, C. E. Lyman, P. Echlin, E. Lifshin, L. Sawyer and J. R. Michael, Scanning electron microscopy and X-ray microanalysis, 3rd Edition, *Kluwer academia/Plenum Publishers* (New York) 2003.
- [76] J. Morgan, J. Notte, R. Hill and B. Ward, An introduction to the Helium Ion Microscope. *Microscopy Today*, 2006.
- [77] G. Ceccone, D. Gilliland and W. Kulisch, Surface analytical characterization of biosensor materials. *Nanotechnological Basis for Advanced Sensors NATO Science for Peace and Security Series B: Physics and Biophysics* chapter 10, 81-102, 2011.
- [78] L. Wang, H. Wei, Y. Fan, X. Liu and J. Zhan, Synthesis, Optical Properties, and Photocatalytic Activity of One-Dimensional CdS@ZnS Core-Shell Nanocomposites. *Nanoscale Research Letters* **4**, 558-564, 2009.
- [79] J. Z. Zhang, Optical Properties and Spectroscopy of Nanomaterials. *World Scientific Publishing Co. Pte. Ltd* (Singapore) 2009.
- [80] Z.-Y. Tian, P. H. Tchoua Ngamou, V. Vannier K. Kohse-Höinghaus and N. Bahlawane, Catalytic oxidation of VOCs over mixed Co-Mn oxides. *Applied Catalysis B: Environment* **125**, 117-118, 2012.

- [81] Z.-Y. Tian, N. Bahlawane, V. Vannier and K. Kohse-Höinghaus, Structure sensitivity of propene oxidation over Co-Mn spinels. *Proceeding of the Combustion Institute* **34**, 2261-2268, 2013.
- [82] P. H. Tchoua Ngamou and N. Bahlawane, Influence of the arrangement of the octahedrally coordinated trivalent cobalt cations on the electrical charge transport and surface reactivity. *Chemistry of Materials* **22**, 4158-4165, 2010.
- [83] N. Bahlawane, P. A. Premkumar, J. Feldmann and K. Kohse-Höinghaus. *Chemical Vapor Deposition* **13**, 118-122, 2007.
- [84] W. C. Wiley and I. H. McLaren, Time-of-flight mass spectrometer with improved resolution. *Review of Scientific Instruments* **26**, 1150-1157, 1955.
- [85] J. C. Biordi, C. P. Lazzara and J. F. Papp, Molecular beam mass spectrometry applied to determining the kinetics of reactions in flames. *Combustion and Flame* **23**, 73-82, 1974.
- [86] C. A. Taatjes, N. Hansen, A. McIlroy, J. A. Miller, J. P. Sensosian, S. J. Klippenstein, F. Qi, L. S. Sheng, Y. W. Zhang, T. A. Cool, J. Wang, P. R. Westmoreland, M. E. Law, T. Kasper and K. Kohse-Höinghaus, Enols are common intermediates in hydrocarbon oxidation. *Science* **308**, 1887-1889, 2005.
- [87] U. Struckmeier, P. Oßwald, T. Kasper, L. Böhling, M. Heusing, M. Köhler, A. Brockhinke and K. Kohse-Höinghaus, Sampling probe influences on temperature and species concentration in molecular beam mass spectroscopic investigations of flat premixed low-pressure flames. *Zeitschrift für Physikalische Chemie* **223**, 503-537, 2009.
- [88] F. Herrmann, Massenspektrometrische Analyse der homogenisierten Niedertemperaturverbrennung in verschiedenen Reaktorsystemen. *Dissertation*, Bielefeld, 2013.
- [89] G. Busca, F. Trifiro and A. Vaccari, Characterization and catalytic activity of cobalt-chromium mixed oxides. *Langmuir* **6**, 1440-1447, 1990.
- [90] P. Poizot, S. Laruelle, S. Grugeon, L. Dupont and J. M. Tarascon, Nano-sized transition metal oxides as negative electrode materials for Lithium-ion batteries. *Nature* **407**, 496-499, 2000.
- [91] Z. Yuan, F. Huang, C. Feng, J. Sun and Y. Zhou, Synthesis and electrochemical performance of nanosized Co_3O_4 . *Materials Chemistry and Physics* **79**, 1-4, 2003.
- [92] Y. J. Mergler, J. Hoebink and B. E. Nieuwenhuys, CO oxidation over a Pt/CoOx/SiO₂ catalyst: A study using temporal analysis of products. *Journal of Catalysis* **167**, 305-313, 1997.
- [93] H. Hamada, Y. Kintashi, M. Inaba, M. Tabata, T. Yoshinari and H. Tsuchida, Role of supported metals in the selective reduction of nitrogen monoxide with hydrocarbons over metal/alumina catalysts. *Catalysis Today* **29**, 53-57, 1996.

- [94] A. S. K. Sinha and V. Shankar, Characterization and activity of cobalt oxide catalysts for total oxidation of hydrocarbons. *Chemical Engineering Journal* **52**, 115-120, 1993.
- [95] T. T. Kodas and M. J. Hampden-Smith, The chemistry of metal CVD. *VCH Verlagsgesellschaft mbHm* (Weinheim, Germany) *VCH Publishers Inc.* (New York) 1994.
- [96] N. S. Borgharkara, G. L. Griffin, A. James and A. W. Maverick, Alcohol-assisted growth of copper CVD films. *Thin Solid Films* **320**, 86-94, 1998.
- [97] P. A. Premkumar, N. Bahlawane and K. Kohse-Höinghaus, CVD of metals using alcohols and metal acetylacetonates, Part I: Optimization of process parameters and electrical characterization of synthesized films. *Chemical Vapor Deposition* **13**, 219-226, 2007.
- [98] P. A. Premkumar, A. Turchanin and N. Bahlawane, Effect of solvent on the growth of Co and Co₂C using pulsed-spray evaporation chemical vapor deposition. *Chemistry of Materials* **19**, 6206-6211, 2007.
- [99] S. Tanase, E. Bouwman, J. Reedijk, W. L. Driessen, M. Ferbinteanu, M. Huber, A. M. Mills and A. L. Spek, Synthesis and structural studies of two new base adducts of bis(2,4-pentanedionato)cobalt(II). *European Journal of Inorganic Chemistry* 1963-1969, 2004.
- [100] B. Atakan and M. A. Siddiqi, Cobalt diketonate complexes as CVD precursors: Issues of stability and vapor pressure. *Proceedings of the International symposium, EUROCV-15, The Electrochemical Society Inc., USA* **15**, 229-236, 2005.
- [101] X. W. Xie, Y. Li, Z. Q. Liu, M. Haruta and W. J. Shen, Low-temperature oxidation of CO catalysed by Co₃O₄ nanorod. *Nature* **458**, 746-749, 2009.
- [102] L. Hu, K. Sun, Q. Peng, B. Xu and Y. Li, Surface active sites on Co₃O₄ nanobelt and nanocube model catalysts for CO oxidation. *Nano Research* **3**, 363-368, 2010.
- [103] Y. Yu, T. Takei, H. Ohashi, H. He, X. Zhang and M. Haruta, Pretreatments of Co₃O₄ at moderate temperature for CO oxidation at -80 °C. *Journal of Catalysis* **267**, 121-128, 2009.
- [104] R. Schlögl and S. B. Abd Hamid, Nanocatalysis: mature science revisited or something really new? *Angewandte Chemie International Edition* **43**, 1628-1637, 2004.
- [105] A. J. Gellman and N. Shukla, Nanocatalysis: More than speed. *Nature Materials* **8**, 87-88, 2009.
- [106] X. Mou, X. Wei, Y. Li and W. Shen, Tuning crystal-phase and shape of Fe₂O₃ nanoparticles for catalytic applications. *CrystEngComm* **14**, 5107-5120, 2012.
- [107] L. P. Zhu, N. C. Bing, L. L. Wang, H. Y. Jin, G. H. Liao and L. J. Wang, Self-assembled 3D porous flowerlike α -Fe₂O₃ hierarchical nanostructures: synthesis, growth

- mechanism, and their application in photocatalysis. *Dalton Transaction* **41**, 2959-2965, 2012.
- [108] J. S. Xu and Y. J. Zhu, α -Fe₂O₃ hierarchically nanostructured mesoporous microspheres: Surfactant-free solvothermal combined with heat treatment synthesis, photocatalytic activity and magnetic property. *CrystEngComm* **14**, 2702-2710, 2012.
- [109] S. Gandhi, S. Sethuraman and U. Maheswari Krishnan, Synthesis, characterization and biocompatibility evaluation of iron oxide incorporated magnetic mesoporous silica. *Dalton Transaction* **41**, 12530-12537, 2012.
- [110] G. Bhargava, I. Gouzman, C. M. Chun, T. A. Ramanarayanan and S. L. Bernasek, Characterization of the “native” surface thin film on pure polycrystalline iron: A high resolution XPS and TEM study. *Applied Surface Science* **253**, 4322-4329, 2007.
- [111] G. K. Pradhan and K. M. Parida, Fabrication, growth mechanism, and characterization of α -Fe₂O₃ nanorods. *ACS Applied Material Interfaces* **3**, 317-323, 2011.
- [112] P. Meakin, Fractals, scaling and growth far from equilibrium. *Cambridge University Press* (London) 1998.
- [113] Ö. Özdemir and S. K. Banerjee, High temperature stability of maghemite (γ -Fe₂O₃). *Geophysical Research Letter* **11**, 161-164, 1984.
- [114] F. Wyrwalski, J. M. Giraudon and J. F. Lamonier, Synergistic coupling of the redox properties of supports and Co₃O₄ for the complete oxidation of volatile organic compounds. *Catalysis Letters* **137**, 141-149, 2010.
- [115] Z.-Y. Tian, N. Bahlawane, F. Qi and K. Kohse-Höinghaus, Catalytic oxidation of hydrocarbons over Co₃O₄ catalyst prepared by CVD. *Catalysis Communication* **11**, 118-122, 2009.
- [116] H. Baussart, R. Delobel, M. Le Bras and J. M. Leroy, Oxidation of propene on mixed oxides of copper and cobalt. *Journal of the Chemical Society, Faraday Transactions 1: Physical Chemistry in Condensed Phases* **75**, 1337-1345, 1979.
- [117] S. Ivanova, C. Petit and V. Pitchon, Application of heterogeneous gold catalysis with increased durability: Oxidation of CO and hydrocarbons at low temperature. *Gold Bulletin* **39**, 3-8, 2006.
- [118] A. C. Gluhoi, N. Bogdanchikova and B. E. Nieuwenhuys, Alkali (earth)-doped Au/Al₂O₃ catalysts for the total oxidation of propene. *Journal of Catalysis* **232**, 96-101, 2005.
- [119] R. Zhang, H. Alamdari, S. Kaliaguine, R. Zhang, H. Alamdari and S. Kaliaguine, Catalytic conversion of NO and C₃H₆ over silver catalysts under stoichiometric or excess oxygen. *Catalysis Letters* **119**, 108-119, 2007.

- [120] M. Machida, K. Ochiai, K. Ito and K. Ikeue, Synthesis, crystal structure and catalytic activity for C₃H₆ combustion of La-Sr-Cu-O-S with K₂NiF₄-type perovskite structure. *Journal of Catalysis* **238**, 58-66, 2006.
- [121] R. J. H. Voorhoeve, J. P. Remeika and D. W. Johnson, Rare-earth manganites: catalysts with low ammonia yield in the reduction of nitrogen oxides. *Science* **180**, 62-64, 1973.
- [122] C. Hu, Q. Zhu, Z. Jiang, L. Chen and R. Wu, Catalytic combustion of dilute acetone over Cu-Doped Ceria catalysts. *Chemical Engineering Journal* **152**, 583-590, 2009.
- [123] L. F. Liotta, M. Ousmane, G. Di Carlo, G. Pantaleo, G. Deganello, G. Marci, L. Retaillieu and A. Giroir-Fendler, Total oxidation of propene at low temperature over Co₃O₄-CeO₂ mixed oxides: Role of surface oxygen vacancies and bulk oxygen mobility in the catalytic activity. *Applied Catalysis A: General* **347**, 81-88, 2008.
- [124] T. Masui, Y. M. Peng, K. I. Machida and G. Y. Adachi, Reduction behavior of CeO₂-ZrO₂ solid solution prepared from cerium zirconyl oxalate. *Chemistry Materials* **10**, 4005-4009, 1998.
- [125] S. Anandan, X. Wen and S. Yang, Room temperature growth of CuO nanorod arrays on copper and their application as a cathode in dye-sensitized solar cells. *Materials Chemistry and Physics* **93**, 35-40, 2005.
- [126] T. J. Richardson, J. L. Slack and M. D. Rubin, Electrochromism in copper oxide thin films. *Electrochimica Acta* **46**, 2281-2284, 2001.
- [127] X. Zhang, G. Wang, W. Zhang, N. Hu, H. Wu and B. Fang, Seed mediated growth method for epitaxial array of CuO nanowires on surface of Cu nanostructures and its application as a glucose sensor. *Journal of Physical Chemistry C* **112**, 8856-8862, 2008.
- [128] M. Vaseem, A. Umar, Y. B. Hahn, D. H. Kim, K. S. Lee, J. S. Jang and J. S. Lee, Flower-shaped CuO nanostructures: Structural, photocatalytic and XANES studies. *Catalysis Communication* **10**, 11-16, 2008.
- [129] M. Zhou, Y. Gao, B. Wang, Z. Rozynek and J. O. Fossum, Carbonate-assisted hydrothermal synthesis of nanoporous CuO microstructures and their application in catalysis. *European Journal of Inorganic Chemistry* **2010**, 729-734, 2010.
- [130] F. Teng, W. Yao, Y. Zheng, Y. Ma, Y. Teng, T. Xu, S. Liang and Y. Zhu, Synthesis of flower-like CuO nanostructures as a sensitive sensor for catalysis. *Sensors and Actuators B: Chemical* **134**, 761-768, 2008.
- [131] A. Y. Oral, E. Mensur, M. H. Aslan and E. Basaran, The preparation of copper (II) oxide thin films and the study of their microstructures and optical properties. *Materials Chemistry and Physics* **83**, 140-144, 2004.
- [132] C. Doornkamp and V. Ponc, The universal character of the Mars and Van Krevelen mechanism. *Journal of Molecular Catalysis A: Chemical* **162**, 19-32, 2000.

- *****
- [133] G. Sedmak, S. Hočevár and J. Levec, Transient kinetic model of CO oxidation over a nanostructured $\text{Cu}_{0.1}\text{Ce}_{0.9}\text{O}_{2-y}$ catalyst. *Journal of Catalysis* **222**, 87-99, 2004.
- [134] Y. F. Shen, P. R. Zerger, R. N. DeGuzman, S. L. Suib, L. McCurdy, I. D. Potter and C. L. O'Young, Manganese oxide octahedral molecular sieves: preparation, characterization, and applications. *Science* **260**, 511-515, 1993.
- [135] M. Yin and S. O'Brien, Synthesis of monodisperse nanocrystals of manganese oxide. *Journal of the American Chemical Society* **125**, 10180-10181, 2003.
- [136] S. L. Brock, N. Duan, Z. R. Tian, O. Giraldo, H. Zhou and S. L. Suib, A review of porous manganese oxide materials. *Chemistry of Materials* **10**, 2619-2628, 1998.
- [137] M. Fernandez-Garcia, A. Martinez-Arias, J. C. Hanson and J. A. Rodriguez, Nanostructured oxides in chemistry: Characterization and properties. *Chemical Review* **104**, 4063-4104, 2004.
- [138] Y. Li, H. Tan, X.-Y. Yang, B. Goris, J. Verbeeck, S. Bals, P. Colson, R. Cloots, G. V. Tendeloo and B.-L. Su, Well shaped Mn_3O_4 nano-octahedra with anomalous magnetic behavior and enhanced photodecomposition properties. *Small* **7**, 475-483, 2011.
- [139] V. A. M. Brabers, F. M. Setten and P. S. A. van Knapen, X-ray photoelectron spectroscopy study of the cation valencies in nickel manganite. *Journal of Solid State Chemistry* **49**, 93-98, 1983.
- [140] B. Gillot, M. El Guendouzi and M. El Laarj, Particle size effects on the oxidation-reduction behavior of Mn_3O_4 hausmannite. *Materials Chemistry and Physics* **70**, 54-60, 2001.
- [141] N. S. McIntyre and D. G. Zetaruk, X-ray photoelectron spectroscopic studies of iron oxides. *Analytic Chemistry* **49**, 1521-1529, 1977.
- [142] M. Oku and K. J. Hirokawa, XPS of Co_3O_4 , Fe_3O_4 , Mn_3O_4 and related compounds. *Journal of Electron Spectroscopy and Related Phenomena* **7**, 465-473, 1975.
- [143] B. R. Strohmeier and D. M. Hercules, Surface spectroscopic characterization of manganese/aluminum oxide catalysts. *Journal of Physical Chemistry* **88**, 4922-4929, 1984.
- [144] V. Iablokov, K. Frey, O. Geszti and N. Kruse, High catalytic activity in CO oxidation over MnOx nanocrystals. *Catalysis Letter* **134**, 210-216, 2010.
- [145] N. Rezlescu, C. Doroftei, E. Rezlescu and P. D. Popa, Lithium ferrite for gas sensing applications. *Sensors Actuators B: Chemical* **133**, 420-425, 2008.
- [146] H. Yang, J. Yan, Z. Lu, X. Cheng and Y. Tang, Photocatalytic activity evaluation of tetragonal CuFe_2O_4 nanoparticles for the H_2 evolution under visible light irradiation. *Journal of Alloys and Compounds* **476**, 715-719, 2009.

- [147] A. Kraus, K. Jainae, F. Unob and N. Sukpirom, Synthesis of MPTS-modified cobalt ferrite nanoparticles and their adsorption properties in relation to Au(III). *Journal of Colloid and Interface Science* **338**, 359-365, 2009.
- [148] K. Praveena, K. Sadhana, S. Bharadwaj and S. R. Murthy, Development of nanocrystalline Mn-Zn ferrites for high frequency transformer applications. *Journal of Magnetism and Magnetic Materials* **321**, 2433-2437, 2009.
- [149] G. Evans, I. V. Kozhevnikov, E. F. Kozhevnikova, J. B. Claridge, R. Vaidhyanathan, C. Dickinson, C. D. Wood, A. I. Cooper and M. J. Rosseinsky, Particle size-activity relationship for CoFe₂O₄ nanoparticle CO oxidation catalysts. *Journal of Materials Chemistry* **18**, 5518-5523, 2008.
- [150] P. T. A. Santos, A. C. F. M. Costa, R. H. G. A. Kiminami, H. M. C. Andrade, H. L. Lira and L. Gama, Synthesis of a NiFe₂O₄ catalyst for the preferential oxidation of carbon monoxide (PROX). *Journal of Alloys and Compounds* **483**, 399-401, 2009.
- [151] L. Menini, M. C. Pereira, L. A. Parreira, J. D. Fabris and E. V. Gusevskaya, Cobalt- and manganese-substituted ferrites as efficient single-site heterogeneous catalysts for aerobic oxidation of monoterpenic alkenes under solvent-free conditions. *Journal of Catalysis* **254**, 355-364, 2008.
- [152] R. Nongjai, S. Khan, H. Ahmad, I. Khan and K. Asokan, Study of structural property of Co ferrite thin film grown by pulsed laser deposition technique. *AIP Conference Proceedings* **1451**, 163-165, 2012.
- [153] F.-X. Qin, S.-Y. Jia, Y. Liu, X. Han, H.-T. Ren, W.-W. Zhang, J.-W. Hou and S.-H. Wu, Metal-organic framework as a template for synthesis of magnetic CoFe₂O₄ nanocomposites for phenol degradation. *Materials Letters* **101**, 93-95, 2013.
- [154] N. Bahlawane, P. H. Tchoua Ngamou, V. Vannier, T. Kottke, J. Heberle and K. Kohse-Höinghaus, Tailoring the properties and the reactivity of the spinel cobalt oxide. *Physical Chemistry Chemical Physics* **11**, 9224-9232, 2009.
- [155] C. Altavilla, E. Ciliberto, A. Aiello, C. Sangregorio, and D. Gatteschi. A shortcut to organize self-assembled monolayers of cobalt ferrite nanoparticles on silicon. *Chemistry of Materials* **19**, 5980-5985, 2007.
- [156] W. F. Wei, W. X. Chen and D. G. Ivey, Rock salt-spinel structural transformation in anodically electrodeposited Mn-Co-O nanocrystals. *Chemistry of Materials* **20**, 1941-1947, 2008.
- [157] F. Nakagomi, S. W. da Silva, V. K. Garg, A. C. Oliverira, P. C. Morais, A. Franco Júnior and E. C. D. Lima, The influence of cobalt population on the structural properties of Co_xFe_{3-x}O₄. *Journal of Applied Physics* **101**, 09M514-09M517, 2007.
- [158] Z. Zhou, Y. Zhang, Z. Wang, W. Wei, W. Tang, J. Shi and R. Xiong, Electronic structure studies of the spinel CoFe₂O₄ by X-ray photoelectron spectroscopy. *Applied Surface Science* **254**, 6972-6975, 2008.

Bibliographic References

- *****
- [159] A. W. Moses, H. G. Garcia Flores, J.-G. Kim and M. A. Langell, Surface properties of LiCoO₂, LiNiO₂ and LiNi_{1-x}Co_xO₂. *Applied Surface Science* **253**, 4782-4791, 2007.
- [160] M. C. Biesinger, B. P. Payne, A. P. Grosvenor, L. W. M. Lau, A. R. Gerson and R. St. C. Smart, Resolving surface chemical states in XPS analysis of first row transition metals, oxides and hydroxides: Cr, Mn, Fe, Co and Ni. *Applied Surface Science* **257**, 2717-2730, 2011.
- [161] L. F. Liotta, H. Wu, G. Pantaleo and A. M. Venezia, Co₃O₄ nanocrystals and Co₃O₄-MO_x binary oxides for CO, CH₄ and VOC oxidation at low temperatures: a review. *Catalysis Science & Technology* **3**, 3085-3102, 2013.
- [162] P. Li, D. E. Miser, S. Rabiei, R. T. Yadav and M. R. Hajaligol, The removal of carbon monoxide by iron oxide nanoparticles. *Applied Catalysis B: Environmental* **43**, 151-162, 2003.
- [163] M. Arenz, K. J. J. Mayrhofer, V. Stamenkovic, B. B. Blizanac, T. Tomoyuki, P. N. Ross and N. M. Markovic, The effect of the particle size on the kinetics of CO electro-oxidation on high surface area Pt catalysts. *Journal of the American Chemical Society* **127**, 6819-6829, 2005.
- [164] R. C. Rai, S. Wilser, M. Guminiak, B. Cai and M. L. Nakarmi, Optical and electronic properties of NiFe₂O₄ and CoFe₂O₄ thin films. *Applied Physics A* **106**, 207-211, 2012.
- [165] Y.-F. Yu Yao, The Oxidation of Hydrocarbons and CO over Metal Oxides III, Co₃O₄ *Journal of Catalysis* **33**, 108-112, 1974.
- [166] P. Thormählen, M. Skoglundh, E. Fridell, and B. Andersson, Low-Temperature CO Oxidation over Platinum and Cobalt Oxide Catalysts *Journal of Catalysis* **188**, 300-310, 1999.
- [167] S. Veleva and F. Trifirò, The role of lattice and adsorbed oxygen in the oxidation of *n*-butene-1 and furan with MnMoO₄-based catalysts. *Reaction Kinetics and Catalysis Letters* **4**, 19-24, 1976.
- [168] H. Liu, P. Cheung and E. Iglesia, Zirconia-supported MoO_x catalysts for the selective oxidation of dimethyl ether to formaldehyde: Structure, redox properties, and reaction pathways. *Journal of Physical Chemistry B* **107**, 4118-4127, 2003.
- [169] H. Lee, J. C. Jung, H. Kim, Y. M. Chung, T. J. Kim, S. J. Lee, S. H. Oh, Y. S. Kim and I. K. Song, oxidative dehydrogenation of *n*-butene to 1,3-butadiene over sulfated ZnFe₂O₄ catalyst. *Catalysis Letters* **131**, 344-349, 2009.

